Magnesium Diboride Superconductors

for Magnet Applications

Magnesium Diboride Superconductors for Magnet Applications

H. van Weeren

ISBN 978-90-365-2519-0

Uitnodiging

Hierbij nodig ik u uit voor het bijwonen van de openbare verdediging van mijn proefschrift getiteld:

Magnesium Diboride Superconductors

for Magnet Applications

op vrijdag 8 juni 2007
om 15:00 uur in
gebouw "De Spiegel"
van de Universiteit Twente.

Hieraan voorafgaand zal ik om 14:45 uur het proefschrift kort toelichten

Aansluitend zal er een receptie worden verzorgd in hetzelfde gebouw

Harald van Weeren
Perikweg 22
7512 DR Enschede

Paranimfen:
Koray Karakaya
Sander Wessel

MAGNESIUM DIBORIDE SUPERCONDUCTORS FOR MAGNET APPLICATIONS

Ph.D. Committee:

Prof. dr. ing. D.H.A. Blank, University of Twente
Prof. dr. ir. H.J.M ter Brake, University of Twente / University of Eindhoven
dr. M. Dhallé, University of Twente
Prof. dr. ing. B. van Eijk, University of Twente / NIKHEF
Prof. dr. R. Flükiger, University of Geneva
dr. ir. B. ten Haken, University of Twente
Prof. dr. ir. J. Huetink, University of Twente
Prof. dr. ir. H.H.J. ten Kate, University of Twente
Prof. dr. P.J. Kelly, University of Twente (Chairman)

The work described in this thesis was performed at the Low Temperature Division, the Special Chair for High Current Superconductivity at the Faculty of Science and Technology, University of Twente, The Netherlands.

This work was supported by the Dutch Technology Foundation STW and also profitted from the EU FP6 research project NMP3-CT2004- 505724 ("HIPERMAG").

H. van Weeren
Magnesium Diboride Superconductors for Magnet Applications
Ph.D. thesis, University of Twente, The Netherlands

ISBN 978-90-365-2519-0

Cover: SEM image of MgB_2 in a sintered Powder-In-Tube conductor (front) and a drawing die (back).

Printed by PrintPartners Ipskamp, Enschede

MAGNESIUM DIBORIDE SUPERCONDUCTORS FOR MAGNET APPLICATIONS

PROEFSCHRIFT

ter verkrijging van
de graad van doctor aan de Universiteit Twente,
op gezag van de rector magnificus,
prof. dr. W.H.M. Zijm,
volgens besluit van het College voor Promoties
in het openbaar te verdedigen
op 8 juni 2007 om 15:00 uur

door

Harald van Weeren
geboren op 14 juli 1975
te Hoorn

Dit proefschrift is goedgekeurd door de promotor en assistent promotor

prof. dr. ir. H.H.J. ten Kate
dr. M. Dhallé

Nomenclature

Symbol	Meaning	Unit
A	Area	[m^2]
A_m	Cross-sectional area of the matrix	[m^2]
A_{sc}	Cross-sectional area of the superconductor	[m^2]
B	Magnetic field	[T]
B_0	Applied magnetic field	[T]
B^*	Irreversibility field	[T]
B_0^*	Irreversibility field @ $T = 0$ K	[T]
B_{100}	Magnetic field at which $J_c = 100\text{A/mm}^2$	[T]
B_c	Thermodynamic critical field	[T]
B_{c2}	Second critical field	[T]
$B_{c2,0}$	Second critical field @ $T = 0$ K	[T]
B_n	Exponential decay field of n-value	[T]
$B_{n,0}$	Exponential decay field of n-value @ $T = 0$ K	[T]
B_{offset}	Offset field in resistive transition	[T]
$B_{\text{offset},0}$	Offset field @ $T = 0$ K	[T]
B_{onset}	Onset field in resistive transition	[T]
$B_{\text{onset},0}$	Onset field @ $T = 0$ K	[T]
B_p	Exponential current decay field	[T]
$B_{p,0}$	Exponential current decay field @ $T = 0$ K	[T]
c	Volumetric heat capacity	[$\text{Jm}^{-3}\text{K}^{-1}$]
d	Diameter	[m]
D	Diffusivity	[m^2s]
D_m	Magnetic diffusivity	[m^2s]
D_T	Thermal diffusivity	[m^2s]
E_Y	Youngs' modulus	[GPa]
E	Electric field	[V/m]
E_c	Electric field criterion for I_c determination	[V/m]
f	Superconductor filling factor	[%]
f_i	Fraction of the i^{th} component in the composite	[%]

Continued on next page

Symbol	Meaning	Unit
h	Height	[m]
h_t	Heat transfer coefficient	[$\mathrm{Wm^{-2}K^{-1}}$]
H_v	Vickers hardness	[-]
I	Transport current	[A]
I_c	Critical current	[A]
$I_{c,0}$	Critical current @ $T = 0$ K and $B = 0$ T	[A]
I_0	Total transport current	[A]
I_m	Current in the matrix	[A]
I_{sc}	Current in the superconductor	[A]
J	Transport current density	[$\mathrm{Am^{-2}}$][1]
J_c	Critical current density	[$\mathrm{Am^{-2}}$][1]
$J_{c,0}$	Critical current density @ $T = 0$ K; $B = 0$ T	[$\mathrm{Am^{-2}}$][1]
$J_{c,0}^T$	Critical current density @ $B = 0$ T	[$\mathrm{Am^{-2}}$][1]
J_0	Total transport current density	[$\mathrm{Am^{-2}}$][1]
J_m	Current density in the matrix	[$\mathrm{Am^{-2}}$][1]
J_{sc}	Current density in the superconductor	[$\mathrm{Am^{-2}}$][1]
K_{I_c}	Strain dependence of the critical current	[-]
$K_{I_{c,0}}$	Strain dependence of the critical current @ $T = 0$ K; $B = 0$ T	[-]
K_{T_c}	Strain dependence of the critical temperature	[-]
K_{B_0}	Strain dependence of the irreversibility field	[-]
l	Length	[m]
l_{MPZ}	Minimum Propagation Zone length	[m]
MQE	Minimum Quench Energy	[J]
n	n-value in the relation $E \propto I^n$	[-]
n_0	n-value at $B = 0$ T	[-]
P	Power / Heat flux	[W]
P_{initial}	Injected power	[W]
p_{diss}	Dissipating power density	[$\mathrm{Wm^{-3}}$]
p_{initial}	Injected power density	[$\mathrm{Wm^{-3}}$]
Q	Heat	[J]
Q_{initial}	Thermal disturbance	[J]
R	Electrical resistance	[Ω]
R_t	Thermal resistance	[$\mathrm{KW^{-1}}$]
R_o	Initial outer radius of conductor	[m]
R_i	Initial interface radius	[m]
R_{fil}	Initial filament radius	[m]
R_{fo}	Final outer radius	[m]

Continued on next page

[1]The units for current density listed in this table are the official SI units. However, throughout the thesis the more practical unit [$\mathrm{Amm^{-2}}$] is used.

Symbol	Meaning	Unit
R_{fi}	Final interface radius	[m]
t	Time	[s]
T	Temperature	[K]
T_0	Operating temperature	[K]
T_c	Critical temperature	[K]
$T_{c,0}$	Critical temperature @ $B = 0$ T	[K]
T_{cs}	Current sharing temperature	[K]
T_{ns}	Normal state recovery temperature	[K]
T_{offset}	Offset temperature in resistive transition	[K]
T_{onset}	Onset temperature in resistive transition	[K]
T_s	Temperature at which heat generation starts	[K]
V	Voltage	[V]
v_{nz}	Normal zone propagation velocity	[ms^{-1}]
w	Width	[m]
z	Longitudinal coordinate along a conductor	[m]
Greek Symbols		
α	Thermal expansion coefficient	[-]
Δ	Superconducting gap energy	[J]
ϵ	Emissivity	[-]
ϵ	True strain	[-]
ϵ_f	True strain at final diameter	[-]
ε	Mechanical axial strain	[%]
$\varepsilon_{\text{applied}}$	Applied axial strain	[%]
ε_{rev}	Reversible strain limit	[%]
ε_{pre}	Strain induced by thermal pre-compression	[%]
$\gamma_{k,l}$	l^{th} root of the k^{th} order Bessel function Υ_k	[-]
κ	Thermal conductivity	[Wm^{-1}K^{-1}]
κ_m	Thermal conductivity of the matrix	[Wm^{-1}K^{-1}]
κ_{sc}	Thermal conductivity of the superconductor	[Wm^{-1}K^{-1}]
ν	View factor	[-]
μ_0	Magnetic permeability of vacuum ($4\pi \cdot 10^{-7}$)	[Hm^{-1}]
Λ	Current transfer length	[m]
ρ	Electrical resistivity	[Ωm]
ρ_m	Electrical resistivity of the matrix	[Ωm]
ρ_{sc}	Normal state electrical resistivity of the filaments	[Ωm]
ρ_{fil}	Filament density	[kgm^{-3}]
$\rho_{\text{fil},0}$	Initial filament density	[kgm^{-3}]
$\rho_{\text{fil,th}}$	Theoretical filament density	[kgm^{-3}]

Continued on next page

Symbol	Meaning	Unit
σ	Mechanical stress	$[\mathrm{Nm}^{-2}]$
σ_{SB}	Stefan-Boltzmann constant $(5.669 \cdot 10^{-8})$	$[\mathrm{Wm}^{-2}\mathrm{K}^{-4}]$
σ_y	Yield strength	$[\mathrm{Nm}^{-2}]$
τ_T	Thermal diffusion time	[s]
τ_m	Magnetic diffusion time	[s]

Contents

Chapter 1

Introduction

Magnesium diboride has several attractive features justifying its development into a new technical superconductor for use in magnet systems. It is relatively simple to synthesize, its raw-material costs are low, conductors can be made with existing technologies and operated at higher temperatures. But just like any other technical superconductor its applicability in magnets depends on several performance aspects on a fundamental- as well as a technological level. These issues are introduced in this chapter.

1.1 Magnesium Diboride

Magnesium diboride was first synthesised in the 1950's but it took until 2001 before its superconducting properties were discovered [1]. MgB_2 is sometimes considered as a medium-T_c superconductor. With low-T_c materials it has its metallic character in common, its relatively simple crystal structure and superconducting pairing that occurs through a BCS-like phonon mediated electron-electron interaction [2]. However, its T_c of 40 K is much higher than all previously known metallic superconductors. Moreover, like the high-T_c cuprates, it has a layered structure leading to significantly anisotropic properties [3]. Finally, MgB_2 shows two-gap superconductivity, a phenomenon that was considered theoretically possible in the past [4], but is experimentally observed for the first time in this material [5].

In terms of prospects for applications, its T_c makes MgB_2 attractive for operation at $\sim$ 20 K, a temperature that is reached relatively easily with cooling machines, cutting out the need for a liquid cryogen and simplifying the cryostat. Compared to high-T_c superconductors MgB_2 is attractive mostly because of its relative ease of synthesis. Together with the abundance of magnesium and boron, simpler production causes its presently estimated cost-to-performance ratio to be about 1 €/kA-m at an operating temperature of 4.2 K and a magnetic field of 2 T, instead of 50-200 €/kA-m for high-T_c conductors at 77 K and self-field [6,7].

1.2 Magnesium Diboride in Magnets

A major interest in the use of MgB_2 superconductors is in medium-field magnets. Superconductors in magnet systems drastically reduce power consumption, but the application of a superconducting magnet is restricted by the critical surface of the material used. As an example, the critical surface of an optimised MgB_2 conductor is presented in figure 1.1 [8]. Three critical parameters indicate the intersection of the critical surface with the current-, field- and temperature axes: the critical current density ($J_{c,0}$), the upper critical field ($B_{c2,0}$) and the critical temperature (T_c). Below the critical surface, the material is in the superconducting state, above it is resistive.

When considering superconducting electromagnets purely from a performance point of view, a high-T_c material would be the conductor of choice. Indeed, a conduction-cooled Magnetic Resonance Imaging (MRI) demonstrator operating at 20 K with coils wound from $Bi_2Sr_2Ca_2Cu_3O_x$ was successfully constructed [9], while a record-breaking hybrid solenoid system was recently announced generating 25 T, using a $Bi_2Sr_2Ca_1Cu_2O_x$ insert coil to provide 5 T extra inside a resistive magnet of 20 T [10]. However, both $Bi_2Sr_2Ca_2Cu_3O_x$ and $Bi_2Sr_2Ca_1Cu_2O_x$ are considered too expensive for large magnet systems, while $YBa_2Cu_3O_x$ coated conductors are not yet commercially available in sufficient length [11]. At present the vast majority of superconducting magnets are made with Nb-Ti wires or, if higher fields are required, a combination of Nb-Ti outer coils and Nb_3Sn inner high-field coils.

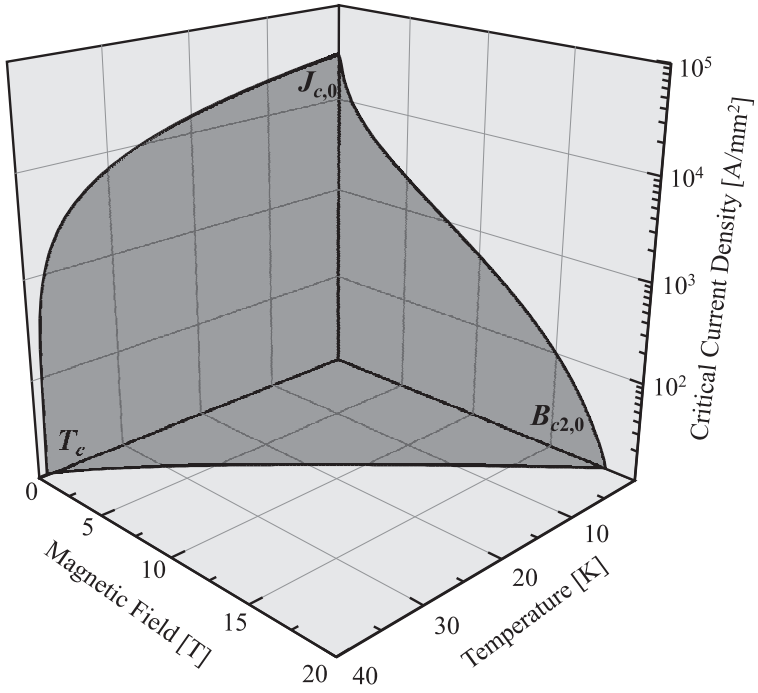

Figure 1.1: Critical surface of a MgB_2 conductor characterised by the three critical parameters: the critical current density ($J_{c,0}$), the upper critical field ($B_{c2,0}$) and the critical temperature (T_c) (based on the data in [8]).

The critical surfaces of state-of-the-art Nb_3Sn [12] and Nb-Ti [13,14] are compared with that of the present "record" MgB_2 conductor [8] in figure 1.2. The performance of Nb_3Sn is superior in terms of T_c and $B_{c2,0}$ to that of Nb-Ti, but economical arguments dictate the use of Nb-Ti in less demanding applications. Whereas the cost of commercial Nb-Ti is about 1 €/kA-m (at 4.2 K/5 T), Nb_3Sn is more complicated to produce and its costs fall in the range of 5-25 €/kA-m (at 4.2 K/12 T), depending on the fabrication process [6]. The operational requirements in terms of current density and magnetic field of actual large superconducting magnet applications are also projected in the current-field plane of figure 1.2. Note that superconducting research magnets are excluded since they can be considered as a "niche"-application in terms of both number of units and system size (and thus conductor lengths required) compared to superconducting magnets for MRI, Nuclear Magnetic Resonance (NMR), High Energy Physics (HEP) and Nuclear fusion (ITER). Among these application areas, the conductor choice for HEP and ITER magnets is presently mostly determined by performance and

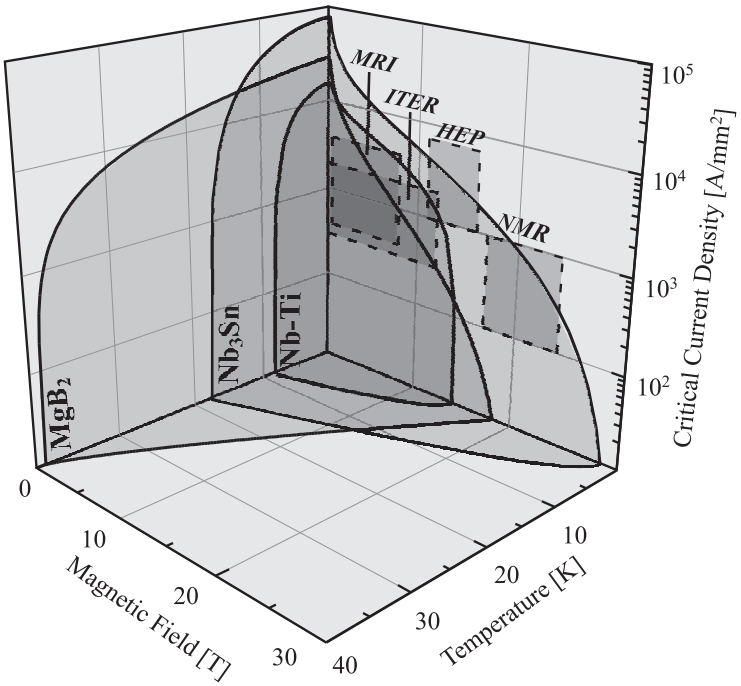

Figure 1.2: Comparison of the critical surfaces of MgB_2 and the most widely used superconducting materials Nb_3Sn and Nb-Ti (after [12–14]). The current-field projections of important applications, such as Magnetic Resonance Imaging (MRI), Nuclear Magnetic Resonance (NMR), High Energy Physics (HEP) and Fusion Energy (ITER) are also indicated.

other technical issues. MRI and NMR, on the other hand, are typical commercial products in the sense that a large and very competitive market dictates choices not only in technical but also in cost terms. As the present current-field behaviour of Nb-Ti and MgB_2 at 4.2 K is quite similar, both materials are of interest for applications such as MRI and medium performance research magnets. For commercial markets cost is a key issue. Indeed, MgB_2 will only be a true alternative for Nb-Ti if the production and running cost of a MgB_2 magnet system is less than that of a Nb-Ti-based magnet system generating a similar magnetic field. An indication for the potential for MgB_2 to be a economical technical superconductor is the fact that its raw materials costs are about 0.80 €/m, which is about half the cost of Nb-Ti [6].

The present $J_c(B)$ performance at 4.2 K of several commercial and laboratory-scale MgB_2 conductors [8, 17–23] is compared to that of state-of-the-art commer-

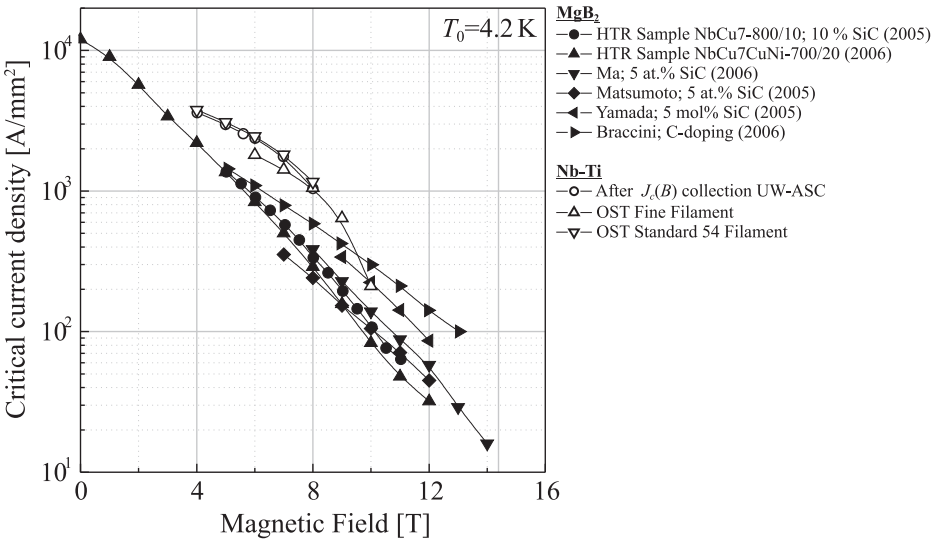

Figure 1.3: Collection of critical current density versus magnetic field characteristics of Nb-Ti and MgB_2 conductors from several authors. Nb-Ti data from [15,16], MgB_2 data obtained from [17–23]. Note: HTR stands for HyperTech Research.

cial Nb-Ti [15,16] in figure 1.3. For fields lower than $\sim$ 10 T, the $J_c(B)$ performance of MgB_2 falls slightly below that of Nb-Ti so that the cost-to-performance ratio is estimated as the earlier mentioned numbers of 1 €/kA-m at 2 and 5 T for MgB_2 and Nb-Ti respectively.

However, the microstructure of Nb-Ti is considered to be close to optimal, with a very fine distribution of α-Ti pinning sites (on the scale of $\sim$ 100 nm) and a carefully tuned composite conductor layout in terms of number and size of the filaments, superconductor filling factor, matrix conductivity and strength. MgB_2 in comparison is considered to be in an early stage of development and further scope for improvement seems realistic. In this respect it is quite likely that the cost-to-performance ratio of MgB_2 will improve further and become comparable to or even better that of Nb-Ti. An important improvement of the $J_c(B)$ performance was first reported by Dou *et. al.* in 2002 [24] who doped MgB_2 with SiC and increased J_c in higher magnetic fields with a factor of 5-10 compared to un-doped samples, while the present-day record laboratory scale conductor by Braccini *et. al.* [8] is a carbon doped conductor with a technical upper field limit at 4.2 K of 13 T, above which $J_c < 100\mathrm{A/mm}^2$. Furthermore, even the latest un-doped wires from HyperTech Research (e.g. sample NbCu7CuNi-700/20 from [19] in figure 1.3) have similar $J_c(B)$ characteristics to most SiC doped samples. Altogether this is indicative for the steady progress of MgB_2 conductors made since 2001.

Although the improvement of the cost-to-performance ratio can be expected to

continue it should also be mentioned that MgB_2 conductors, like Nb_3Sn, require a heat-treatment which adds to the cost of magnet production. In this sense, it will be beneficial if MgB_2 conductors permit a react-and-wind technique, i.e. that the conductor is heat treated prior to magnet winding. However, this will impose mechanical constraints on the conductor behaviour.

The high T_c of 40 K allows a MgB_2-based magnet system to be operated at higher temperatures. The $J_c(B,T)$ performance of the MgB_2 conductor from [17] shows that it can carry about 1 kA/mm^2 at a magnetic field of 4 T and an operating temperature of 20 K. These values directly meet the current-field requirements of MRI systems depicted in figure 1.2. Since 20 K is easily reached with present state-of-the-art cryocoolers, the cooling cost can be reduced significantly by the construction of a conduction-cooled MRI magnet system instead of using a relatively expensive liquid helium cryostat at 4.2 K.

Another possible area of application at 20 K is the foreseen emergence of hydrogen technology in the area of sustainable energy. In order to maximise mass density (and thus chemical energy density), H_2 might well be stored in the form of a cryogenic liquid, i.e. at or below its boiling point of 20.28 K. This raises the intriguing prospect of combining cryogenic chemical energy storage with various superconducting applications. For example, a H_2 operated fuel cell that converts the chemical energy released in the reaction $2H_2+O_2 \rightarrow 2H_2O$ to electrical energy works best with constant loads [25]. For applications that require peak loads, a buffer is required. Since batteries, that are presently used in prototypes, are often limited in terms of in- and output power, Superconducting Magnetic Energy Storage (SMES) can fulfill this buffer role as it is capable of storing and delivering large power levels [26].

Since the high-field $J_c(B,T)$ performance of MgB_2 at 4.2 K might surpass that of Nb-Ti, it is likely to be used in combination with Nb_3Sn conductors as well. NMR –another very competitive market– typically uses Nb-Ti/Nb_3Sn hybrid magnet systems (see for example [27]). Nb_3Sn is used in the high-field insert coils, while Nb-Ti is used in the low-field outsert coils. Replacing Nb-Ti in the outsert by MgB_2 might enable it to generate a higher field, requiring a less voluminous insert coil. This way cost can be significantly reduced since Nb_3Sn is a relative expensive material.

1.3 Design of Practical Superconductors

The design of a practical superconductor is dictated by the requirements of stable and safe operation. In practice a superconductor is a composite with a large number of fine superconducting filaments embedded in a highly conducting matrix, as depicted in figure 1.4.

Two important requirements that are treated in this thesis are: 1) the superconductor should be thermally stable and it should be possible to protect it against thermal instabilities; 2) the superconductor should be able to withstand

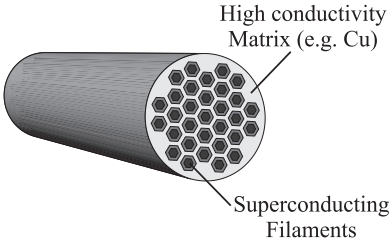

Figure 1.4: Typical cross-section of a superconducting wire in which the superconducting filaments are embedded in a highly conducting matrix.

the electromagnetic forces that act on it during magnet operation[1].

1.3.1 Thermal Stability

The lossless transport of very high current densities by a superconductor can, in a certain sense, be seen as a metastable process. When a superconductor carries a current, a small heat release of several micro-joules may already be enough to increase the local temperature well above T_c [28]. These small heat releases have, for example, a mechanical origin when the magnet is energised and large Lorentz forces start to act on the windings. The resulting "hot-spot" is in the ohmic state (the normal zone) and generates more heat. If heat is generated faster than it is drained, the zone will expand and eventually the whole wire will revert to the normal state, while continuing to carry a high current. When this happens in a magnet, the process is referred to as a quench. In such a process the temperature can rise dangerously fast and the wire might even locally melt or evaporate.

The possibility that an expanding normal zone occurs is inversely proportional to the minimum quench energy MQE. MQE is determined by the thermal margin that needs to be overcome to bring the superconductor locally in the normal state; by the corresponding heat, determined by the volumetric heat capacity c; by the initial heat generation ρJ^2; and by the degree of heat drainage, determined by both the volumetric heat capacity c and the thermal conductivity κ.

The impact of a normal zone is determined by the speed of its propagation along the conductor. A faster propagation implies that the generated heat is quickly distributed over a larger volume so that the local temperature rise remains limited. Furthermore, protection schemes that drain the energy stored in the magnet and thus prevent magnet damage typically trigger above a certain voltage level [28]. A faster propagating normal zone means that the voltage across a magnet section rises faster, the normal zone is detected earlier and the protection circuit is triggered faster. The velocity of the normal zone is determined by the

[1] There are further requirements like sufficiently low AC-loss. This issue is not treated in this thesis. Interested readers are referred to [28] for a general introduction and to [29] for the first AC-loss studies on MgB_2 conductors.

Table 1.1: Comparison of thermal stability related parameters of Nb_3Sn, MgB_2 and $Bi_2Sr_2Ca_2Cu_3O_x$.

		Nb_3Sn	MgB_2		$Bi_2Sr_2Ca_2Cu_3O_x$
		$T = 4.2$ K	$T = 4.2$ K	$T = 20$ K	$T = 77$ K
Matrix		Cu	Cu (Fe)[b]		Ag
f	[%]	55	55 [c]		30
B[a]	[T]	10	3		0
T_c(B)[a]	[K]	13	35		110
J_c(B)[a]	[$\cdot 100$A/mm^2]	40	20	6	2
κ[a]	[W/mK]	384	173 (3)	691 (35)	436
ρ[a]	[$\cdot 10^{-9}\Omega$m]	0.3	0.6 (15)	0.6 (14)	5
c[a]	[$\cdot 10^3$J/m^{3}K]	1.2	0.7 (1.7)	34 (20)	1550
D_T	[$\cdot 10^{-3}$m^2/s]	329	243 (1.5)	21 (1.7)	0.3
MQE	[$\cdot 10^{-3}$J]	0.1	3.3 (0.04)	90 (0.14)	611

[a] The data presented in this table are obtained from [19, 30–36]. The magnetic field B is chosen in such a way that the J_c values of the conductors are comparable.

[b] As will be shown later Cu is for chemical reasons not the ideal matrix material for MgB_2, therefore the values for ARMCO Fe are also added between brackets.

[c] This filling factor is chosen for comparison with the Nb_3Sn conductor and is the envisaged value. However at present the filling factor for typical MgB_2 conductors is closer to 30%.

conductors' thermal diffusivity $D_T = \kappa/c$; by the heat generation ρJ^2 in the normal zone; and by the thermal margin.

Both MQE and the velocity of a normal zone thus depend on the choice of matrix material. A highly conducting matrix causes heat to drain faster, which explains its use in composite conductors. The operating temperature of a conductor is also a key parameter since all relevant material properties are temperature dependent. For comparison, table 1.1 shows values of stability-related parameters for Nb_3Sn, MgB_2 and $Bi_2Sr_2Ca_2Cu_3O_x$ composite conductors at their usual operating temperatures. The effective volumetric heat capacity of the three materials increases drastically with operating temperature. Correspondingly, the diffusion constant decreases, while MQE increases. This results in a clear qualitative difference between the behaviour of low-T_c- and high-T_c conductors. The minimum quench energy of Nb_3Sn is relatively small compared to typical thermal disturbances that can occur inside a magnet, increasing the risk of a quench. However, due to the large thermal diffusivity the generated heat is rapidly distributed along the conductor, limiting the temperature rise. Moreover, the normal zone voltage across the conductor is easily measured. In $Bi_2Sr_2Ca_2Cu_3O_x$ the situation is reversed. MQE is large compared to typical disturbances, so there is a low risk that the conductor will quench. However, if such an event does occur, heating remains localised because of the low thermal diffusivity and a rapid growth of the local

temperature can be expected. The normal zone is difficult to detect because of its slow expansion. At an operating temperature of 4.2 K the characteristics of MgB_2 are quite similar to Nb_3Sn, depending on the matrix material. However, the envisaged operating temperature of MgB_2 can also be about 20 K. Thus, to gauge the suitability of MgB_2 conductors for magnet systems running at ~ 20 K, conductor properties will need to be carefully modeled and measured. Such study is the subject of chapter 4 of this thesis.

1.3.2 Mechanical Strain

Besides thermal stability, the response to mechanical stress can also impose stringent boundary conditions on the design of a practical superconductor. Strain is the response of a material to external stress, which at high levels causes irreversible changes of the superconducting properties due to damage in the superconducting filaments, especially in brittle materials like Nb_3Sn, MgB_2 and high-T_c conductors. At lower strain levels the superconducting properties change reversibly. Hydrostatic pressure experiments on superconducting materials indeed show a T_c reduction when the pressure is increased [37, 38]. This effect can to first order be explained by BCS theory through a reduced electron-phonon coupling energy due to lattice deformation [39].

Although the effects of hydrostatic pressure (i.e. lattice deformations) on the superconducting properties were already evident in the early 1960's [37], it took until the mid-1970's before technical superconductors were not only characterised by their critical current, upper critical field and critical temperature but also by their response to mechanical stress or strain [40]. Nb-Ti superconductors were subjected to longitudinal stress and a degradation of J_c was observed that could not be attributed to the reduction in cross-sectional area of the filaments induced by the conductor's elongation. In Nb-Ti this effect is small: a 10 % reduction of I_c requires an applied strain of about 2 % or 800 MPa of applied stress. Nb_3Sn and other A15 compounds are much more sensitive to strain. Early measurements by Ekin *et. al.* [41] showed 10 % degradation of I_c at only 0.2 % strain or an equivalent stress of 100 MPa, which is roughly a factor of 10 lower than in Nb-Ti. In view of the technical relevance of the strain response of superconductors, Ekin described a four dimensional J-B-T-ε critical surface for A15 based technical superconductors which is described by a scaling law [42, 43]. An example of the J-B-ε critical surface of a commercial Nb_3Sn conductor [43] is reproduced in figure 1.5. The $A - B$ line shows the $J_c(B)$ curve at zero strain state, whereas the curves on both sides are the loci at which the critical current at $B = 1$ T is degraded by 10, 20 and 30% with respect to its unstrained value.

Meanwhile, other models have been developed to describe the strain response in A15 based practical superconductors [12, 44]. Although they accurately predict the strain response of the whole critical surface with just a small number of observations, they all have in common that they are empirical and do not explain the physical background of the strain response of the critical parameters. Microscopic models that describe the pressure dependence of T_c are based

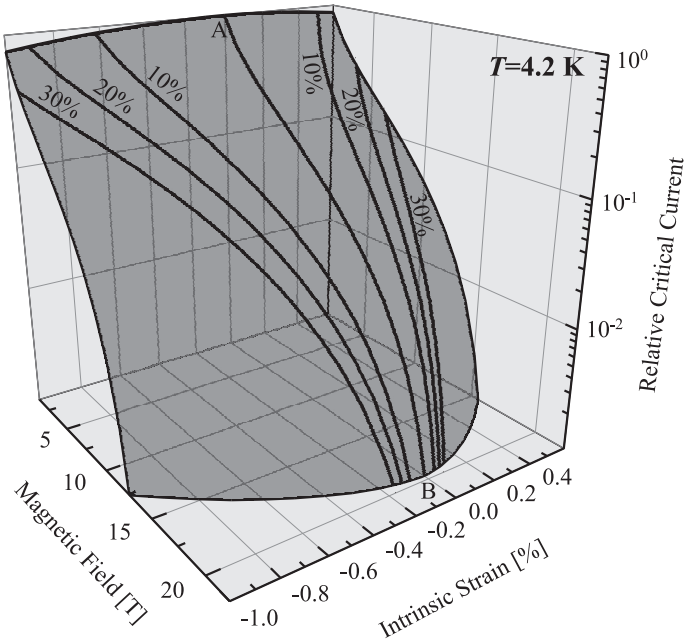

Figure 1.5: *J-B-ε* critical surface of a multifilamentary Nb_3Sn superconductor (after [43]). Line $A - B$ represents the maximum strain-free value of the critical current as a function of magnetic field. The loci to the left and right of the $A - B$ line represent 10, 20 and 30% degradation of I_c at $B = 1$ T with respect to its strain free value. Note that the critical current is normalised over its strain-free value at B=1 T.

on hydrostatic pressure and thus hydrostatic strain. For technical applications, however, non-hydrostatic terms have a significant influence and must be included. Recently, Markiewicz [45, 46] presented a full three-dimensional, strain-invariant analysis of the strain dependence of T_c for Nb_3Sn conductors. The central assumption of this analysis is that the strain dependence of T_c results from the strain dependence of the phonon frequencies in the Nb_3Sn lattices. The model correctly predicts the strain dependence of practical Nb_3Sn superconductors based on physical assumptions, rather than being empirical.

Strain in practical superconductors is caused by three effects: firstly, thermal stresses and strains built up in a composite superconductor when it is cooled down from the heat treatment temperature (> 600 °C) to the operating temperature, due to differences in thermal contraction coefficient of filaments and matrix. Secondly, especially in react-and-wind type of applications, conductors are subjected to a range of bending, torsion and tension when they are first bundled into

a cable and subsequently wound into a coil. Thirdly and arguably most important, stresses build up due to the considerable Lorentz forces generated by the combination of high current and high magnetic field.

To illustrate the technical relevance of the strain response of the critical parameters, consider a solenoid of 8 T with inner and outer radii of about 73 and 100 mm, respectively. The maximum stress that is exerted by the magnetic field in the windings is approximately 120 MPa [47]. For a Nb_3Sn wire this corresponds to an axial strain of about 0.35 % [48], which reduces its critical current by about 20 % [49]. Moreover, this strain level is already in the irreversible regime, so that the filaments are damaged.

Evidently, for proper magnet engineering the strain sensitivity of MgB_2 should be studied in order to predict changes to the critical surface of the conductors under the influence of electromagnetic forces. MgB_2 and Nb_3Sn are alike in the sense that they are both brittle materials so that the irreversible regime can be expected to occur at low strain levels in comparison to Nb-Ti. For this reason it is important that not only the response in the reversible regime is explored, but also that the maximum reversible strain level is studied. These studies are the topic of chapter 5.

1.4 Fabrication of MgB_2 Conductors

Practical superconductors consist of several filaments of superconducting material embedded in a highly conducting matrix. Wires are usually reduced in size by extrusion or drawing, depending on the desired reduction and batch length. For the ductile alloy Nb-Ti, this is a relatively easy process. MgB_2, on the other hand, is like Nb_3Sn a hard intermetallic compound, which is more difficult to deform. For Nb_3Sn this problem is avoided with the Bronze, Internal Tin and Powder-In-Tube processes [12]. Essentially a billet is assembled that contains niobium and tin as separate phases. Due to the ductility of the separate elements, it is relatively easy to deform a billet into a wire. In the final wire form, the Nb_3Sn is phase formed during a diffusion heat treatment. Similar strategies are adopted for MgB_2.

Only months after the discovery of superconductivity in MgB_2, the first trials were made to produce practical superconducting wires. One of the first attempts consisted of a boron clad tungsten wire that was exposed to magnesium vapour at 950 °C [50, 51]. The resulting 160 μm diameter wire was of very high purity. A successful variation of this method is the "coated conductor" route, in which a boron cladded Hastelloy substrate is exposed to magnesium vapour [52]; the "liquid infiltration" technique, in which a boron tube is filled with magnesium and reacted [53]; and, recently, a solid state diffusion route, in which boron powder is deformed inside a Fe-Mg alloy tube and then reacted [54]. However, for long length production of MgB_2 wires the Powder-In-Tube process (PIT) might be a more convenient and proven method. Figure 1.6 shows a simplified schematic of the PIT fabrication process of a multi-filament wire. In this example deformation

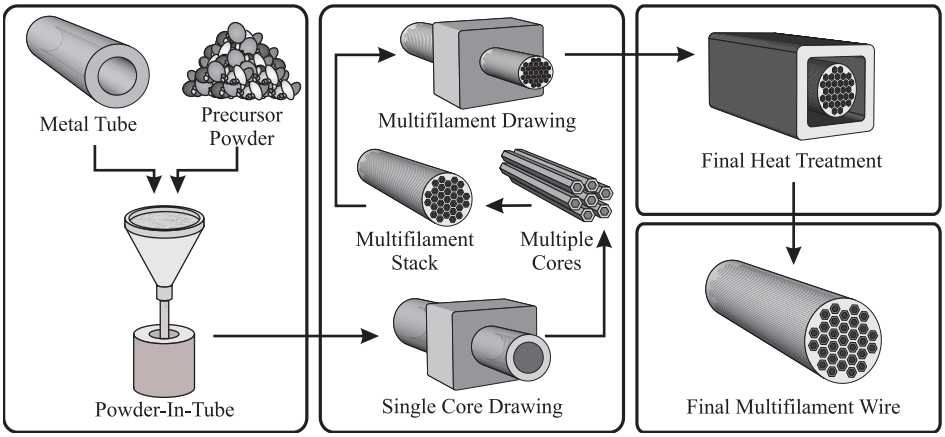

Figure 1.6: Simplified representation of the Powder-In-Tube fabrication method. The precursor powder can be pre-reacted MgB_2 in the ex-situ route or a mixture of Mg and B in the in-situ route.

is performed by drawing. However, other deformation routes are also applied, such as 2-axial rolling, groove rolling and flat rolling [55–59]. Besides the deformation method, there are two main strategies regarding the precursor powder: 1) *the ex-situ route*, in which pre-reacted MgB_2 powder is put into a tube; and 2) *the in-situ route* where magnesium and boron powders are well mixed and put into a tube. In both cases the powder-tubes are deformed into single-core wires. The wires are then stacked into a multi-filament billet. After deformation of the billet into a wire, it is heat treated. In the ex-situ route the purpose of the heat treatment is to increase the cross-section of the grain-to-grain current path by sintering the powder grains. With the in-situ route the MgB_2 phase is formed during this heat treatment.

Since the tube in which the powder is filled will be part of the matrix in the final wire, it should preferably be a material with high thermal and electrical conductivity, such as copper or aluminium. Moreover, such materials are often ductile and easy to deform. In Nb_3Sn conductors copper is usually applied. However, MgB_2 reacts strongly with materials such as copper, aluminium or silver [56,60–62]. Materials that are chemically compatible with MgB_2 are iron, steel or nickel, but these metals are not excellent conductors and rather hard. Another requirement is that optimal $J_c(B,T)$ performance implies a high degree of electrical connectivity between the grains. Chapter 2 will show how grain-to-grain connectivity depends strongly on various process parameters.

To have a broader overview of possibilities and trends in terms of the $J_c(B,T)$ performance, a literature study is presented of reported MgB_2 conductors prepared with different deformation techniques and precursor powders. Conclusions drawn from this study are the topic of chapter 3.

1.5 Scope of the Thesis

In this thesis the focus is on the question whether MgB_2 conductors are suitable for use in superconducting magnets. To arrive at a conclusion several questions have to be addressed:

> *1) Is the $J_c(B,T)$ performance of MgB_2 conductors suitable for magnet applications?*

The answer to this question depends on the preparation route of the conductors. High $J_c(B,T)$ values require a high densification of the powder core in order to increase the cross-sectional area of the current path. The degree of densification depends on the deformation method, matrix material and precursor powder. How combinations of these parameters affect the $J_c(B,T)$ performance is the subject of chapter 2. Results are put in a broader perspective in chapter 3 with a literature survey that reveals prospects and trends in the development of MgB_2 conductors.

Since a magnet system must be protected against thermal instabilities to avoid a burnout, the second question is:

> *2) Given the conductors matrix materials and operating temperature, can a MgB_2 magnet be protected against thermal instabilities?*

Choice in composition of the matrix is complicated by the fact that MgB_2 reacts strongly with most high-conductivity metals. Therefore poorly conducting materials are typically present in the composite. Together with the prospect of a relatively high operating temperature, this can compromise the ease of normal zone detection. On the other hand, a higher operating temperature may decrease the possibility of normal zone to occur. The influence of matrix composition and operating temperature on the normal zone propagation and minimum quench energy are presented in chapter 4.

Since electromagnetic forces in magnets can be significant and affect the critical parameters of MgB_2 conductors, the third question is:

> *3) Given a MgB_2 conductor with a certain matrix, does it support the electromagnetic forces acting on a magnet?*

MgB_2 is a brittle material so that this question should be separated in two parts: 1) is the strain level at which the irreversible regime starts high enough to prevent damage of the filaments?; and 2) to what extent are the critical parameters influenced by strain in the reversible regime? These issues are addressed in chapter 5 by mapping the strain response of several MgB_2 conductors in the reversible regime and by exploring the irreversible strain limit.

Finally, in chapter 6 the main conclusions of this thesis are summarised. The coherence between the chapters is illustrated in figure 1.7.

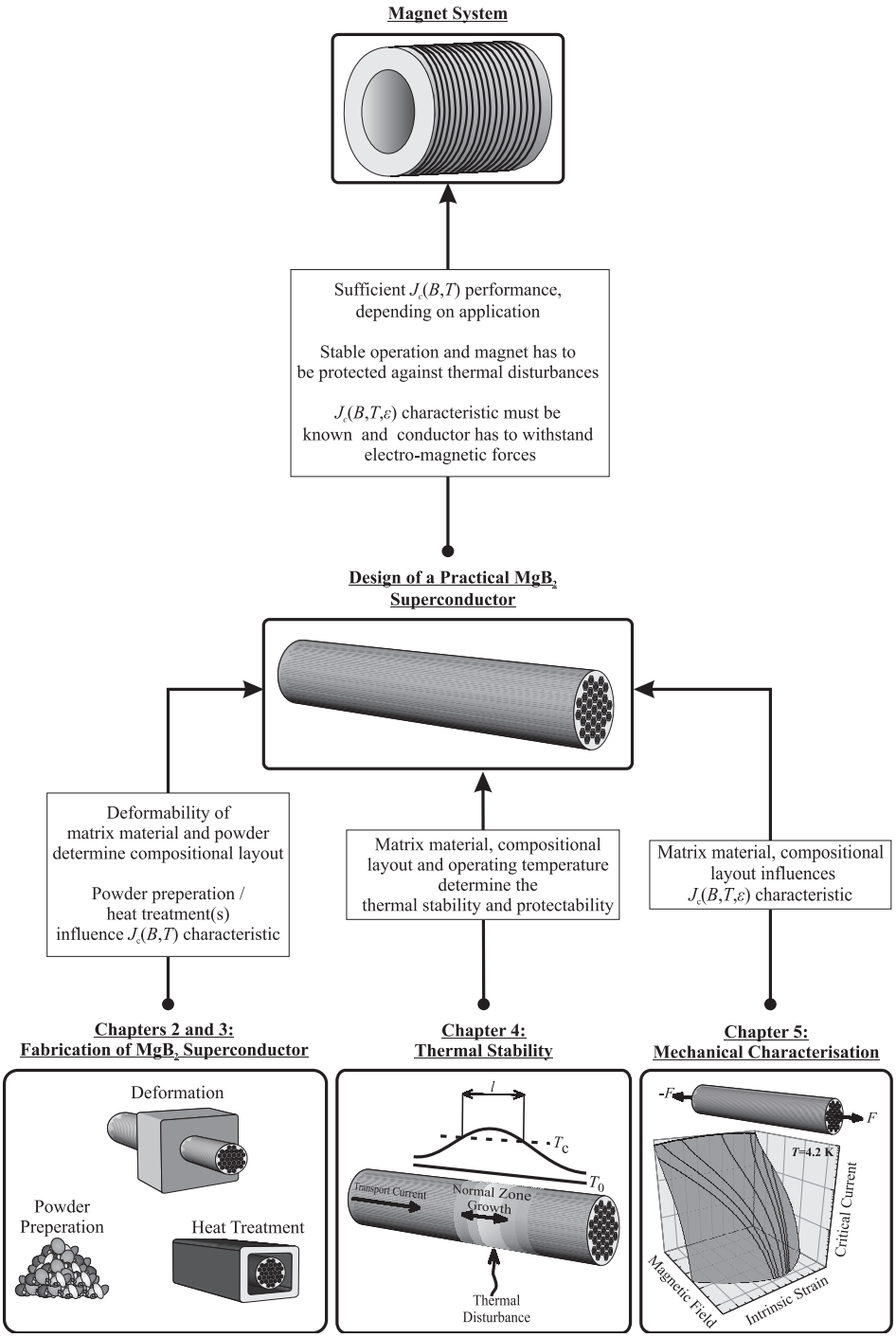

Figure 1.7: Coherence of chapters in the thesis.

Chapter 2

Preparation of Ex-Situ Magnesium Diboride Conductors

In this chapter the development of ex-situ PIT conductors using different precursor powders, matrix materials and deformation methods is discussed. Precursor powder preparation with a relatively simple method is presented. Causes of conductor fracture during deformation are explored and possibilities to prevent them are discussed. Finally, the combination of parameters that offers the best $J_c(B,T)$ performance is presented.

2.1 Introduction

The two main development routes for technical PIT MgB_2 conductors are the in-situ and ex-situ techniques (see also §1.4). The advantage of using the in-situ route is that the soft Mg acts as a lubricant for powder flow in the filament during deformation. As will be shown in §3.4.2 this results in a high filament density and high critical current densities. Low-level doping can also be better controlled in in-situ conductors so that the field retention of J_c can be significantly enhanced [24]. On the other hand, ex-situ conductors show better n-values due to more homogeneous morphology. Furthermore, recent developments show that effective pinning centers can also be introduced in ex-situ powder [8], increasing the practical upper field limit at which $J_c = 100$ A/mm^2 to as high as 13 T.

In this chapter the development of ex-situ PIT conductors is described. A key requirement in the deformation of ex-situ conductors is to reach sufficient filament density with the hard MgB_2 powder in order to obtain high critical current density values. Parameters that influence filament densification are the deformation method, the yield strength of the matrix material and the powder morphology.

For high current density MgB_2 conductors it is important that the grains are small (~ 1 μm). Not only do small grains lead to improved grain-boundary pinning and enhanced J_c values [63], but they also prevent stress concentrations in the matrix material, which can cause early breakage of the conductor. The technique to reduce the particle size of the as-purchased powder is presented in §2.2. Moreover, to further enhance the deformation capacity the effect of adding the soft metal Pb is also tested. Lead additions also influence the current carrying capability of ex-situ conductors. The preparation of MgB_2/Pb mixtures and their influence on the superconducting properties is discussed in §2.2.

To gauge which deformation method is best suited for ex-situ conductors, wires were fabricated both by drawing and two-axially rolling, while tapes were fabricated with the flat-rolling technique. Different matrix materials were used to test their influence on the powder densification in the filaments. One option tested is a bi-metal Cu/Fe composite in which the relatively soft and highly conducting Cu acts as a thermal stabiliser, while the relatively hard Fe provides the strength for powder densification. How combinations of the various parameters including Pb additions affect the filament densification and maximum achievable area reduction is the subject of §2.3.

The critical current density of as-deformed ex-situ MgB_2 PIT conductors can be significantly enhanced by a heat-treatment that causes recrystallisation and sintering of the MgB_2 grains [64]. The effects of the final heat treatment on the microstructure and superconducting properties of the differently deformed conductors with different matrix materials and varying concentrations of Pb are discussed in §2.4.1. The best-performing conductors presented in this work are compared to conductors reported elsewhere over the years 2003-2006.

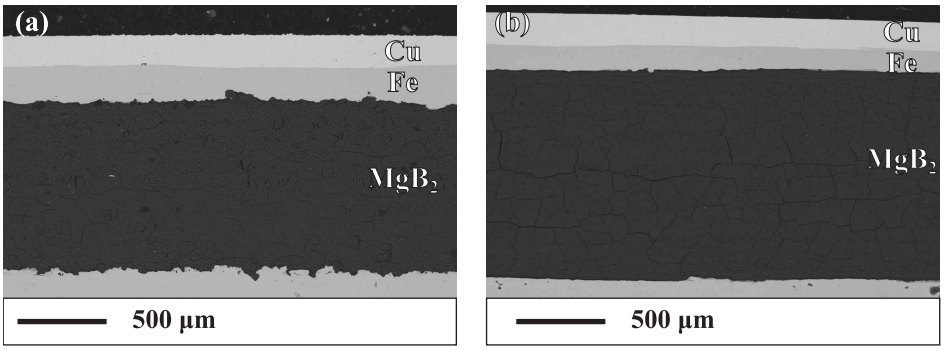

Figure 2.1: (a) SEM image of the longitudinal cross-section of a MgB_2/Fe/Cu as-drawn sample with as-purchased powder and (b) a similar sample with 48-hours milled powder.

2.2 Powder Processing

To optimise the effective current path in PIT conductors, the powder density in the filaments after deformation should be as high as possible. The maximum density that can be obtained is influenced by the force that the matrix materials can exert on the powder core and by the flow characteristics of the powder. The latter depends on the morphology and mechanical properties of the powder particles[1].

Since MgB_2 is a relatively hard material, particle size distribution is a key issue. This is illustrated in figure 2.1, where as-drawn wires with an identical matrix and deformation history but with different starting powders are compared. The tube in figure 2.1a was filled with as-purchased powder with particles up to $\sim$ 100 μm, while the tube in figure 2.1b was filled with powder particles up to $\sim$ 2 μm in size. The as-purchased powder results in a rougher core/matrix interface as the large particles penetrate into the Fe. This gives rise to local stress concentrations and may cause the appearance of micro-cracks in the core or even premature breaking of the wire during drawing. The conductor made with the finer powder shows a much smoother interface. Also in light of development of multi-filament conductors [19,65] with filament sizes of < 50 μm, it is essential to reduce the particle size.

Apart from improved connectivity and thus higher J_c values, particle size reduction might also lead to better field retention of the critical current. It was found by [66] that smaller grains increase the irreversibility field B^*, which may

[1] In the context of powder processing, the general term "particle" is used since the powders do not only consist of single-crystalline grains, but also of hard agglomerates and polycrystalline lumps of the various materials.

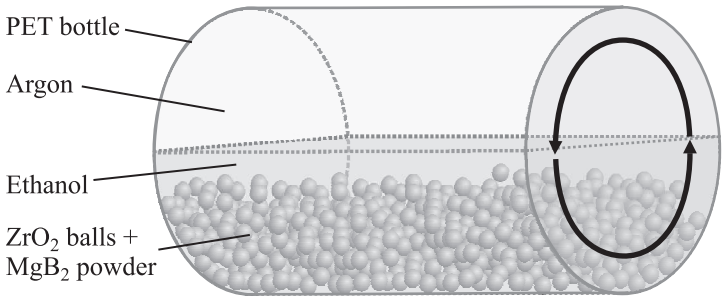

Figure 2.2: Schematic drawing of the shear milling process used to reduce the MgB_2 particle size.

be associated with improved grain boundary pinning[2].

In this work, the particle size of the as-purchased MgB_2 is reduced using a relatively simple but effective shear milling technique or by particle selection through sieving. The details and efficiency of these methods are discussed in §2.2.1.

The method used to reduce the particle size should not influence the purity of the powder, since this might deteriorate the superconducting properties. These issues are discussed in §2.2.2.

Another method to achieve higher density and better grain-to-grain connectivity is the addition of soft metals. These additions may act as a lubricant for powder flow and thus prevent crack formation. Moreover, when finely distributed in-between the grains, the metal might influence the grain connectivity through proximity coupling [67]. In this work Pb is used to test the effect of soft metal additions. The details are described in §2.2.3.

2.2.1 Reducing Particle Size

Shear Milling

With the shear milling technique used in this work particles are reduced in size by impact as well as shear stresses [68]. Other milling techniques commonly used for MgB_2, such as planetary ball milling, mainly reduce particle size by impact of the milling balls. The shear milling technique is schematically shown in figure 2.2. The powder is placed in a cylindrical container together with a relative large amount of milling balls. A fluid is added to the mixture, which increases the efficiency of the milling process by reducing the packing of particles and preventing the formation of inactive corners in the container. The container is rotated so that

[2]Pinning mechanisms in MgB_2 conductors are further discussed in §3.4.

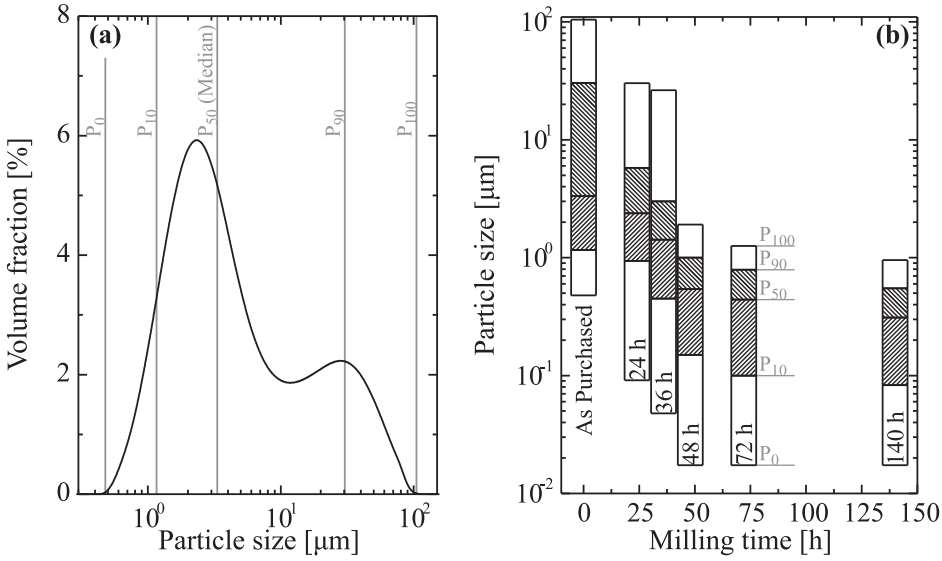

Figure 2.3: (a) particle size distribution of as purchased MgB_2 powder; and (b) the particle size distribution (plotted as floating columns) as a function of milling time. Indicated are the 0, 10, 50 (median), 90 and 100 % percentiles.

the milling balls cascade. The powder particles in-between the milling balls are crushed through impact and shear stress.

The chosen suspension fluid is ethanol, which is widely available and does not react with MgB_2. For the milling balls, ZrO_2 with a diameter of ≈ 3 mm is used. The Vickers hardness H_v of the milling balls is about 1300, exceeding that of single crystal MgB_2 ($H_v \sim 1100$ [69]). The mixture MgB_2:ethanol:ZrO_2 with weight ratio 5:10:90 is prepared in an Ar-filled glove-box to prevent oxygen contamination. The mixture is poured in a polyurethane container, which is then rotated on a rolling bench. After milling, the balls are removed and the MgB_2/ethanol suspension is sealed in a closed container. To dry the powder, this container is connected to a vacuum pump and the ethanol is evaporated.

The particle size distribution of the powders, represented as a volume fraction versus particle size, is measured with a Malvern Instruments Mastersizer 2000, with the MgB_2 powder suspended in ethanol. Since gas bubbles and agglomerates appear as large particles, the intensity and duration of degassing and ultrasonic vibration of the suspension is varied until the distribution remains constant. As an example, the particle size distribution of the as-purchased powder is shown in figure 2.3a. The 0, 10, 50 (median), 90 and 100 % percentiles (P_0, P_{10}, P_{50}, P_{90} and P_{100}) of the volume fraction are also indicated.

How the particle size distribution changes as a function of milling time is shown in figure 2.3b, with particle size distributions represented as floating columns of

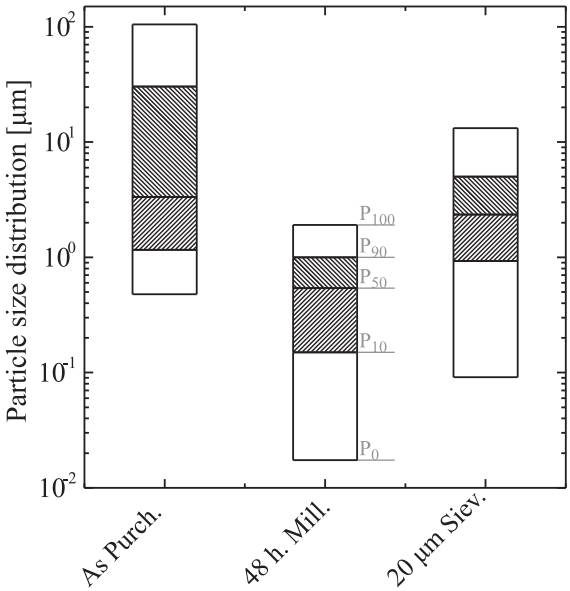

Figure 2.4: Comparison of the particle size distribution of as purchased, 48 h shear milled and 20 μm sieved powders.

the percentiles. During the first 48 h the maximum particle size steadily reduces from 100 μm to 2 μm. After that, the particle size distribution changes relatively little. To minimise effects of contamination due to wear of the milling balls, the standard milling time is set to 48 h.

Note that this shear milling technique not only efficiently reduces the particle size, but also that its yield is virtually 100 %. Furthermore, it can be scaled-up to larger volumes relatively simply.

Sieving

A disadvantage of any milling method is contamination associated with wear of the milling tools. Figure 2.3a shows that, although the maximum particle size in the as-purchased powder is too large, 50 vol.% of the particles are already smaller 3 μm. In principle sieving the powder should still result in a reasonable yield, without the risk of excessive contamination.

For sieving, $\sim$ 100 g as-purchased MgB_2 is suspended in 1 l of ethanol. This suspension is then poured through a cascade of sieves with mesh sizes of 90, 63, 40 and 20 μm. Reducing the mesh size even further significantly reduces the yield due to excessive clogging of the finer meshed sieves. After sieving, the powder is dried in a similar fashion as with the milled powder. The resulting particle size distribution is plotted in figure 2.4 and compared to the distributions of as-purchased and 48 h milled powders. Compared to milling, sieving is less effective

in terms of particle size reduction. Also, the yield of $\sim$ 20 % is relatively low, mainly due to clogging of the sieves. Nevertheless, in the remainder of this work sieved powders are used, since the milling procedure with ethanol described above turns out to cause excessive contamination as discussed in the next paragraph.

2.2.2 Superconducting Properties and Contamination

Magnetisation Measurements

Magnetisation measurements were carried out on pellets pressed from four differently treated powders to check whether various processing steps introduce contamination. The first powder was the as-purchased one, the second the shear milled, the third the sieved and the last one the as-purchased after soaking in ethanol for 48 h and drying. The latter powder served to distinguish between prolonged exposure to ethanol and the actual milling or sieving procedures.

Each of the four powder types was prepared from two different batches of commercial Alpha-Aesar MgB_2. The eight powder samples were pressed into pellets of 6 mm diameter and $2-3$ mm thickness with a force of 3 kN, corresponding to a pressure of $\sim$ 1 GPa. Magnetisation loops were recorded at $T = 10$ K with a VSM, using a field ramp rate of 2 T/min.

The magnetisation loops of four pellets from the same batch are shown in figure 2.5a. Differences with corresponding loops recorded for the other batch are negligible. Soaking the as-purchased powder in ethanol has no significant influence on the superconducting properties: differences between the loops for the as-purchased and soaked powder can simply be attributed to the uncertainty in the pellets' volume, which is about $\sim$ 10 %. The 45 % smaller magnetisation loop of the pellet made from sieved powder can probably be attributed to a higher porosity of the pellet. The mass density of the pellets of as-purchased or soaked powders is 75 ± 3 % of the theoretical MgB_2 density (≈ 2.62 g/cm^3 [64]), while that of the milled or sieved powder pellets is 72 ± 2 %. The difference can be related to the narrower particle size distributions of the milled and sieved powder (2.4), which leads to less efficient packing in the pressed pellets. Correspondingly, the intergranular J_c will decrease and the magnetisation loop will become smaller. However, it is difficult to explain the reduction of the milled powders' loop by an order of magnitude compared to that of the as-purchased one with such a porosity argument.

To understand the nature of the reduction after milling, the length scale Λ over which coherent macroscopic current loops flow is determined. A magnetisation loop of a polycrystalline superconductor contains contributions of both inter- and intragranular current flows so that the magnetic moment Δm can generally be described as follows [70]:

$$\Delta m = (2/3) V_{\mathrm{core}} (J_{\mathrm{inter}} \Lambda + J_{\mathrm{intra}} a_0), \tag{2.1}$$

where V_{core} is the volume of the superconducting core, J_{inter} and J_{intra} the inter- and intragranular current densities, a_0 the typical grain size and Λ the typical

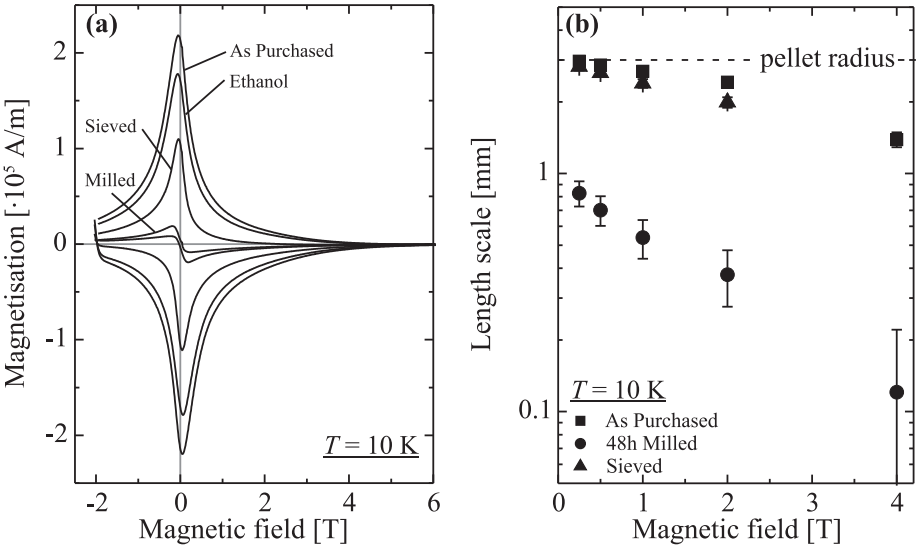

Figure 2.5: (a) shows magnetisation measurements at $T = 10$ K of the as purchased MgB_2, MgB_2 that is submerged in ethanol for 48 h, 48h milled MgB_2 and 20 μm sieved MgB_2. (b) shows the corresponding length scales of the super-currents in the pellets.

size of intergranular current loops. For homogeneous samples Λ has the value of the sample radius R and the first term in equation (2.1) dominates provided that

$$\frac{J_{\text{inter}}}{J_{\text{intra}}} > \frac{a_0}{R} \ (\approx 0.001 - 0.01).$$

For inhomogeneous samples, Λ will decrease below the sample size. The actual length scale in the pellets is determined with an independent experiment, through detailed analysis of the $m(H)$ behaviour after field sweep reversal. The initial repenetration slope $dm/dH \propto \Lambda^3$ is independent of the magnitude of the critical current density [71].

The length scale Λ of the different powder pellets as a function of magnetic field is shown in figure 2.5b. Both the as-purchased and the sieved powder show a length scale of the order of the pellet radius, indicating homogeneous intergranular current flow. This is not the case for the milled powder, in which the length scale becomes nearly an order of magnitude lower than the pellet radius. Together with the strong reduction of the loop amplitude, this indicates a strong suppression of the intergranular currents in the milled powder pellet.

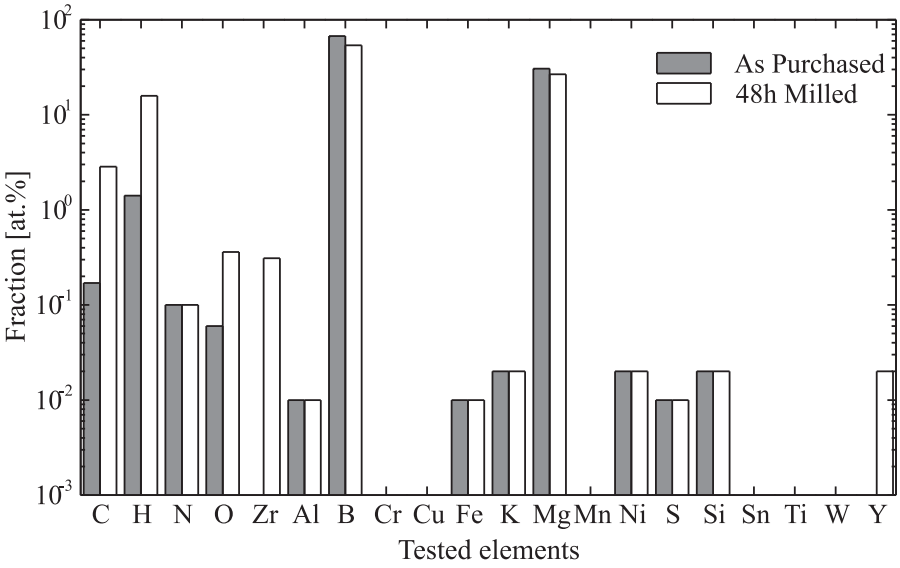

Figure 2.6: Fraction of tested elements found in as-purchased MgB_2 and 48 h milled MgB_2.

Chemical Analyses

To clarify the mechanism behind the reduction of the intergranular J_c, various chemical analyses are performed.

First, the chemical composition of the milled and the as-purchased powders is compared. The concentration of the relatively light elements C, H, N, O was determined with a Carlo-Erba Elemental Analyser, while all other elements were determined with ICP measurements. As shown in figure 2.6, the milled powder has a significantly higher concentration of Zr, O and Y. This is a direct reflection of the wear of the Y_2O_3 stabilised ZrO_2 balls. Furthermore, the C and H concentration in the milled powder is an order of magnitude higher than in the as-purchased powder. The only possible source of these two elements is the ethanol in which the powder is milled, indicating a chemical reaction.

Independently, the gas present in the polyurethane container after milling was analysed. This was motivated by the observation that after 48 h of milling the pressure inside the container had increased significantly, again indicating a chemical reaction. Gas chromatography revealed a final atmosphere of ~ 50 % H_2 and ~ 50 % Ar, where the initial gas in the bottle only contained Ar and traces of O_2 and H_2O (< 1 ppm).

The order of magnitude higher concentration of C in the milled powder together with the H_2-gas in the polyurethane bottle leads to the conclusion that

the ethanol is partially converted into methanol, releasing H_2 gas and C:

$$C_2H_5OH \rightarrow CH_3OH + C + 2H.$$

Based on this chemical reaction, it is estimated that ~ 0.5 vol.% of the ethanol is converted into methanol[3]. Thus the mechanism behind intergranular current suppression by milling can be summarised as follows: during shear milling in ethanol, the ethanol is partly converted into methanol leaving C as impurity in-between the MgB_2 grains. In order to preserve the superconducting properties while still reducing the particle size with this effective shear milling technique, a more inert fluid should be found.

Isopropanol was tested as an alternative, but also in this case gas chromatography showed a final gas atmosphere still containing about ~ 35 % H_2. Also ICP measurements after replacing ZrO_2 balls with SiC ones lead to a similar C concentration as the ones shown in figure 2.6.

2.2.3 Soft Metal Additions

Advantages of soft metal additions in ex-situ conductors can be three-fold. First, soft metal additions can significantly enhance the critical current density [72, 73] due to formation of S/N/S junctions between the normal metal and MgB_2. Effectively this leads to better grain-to-grain connectivity and an enhancement of the self-field J_c. Second, soft metals may improve the powder flow as it acts as a lubricant during deformation, reducing the friction between the MgB_2 grains and reducing the risk of crack formation in the filaments. Third, soft metal additions generally have a higher thermal and electrical conductivity than MgB_2 and can therefore act as an internal thermal stabiliser [74].

In this work, Pb powder with a typical grain size of < 100 μm is mixed in an Ar atmosphere with 20 μm sieved MgB_2 powder. To test the effect of Pb additions on the deformation behaviour of conductors, critical current density and thermal stability, powder mixtures were prepared with Pb concentrations varying from 0 to 15 vol.%. These powders were used in different types of conductors (rolled or drawn) and the resulting properties are discussed in paragraphs 2.3 and 2.4.

2.3 Deformation

The maximum achievable powder densification in the PIT process depends on the morphology of the powder, but also on the deformation route and the choice of matrix material.

Different deformation processes impose different powder flow profiles so that the maximum achievable powder density may differ as well. In case of drawing, densification is obtained by the radial force that the die exerts on the conductor, but the axial pulling force counteracts this. For flat-rolling on the other hand, only

[3] It is assumed that the H found in the MgB_2 powder is bound to C.

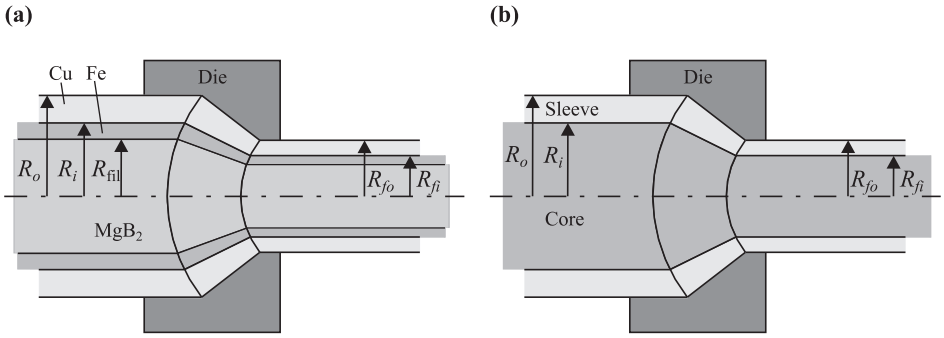

Figure 2.7: Schematic view of co-deformation of a MgB_2 conductor with a Cu/Fe matrix (a) and a bi-metal rod (b) by drawing.

a transverse force is involved. To test which deformation procedure is best suited for the deformation of ex-situ conductors, three methods were tested: drawing, flat-rolling and two-axial rolling.

The maximum densification is also determined by the amount of force that the matrix material can transmit to the powder. The choice of materials is limited by requirements of chemical compatibility and thermal stabilisation. Therefore two types of matrix were used: 1) a combination of Cu and Fe, in which Cu provides the thermal stability and Fe acts as a reaction barrier; and 2) a thicker Fe matrix that provides more strength for increased powder densification. Although pure Fe has a lower conductivity, in combination with a MgB_2/Pb powder mixture it may still yield a conductor with sufficient thermal stability.

Critical in each deformation method is the hardness evolution of the matrix material, which in the worst case leads to fracture before sufficient powder density has been reached. Conductor processing is further controlled by various details of the deformation process and matrix layout, especially in the case of the Cu/Fe combination. Which parameters are important for "successful" deformation is explored in §2.3.1.

In order to test the powder densification, both the evolution of the filament density and the J_c of the as-deformed conductors are monitored. The results are discussed in §2.3.2.

2.3.1 Parameters Controlling Deformation Processes

Drawing

To explore the parameter space for the drawing process, a model developed by Avitzur *et. al.* [75] for the deformation of bi-metal rods is applied (see figure

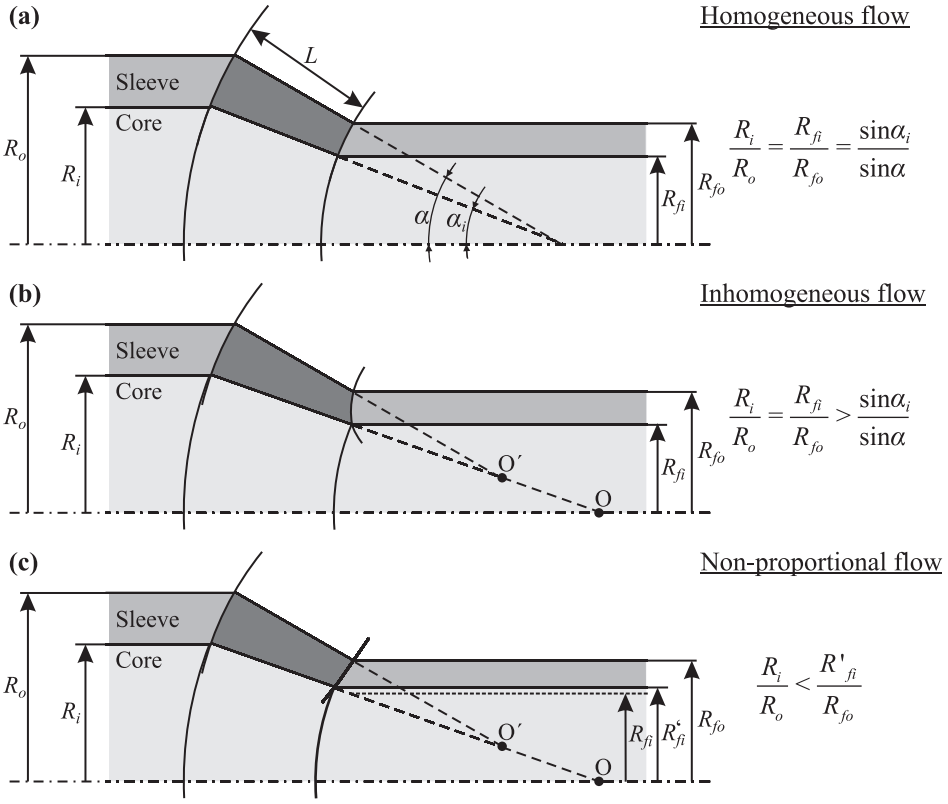

Figure 2.8: Flow modes during co-drawing two different metals. (a) shows homogenous flow; (b) inhomogeneous flow; and (c) non-proportional flow.

2.7b)[4]. The model is used as a simplified representation of PIT conductors with a matrix consisting of two metals with different hardness, such as Cu/Fe, and does not include the powder core (figure 2.7a). It predicts the existence and location of a boundary between fracture and successful drawing of a bi-metal rod and is a function of various drawing parameters.

During drawing, a bi-metal rod can follow three types of flow patterns. When the two metals have comparable hardness, the rod flows homogeneously (figure 2.8a). In this case the radii of the sleeve and core have the same relative reduction so that:

$$\frac{R_i}{R_o} = \frac{R_{fi}}{R_{fo}}, \tag{2.2}$$

with R_i and R_o the outer radii of the core and sleeve before deformation and R_{fi}

[4]Only the essence of Avitzur's model is presented here. For a full discussion, the reader is referred to [75–77].

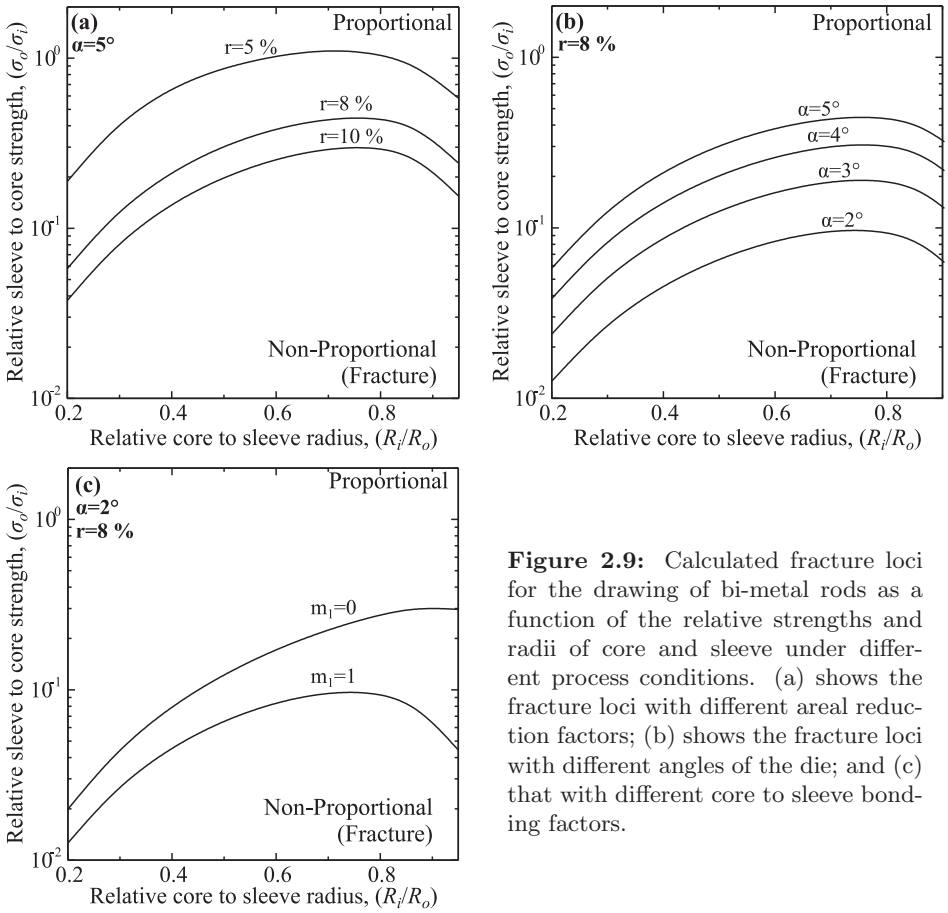

Figure 2.9: Calculated fracture loci for the drawing of bi-metal rods as a function of the relative strengths and radii of core and sleeve under different process conditions. (a) shows the fracture loci with different areal reduction factors; (b) shows the fracture loci with different angles of the die; and (c) that with different core to sleeve bonding factors.

and R_{fo} after. Furthermore, the velocity field of the sleeve and core point towards the same origin O so that the angle of deformation of the core α_i is related to the semicone angle of the die α as:

$$\frac{\sin(\alpha_i)}{\sin(\alpha)} = \frac{R_i}{R_o}. \tag{2.3}$$

When the core is harder than the sleeve, it tends to deform less (figure 2.8b). As a result the angles α_i and α are no longer related anymore by (2.3), but rather:

$$\frac{\sin(\alpha_i)}{\sin(\alpha)} < \frac{R_i}{R_o}. \tag{2.4}$$

The velocity field of the core and sleeve point to different origins. This type of flow is referred to as inhomogeneous flow, but it can still be proportional so that (2.2) still holds. However, depending on the drawing parameters, inhomogeneous

flow can also lead to relative thinning of the sleeve and thus non-proportional flow:

$$\frac{R_i}{R_o} < \frac{R_{fi}}{R_{fo}}. \tag{2.5}$$

If powder densification inside the core can be neglected, the volume remains constant and (2.5) implies that the sleeve elongates more than the core, so that the latter undergoes a tensile force. This is when fracture of the core may occur.

Whether the flow is non-proportional for a given combination of process parameters is determined by searching the R_{fi}/R_{fo} ratio that corresponds to the minimum power required for drawing. The process parameters that can be investigated in the model are: the area reduction $r = 1 - (R_{fo}/R_o)^2$; the semicone angle of the die α; the length of the bearing of the die L; the friction between the outer surface of the sleeve and the bearing of the die; the bonding strength between core and sleeve m_1; the relative core to sleeve radius (R_i/R_o); the relative yield moduli of sleeve and core $(\sigma_\mathrm{o}/\sigma_\mathrm{i})$; and the outgoing velocity of the rod.

As an example, calculated fracture loci are plotted in figure 2.9 as a function of (R_i/R_o) and $(\sigma_\mathrm{o}/\sigma_\mathrm{i})$. In all cases, the harder the core $(\sigma_\mathrm{o}/\sigma_\mathrm{i} < 1)$, the more likely it is to fracture. This is especially true for intermediate cores sizes $(R_i/R_o \approx 0.5)$. As the relative core size increases $(R_i/R_o \to 1)$, the flow may still be inhomogeneous, but will tend towards proportional so that the critical $(\sigma_\mathrm{o}/\sigma_\mathrm{i})$ value decreases.

Figure 2.9a shows how the fracture locus shifts with increasing area reduction. At a constant semicone angle α, an increase in r implies a longer die bearing L, which promotes homogeneous flow. Vice versa, increasing the semicone angle at constant area reduction results in a shorter L so that fracture is promoted (figure 2.9b). Furthermore, 2.9c shows that better bonding of the sleeve and core $(m_1 = 1)$ also promotes homogeneous flow.

Despite the strong simplification made by neglecting the specific properties of the powder core, it will be shown that this model does allow a qualitatively correct choice of process parameters such as the ratio of core to sleeve radius or the relative sleeve to core strength.

Comparison with Experiments

The wires that were drawn are listed in table 2.1. Five different matrix layouts are used, while the powders are either pure MgB_2 or contained 10 vol. % Pb. Drawing was done with the facilities at Shape Metal Innovation and at the University of Geneva. Area reduction per pass is typically 10 %, while the semicone angle of the dies is typically $\sim$ 5 %. The listed final radius R_f is determined as the radius at which further drawing is impossible due to repeated breaking of the wire. The effective true strain ϵ_f at the final radius is also listed so that samples

Table 2.1: Overview of drawn conductors, together with their final dimensions.

Wire #	Matrix	Pb [vol.%]	Initial R_o [mm]	Initial R_i [mm]	Initial R_{fil} [mm]	Initial (R_i/R_o)	Final R_{fo} [mm]	Final ϵ_f
1-D	Cu/Fe	-	6.00	4.00	2.50	0.67	1.7	2.6
1-Pb10-D	Cu/Fe	10	6.00	4.00	2.50	0.67	1.7	2.6
2-D	Cu/Fe	-	5.00	4.00	2.50	0.80	1.5	2.5
2-Pb10-D	Cu/Fe	10	5.00	4.00	2.50	0.80	1.3	2.8
3-D	Cu/Fe	-	5.50	4.75	4.25	0.86	0.8	3.8
3-D-II	Cu/Fe	-	5.50	4.75	4.25	0.86	0.6	4.4
3-Pb10-D	Cu/Fe	10	5.50	4.75	4.25	0.86	0.7	4.2
4-D	Cu	-	5.50	-	4.75	-	1.8	2.3
4-Pb10-D	Cu	10	5.50	-	4.75	-	1.9	2.2
5-D	Fe	-	-	4.00	2.50	-	0.6	3.9

with different initial radii can be compared. It is defined as:

$$\epsilon_f = 2 \ln \left(\frac{R_o}{R_{fo}} \right). \tag{2.6}$$

It can readily be seen that wires with different core to sleeve ratios indeed tend to arrive at different true strain values, as predicted by the model discussed above. It should be noted that Fe work-hardens faster than Cu [78,79], so that the relative yield modulus (σ_o/σ_i) changes from one drawing step to the next. The drawing process starts above the fracture locus shown in figure 2.9 but (σ_o/σ_i) will steadily decrease so that fracture can be expected at some point.

The relative Cu to Fe strain hardening curve is plotted in figure 2.10a. The curve is calculated as the ratio of true stress to true strain data of annealed Cu to those of ARMCO Fe [78,79]. Note that this curve is a rough approximation of the actual relative work-hardening of the Cu/Fe matrices, as the actual yield strengths of the wires are not measured. However, for all conductors similar annealed OFHC Cu is used and the initial value for σ_o is assumed to be 60 MPa [78, 80]. For samples 1-D, 1-Pb10-D, 2-D and 2-Pb10-D as-annealed 99.5 % pure Fe tubes are used, while for samples 3-D, 3-D-II and 3-Pb10-D as-drawn ARMCO Fe tubes were annealed at 550 °C for 2 hr. For σ_i the starting value 180 MPa of annealed ARMCO Fe is used. Thus, drawing starts at $(\sigma_i/\sigma_o \approx 0.33)$, as indicated by the dot in figure 2.10a.

Converting the curve of 2.10a to a plot of (σ_i/σ_o) versus (R_i/R_o), results in figure 2.10b. The dots again indicate the estimated starting point of each

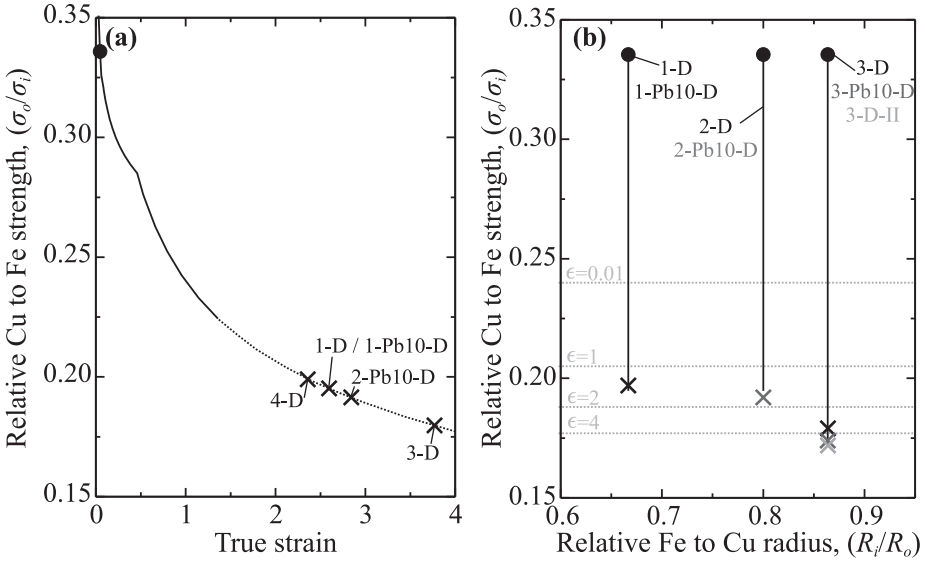

Figure 2.10: (a) shows the relative Cu to Fe strength ratio plotted against true strain (calculated from [78, 79]). The dot indicates the estimated relative strength of the starting tubes, the crosses the final true strain of selected wires. (b) shows the same data, but this time plotted in a similar way as the model predictions of figure 2.9.

conductor, while the crosses indicate where the wires broke repeatedly. Just as predicted by the model, the wires with relatively high (R_i/R_o) ratio can be drawn further, corresponding to a lower critical (σ_i/σ_o) value. It should be noted that no quantitative conclusions can be drawn from figure 2.10b as the actual relative work hardening and initial (σ_i/σ_o) of the Cu/Fe matrices were not measured.

Figure 2.11 shows the SEM micrographs of the longitudinal cross-section of the as-drawn samples with pure MgB_2 at their final diameter. Samples 1-D and 2-D with the lower (R_i/R_o) values clearly show how Fe fractures inside the Cu sleeve. The 45° fracture angle indicates shear stress to be the main cause of fracture [81]. In contrast, sample 5-D has the same Fe matrix but no Cu outer sleeve and could be drawn to a $\sim$ 70 % higher strain level. The final true strain level of this wire was not determined by fracture, but simply by the lack of smaller dies. Together, these observations illustrate that Fe in the composite tubes fractures due to non-proportional flow, in which the Cu sleeve exerts a tensile force on the Fe core.

Also in samples 3-D and 3-D-II this can be the mechanism of failure, even if no internal fracture planes are observed in the longitudinal cross-sections. Samples 1-D and 2-D have a $\sim 30-65$ % larger Cu thickness so that the Cu sleeve is still able to support the drawing force by itself after the Fe has fractured. For samples

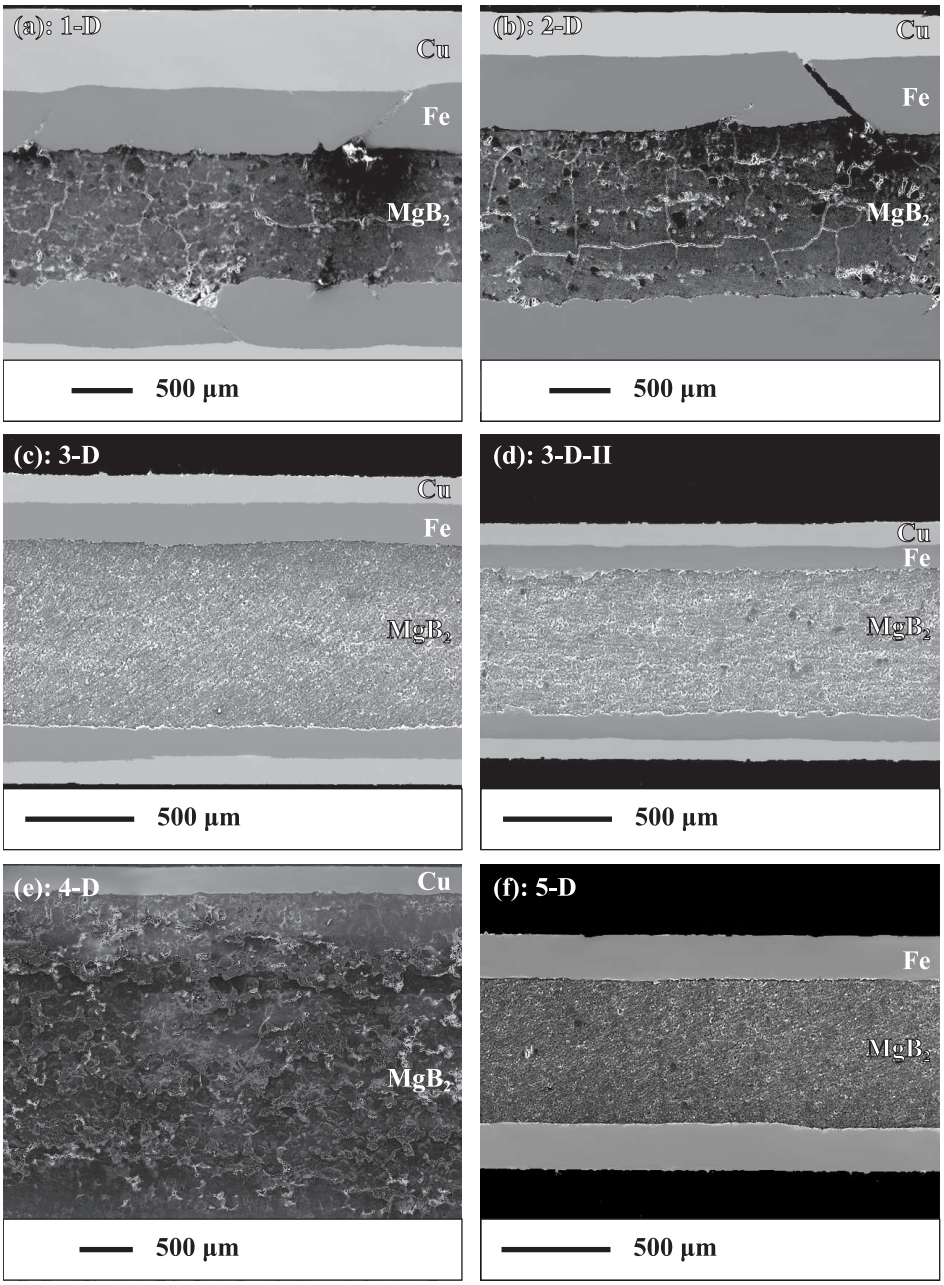

Figure 2.11: SEM micrographs of the longitudinal cross-section of as-drawn wires, all with pure MgB_2 cores but different matrix layout at their final dimensions.

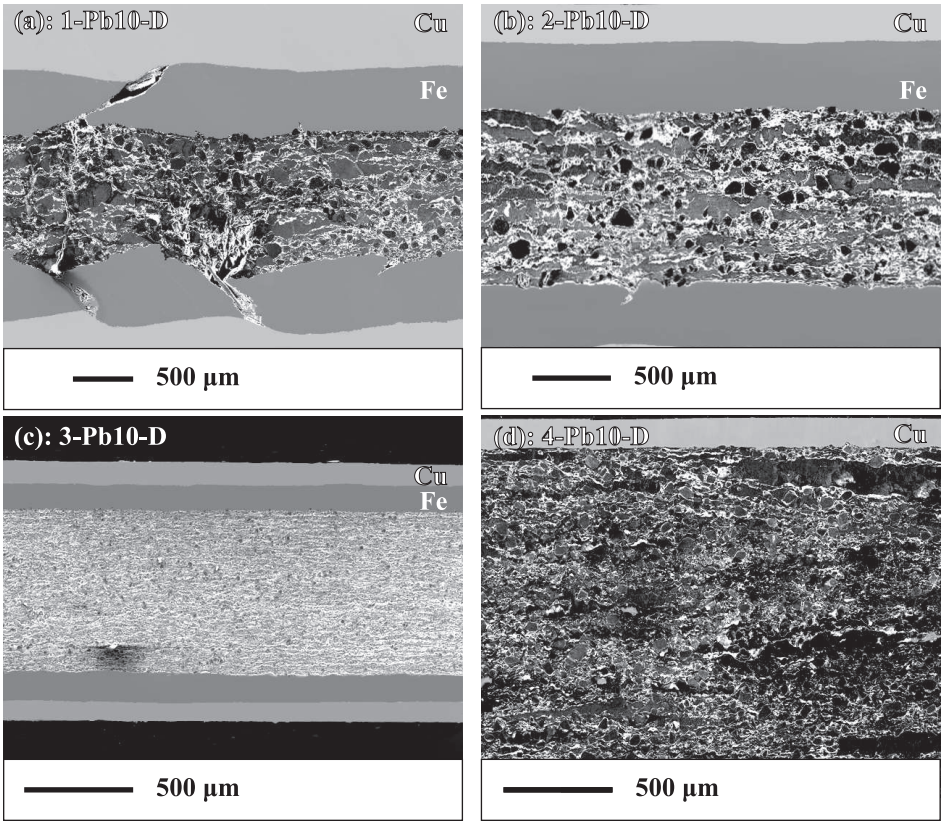

Figure 2.12: SEM micrographs of the longitudinal cross-section of as-drawn wires, all with 10 vol.% Pb-containing powder cores but with different matrix layout at their final dimension. The bright regions in the powder core correspond to Pb-rich areas.

3-D, 3-D-II, the Cu is likely to be too thin so that the whole wire breaks when the Fe first fails. Note also that sample 3-D-II could be drawn to a 16 % higher ϵ_f level than sample 3-D, due to the use of different dies.

For sample 4-D, with just a Cu matrix, only a relatively small true strain of 2.3 could be reached. Also in this sample the Cu is relatively thin and unable to support the drawing force.

The longitudinal cross-sections in figure 2.12 are those of samples that contain 10 vol.% Pb. Also here drawing failure is caused by fracture of the Fe, which is clearly visible in figures 2.12a and b. Between samples 1-D and 1-Pb10-D, no difference in the maximum achievable true strain ϵ_f is observed, indicating that the relative strain hardening of Cu and Fe dominates the deformation behaviour. On the other hand, samples 2-Pb10-D and 3-Pb10-D could be drawn to $\sim$ 12 %

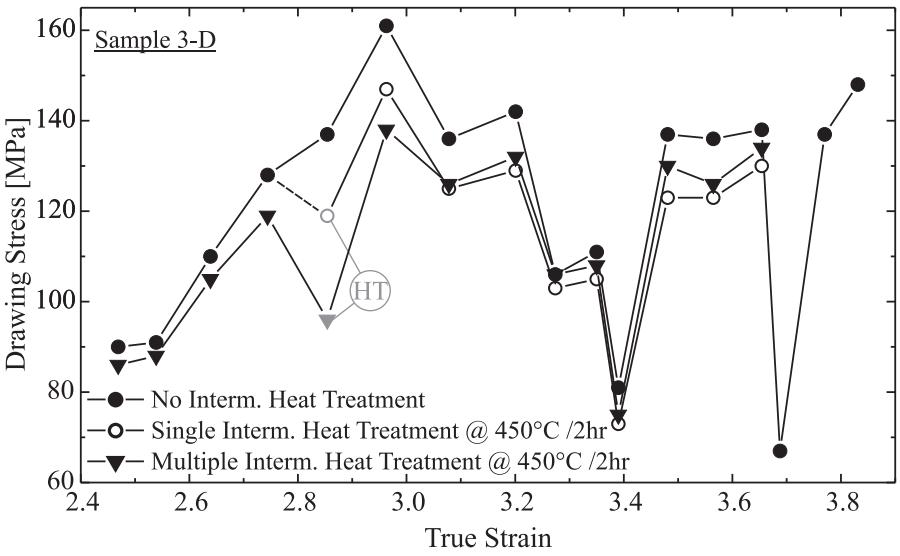

Figure 2.13: Influence of intermediate softening heat treatment on the drawing force of sample 3-D.

higher ϵ_f levels than their Pb-free counterparts. For higher (R_i/R_o) values, Pb additions thus indeed seem to promote proportional flow. For sample 4-Pb10-D, no difference in ϵ_f is observed compared to 4-D. Just like with 1-Pb-10, the properties of the matrix (the ultimate strength of Cu) determine its overall behaviour irrespective of the powder characteristics.

The drawing experiments show that the maximum achievable true strain ϵ_f is mainly limited by the level of relative Cu to Fe strain hardening. In an attempt to increase ϵ_f, pieces cut from sample 3-D were subjected to several softening heat treatments in-between the drawing steps. Figure 2.13 shows the effect of the intermediate heat treatments on the overall drawing stress.

The wire subjected to a single intermediate heat treatment was cut from the untreated sample 3-D at a true strain value of $\sim$ 2.75 and heat treated at 450°C/2 hr. Another piece was subjected to multiple heat treatments at 450°C/2 hr each time ϵ increased by 1. In figure 2.13, the indicated heat treatment of this piece is the last one, since no force measurements could be performed at diameters d larger than 3.5 mm. Heat treatments at 550°C/2 hr were also tested, with similar results.

The intermediate heat treatment clearly affects the drawing stress, reducing its value by $\sim$ 14 % for the single- and $\sim$ 28 % for the multiple heat treated pieces compared to the untreated sample. Although the matrix materials are indeed softened by the heat treatments, the effect disappears rapidly. In fact, the drawing stress coincides again with that of the untreated sample after only 4

Table 2.2: Overview of Two-Axially-Rolled and Flat-Rolled conductors.

Cond #	Matrix	Pb [vol.%]	A_o [†] [mm^2]	A_f [mm^2]	f [%]	ϵ_f
Two-Axial-Rolling:						
3-T	Cu/Fe	-	$\pi \times 5.50^2$	1.40^2	49	3.9
3-T4	CuNi/Cu/Fe	-	$5.20^{2\ddagger}$	1.10^2	22	7.0[¶]
3-Pb10-T	Cu/Fe	10	$\pi \times 5.50^2$	1.40^2	51	3.9
3-Pb10-T16	CuNi/Cu/Fe	10	$7.96^{2\ddagger}$	2.45^2	-	6.2[¶]
Flat-Rolling:						
5-FR	Fe	-	$\pi \times 4.00^2$	4.11×0.38	34	3.5
5-Pb05-FR	Fe	5	$\pi \times 4.00^2$	4.01×0.38	33	3.5
5-Pb10-FR	Fe	10	$\pi \times 4.00^2$	4.08×0.38	32	3.5
5-Pb15-FR	Fe	15	$\pi \times 4.00^2$	4.02×0.37	30	3.5

[†] Initial dimensions of samples 3-T and 3-Pb10-T are the same as those of samples 3-D and 3-Pb10-D in table 2.1, while the initial dimensions of samples 5-FR to 5-Pb15-FR are identical to that of sample 5-D.

[‡] Initial cross-sectional area of the assembly of mono-cores and CuNi outer tube.

[¶] Cumulative true strain build up from the deformation of the mono-core and that of the stacked assembly.

drawing steps, when the true strain is increased by ~ 0.4. As a consequence, the heat treated pieces could not be drawn any further than the untreated samples. Clearly, to reach higher true strain levels more intermediate heat treatments would be necessary. Furthermore, as shown below the powder density reduces after heat treatment, supposedly due to the altered force balance between the powder core and the softened matrix.

Two-Axial Rolling and Flat Rolling

The samples fabricated using two-axial and flat rolling are listed in table 2.2. Two-axial rolling was performed at the Institute of Electrical Engineering, Bratislava, while tapes were flat-rolled at the University of Geneva.

For samples 3-T and 3-Pb10-T the same Cu and Fe tubes are used as for wires 3-D, 3-D-II and 3-Pb10-D (table 2.1). The samples were drawn to a diameter of 2.02 mm and then two-axially rolled to 1.4×1.4 mm^2 with an area reduction per pass of 5 to 10%. Attempts to roll further led to splitting of the matrix, i.e. longitudinal cracks appearing at the surface of the samples.

From the two mono-core square wires, the two multifilamentary conductors 3-T4 and 3-Pb10-T16 were fabricated. Pieces of samples 3-T and 3-Pb10-T were

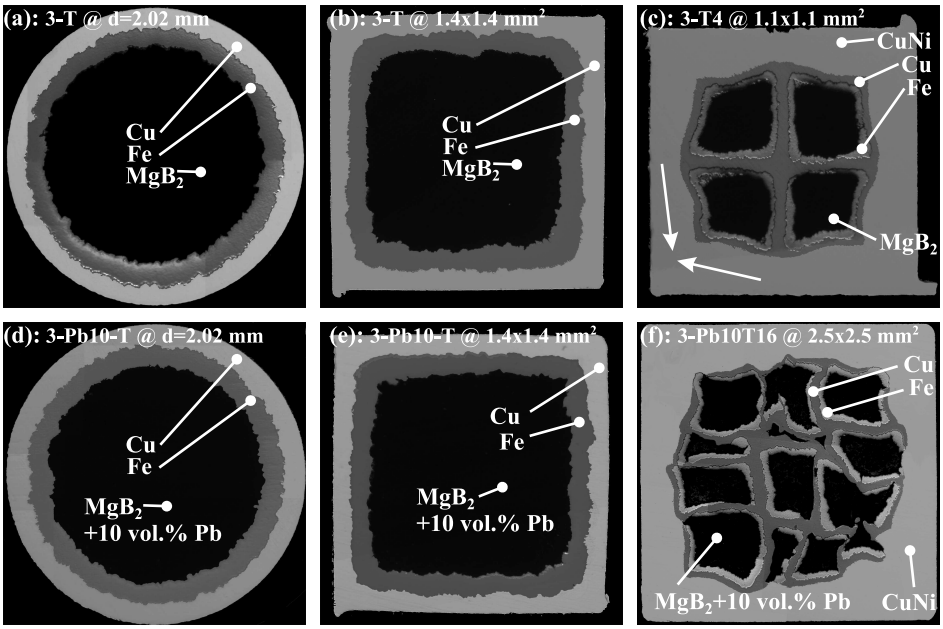

Figure 2.14: Optical micrographs of the two-axially rolled samples in different deformation stages. (a) and (d) show samples 3-D and 3-Pb10-D, drawn to $d = 2.02$ mm; (b) and (e) show the mono-core two-axially rolled samples 3-T and 3-Pb10-T; (c) and (f) show the multifilament two-axially-rolled samples. The arrows in (c) indicate the flow of the matrix material.

stacked into a Cu-Ni outer tube in a 2×2 and a 4×4 arrangement. As discussed above, Pb-containing wires can be drawn to higher true strain levels than samples without Pb. Therefore, the amount of filaments for sample 3-T4 was limited to 4, while sample 3-Pb10-T16 contained 16 filaments. The multifilamentary wires were rolled to 1.1×1.1 mm^2 and 2.5×2.5 mm^2, respectively. As with the square mono-core wires, their final dimensions were limited by splitting of the surface.

Figure 2.14 shows optical micrographs of the cross-section of the two-axially rolled wires at different deformation stages. To ensure successful sintering the Fe matrix should remain thick enough ($\sim 30\mu$m) to prevent reaction between Cu and MgB_2 [82]. However, in both mono-core and multifilamentary conductors the filaments tend to take a circular shape due to the flow of matrix material towards the corners [83], as indicated by the arrows in figure 2.14c. In the case of sample 3-T4 the non-uniform matrix deformation leads to a Fe reaction barrier that is too thin at some places (down to 12 μm). As discussed below, this leads to a strong reaction between MgB_2 and Cu during the final heat treatment.

In the 16-filaments conductor, on the other hand, figure 2.14f shows that the individual filaments are inhomogeneously deformed: of the 16 filaments only

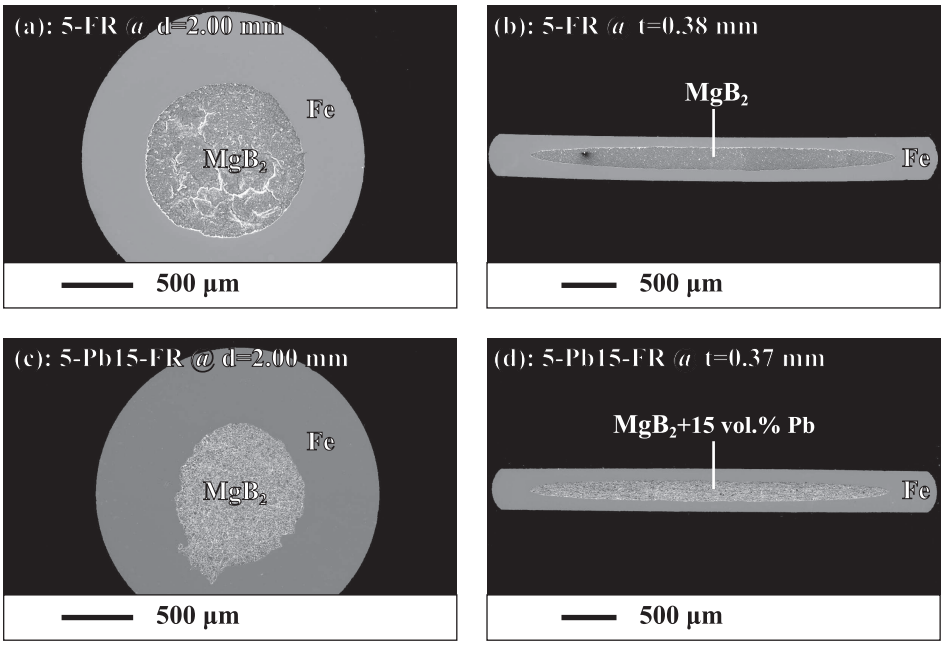

Figure 2.15: SEM micrographs of the flat-rolled samples without Pb ((a) and (b)) and with 15 vol.% Pb (c) and d)). The bright regions in images (c) and (d) indicate Pb-rich areas.

13 can be observed in this particular section. Also this is caused by the flow of matrix material towards the corners, in combination with the relatively thin Cu/Fe matrix in-between the filaments.

Cross-sections of the flat-rolled samples 5-D and 5-Pb15-D at different deformation stages are shown in figure 2.15. The Fe tubes used for these samples are the same as in sample 5-D. Similar to wire 5-D, the flat-rolled conductors are first swaged from a diameter of 8 mm down to 3.85 mm and then further drawn to 2 mm. At this point, the conductors were flat-rolled to their final thickness of ~ 0.38 mm. To account for the work hardening of Fe the area reduction per pass was gradually reduced from 7 % at the first deformation steps down to 1 % for the last.

Figure 2.16 shows longitudinal cross-sections of the 4 samples with different Pb concentrations. In the SEM images, Pb shows up as a bright minority phase inside the grey MgB_2 filament. At lower concentrations it is clearly visible how Pb is distributed as stripes in the rolling direction of the tapes. The density of these stripes increases with the Pb concentration. This indicates that the softer Pb indeed flows in-between the harder MgB_2 particles and acts as a lubricant during the deformation. Furthermore, table 2.2 shows a clear trend towards lower

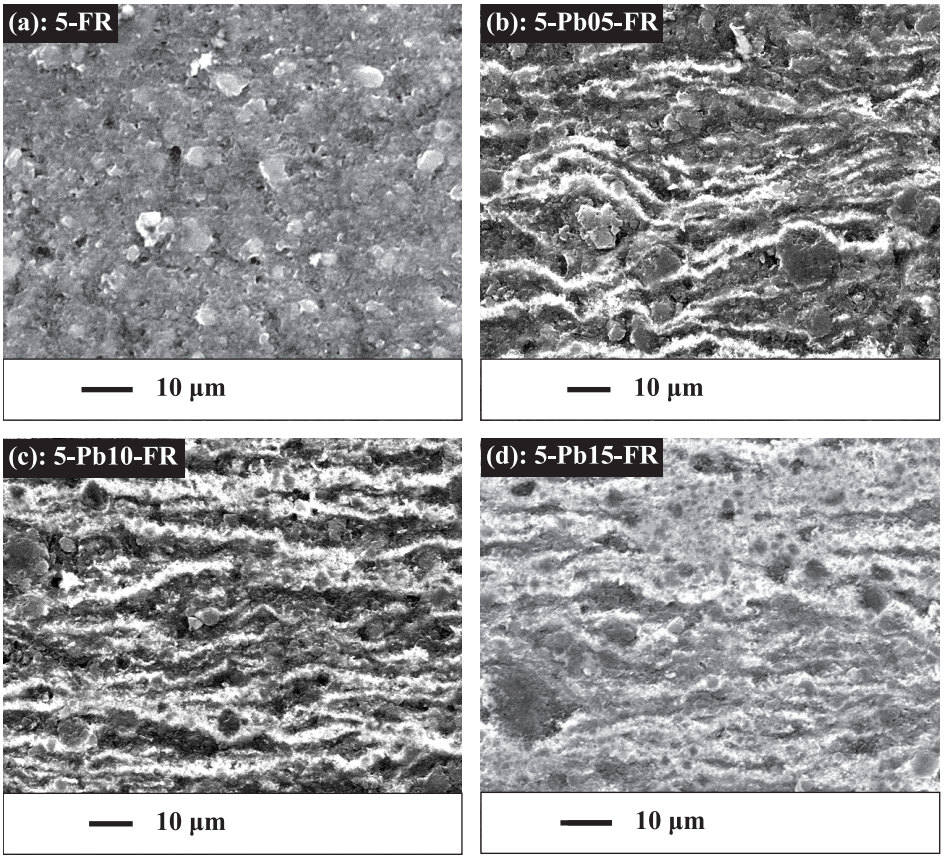

Figure 2.16: SEM micrographs of longitudinal cross-sections of the as-rolled flat tapes with 0, 5, 10 and 15 vol.% Pb. The rolling direction is horizontal.

filling factors for higher Pb concentrations. Since the initial filling factor $\rho_{\mathrm{fil},0}$ was 39 % for all tapes, this is an indication for the higher powder densification that is obtained. In the next paragraph, the powder densification that can be obtained with different deformation routes is further discussed.

2.3.2 Powder Densification

Normalised density versus True Strain

The different deformation procedures, matrix materials and Pb concentrations lead to a different filament density of the final conductor and thus to different critical current densities. To keep track of the powder densification during deformation, the length and cross-sectional area change at each deformation pass is

recorded. The critical current density of green samples in different deformation stages is also measured, which will be discussed in the next paragraph[5].

Since the volume of the matrix remains constant, the filament density ρ_{fil} at any stage of deformation can be estimated as:

$$\frac{\rho_{\mathrm{fil}}}{\rho_{\mathrm{fil},0}} = \frac{f_0\,(l_0/l)}{(A/A_0) - (1-f_0)\,(l_0/l)}, \tag{2.7}$$

with $\rho_{\mathrm{fil},0}$ the initial powder density after filling the tube; l_0 the initial length; A_0 the initial overall cross-section; and f_0 the initial filling factor. The overall cross-sectional area A and the length l at intermediate stages of deformation are simply measured.

The density evolution is presented as a percentage of the theoretical filament density ($\rho_{\mathrm{fil}}/\rho_{\mathrm{fil,th}}$) versus the true strain ϵ. The theoretical filament density $\rho_{\mathrm{fil,th}}$ of the samples with Pb is determined as:

$$\rho_{\mathrm{fil,th}} = (1 - f_{\mathrm{Pb}})\,\rho_{\mathrm{MgB_2}} + f_{\mathrm{Pb}}\rho_{\mathrm{Pb}}, \tag{2.8}$$

with f_{Pb} the volume fraction of Pb in the powder and $\rho_{\mathrm{MgB_2}}$ or ρ_{Pb} the densities of MgB_2 or Pb ($\rho_{\mathrm{MgB_2}} = 2.62$ g/cm^3 and $\rho_{\mathrm{Pb}} = 11.3$ g/cm^3). The true strain is determined from the reduction of cross-sectional area:

$$\epsilon = \ln\left(\frac{A_0}{A}\right). \tag{2.9}$$

Figure 2.17a shows how the density evolves during the drawing of wires 3-D and 4-D with Cu/Fe and Cu matrix. For both wires, the density saturates at approximately 82 % of its maximum theoretical value, even though sample 4-D has a higher initial density than 3-D. The plot also indicates the effect of the softening heat treatment on the evolution of the filament density of wire 3-D. As discussed above, heat treatments were applied at 450°C for 2 hours at true strain values of 1, 2 and 3. Already after the first heat treatment at $\epsilon = 1$, the density decreases by about 10 %. This clearly shows the strong relation between matrix hardness and powder densification.

Figure 2.17b shows how densification during drawing and flat rolling differ by comparing sample 3-D and 5-FR. It should be noted that during initial swaging and drawing of sample 5-FR, no length change was recorded. The first point of the density evolution during rolling is just after the last drawing step at a diameter of 2 mm ($\epsilon = 2.8$). The filling factor f_0 at this point is determined from the cross-sectional SEM image in figure 2.15a, while the initial powder density $\rho_{\mathrm{fil},0}$ is determined from the weight and volume of a piece cut of the wire.

Up to $\epsilon = 2.8$ sample 5-FR has gained a similar density as sample 3-D, despite its harder and thicker Fe matrix and the fact that it is also swaged (up to $\epsilon = 1.5$;

[5]Note that for the two-axially rolled samples the densification was not recorded. Furthermore, these samples were prepared from milled powder with a poor J_c. Therefore, densification of the two-axially rolled samples is not discussed.

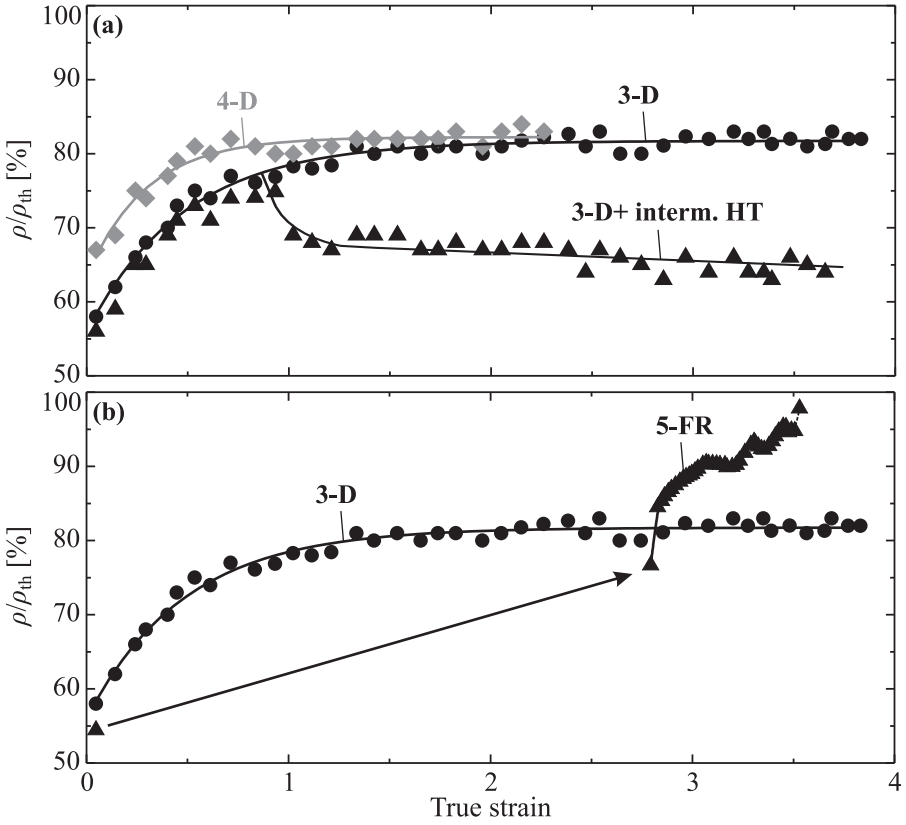

Figure 2.17: (a) shows the densification during drawing of samples 3-D and 4-D. Also shown is the effect of the softening heat treatment on the densification of sample 3-D. (b) shows the densification during the drawing of sample 3-D and the rolling of sample 5-FR. The **solid lines** are a guide to the eye.

$d = 3.85$ mm). However, already during the first rolling step the density increases by ~ 10 % and then continues to increase with true strain, while with drawing it saturates. The enhanced densification during flat rolling may result from the absence of a pulling force which counteracts the densification.

The difference in densification during drawing of samples with and without Pb is shown in figure 2.18a. In both samples 3-D and 3-Pb10 the density saturates. However, the maximum level is ~ 86 % in 3-Pb10-D, which is 4 % higher than in 3-D. Also for the flat-rolled tapes in figure 2.18b, a trend towards higher density with increasing Pb concentration can be observed. This suggests that the soft Pb fills the voids in-between the hard MgB_2 grains.

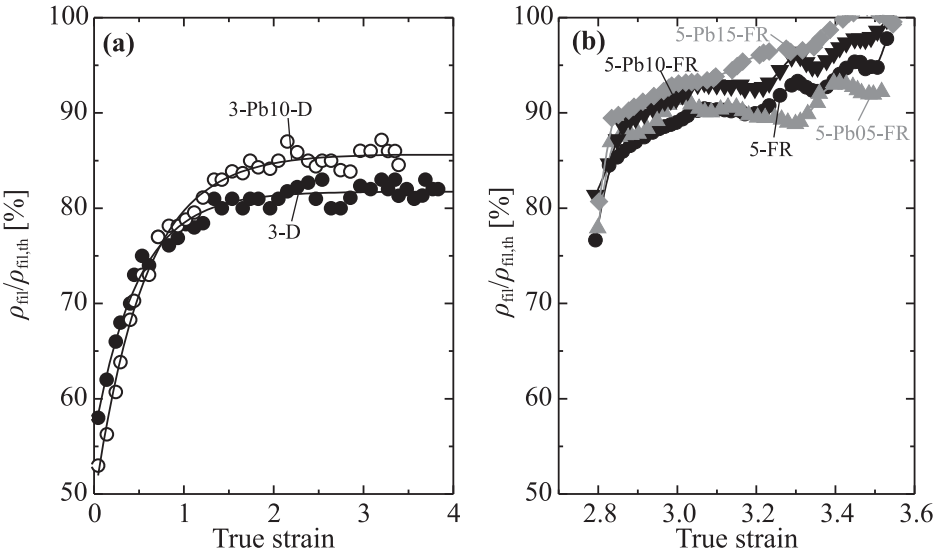

Figure 2.18: Influence of Pb additions on the densification. (a) shows the densification of the drawn wires 3-D and 3-Pb10-D and (b) of the flat rolled tapes 5-FR to 5-Pb15-FR. The **solid lines** are a guide to the eye.

Critical current versus True Strain

To keep track of the evolution of J_c during drawing and flat-rolling, pieces of the conductors were cut at several stages of deformation. J_c of the as-deformed samples was measured in a magnetic field parallel to the tape surface and at $T_0 = 4.2$ K. The voltage taps were placed ~ 1 cm apart and an electric field criterium of 100 μV/m was used.

In figure 2.19a the drawn samples with either Fe or Cu/Fe matrix are compared. Samples 5-D and 3-D-II were subjected to the same swaging/drawing deformation and are both measured at $B = 1$ T. The harder and thicker Fe matrix of sample 5-D causes a higher densification and higher J_c than the relatively thin Cu/Fe matrix of sample 3-D-II. Similarly, the piece of sample 3-D that was subjected to intermediate heat treatments has a significantly lower J_c value than the one without. Comparison with figure 2.17 shows that this is likely due to the reduced filament density after heat treatment.

Figure 2.19b shows how the J_c value of samples 5-D and 5-FR evolves during deformation. Both conductors were subjected initially to the same swaging and drawing deformation up to $d = 2$ mm ($\epsilon = 2.77$). After that point, sample 5-D was further drawn, while sample 5-FR was flat-rolled. As expected, both samples have a similar J_c value at $\epsilon = 2.77$. However, further flat-rolling clearly increases J_c to a larger extent than continued drawing. This is in agreement with the

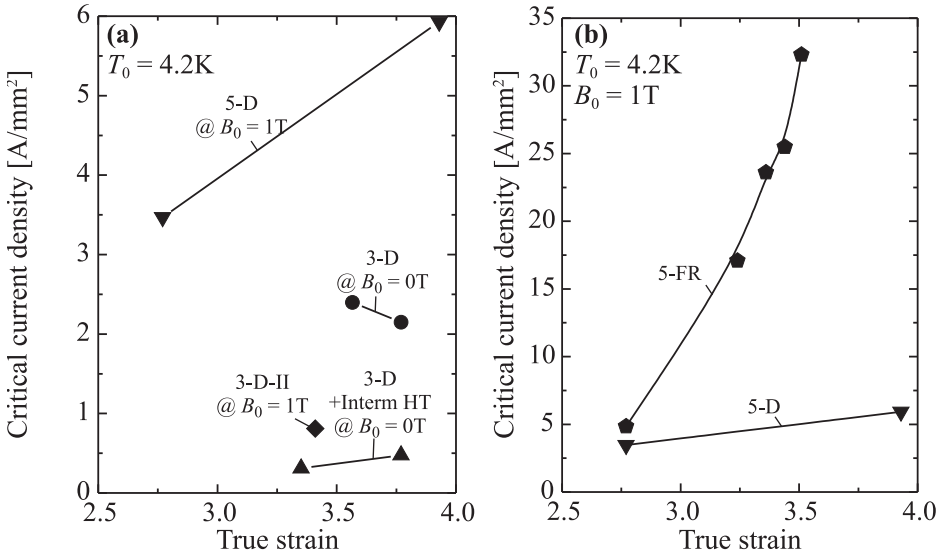

Figure 2.19: Evolution of the critical current density as function of true strain of as-deformed samples. (a) samples with different matrix materials and varying hardness; (b) samples that are either drawn or flat-rolled.

difference in the density evolution during the two processes as shown in figure 2.17b.

The influence of Pb on the evolution of the J_c value in as-deformed samples is shown in figure 2.20. In figure 2.20a it is shown that sample 3-Pb10-D has a J_c value at $B = 0$ T that is nearly two orders of magnitude larger than that of sample 3-D. At $B = 1$ T, however, its J_c has decreased significantly. This shows that at $B = 0$ T, most of the current is carried by the Pb, which is superconducting at this field. At $B = 1$ T, Pb is not superconducting anymore and only the MgB_2 grains carry a supercurrent. Similarly, it is shown in figure 2.20b that at $B = 1$ T, the flat-rolled samples with higher Pb concentrations tend to have lower critical current densities. These two observations lead to the conclusion that Pb in the normal state hampers the MgB_2 grain-to-grain connectivity and thus lowers J_c.

Similar to the samples without Pb, the J_c value of the Pb-containing wires is approximately constant during drawing, but increases with progressive flat-rolling.

2.4 Final Heat Treatment

It is generally observed that the final heat treatment of as-deformed ex-situ conductors causes an increase in J_c by approximately one order of magnitude [64]. In

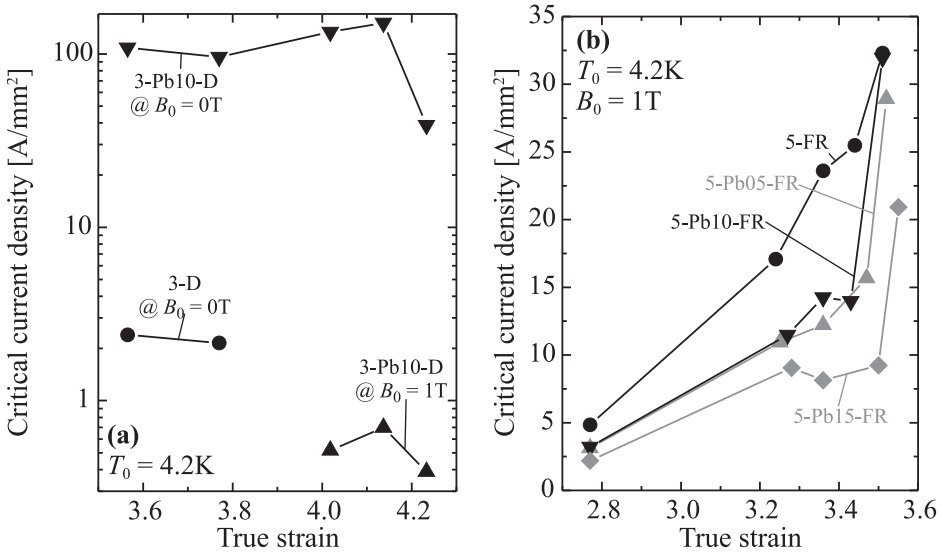

Figure 2.20: Evolution of the critical current density as function of true strain of as-deformed samples with and without Pb. (a) drawn samples (note the logarithmic scale of the critical current density); (b) flat rolled samples.

this paragraph, the interplay between microstructure and critical current behind this improvement is discussed.

In §2.4.1 the influence of the heat treatment on the microstructure is presented. As mentioned above, different deformation routes result in different final filament densities and thus the microstructure might evolve differently during heat treatment. Possible chemical reactions of the MgB_2 with matrix materials are also discussed. Furthermore, it is shown how the heat treatment influences the microstructure of filaments in Pb-containing samples.

Then, in §2.4.2 the influence of the heat treatment on the critical current densities is discussed for differently deformed samples with or without Pb.

All final heat treatments discussed in this paragraph were at 950 °C for 0.5 hr in vacuum. The Pb-containing samples were vacuum-sealed in a quartz tube together with a lump of metallic Pb to prevent excessive Pb evaporation out of the filaments.

2.4.1 Microstructure

Sintering

Figure 2.21 shows the microstructure of the MgB_2 core in tape 5-FR before (a) and after heat treatment (b). The microstructure clearly changes during the heat

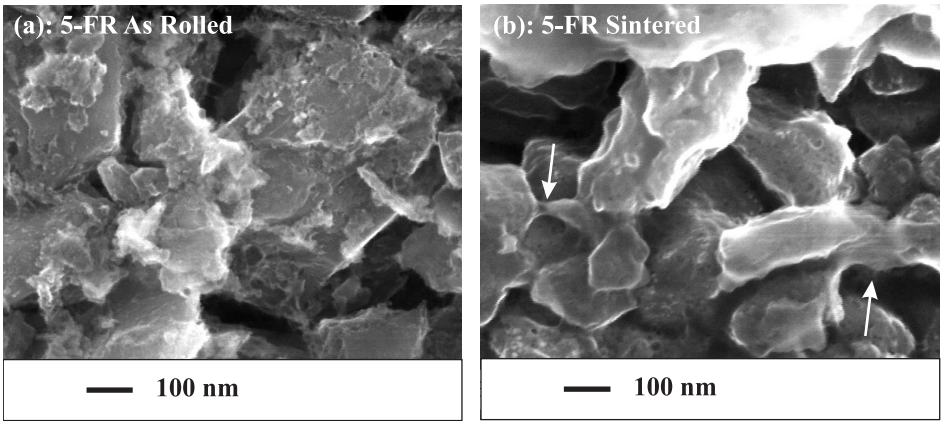

Figure 2.21: HRSEM micrographs of the MgB_2 filament of sample 5-FR. (a) for the as-rolled sample and (b) for the tape sintered at 950 °C for 0.5 hr. The **arrows** in (b) indicate locations where neck formation has occurred.

treatment. First, it can be seen that the MgB_2 grains have recrystallised as the grain surfaces are rounded and smoother than before heat treatment. Furthermore, the arrows in figure 2.21b indicate sites where "necks" between grains have formed, which is typical for sintering [84]. In this way, the heat treatment strongly improves the grain-to-grain connectivity and thus increases J_c. Note that this is in direct contrast to [85], where no sintering was observed in bulk MgB_2 samples up to $T = 1100$ °C.

Reaction Layer

The main purpose of Fe in the matrix is to prevent the strong reaction between Cu and MgB_2 [56, 60–62]. However, Fe and MgB_2 also react to some extent, which at 950 °C for typical heat treatment times of 0.5 hr leads to the formation of interface layers of 12 to 35 μm thickness [86]. Therefore, the Fe reaction barrier should be about 3 times as thick to prevent contact between Cu and Mg [82]. As discussed above, the multifilamentary two-axially rolled conductor 3-T4 has a relatively thin Fe reaction barrier, in some places down to 12 μm (see figure 2.22a). Figure 2.22b and c show sample 3-T4 before and after heat treatment. The Fe reaction barrier was clearly too thin, causing Cu to diffuse into the filaments leaving voids in the matrix. Even if in this particular conductor the filaments were deformed non-uniformly and the Fe barrier became too thin only at some places, the requirement of a thick reaction barrier may impose filament size limits on the development of multifilamentary conductors with a Cu/Fe matrix.

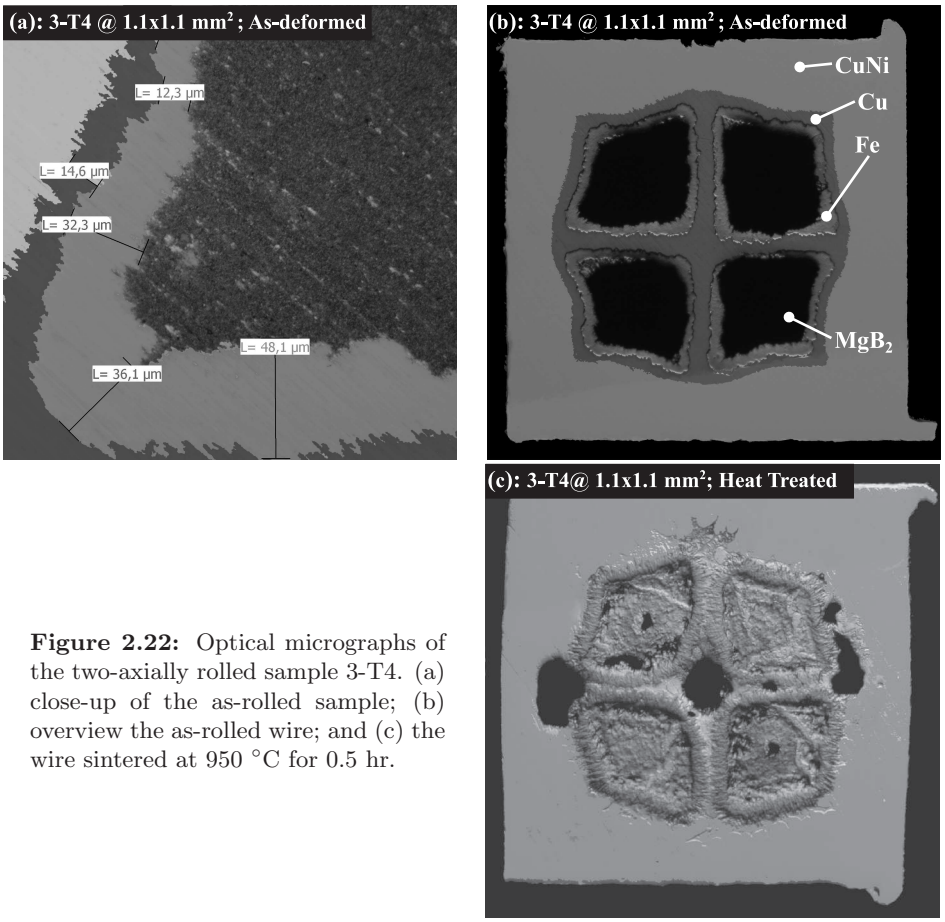

Figure 2.22: Optical micrographs of the two-axially rolled sample 3-T4. (a) close-up of the as-rolled sample; (b) overview the as-rolled wire; and (c) the wire sintered at 950 °C for 0.5 hr.

Lead Addition

The motivation to investigate Pb-additions was not just improved deformation, but also possible J_c enhancement. Lead could improve intergrain connectivity by the formation of S/N/S junctions, but might also facilitate sintering. The envisaged mechanism is that the presence of a liquid phase significantly increases diffusivity and thus enhances neck growth and grain-to-grain connectivity.

Lead melts at $T \approx$ 330 K so that it can redistribute in the filament well before the sintering temperature 950 °C is reached. In this way, enhanced neck growth of the MgB_2 grains would occur uniformly throughout the filament. Furthermore, in an O-poor environment no chemical reaction of Pb with either Fe, Mg and B should occur, since the only binary phase in this system, Mg_2Pb, is not stable above 550 °C [87].

Figure 2.23 shows the EDX chemical mapping of Mg and Pb in sample 5-Pb15-FR before and after heat treatment (a to c and d to f, respectively). In the

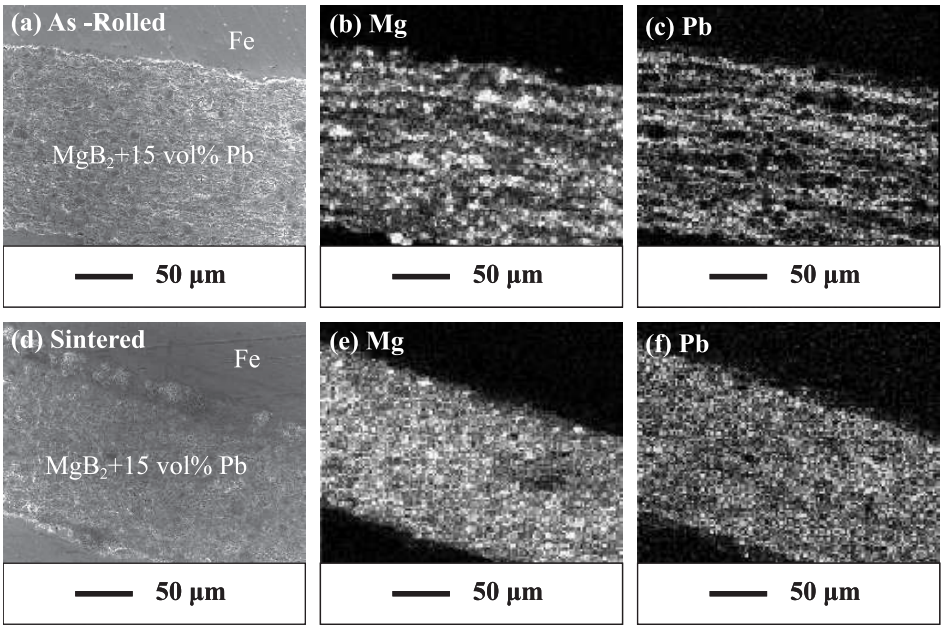

Figure 2.23: EDX mapping of the as-rolled ((a) to (c)) and sintered tape 5-Pb15-FR ((d) to (f)). (a) and (d) show the SEM images of the mapped area; (b) and (e) the distribution of Mg in the filament; and (c) and (f) the distribution of Pb in the filament.

as-rolled tape, the Pb stripes in the rolling direction are visible as discussed in the context of figure 2.15. After the heat treatment, Pb is redistributed across the filament.

HRSEM micrographs, did not reveal any improvement of the neck growth between the MgB_2 grains. Nevertheless, the distributed Pb in-between the MgB_2 grains may still improve the $J_c(B)$ characteristic through the formation of S/N/S junctions or through thermal stabilisation.

2.4.2 Critical Current Density

In the previous paragraph it was shown that the MgB_2 grains in sample 5-FR indeed show neck growth and that sintering thus enhances the grain-to-grain connectivity. However, as-drawn conductors show a significantly lower filament density than flat-rolled ones so that J_c after heat treatment is expected to be lower.

In figures 2.24a and b it is shown how the $J_c(B)$ characteristic of the drawn wires 3-D-II and 5-D improves with heat treatment. Wire 5-D has a relatively hard Fe matrix compared to the softer Cu/Fe matrix used in sample 3-D-II. It

was already shown that this results in a higher filament density and an as-drawn J_c value of a factor 10 higher than in sample 3-D-II. This difference remains the same after sintering: both conductors show a factor 10 improvement of J_c after heat treatment irrespective of the as-drawn filament density.

A measure for the homogeneity in a conductor is the slope of its voltage-current characteristic:

$$E = E_c \left(\frac{J}{J_c} \right)^n , \tag{2.10}$$

with E the electric field, E_c the electric field at which the critical current density J_c is defined, J the current density in the superconducting filaments and n the exponent of the power law. A smooth slope is characterised by a low n-value and indicates poor homogeneity in the filaments. The relatively high n-values of sample 5-D are typical for ex-situ MgB_2 conductors and are about a factor of 10 higher than those for sample 3-D-II. Furthermore, sample 3-D-II does not show a clear field dependence of the n-value. Together, these observations demonstrate a relatively poor homogeneity of the filament in sample 3-D-II.

In figure 2.25, it is shown that also in the flat-rolled tapes a significant improvement is obtained in the flat-rolled samples during heat treatment. For sample 5-FR with no Pb, J_c at 4.2 K, 4 T increases by a factor 20. However, the apparent $J_c(B)$ characteristic of the Pb-free reacted tape shows a clear plateau at fields lower than 6 T, caused by lack of thermal stabilisation due to the poor conductivity of the pure Fe matrix. This poor thermal stabilisation causes thermal runaways at high currents, which will be further elaborated in chapter 4. The plotted data of sample 5-FR below 6 T are strictly speaking not critical current density values, but rather quench current densities at which thermal runaways occur. As will be shown in §3.2.1 the "true" $J_c(B)$ dependence in most MgB_2 conductors can be well approximated with:

$$J_c(B) = J_{c,0}^T \exp \left[-\frac{B}{B_p(T)} \right] , \tag{2.11}$$

with $J_{c,0}^T$ the zero field extrapolation of the critical current at a given temperature and B_p the characteristic current decay field. Fitting the $J_c(B)$ curve of sample 5-FR with (2.11) through the J_c curve above 6 T results in the gray dotted line. Assuming the $J_c(B)$ expression holds and using it to estimate "non-quench" J_c values below 6 T, an improvement of a factor $\sim$ 100 is attained during heat treatment. Compared to the drawn samples this is a relatively large gain, indicating that the higher as-rolled filament density in the tapes causes more contact areas between the grains that can serve as necking sites during sintering and thus improve J_c to a larger extent.

The main advantage of using Pb becomes clear by comparing the Pb-free sample 5-FR with the Pb-containing tapes 5-Pb05-FR and 5-Pb10-FR. The latter two samples do not show a plateau and J_c continues to increase towards lower field. This clearly shows that Pb works as an internal thermal stabiliser. On

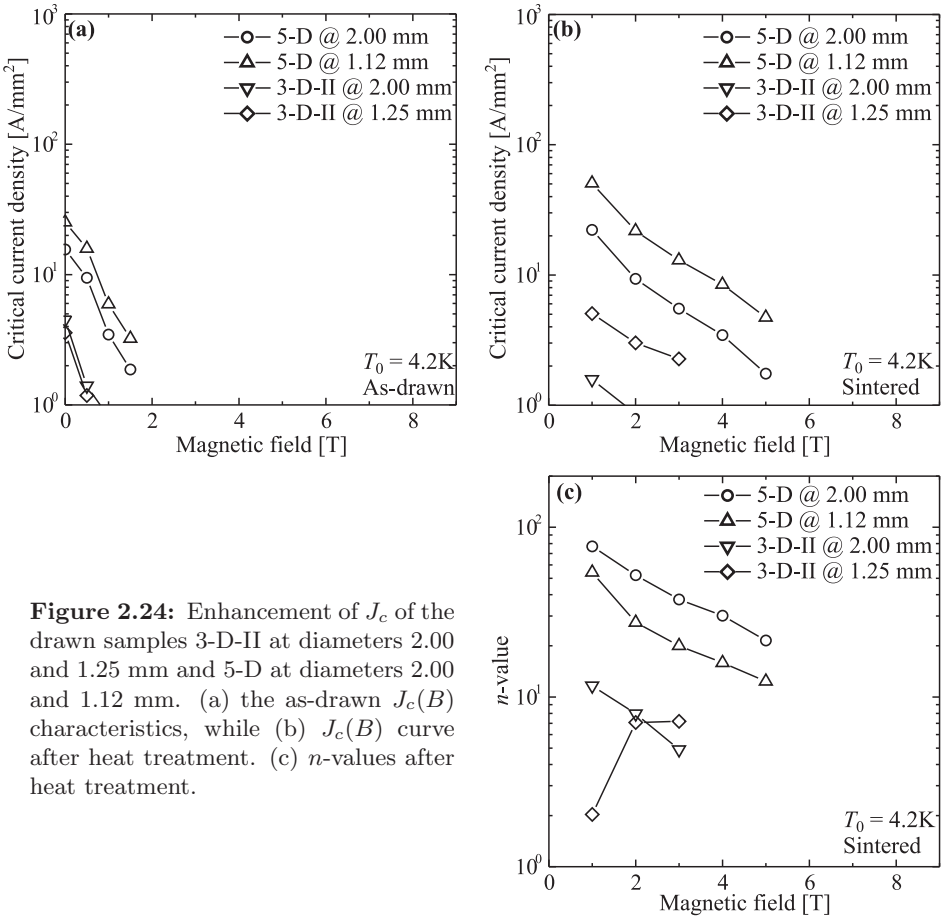

Figure 2.24: Enhancement of J_c of the drawn samples 3-D-II at diameters 2.00 and 1.25 mm and 5-D at diameters 2.00 and 1.12 mm. (a) the as-drawn $J_c(B)$ characteristics, while (b) $J_c(B)$ curve after heat treatment. (c) n-values after heat treatment.

the other hand, the $J_c(B)$ curves of these tapes indicate poorer grain-to-grain connectivity, since the estimated $J_c(B)$ curve of sample 5-FR obtained with (2.11) is generally higher than that of the Pb-containing samples. Lead thus hampers the connectivity rather than improving it. Furthermore, in figure 2.25c, it is shown that the the n-values decrease with increasing Pb concentration, again indicating poorer homogeneity in the filaments.

Further proof that Pb indeed compromises the homogeneity of current flow in the filaments is also strikingly seen in the voltage-current characteristics at high currents and low magnetic fields. Figure 2.26a shows the voltage-current characteristic of the heat treated wire 1-Pb10-D at self-field. Voltage jumps are visible which are very similar to the ones occurring during a thermal runaway. However, after such a voltage jump a new stable level is reached at a significantly lower voltage level than that corresponding to a completely normal conducting wire. Furthermore, when the current is ramped down again, a hysteresis effect

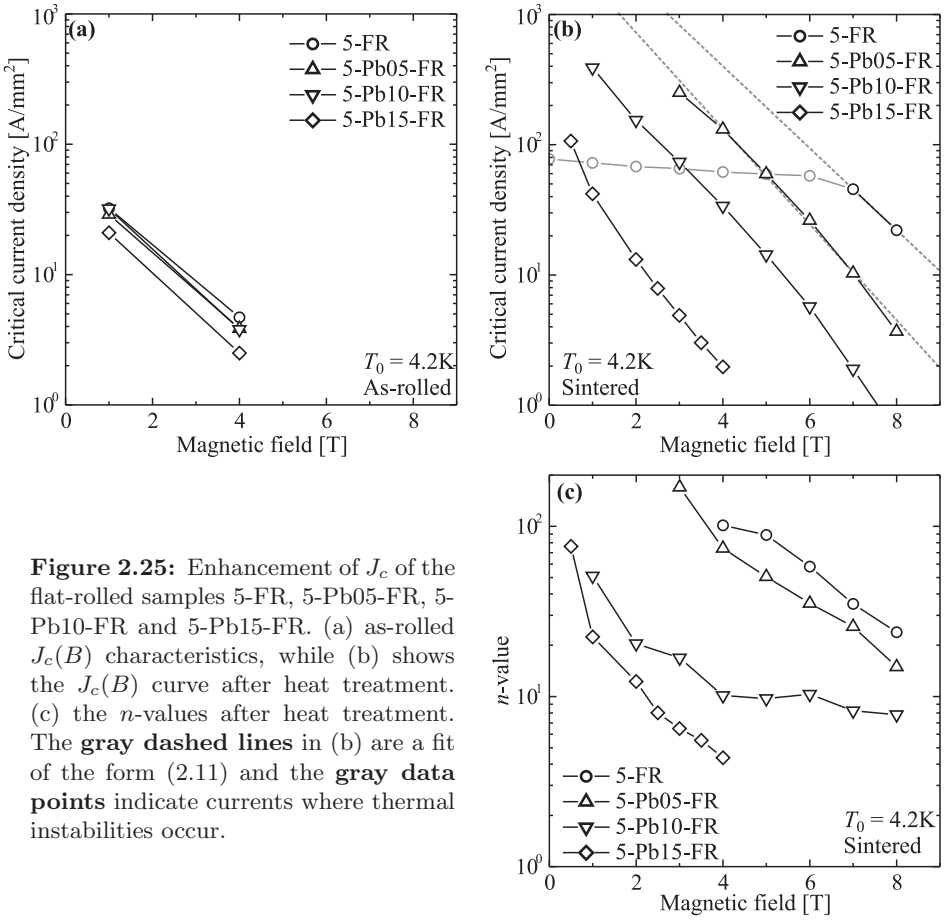

Figure 2.25: Enhancement of J_c of the flat-rolled samples 5-FR, 5-Pb05-FR, 5-Pb10-FR and 5-Pb15-FR. (a) as-rolled $J_c(B)$ characteristics, while (b) shows the $J_c(B)$ curve after heat treatment. (c) the n-values after heat treatment. The **gray dashed lines** in (b) are a fit of the form (2.11) and the **gray data points** indicate currents where thermal instabilities occur.

becomes apparent. These effects were also observed by Boschmann in Nb-Ti conductors [88], although at 10 to 1000 times higher voltage levels, and are explained by the existence of static normal zones in poorly conducting parts of the filament (figure 2.26b). In order to improve the grain-to-grain connectivity while maintaining the enhanced thermal stability, further tests with Pb concentrations between 1-5 vol.% are needed.

Comparison with Published Conductors

In chapter 3, a complete literature survey of MgB_2 conductor data published over the years 2003-2006 is presented in detail. Here, some of the data is already used to compare tapes 5-FR and 5-Pb05-FR to samples produced elsewhere. The characteristic values $J_{c,0}^T$ and B_p defined in (2.11) are used to compare between samples. In addition a third parameter B_{100} is used, which is the magnetic field at which $J_c = 100$ A/mm^2 and can be seen as a rough upper field limit for the use

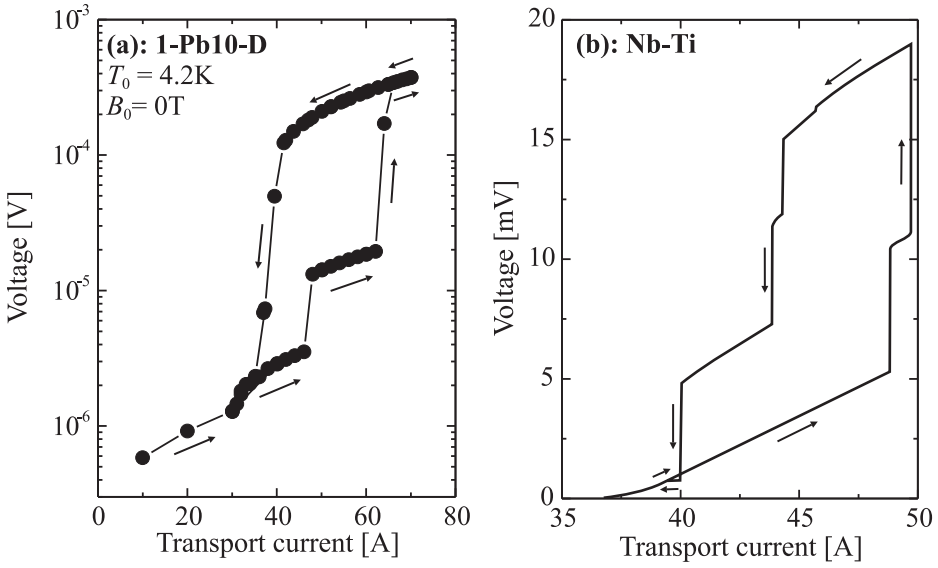

Figure 2.26: Hysteresis in the voltage-current characteristic of the heat treated Pb-containing wire 1-Pb10-D (a) and that of a Nb-Ti conductor (b) after Boschmann [88]. Note the log-scale in (a) and the factor 10-1000 higher voltage scale of (b).

of technical MgB_2 superconductors. Note that B_{100} depends on both $J_{c,0}^T$ and B_p.

Figure 2.27 shows the distributions of B_{100}, B_p and $J_{c,0}^T$ values of the published ex- and in-situ conductors. As explained in chapter 3, the distributions are plotted as floating columns indicating the 5, 25, 50, 75 and 95 percentiles. The solid lines indicate the values of the three characteristic parameters of samples 5-FR and 5-Pb05-FR.

Compared to other published ex-situ conductors, sample 5-FR shows an above-average performance in terms of all three parameters as their values all lie above the median values P_{50}. For the Pb-containing sample 5-Pb05-FR, its B_p value is slightly lower than the median value. However its $J_{c,0}^T$ value is about a factor 2 lower than the median and as a result also its B_{100} value is lower than the median. As will be discussed in §3.4.2, this is a general tendency of ex-situ conductors with additions, indicating compromised connectivity.

Compared with the in-situ conductors, the characteristic parameters of ex-situ samples 5-FR and 5-Pb05-FR all lie below the median values. As discussed in §3.4.1 and §3.4.2 in-situ conductors show a general tendency towards higher B_p values, associated with pinning or B_{c2} enhancement through doping. This trend results also in higher B_{100} values.

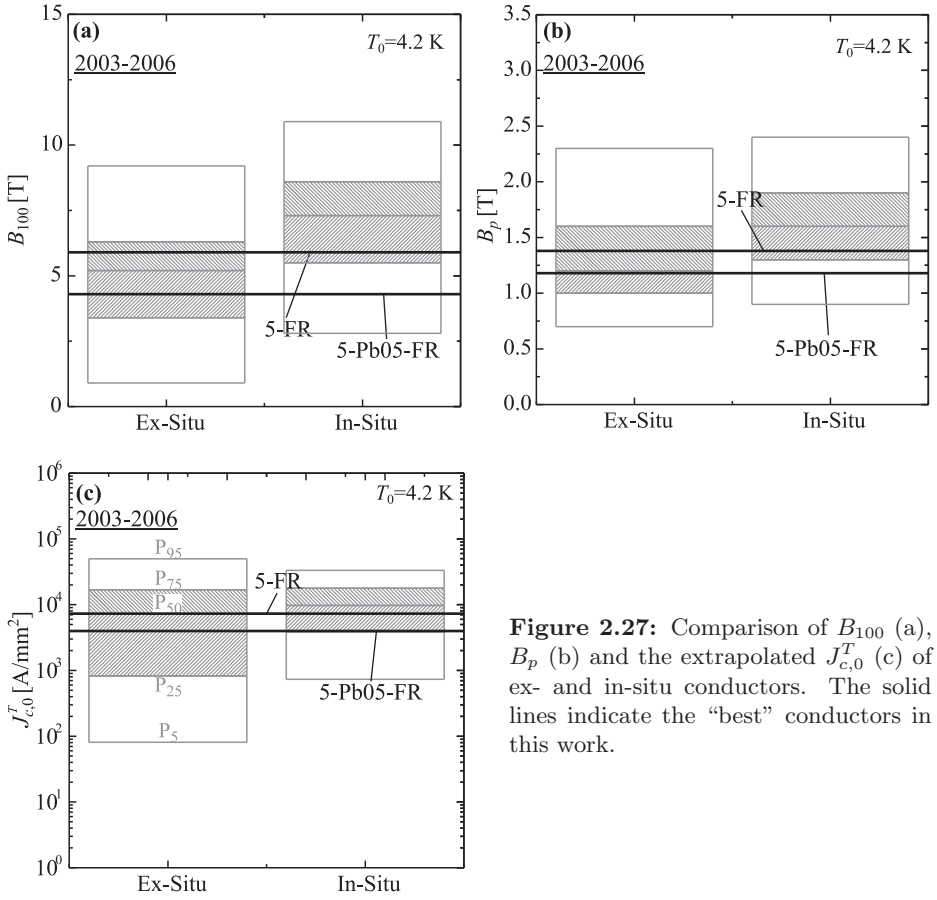

Figure 2.27: Comparison of B_{100} (a), B_p (b) and the extrapolated $J_{c,0}^T$ (c) of ex- and in-situ conductors. The solid lines indicate the "best" conductors in this work.

2.5 Conclusion

To draw PIT conductors down to small diameters using the ex-situ route it is important to reduce the particle size of the as-purchased MgB_2 powder. With finer particles stress concentrations in the matrix during deformation can be avoided. Furthermore J_c can be improved due to enhanced grain boundary pinning. Shear milling is a suitable method to effectively reduce the particle size. With this relatively simple technique the maximum particle size of the as-purchased MgB_2 is reduced from ~ 100 μm to ~ 2 μm after 48 h milling. However, the milling fluid should be inert to prevent reaction with MgB_2. The tested ethanol turns out to decompose into methanol, leaving C as impurities in-between the grains and reducing the intergrain critical current density.

The combined requirements of sufficient densification, no reaction with MgB_2 and enough thermal stability suggest a bi-metal matrix. The outer metal provides the thermal stability, while the inner material acts as a reaction barrier between

the chemical incompatible thermal stabiliser and the MgB_2 filament. Highly conducting thermal stabilisers such as Cu are usually soft materials, while reaction barriers are usually hard. For drawing this may lead to fracture of the reaction barrier due to non-proportional flow during plastic deformation since the harder reaction barrier tends to deform less than the softer stabiliser. As a result, the thermal stabiliser exerts a tensile force on the reaction barrier. However, barrier fracture can be prevented by using either materials with similar yield strengths and work hardening rates or by a high barrier-to-stabiliser radius ratio. After deformation the reaction barrier should still be thick enough to prevent reaction between stabiliser and MgB_2. This may impose limits on the development of $Cu/Fe/MgB_2$ conductors with finer filaments.

The densification of the MgB_2 filament during drawing saturates at ~ 80 % of the maximum theoretical density, while with flat-rolling the filament density continues to increase to ~ 95 %. Compared to drawing, this leads to a factor 5-10 higher as-deformed J_c values. The as-deformed filament density turns out to be also important for the efficiency of the grain-to-grain neck growth during sintering. After heat treatment, J_c in the drawn wires has improved by a factor of 10 compared to the as-drawn value, while for the flat-rolled samples J_c improves by a factor of 50-100. For the fabrication of ex-situ conductors with high current densities, flat-rolling is a more suitable technique than drawing.

The advantage of using a mixture of hard MgB_2 powder with soft Pb is that Pb acts as a lubricant during deformation, indicated by a ~ 7 % higher filament density compared to samples with pure MgB_2. As a result, Pb-containing wires can be drawn to ~ 10 % higher true strain levels. The effect of Pb on the superconducting properties is mainly in enhancing thermal stability. However, grain-to-grain connectivity and thus J_c is compromised by the addition of Pb. Further optimisation of the Pb concentration between 1 and 5 vol.% are needed to increase the grain-to-grain connectivity while maintaining the enhanced thermal stability.

In this work the conductors with the best J_c values are fabricated using flat-rolling and have a Fe matrix with a filament containing either pure MgB_2 or a mixture with 5 vol. % Pb. Compared to ex-situ conductors that were reported over the years 2003-2006, the tape with pure MgB_2 performs above average in terms of the zero-field extrapolation of J_c as well as field retention of J_c. The tape with Pb shows reduced field retention and zero field extrapolation of J_c compared to the one with pure MgB_2, but also shows better thermal stability at lower fields and high currents.

Chapter 3

Critical Current

A literature study is presented of $J_c(B,T)$ data for conductors reported over the years 2003-2006. Statistical analysis is used to reveal general trends and prospects for further development. The main mechanism behind the progress made during these years is discussed and the prospects for further development with the different deformation routes is explored. Also the different effects of additions in ex-situ conductors and in in-situ conductors is presented. Finally it is shown that non-carbon and carbon based additions differently affect the field retention of J_c, possibly on a fundamental level.

3.1 Introduction

The development of practical MgB_2 superconductors has followed different approaches that vary regarding several aspects.

A first aspect is the precursor powder. Conductors are developed using the ex-situ and in-situ routes [89,90]. In both routes progress in the field-dependence of the critical current has been achieved by optimising the starting powder in terms of powder purity and morphology [65, 90, 91]. Also, substantial improvement of the $J_c(B)$ performance has been made with additions to the MgB_2 powder, such as nanometric SiC [24].

A second aspect is the deformation route. The two commonly applied processes are drawing into wires and flat-rolling into tapes [65, 89, 90, 92]. Both conductor types are fabricated using the in- and ex-situ techniques, with and without additions. Important in view of AC-losses, thermal stability and mechanical behaviour is the development of multi-filament conductors. At present all conductor types are successfully fabricated [19,65], with increasing number of filaments and thus reduction of their size.

The development of a new superconducting material into a practical conductor only makes sense if it will offer specific advantages over existing technology. MgB_2 may become an economical conductor for use in medium-range magnetic fields, similar to Nb-Ti but able to operate also at a higher temperature. Indeed, MgB_2 conductors with a high-field $J_c(B)$ performance at 4.2 K better than that of Nb-Ti wires have already been reported [8,17], see figure 1.3.

In the present chapter it is discussed whether this development can reasonably be expected to continue further, or whether the $J_c(B)$ performance of MgB_2 conductors already appears to approach intrinsic limits. A second question to be addressed is whether any of the development lines sketched above is more successful than others.

In an attempt to answer these questions, the literature regarding published transport $J_c(B)$ characteristics of MgB_2 conductors was surveyed over the years 2003 to 2006. Characterising the $J_c(B)$ curves with only three figures of merit allows to perform a statistical analysis of trends in the development of MgB_2 conductors. With such statistical analysis it is also possible to distinguish between conductor-types categorised by ex-situ versus in-situ or tape versus wire, regardless of laboratory-specific fabrication conditions. Also, distribution functions of the three figures of merit allow to reveal possible intrinsic limits, based on the $J_c(B)$ data so far.

It should be noted, however, that a meaningful statistical analysis requires a sufficient amount of samples (typically ≥ 15). It is not possible with this method to study trends in less common conductor-types, such as those fabricated using the liquid infiltration technique [53] or "coated conductor" routes [50,52,93]. Another important remark concerns "record" performance conductors. By its very nature, a statistical analysis will not reveal the combination of factors leading to such "best" performance. Instead, it will indicate trends and thus help to clarify the general potential of certain development routes.

In the survey described in this chapter, the published conductors are first discriminated according to their publication year, which allows to study the progress over the years in §3.3.

To study the effect of different precursor powders, the conductors are also categorised by either in-situ or ex-situ fabrication route. Also the group of conductors that contain pure MgB_2 and those also containing additions are distinguished. How the $J_c(B)$ characteristics among these categories tend to differ is subject of §3.4.

From a deformation point of view samples are categorised as wires or tapes and mono- or multi-filament. In §3.5 it is discussed how the $J_c(B)$ curves of wires and tapes tend to differ. Whether further deformation and down-scaling of the filaments in multi-filament conductors tend to affect the $J_c(B)$ characteristic is also considered.

The chosen $J_c(B)$ parametrisation is presented in §3.2 together with the method and overall results of the literature survey.

3.2 Literature Survey

In §3.2.1 it is illustrated how the $J_c(B)$ dependence of the conductors is parameterised with three "figures of merit": the extrapolated self-field J_c-value and two characteristic fields B_p and B_{100}. Which published $J_c(B)$ curves are included in the survey and which not is described in §3.2.2 together with the overall results. In order to study the influence of several variables on the $J_c(B)$ behaviour (year, in versus ex-situ, pure MgB_2 versus additions) distribution functions of the three figures of merit are also introduced in this paragraph.

3.2.1 Critical Current Characterisation

To describe the critical current density of MgB_2 conductors as a function of magnetic field and temperature the following approximation [94] is fitted to the published $J_c(B)$ results (see also figure 3.1):

$$J_c(B,T) \approx J_{c,0}^T \exp\left[-\frac{B}{B_p(T)}\right] \text{ with } J_{c,0}^T(T) = J_{c,0}\left(1-\frac{T}{T_c}\right) \text{ and } B_p(T) = B_{p,0}\left(1-\frac{T}{T_c}\right), \tag{3.1}$$

where $J_{c,0}^T$ is the temperature-dependent zero-field extrapolation of the critical current density; $J_{c,0}$ the zero-temperature zero-field extrapolation of J_c; $B_p = \partial B/\partial \ln(J_c)$ the temperature-dependent exponential current decay field; and $B_{p,0}$ its zero temperature extrapolation. With approximation (3.1), the parameters $J_{c,0}^T$ and B_p fully describe the $J_c(B)$ curve of a given conductor at a given temperature. $J_{c,0}^T$ is the maximum critical current density at that temperature. A-priori, it might be determined by the grain-to-grain connectivity or effective cross-section

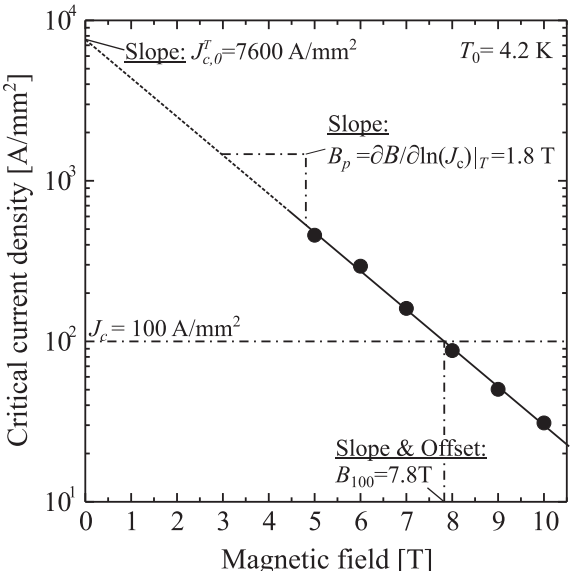

Figure 3.1: Example of fitted $J_c(B)$ data [95]. Indicated are the zero field extrapolation of the critical current density $J^T_{c,0}$; the slope $-1/B_p$ of the $J_c(B)$ curve; and the magnetic field B_{100} where J_c falls below a value of 100 A/mm^2.

in the filaments, but also by the intra-granular pinning of vortices. B_p describes the field retention of J_c and is influenced by both flux-pinning and B_{c2}. Note that B_p is also the magnetic field at which the pinning force $F_p = J_c B$ is maximum.

Figure 3.1 illustrates how the parameters $J^T_{c,0}$ and B_p are extracted from the data published in [95]. These $J_c(B)$ data are typical in the sense that the authors only published results at higher fields ($B \geq 5$ T). At low fields insufficient thermal stabilisation often causes thermal runaways or a homogeneous rise of the sample temperature so that the apparent $J_c(B)$ curve tends to "level off" towards zero field.

This implies that the parameter $J^T_{c,0}$ usually needs to be extrapolated, introducing uncertainty on the obtained results. Therefore a third parameter B_{100} was extracted from the data, defined as:

$$B_{100} \equiv B_p(T) \ln \left(\frac{J^T_{c,0}}{100\ [\mathrm{A/mm^2}]} \right). \tag{3.2}$$

B_{100} is the field at which the value of J_c falls below 100 A/mm^2. The value 100 A/mm^2 is an arbitrary choice, but can reasonably be seen as a lower limit for the usefulness of technical superconductors. B_{100} can therefore be considered as a practical upper field limit for the use of a given superconductor. The advantage of using B_{100} is that in most papers it falls within the published data range.

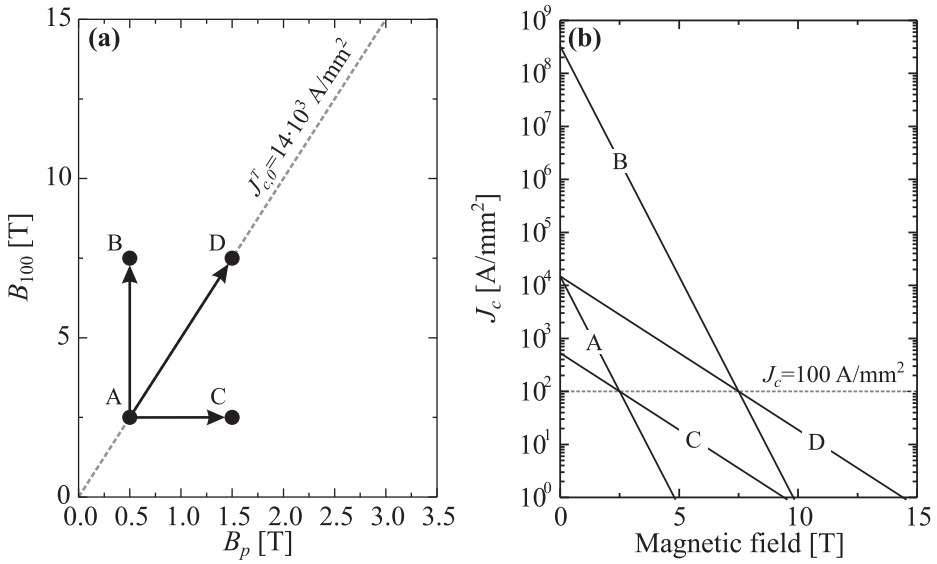

Figure 3.2: (a) shows the B_{100}-B_p plot in which the four hypothetical conductors A, B, C and D are indicated. The dotted line indicates the zero field extrapolation of J_c of conductors A and B. (b) shows their corresponding $J_c(B)$ curves.

Note that its value depends on grain-to-grain connectivity as well as on the field retention of J_c. Obviously, the three parameters $J_{c,0}^T$, B_p and B_{100} are not independent.

To illustrate their relation, figure 3.2a shows the B_p and B_{100} values of four hypothetical conductors A-D, while figure 3.2b shows their corresponding $J_c(B)$ curves. Conductor A has relatively low B_p and B_{100} values, corresponding to a steep decay of J_c with magnetic field and a relatively low overall J_c. Conductor B has the same B_p value as conductor A. However, its B_{100} value is higher due to a higher overall J_c [1]. Thus, conductor B has a better connectivity than conductor A. Conductor C shows a higher B_p value, corresponding to a better field retention of J_c. However, the B_{100} values of conductors A and C are similar due to its lower $J_{c,0}^T$. Compared to conductor A, conductor D has the same $J_{c,0}^T$ value but a better field retention, resulting in a higher B_{100}. Thus, it is pinning or a higher B_{c2} causing conductor D to perform better than A.

3.2.2 Result of the Literature Survey

For the survey, the literature database INSPEC was used to collect a publication record [96]. The search term "(MgB_2 wire) or (MgB_2 tape) or (MgB_2 conductor)"

[1] Note that the zero field extrapolation of $J_c \sim 10^8$ A/mm^2 in this hypothetical sample is unrealistically high.

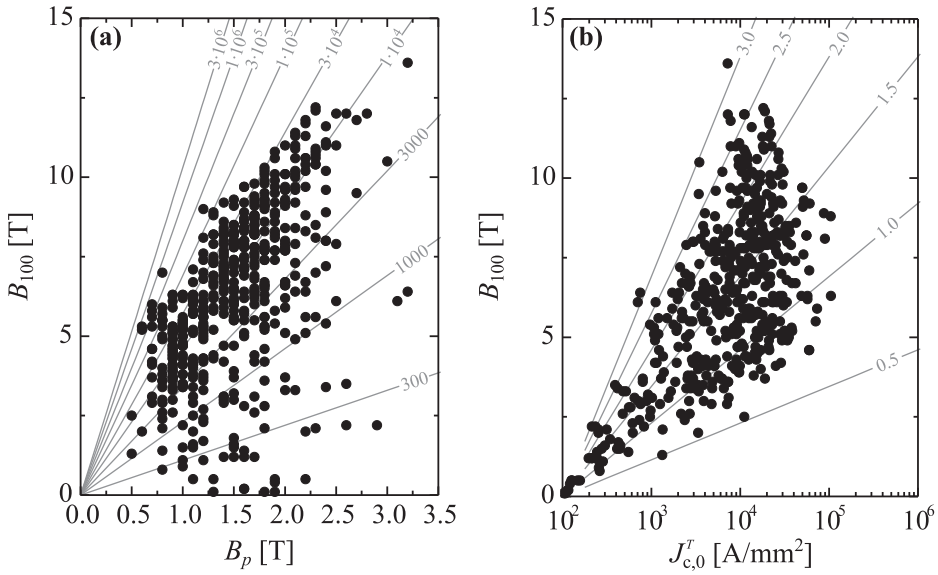

Figure 3.3: (a) shows the B_{100} versus B_p plot in which all investigated conductors are indicated. The gray lines indicate constant $J^T_{c,0}$ values (units are [A/mm^2]). (b) shows the equivalent B_{100} versus $J^T_{c,0}$ plot. The gray lines indicate constant B_p values.

yields about 300 articles over the years 2003-2006. Earlier conductor development, covering 2001 and 2002, is described in the review [56]. Approximately 110 of the 300 papers present transport $J_c(B)$ or $I_c(B)$ data together with information on the filling factor. Overall, the survey comprises $J_c(B)$ curves of approximately 550 different MgB_2 conductors. The publications used are [19–22,53,55,58,65,74,89–92,95,97–189] and selected properties of the conductors are tabulated in appendix A. Note that this survey focusses on the $J_c(B)$ curves at 4.2 K. Only < 5 % of published $J_c(B)$ characteristics were measured at the anticipated operating temperature of ~ 20 K, which would lead to poor statistics in the further analysis. Nevertheless, a general comparison between the available data at 20 K and those at 4.2 K is presented in §3.6.

The overall result of the literature survey is summarised in figures 3.3a and b, showing B_{100} as a function of B_p or of $J^T_{c,0}$, respectively. With respect to the self-field current, the majority of conductors tend to lie grouped around $J^T_{c,0} = 10^4$ A/mm^2, while B_{100} and B_p values are rather scattered and a trend is relatively difficult to deduce.

To study correlations between the three figures of merit and various selected properties or processing conditions (in- versus ex-situ), distributions are determined. Figure 3.4a to c show the overall distributions of B_{100}, B_p and $J^T_{c,0}$. Also indicated in the plots are the 5, 25, 50 (median), 75 and 95 % percentiles of each

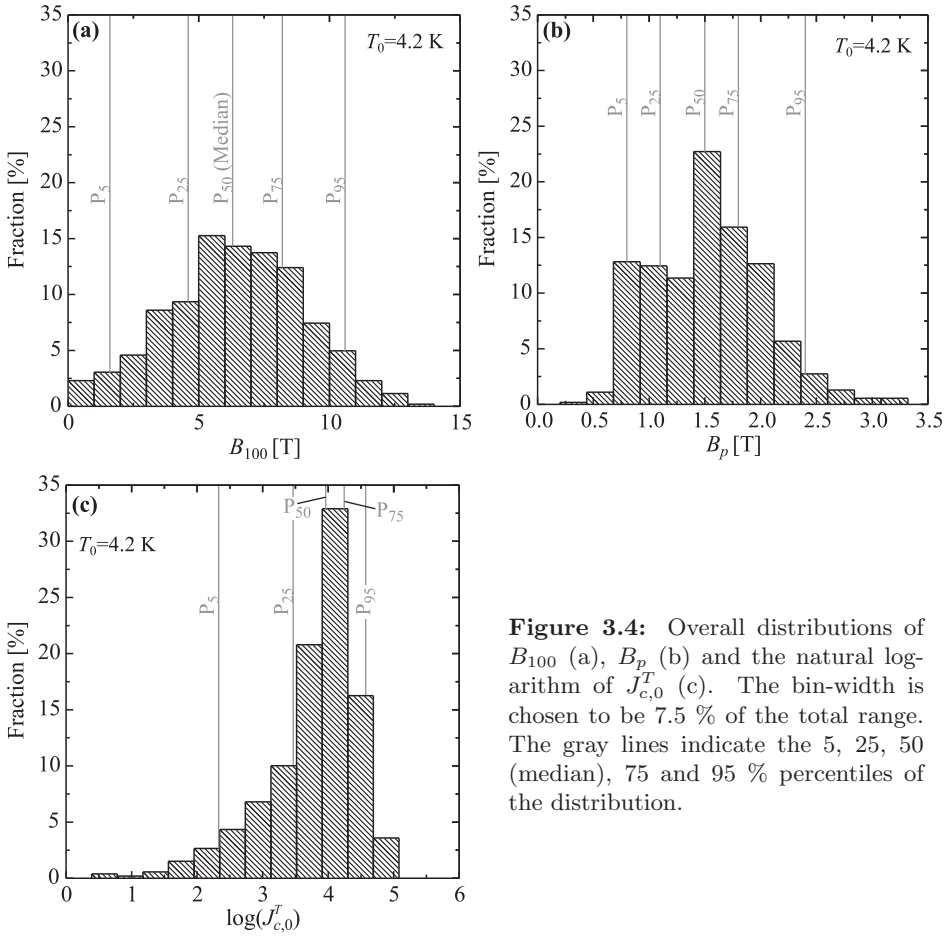

Figure 3.4: Overall distributions of B_{100} (a), B_p (b) and the natural logarithm of $J_{c,0}^T$ (c). The bin-width is chosen to be 7.5 % of the total range. The gray lines indicate the 5, 25, 50 (median), 75 and 95 % percentiles of the distribution.

distribution, which will be indicated by P_5, P_{25}, P_{50}, P_{75} and P_{95}. As an example, the P_{25} value of B_{100} lies at 4.6 T which means that 25 % of the published conductors have a B_{100} value $\leq$ 4.6 T.

Of the three figures of merit B_{100} is arguably the most important one from a technological point of view. Therefore, in the remainder of this chapter variations in B_{100} are discussed in terms of variations in B_p and $J_{c,0}^T$. However, equation (3.2) shows that variations in B_{100} depend on variations in $\ln(J_{c,0}^T)$ rather than $J_{c,0}^T$ itself. For this reason figure 3.4c shows the distribution of $\log(J_{c,0}^T)$.

The first impression in figure 3.3b that the $J_{c,0}^T$ value of the conductors are grouped around the $J_{c,0}^T = 10^4$ A/mm^2 line is reflected in figure 3.4c by a strong peakedness in the $J_{c,0}^T$ distribution. This distribution is also strongly asymmetric. Below the median $P_{50} \sim 10^4$ A/mm^2 the distribution shows a tail towards lower $J_{c,0}^T$ values, while above the median there is a strong drop-down. This is an

indication that the top 50 % of the conductors display $J_{c,0}^T$ values near a maximum. B_{100} and B_p, shown in figure 3.4a and b, have a relatively wider distribution and a less pronounced peakedness.

Note that in figures 3.4a to c all conductors are lumped together, i.e. no distinction is made yet between in- and ex-situ, doped and un-doped and tapes and wires. In the following paragraphs these different variables will be distinguished. However, first in §3.3 the evolution of B_{100} , B_p and $J_{c,0}^T$ over the years 2003-2006 will be discussed.

3.3 Evolution over the Years

Figures 3.5a to c show how the distributions of the B_{100}, B_p and $J_{c,0}^T$ evolve over the years 2003-2006. The distributions are presented as floating columns, indicating the P_5, P_{25}, P_{50}, P_{75} and P_{95} values. The numbers on top of each column indicate the total number of samples in each year. No distinction is made between the precursor powder, mono- or multi filament and tapes or wires. Note that the numbers of samples in each year are not always the same for B_{100}, B_p and $J_{c,0}^T$, partly because unrealistically high values of $J_{c,0}^T (> 10^6 \mathrm{A/mm^2})$ are disregarded and partly because some conductors had self-field J_c values below 100 $\mathrm{A/mm^2}$, so that B_{100} is meaningless. B_p, however, could be determined for all samples.

Figures 3.5a to c show that the median value of all parameters appears to increase over the years. Whether such a variation is significant or not can be determined with the so-called Kruskal-Wallis test [190]. This method tests the significance of the differences between non-uniform distributions of *groups* (in this case the samples reported in a year) that also have unequal variances. It is similar to the better-known ANOVA test of variance, which is only applicable to normal distributions that have similar variances. The main outcome of the test is a *p-value* that indicates the probability that observed differences are purely coincidental. When the p-value is large, the probability is high so that the differences between groups are insignificant. A low p-value indicates that coincidence can be rejected so that the differences are significant. In practice a threshold of 5 % is often adopted, i.e. p $\leq$ 5 % implies a significant difference.

The p-values of the time evolution of each parameter are also indicated in the figures. All are well below the practical threshold of 5 % so that the time evolution is significant for all parameters. From 2003 to 2006, the median values of both characteristic fields B_{100} and B_p increase by about 30 %, while the median value of $\log(J_{c,0}^T)$ increases by about 18 %. However, the distribution of $J_{c,0}^T$ is much wider than that of B_{100} and B_p. As a result also its p-value is higher than that of the characteristic fields (although still lower than 5 %) and the evolution in $J_{c,0}^T$ is thus less significant.

Assuming that $J_{c,0}^T \approx 10^4 \mathrm{A/mm^2}$ and only varies little over the years, a 30 % increase in B_p would indeed induce a 30 % increase of B_{100} (similar to conductors A and D in figure 3.2). Thus, the main improvement over the years appears

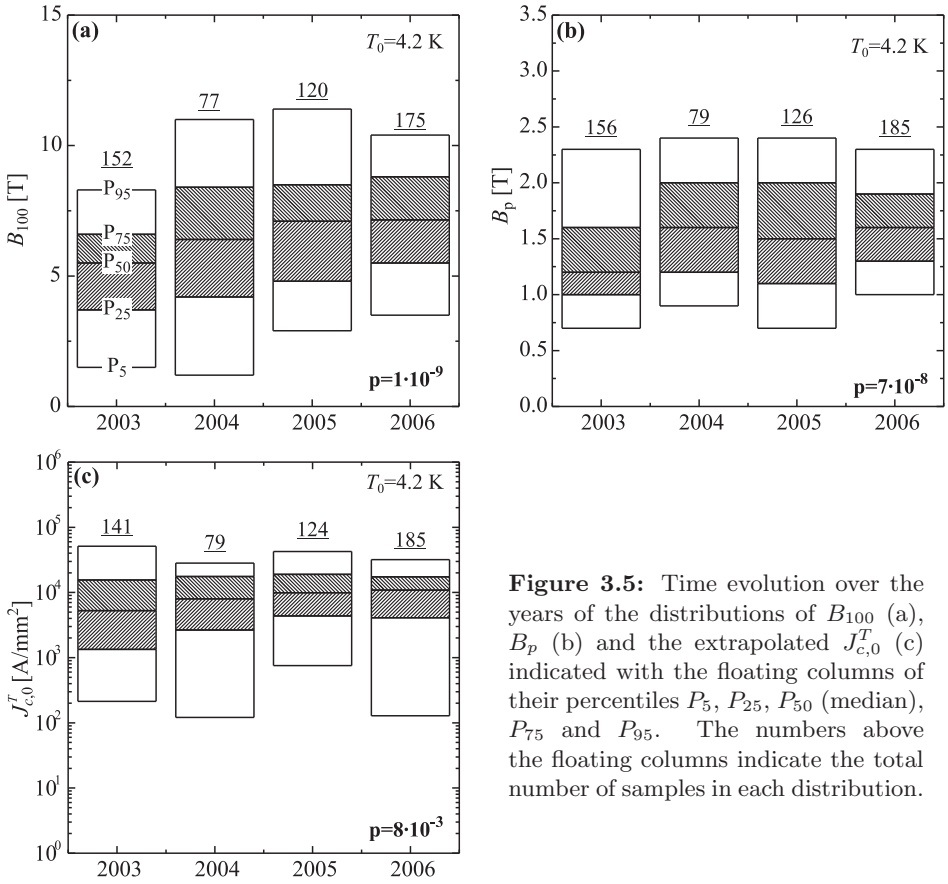

Figure 3.5: Time evolution over the years of the distributions of B_{100} (a), B_p (b) and the extrapolated $J_{c,0}^T$ (c) indicated with the floating columns of their percentiles P_5, P_{25}, P_{50} (median), P_{75} and P_{95}. The numbers above the floating columns indicate the total number of samples in each distribution.

to be the enhancement of B_p, which corresponds to enhanced pinning or higher B_{c2} values.

Related to this observation is figure 3.6, where the evolution of the fraction of ex- and in-situ prepared conductors are plotted over the years 2003-2006. No distinction is made yet between samples that contain pure MgB_2 or samples that also contain additions (e.g. SiC). Samples that are fabricated with another procedure, such as the liquid infiltration technique [53] or the hybrid technique used by [22] are disregarded in this comparison. Strikingly, in 2003 60 % of published conductors were ex-situ, while in 2006 this amount is reduced to about 10 %. As will be shown in the next paragraph, in-situ conductors typically display significantly higher B_p and B_{100} values, mainly since enhancement of B_p and B_{100} through additions in in-situ conductors turns out to be more effective than in ex-situ samples.

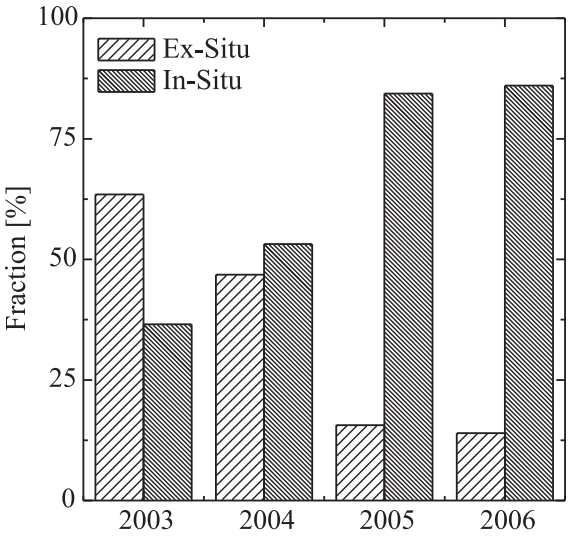

Figure 3.6: Evolution over the years of published $J_c(B)$ curves (at 4.2 K) of ex- and in-situ conductors.

3.4 Influence of Precursor Powder

The influence of the precursor powder on the $J_c(B)$ behaviour is described in this paragraph, distinguishing between conductors that contain pure ex- or in-situ powder and those that contain additions.

A comparison between ex-situ and in-situ conductors is the subject of §3.4.1. In §3.4.2 it is discussed how additions in ex-situ conductors tend to have a different effect that in in-situ conductors. Also, it turns out that carbon based additions in in-situ conductors tend to differ significantly from those with non-carbon based additions. This will be the subject of §3.4.3.

3.4.1 Ex-Situ versus In-Situ

A comparison between B_{100} , B_p and $J_{c,0}^T$ of grouped ex- and in-situ conductors is shown in figures 3.7a to c. The median values of the two characteristic fields B_{100} and B_p are significantly higher by ~ 30 % for in-situ conductors. The median value of $\log(J_{c,0}^T)$ of in-situ conductors is only ~ 5 % higher, while the significance of the difference is lower than for the two characteristic fields. Thus the higher typical B_{100} value observed for in-situ conductors is mainly caused by a higher B_p, i.e. better pinning or a higher B_{c2}. It should be stressed that within each group, no distinction is made yet between conductors that contain pure MgB_2 and those with additions. This distinction is made below in §3.4.2 and will clarify the

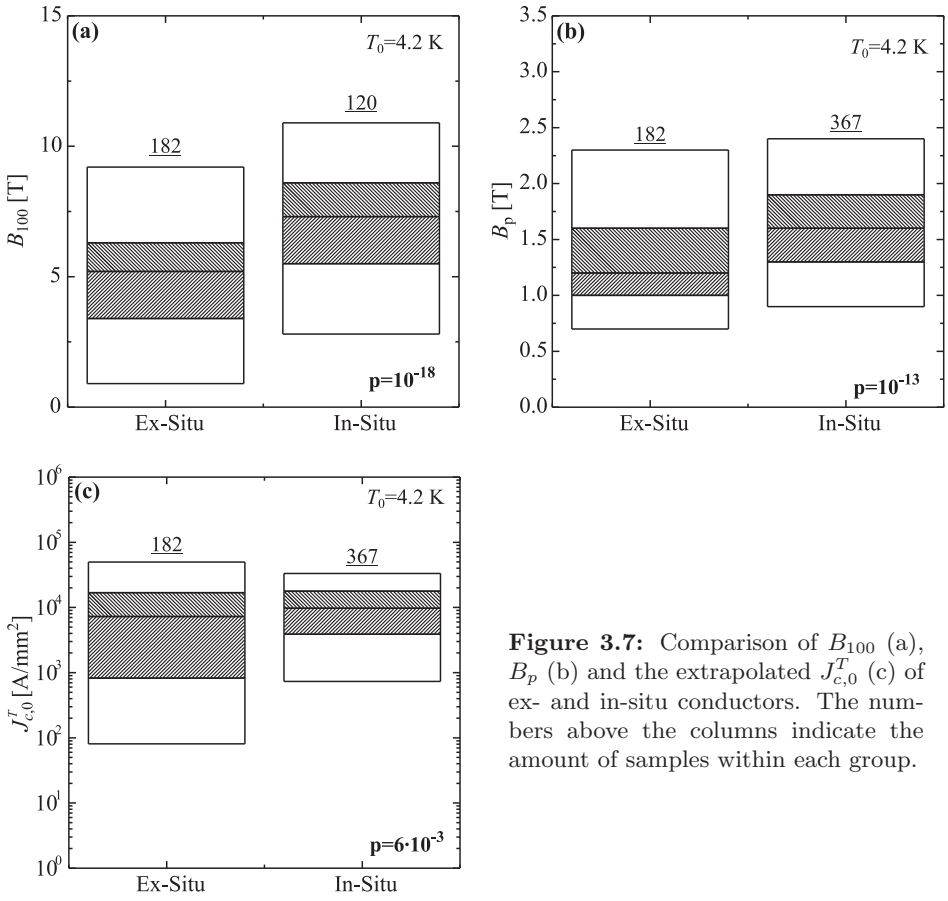

Figure 3.7: Comparison of B_{100} (a), B_p (b) and the extrapolated $J_{c,0}^T$ (c) of ex- and in-situ conductors. The numbers above the columns indicate the amount of samples within each group.

origin of the significantly different median B_p values.

Also worth noting is that the $J_{c,0}^T$ values of ex-situ conductors display a wider distribution than in-situ ones, which is quantified by the 40 % higher standard deviation.

3.4.2 Additions in Ex-Situ and In-Situ Conductors

In an attempt to improve the $J_c(B)$ behaviour of conductors, additions to the MgB_2 precursor powder are extensively studied. In this paragraph statistical analysis is applied to show how B_{100}, B_p and $J_{c,0}^T$ tend to vary with additions.

The first additions in MgB_2 were chemical substitutions to enhance T_c (see the review by Buzea *et. al.* [191] and references therein). Examples of studied dopants are Si, Li, Ni, Fe, Co and Mn. However, as most of these tend to lower T_c, straightforward doping is rarely applied in conductors.

A breakthrough came in 2002, when Dou *et. al.* [24] reported that nanometric

SiC added to the precursor powder substantially improved the resulting $J_c(B)$ characteristic. Since then, many other nanometric additions such as SiO_2, $ZrSi_2$ and B_4C have been tried. The results are described below.

Another type of additions are soft metals like Pb or In [72, 73]. These materials facilitate easier deformation, especially in the case of ex-situ conductors. Improvement of $J_c(B)$ is explained as a possible proximity effect in an ensemble of S/N/S junctions, which would enhance the grain-to-grain connectivity [72]. Since this type of additions is already discussed in chapter 2, the remainder of this chapter will focus on the nanopowder additions.

A priori, improvement of the $J_c(B)$ characteristic following from nanometric additions might be explained through enhanced pinning or through an increase of B_{c2}. In the first scenario nanometric particles are incorporated into the MgB_2 crystallites as a whole and directly or indirectly form pinning centers. An analogous system is top seeded melt grown $(RE)Ba_2Cu_3O_{7-\delta}$ that contains the secondary phase $(RE)_2BaCuO_5$ as nano-inclusions [192][2]. Although this material has important applications in powerful trapped-field magnets and has been intensively studied for several years, the detailed mechanism of pinning enhancement is still under debate. Often cited possibilities are core pinning at oxygen-vacancy clusters in the vicinity of the inclusions or the presence of strain fields at the $(RE)Ba_2Cu_3O_{7-\delta}/(RE)_2BaCuO_5$ interface that cause local variations of the order parameter. Also in MgB_2 TEM studies show that nanometric SiC additions are indeed incorporated in the MgB_2 crystallites, e.g. [193], so that similar pinning mechanisms may also apply here.

Another possible mechanism is pinning of magnetic flux at grain boundaries. In Nb_3Sn this is believed to be the primary pinning mechanism, since the maximum pinning force strongly correlates with grain size [12]. Also in MgB_2 smaller grains were found to enhance the irreversibility field B^*, which is associated with improved pinning [66]. In this context, Mikheenko *et. al.* suggested an indirect role of nanometric additions: that of grain-growth inhibitor [63]. It was found that polycrystalline MgB_2 samples containing nanometric particles systematically have smaller grains. As a consequence the amount of grain boundaries increases and pinning is improved.

In the second scenario, in which $J_c(B)$ is enhanced by increasing B_{c2}, the nanometric particles are thought to act as a source for low-level doping. As an analogy, in Nb_3Sn conductors Ta and Ti additions are incorporated in the crystal structure on Nb sites [12]. As a consequence the electronic mean free path decreases, resulting in a higher normal state resistivity and a lower effective coherence length below T_c. In this so-called dirty limit, the smaller coherence length causes B_{c2} to increase [67]. In MgB_2, low-level C substitution on B sites is believed to play a similar role, but with a much stronger effect due to the two-gap nature of MgB_2 [194–196]. This scenario is supported by observations in C doped single crystals, where point-contact spectroscopy reveals strongly increased coupling between the two gaps [197]. In bulk samples and conductors, X-ray

[2] RE stands for Rare Earth.

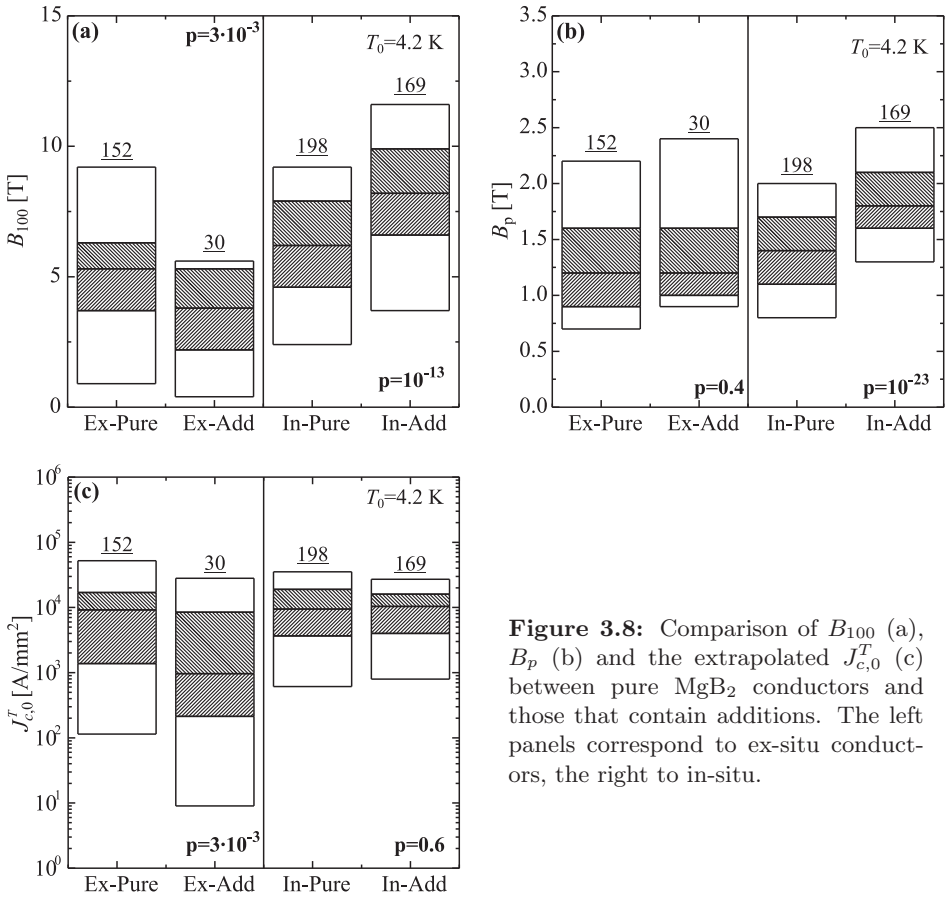

Figure 3.8: Comparison of B_{100} (a), B_p (b) and the extrapolated $J_{c,0}^T$ (c) between pure MgB_2 conductors and those that contain additions. The left panels correspond to ex-situ conductors, the right to in-situ.

diffraction experiments have also shown that C can replace B leading to improved $J_c(B)$ characteristics [175, 198].

In §3.3 it was already suggested that the overall increase in B_{100} values over 2003 to 2006 can to a large extent be attributed to additions, specifically in in-situ conductors. Below, a statistical analysis is performed to demonstrate that additions indeed tend to behave fundamentally different in- or ex-situ conductors and to clarify the role of connectivity, pinning and B_{c2} enhancements in these trends.

Figures 3.8a to c show how B_{100}, B_p and $J_{c,0}^T$ are all differently affected by additions in ex-situ and in-situ conductors. In general, additions in ex-situ conductors leave B_p unchanged, indicating that neither pinning nor B_{c2} changes. It should be stressed once more, however, that this statistical study only clarifies trends. Indeed, the record B_{100} and B_p values ($\sim$ 13 T and $\sim$ 3 T, respectively) at the writing of this thesis are reported in carbon-added ex-situ tapes [8].

The B_{100} distribution of ex-situ conductors, on the other hand, changes significantly with additions, decreasing by ~ 25 %. Since B_p tends to remain constant this is directly related to the significant decrease with ~ 25 % of the $\log(J_{c,0}^T)$ distribution. A reasonable explanation for these observation might be that additions in ex-situ conductors tend not to be incorporated inside the MgB_2 crystallites and thus leave B_p unchanged. Instead, they remain between the grains, reducing connectivity and thus lowering $J_{c,0}^T$ and B_{100}.

The trends are drastically different in the case of in-situ conductors. Here, additions do significantly improve the median value of B_p, by as much as ~ 30 %. Thus, in general they clearly improve pinning or increase B_{c2}. In contrast, the $\log(J_{c,0}^T)$ distribution of in-situ conductors does not change significantly. This latter observation allows to draw two interesting conclusions: 1) in contrast to the ex-situ process additions in in-situ conductors are easier incorporated inside the MgB_2 crystallites during formation of the phase; and 2) $J_{c,0}^T$ is not influenced by the increase in pinning and thus appears to be "purely" determined by connectivity. The observed increase of ~ 30 % in the B_{100} distribution is therefore only due to the improved B_p values.

3.4.3 Non-Carbon versus Carbon Based Additions in In-Situ Conductors

In an attempt to make a possible distinction between improved pinning or enhanced B_{c2} in in-situ conductors with additions, the statistical analysis is further refined by considering carbon based and non-carbon based additions separately. Figure 3.9a to c show how B_{100}, Bp and $J_{c,0}^T$ tend to change when either non-carbon or carbon based additions are added to in-situ conductors.

It is clear that in general both non-carbon and carbon based additions leave $J_{c,0}^T$ unchanged, again indicating that it is a parameter that is mainly determined by connectivity.

Both types of additions improve B_p and B_{100}. However, the median values of the characteristic fields is significantly higher for carbon based additions than for non-carbon based additions (~ 50 % and ~ 15 % respectively). This observation might indicate that carbon based additions improve B_{c2} and possibly also pinning, while non-carbon based additions improve only pinning. Which pinning mechanism is dominant can not be revealed with this statistical analysis.

3.5 Influence of Cross-Sectional Layout

The cross-sectional layout resulting from different deformation routes may also influence B_{100}, B_p and $J_{c,0}^T$. Not only the filament density and grain-to-grain connectivity are affected by the deformation procedure but flat rolling may also induce texture in the filaments' microstructure. MgB_2 is an anisotropic superconductor with different B_{c2} values depending on the direction of the field with respect to the crystallographic c-axis [191]. Therefore, textured conductors can

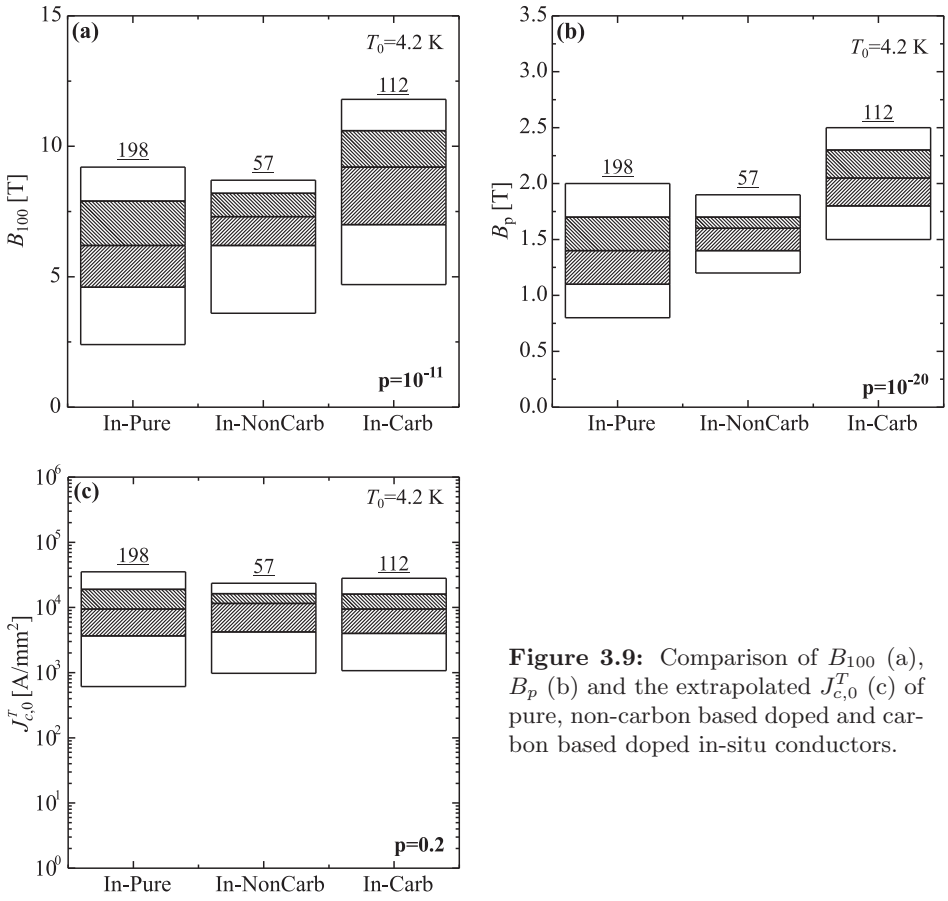

Figure 3.9: Comparison of B_{100} (a), B_p (b) and the extrapolated $J^T_{c,0}$ (c) of pure, non-carbon based doped and carbon based doped in-situ conductors.

also have different B_p and B_{100} values depending on the field orientation. In §3.5.1 it is shown how the three parameters differ between tapes and wires.

Also, one may expect possible differences between mono- and multi-filament conductors. Multi-filament conductors are usually assembled from already deformed mono-core conductors and filament size is reduced with further deformation. This could lead to a higher $J^T_{c,0}$ due to a higher filament density. On the other hand, multi-filament conductors have a larger MgB_2-matrix interface area. This may lead to a lower effective cross-sectional area through chemical reaction during heat treatments. Possible variations of B_{100}, B_p and $J^T_{c,0}$ between mono- and multi-filament conductors are the subject of §3.5.2.

3.5.1 Tape versus Wire

Figures 3.10a to c show the B_{100}, B_p and $J^T_{c,0}$ distributions of wires and tapes. In this comparison no distinction is made with regard to the precursor powder and

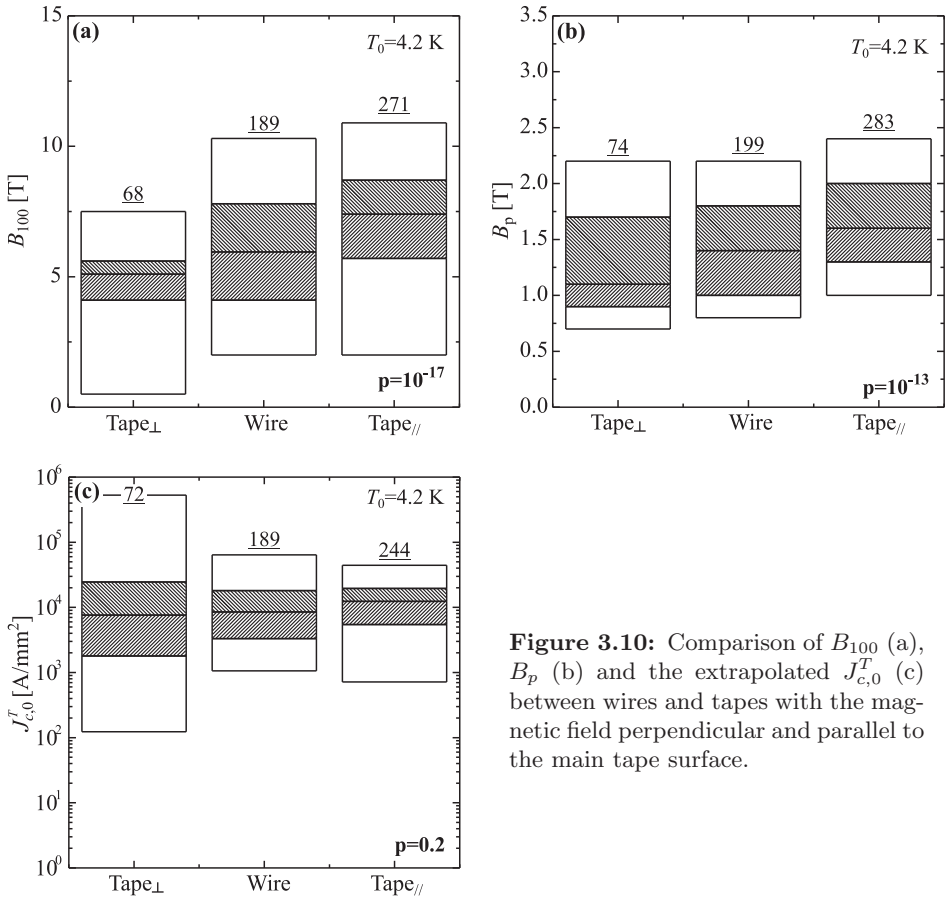

Figure 3.10: Comparison of B_{100} (a), B_p (b) and the extrapolated $J_{c,0}^T$ (c) between wires and tapes with the magnetic field perpendicular and parallel to the main tape surface.

the number of filaments.

It is shown in [156] that the filamentary microstructure in flat-rolled tapes exhibits a certain degree of texture. Due to the anisotropy of B_{c2}, B_p values in parallel magnetic field will then differ from those in perpendicular field, depending on the degree of texture. For this reason the data of tapes are separated into $J_c(B)$ curves measured with the field perpendicular to the main plain of the tape and those measured in parallel field.

Figures 3.10a and b show that the median B_p and B_{100} values of tapes measured in parallel field are indeed significantly higher ($\sim$ 50 %) than those in perpendicular field. Together with the insignificant difference between the median $J_{c,0}^T$ values this observation confirms the conclusion of [144] that the direction-dependent B_p and B_{100} values are caused by texture through the anisotropy of B_{c2}. As expected, the B_p and B_{100} values of wires fall in-between those of tapes in parallel and perpendicular field, demonstrating that texture in wires can be

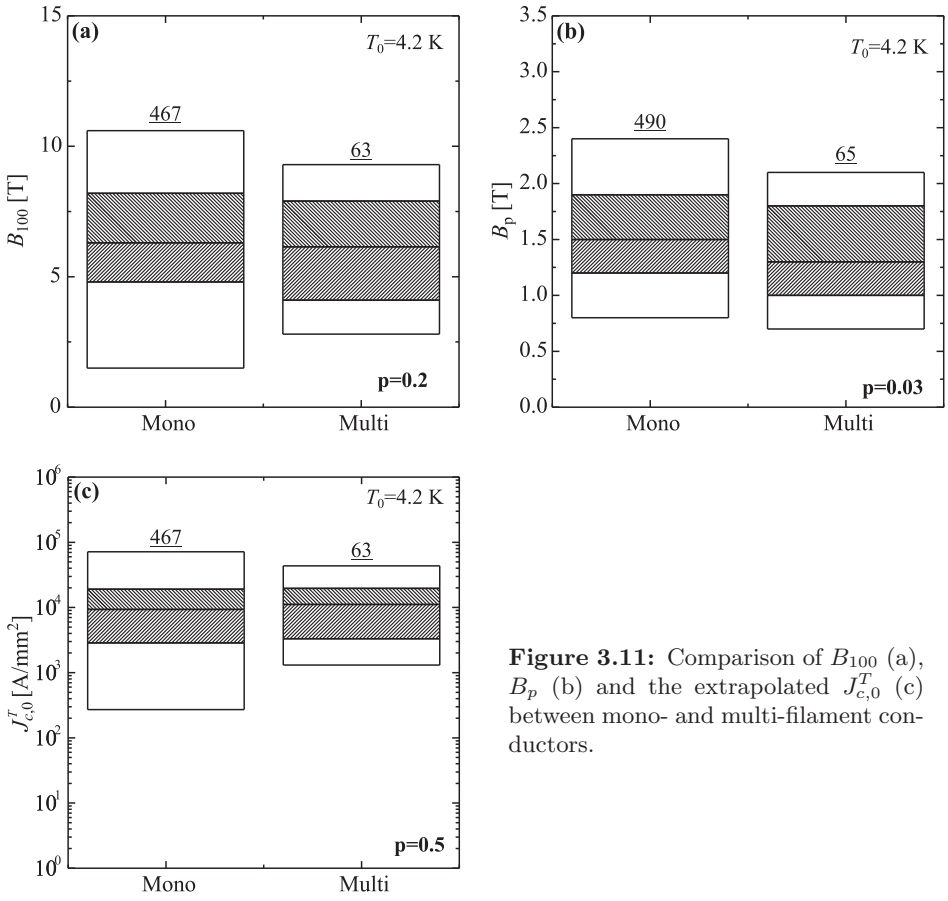

Figure 3.11: Comparison of B_{100} (a), B_p (b) and the extrapolated $J^T_{c,0}$ (c) between mono- and multi-filament conductors.

neglected. Also note the absence of a significant difference in $J^T_{c,0}$ between wires and tapes, which implies that the grain-to-grain connectivity is similar in both.

3.5.2 Mono versus Multi-Filaments Conductors

A comparison of B_{100}, B_p and $J^T_{c,0}$ between mono- and multi-filaments conductors is presented in figures 3.11a to c. Only the median value of B_p of multifilamentary conductors is slightly lower than that of the mono-filament conductors. However, the significance of this difference is rather low since the p-value is close to the threshold of 5 %. The absence of major differences between the $J_c(B)$ behaviour of mono- and multi-filamentary conductors is encouraging, since it indicates that further reduction in filament size should be possible. Note that more detailed statistical analysis in terms of filament size and number was not possible, due to an insufficient number of samples.

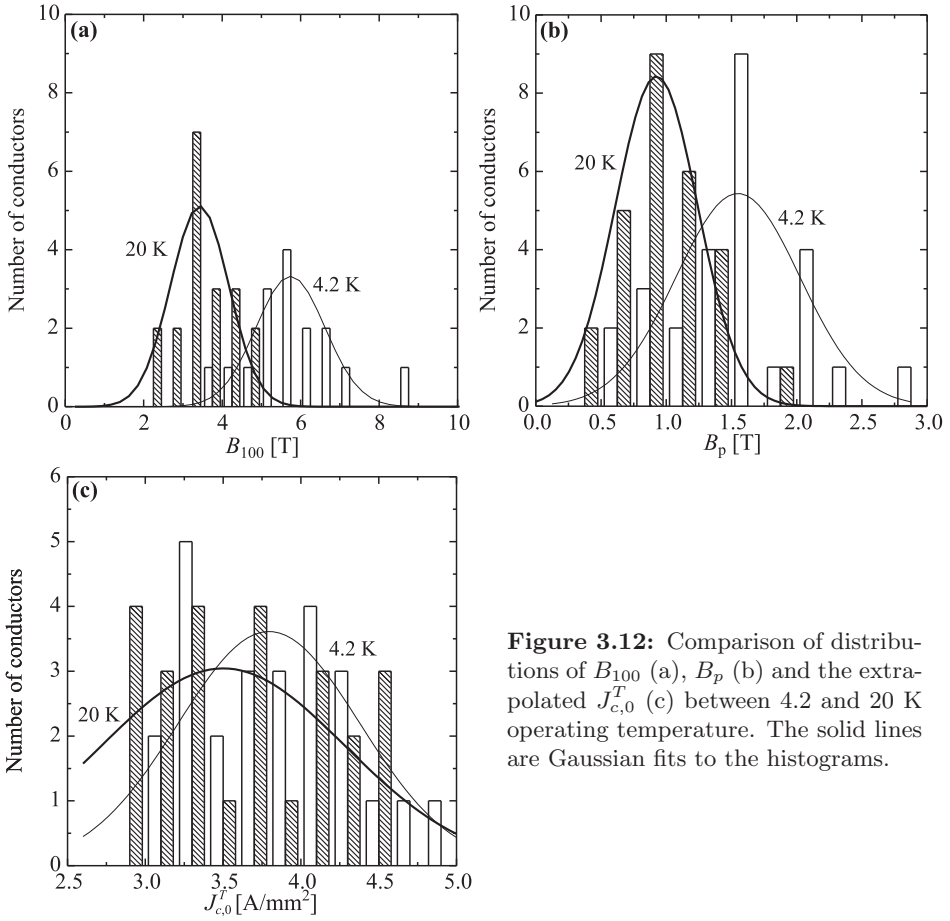

Figure 3.12: Comparison of distributions of B_{100} (a), B_p (b) and the extrapolated $J_{c,0}^T$ (c) between 4.2 and 20 K operating temperature. The solid lines are Gaussian fits to the histograms.

3.6 Influence of Temperature

As mentioned in §3.2, only $\sim$ 5 % of the 550 conductors in this survey were characterised at 20 K. Because data at this temperature is available of only 30 conductors, no statistical study was performed of possible performance differences between in- and ex-situ conductors or of the effect of low level doping at 20 K. Clearly, since 20 K is the anticipated operating temperature of several MgB_2-based applications, more studies are needed at this temperature.

Nevertheless, the available data of these 30 conductors can be used to see what the effect of temperature is on the values of B_{100}, B_p and $J_{c,0}^T$, regardless of precursor powder and deformation route. The distribution functions of these parameters are compared between 4.2 and 20 K in figure 3.12. For both characteristic fields, a clear shift towards lower values can be observed. On average, the ratio of B_{100} at 20 and 4.2 K is $\langle B_{100}(20\text{ K})/B_{100}(4.2\text{ K})\rangle = 0.45 \pm 0.21$, with the indicated uncertainty the standard deviation of the ratios of individual conduct-

ors. Similar values are found for B_p with $\langle B_p(20\text{ K})/B_p(4.2\text{ K})\rangle = 0.50 \pm 0.25$ and $J_{c,0}^T$ with $\left\langle J_{c,0}^T(20\text{ K})/J_{c,0}^T(4.2\text{ K})\right\rangle = 0.61 \pm 0.40$. These ratios are in reasonable agreement with the analytical approximation of the critical surface (3.1). As a rule of thumb, it can be stated that the performance both in terms of field and current decreases by ~ 50 % between 4.2 and 20 K. Note that the conductor with the highest B_{100} value of 13 T at 4.2 K found in the literature survey may thus be expected to have a technical upper field limit of $\sim 6-7$ T at 20 K.

3.7 Conclusion

To study trends and prospects in the development of practical MgB_2 conductors, a statistical study of the transport $J_c(B)$ behaviour of published conductors over the years 2003 to 2006 was conducted.

With respect to the self-field J_c, it is found that the top 50 % of published values fall in a relatively small range of 10^4 to 10^5 A/mm^2. Moreover, self-field J_c values do not correlate with the pinning-related parameter B_p, so that $J_{c,0}^T$ appears to be mainly determined by grain-to-grain connectivity within the filaments. Together, these two observations can indicate that 10^5 A/mm^2 forms an upper limit imposed by grain-to-grain connectivity.

The progress made over the years is mainly in the field retention of J_c. This progress is gauged by the magnetic field at which $J_c = 100$ A/mm^2, which has increased by about 25 %. Related with this is the observation that the focus of research has shifted from ex-situ to in-situ conductors, of which a substantial part contain additions that improve the field retention of J_c.

In general, carbon additions in in-situ conductors improve the field retention of J_c by about 50 %. The mechanism behind this improvement seems to be an enhancement of B_{c2}, but possibly also enhanced pinning. Non-carbon based additions tend to improve the field retention to a lesser extend, by about 15 %. It is suggested that only pinning is affected in this case.

In contrast, additions in ex-situ conductors tend not to influence the field retention, but instead worsen the grain-to-grain connectivity by about 25 %.

Differences between wires and tapes can be explained with the textured nature of the filaments in the latter. As to connectivity, no significant differences are found.

In view of further development of multi-filament conductors, no significant differences were found between mono-filament conductors and the relatively small number of multifilamentary wires and tapes available at present.

For the operation of MgB_2 at 20 K, it is shown that the $J_c(B,T)$ performance decreases by roughly 50 % in terms of both field and current compared to 4.2 K.

Overall, the main progress from 2003 to 2006 has been obtained with in-situ conductors, in which low-level doping seems to be better controllable. It should be noted that al conclusions mentioned above concern the “average” behaviour of MgB_2 conductors: an important exception is formed by the record B_{100} value of 13 T at 4.2 K, which was reported for an ex-situ conductor. In contrast to the

self-field J_c value, an upper limit in the field retention seems not to be reached yet and realistic predictions are difficult due to the ongoing progress and the lack of understanding of the precise mechanism behind improvements obtained with carbon-based dopants. Further insights in this area may well lead to further enhancement of the field retention.

Chapter 4

Normal Zone Development

The occurrence of a normal conducting zone and the following heating effect can cause permanent damage to a superconducting magnet. The probability of such an event and the ability to protect a MgB_2-based magnet from damage is discussed in this chapter in terms of the minimum quench energy MQE *and the normal zone propagation velocity* v_{nz}*. Both depend on the conductors thermal properties and on operating conditions such as transport current, magnetic field and temperature. Especially the latter is important for MgB_2 because of its possible use at about 20 K rather than 4.2 K. A new experimental set-up is developed to investigate intrinsic* MQE *and* v_{nz} *values as a function of current, field and temperature. How* MQE *and* v_{nz} *depend on the three operating parameters is discussed. As a tool for magnet and conductor design a new algorithm is developed that takes into account the temperature dependent conductor properties and detailed filament properties. Calculations with the algorithm shows excellent agreement with the measurements.*

4.1 Introduction

When a thermal disturbance occurs in a practical superconductor, the temperature rises locally and the critical current drops accordingly. If the temperature rise is large enough, the critical current drops below the transport current. The superconducting filaments cannot carry the full transport current anymore and current is redistributed over filaments and matrix. The conductor now locally generates heat. When the heat is generated faster than it can be dispersed, an "avalanche" effect occurs since temperature rises even further, more current diffuses in the matrix, the normal zone grows and still more heat is generated. Such an avalanche effect may even cause the conductor to burn out, in which case the superconducting magnet will be permanently damaged.

Being able to predict the response of a superconductor to a thermal disturbance is thus very important in order to protect a superconducting device from permanent damage. Three parameters are of importance:

1. the amount of heat that is needed to trigger the avalanche effect, referred to as the "minimum quench energy" MQE. This parameter is a measure for the stability of a conductor.

2. the "normal zone propagation velocity" v_{nz}, i.e. how fast a normal conducting zone grows along the conductor. A large v_{nz} has the advantage that heat is distributed over a relatively large volume so that the temperature rise remains limited. Furthermore, a fast-growing normal zone also means that the voltage rise across the conductor is easier to detect and that appropriate measures can be taken faster.

3. the temperature at the position of the thermal disturbance, referred to as the "hot-spot temperature". This is ultimately the factor that will decide whether permanent damage will occur in a conductor.

These parameters can, to a large extent, be controlled by the choice of the matrix material. MQE, for example, is determined by the volumetric heat capacity of the composite c (a higher heat capacity means that more heat is required); by the thermal conductivity κ that determines the cooling rate[1]; and by the electrical resistivity ρ that determines how much heat is generated for a given current density. v_{nz} is determined by the matrix' thermal diffusivity (the ratio of κ and c) and, just like MQE, the amount of generated heat.

Apart from the matrix' properties, the properties of the superconducting filaments also play an important role. The critical temperature, for example, determines the thermal margin and thus how far the temperature needs to be raised before current starts to diffuse into the matrix. Furthermore, the average current density in the conductor section determines how much heat is generated.

[1] In this thesis only the adiabatic case is considered, in which cooling occurs through longitudinal redistribution of heat along the conductor. In most applications, also lateral cooling to neighbouring conductors or to a cryogen plays a role. However, it is the "intrinsic" adiabatic behaviour that characterises a given conductor an that will be the subject of this study.

As mentioned in §1.3.1, the parameters differ quite substantially between low-T_c and high-T_c conductors. Accordingly, their response to a thermal disturbance also differs substantially. In conductors like Nb-Ti and Nb_3Sn, MQE values are relatively low ($\sim \mu$J), due to their relatively low critical temperatures ($\sim$ 9 and $\sim$ 18 K for Nb-Ti and Nb_3Sn respectively) and the fact that their heat capacity at the usual operating temperature (4.2 K) is relatively low. As a consequence, a relatively small amount of heat is needed to initiate a propagating normal zone. However, since these conductors are usually stabilised with a highly conducting Cu matrix, v_{nz} values are relatively high (10 to 100 m/s [199, 200]), which means that heat is quickly distributed and the temperature rise remains limited. Magnets made of these conductors are relatively easy to protect, since the voltage rises fast. Values of MQE and v_{nz} for low-T_c conductors can in most cases be accurately predicted with the aid of analytical formulae [28, 88, 201].

In high-T_c conductors, the situation is reversed. The conductors can be operated at temperatures as high as 77 K, at which the heat capacity is relatively large (roughly 3 orders of magnitude larger than at 4.2 K). Furthermore, their T_c is relatively high ($\sim$ 110 K for $Bi_2Sr_2Ca_2Cu_3O_x$, $\sim$ 90 K for $YBa_2Cu_3O_x$). Together, these factors lead to higher MQE values ($\sim$ 10 J [202]). On the other hand, due to the high heat capacity, thermal diffusion is low and the response of a conductor to a thermal disturbance can be approximated by heating in a static normal zone [203]. Consequently, the voltage rise is slow and it is relatively difficult to detect a normal zone in high-T_c conductors.

MgB_2 can be regarded as a medium-T_c conductor. At the envisaged operating temperature of 20 K, its thermal margin and heat capacity are in-between those of low- and high-T_c conductors. Therefore, typical values of MQE and v_{nz} can be expected to be also in-between those of low- and high-T_c conductors. This would suggest that the response to a thermal disturbance may be approximated with the "classical" analytical formulae for low-T_c conductors. However, as discussed in chapter 2, materials that are chemically compatible with MgB_2 are usually relatively poor electrical and thermal conductors. In contrast to low-T_c conductors, the normal state resistivity of MgB_2 filaments is often comparable to that of the matrix and neglecting heat generation in the filaments (as in in the analytical approximations) can not be justified. Accounting for heat generation in the filaments means also that the voltage-current characteristic of the filaments needs to be considered explicitly.

In this chapter, the minimum quench energy and normal zone propagation velocity of MgB_2 conductors with varying matrix materials and n-values are studied. This is done with the aid of a numerical model that also accounts for the heat generation in the superconducting filaments. To validate the model, experiments are performed on samples with varying cross-sectional layouts (matrix materials and shape).

However, before discussing MQE and v_{nz} of MgB_2 conductors, in §4.2 the diffusion processes of current- and heat in a composite conductor during and after the occurrence of a thermal disturbance are discussed. The diffusion processes are in principle 3-dimensional, but they will be modeled 1-dimensionally. It will

be discussed under which conditions the 1-dimensional assumption is justified.

Next, to provide a better understanding of the mechanisms determining v_{nz} and MQE, the analytical formulae that were developed for low-T_c conductors are first discussed in §4.3. Then the details of the numerical model are discussed and it is shown to what extent heat generation in MgB_2 conductors deviates from the "classical" approximations.

Validation of the numerical model is performed with measurements of MQE and v_{nz} in a quasi-adiabatic set-up. This allows to eliminate extra complications due to lateral cooling terms and also allows to vary the baseline temperature of the conductor straightforwardly. The development of the experimental set-up and measurement procedure are subject of §4.4.

The results of MQE and v_{nz} measurements as a function of transport current, temperature and magnetic field are presented in §4.5. Results are then compared with the parallel-paths calculations in order to validate the numerical model.

Lastly, the parallel current paths model is used to predict the influence of matrix material and n-value on MQE, v_{nz} and hot-spot temperature.

4.2 Diffusion Process

As outlined in §4.1, a thermal disturbance in a superconducting composite can be followed by an avalanche effect when heat generation exceeds cooling. The avalanche effect is driven by the diffusion of current- and heat. In this paragraph, the diffusion process is discussed in more detail. In §4.2.1 the diffusion equation of current and heat are presented. Although diffusion is 3-dimensional, stability of a superconducting composite is usually treated as a 1-dimensional problem. This is also the case in this work and in §4.2.2 the circumstances for which this assumption is justified are discussed.

4.2.1 Diffusion Equations

Figure 4.1 shows a composite superconductor in which current diffuses *radially* into the matrix when a thermal avalanche effect is initiated. The net effect of the avalanche is a *longitudinal* propagation of the normal zone. The speed at which the normal zone propagates along the conductor is referred to as the "normal zone propagation velocity" v_{nz}.

Diffusion of heat is determined by the balance between heat conduction through the composite, the amount of heat that can be stored (thermal inertia), the heat generation and the initial thermal disturbance. The most general form of such a heat balance is:

$$\underbrace{c\frac{\partial T}{\partial t}}_{\text{inertia}} = \underbrace{\nabla(\kappa\nabla T)}_{\text{conduction}} + \underbrace{p_{\text{initial}}}_{\text{thermal dist.}} + \underbrace{p_{\text{diss}}}_{\text{heat diss.}} , \tag{4.1}$$

in which c is the volumetric heat capacity, T the temperature, t the time, κ the thermal conductivity, p_{initial} the heat flux associated with the thermal disturb-

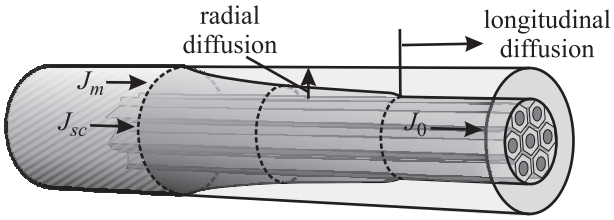

Figure 4.1: A composite superconductor in which the current diffuses into the matrix due to a thermal disturbance.

ance and p_{diss} is the heat dissipation. The heat flux generated by the thermal disturbance can be written as:

$$p_{\text{initial}} = \frac{1}{V}\left(\frac{\mathrm{d}Q_{\text{initial}}}{\mathrm{d}t}\right), \tag{4.2}$$

with Q_{initial} the thermal disturbance and V the volume in which this heat is deposited.

The source term p_{diss} in equation 4.1 results from the diffusion of current throughout the sample. Current diffusion is described by Maxwell equations. For the normal conducting matrix Ohm's law is included in this description, which leads to the following diffusion equation for current:

$$\mu_0 \frac{\partial J_m}{\partial t} = \rho_m \nabla^2 J_m, \tag{4.3}$$

with μ_0 the permeability of vacuum, J_m the current density in the matrix and ρ_m the resistivity of the matrix. For the filaments, which behave non-Ohmic, the current-diffusion equation needs to be modified. Assuming that the voltage-current relation of the superconducting filaments can be described by the power law:

$$E = E_c \left(\frac{J_{sc}}{J_c}\right)^n, \tag{4.4}$$

equation 4.3 becomes:

$$\mu_0 \frac{\partial J_{sc}}{\partial t} = E_c \nabla^2 \left(\frac{J_{sc}}{J_c}\right)^n, \tag{4.5}$$

with E the electric field, E_c the electric field at which the critical current density J_c is defined, J_{sc} the current density in the superconducting filaments and n the exponent of the power law.

4.2.2 Dimensionality of the Diffusion Processes

Treating the diffusion equations in a superconducting composite 1-dimensionally and using "lumped" (averaged over the radial direction) material properties such as κ and c assumes that the temperature over the cross-section of the composite is homogeneous. In order to verify whether this is a reasonable assumption, a criterion for 1-dimensional modeling of dynamic stability can be adopted [28], which states that the characteristic thermal diffusion time in the filaments $\tau_{T,f}$ must be smaller than the characteristic magnetic diffusion time in the composite $\tau_{m,c}$:

$$\tau_{T,f} < \tau_{m,c}. \tag{4.6}$$

This requirement is based on the temperature dependence of J_c in (4.5). When (4.6) is not fulfilled, radial temperature gradients across the filaments are not negligible so that J_c and the heat generation become radially inhomogeneous.

To verify whether (4.6) is satisfied, diffusion equations (4.1) and (4.3) are solved in radial direction assuming cylindrical coordinates. Furthermore, the material properties c and κ are assumed to be temperature independent. The solutions then have the form:

$$T(r,t) = \sum_{l=1}^{\infty} T_l(\gamma_{1,l}\frac{r}{R}) \exp\left(-\frac{{\gamma_{1,l}}^2 D_T}{R^2}\, t\right) \qquad \text{with} \qquad D_T = \frac{\kappa}{c}; \tag{4.7}$$

$$J(r,t) = \sum_{l=1}^{\infty} J_l(\gamma_{1,l}\frac{r}{R}) \exp\left(-\frac{{\gamma_{1,l}}^2 D_m}{R^2}\, t\right) \qquad \text{with} \qquad D_m = \frac{\rho}{\mu_0}, \tag{4.8}$$

where $T_l\left(\gamma_{1,l}\left(r/R\right)\right)$ and $J_l\left(\gamma_{1,l}\left(r/R\right)\right)$ are multiples of the zeroth order Bessel function; $\gamma_{1,l}$ is the l^{th} root of the first order Bessel function of the first kind [204]; and R is the radius of the system under consideration. Decay time constants are associated with the time-dependent exponential factors in (4.7) and (4.8). The slowest decay ($l = 1$) determines the overall characteristic diffusion time τ. Thus the characteristic times of thermal diffusion in the filaments and magnetic diffusion in the composite are:

$$\tau_{T,f} = \frac{R_f^2}{\gamma_{1,1} D_{T,f}}; \tag{4.9}$$

$$\tau_{m,c} = \frac{R_c^2}{\gamma_{1,1} D_{m,c}}, \tag{4.10}$$

where R_f and R_c are the radii of the filament and composite, respectively. With these characteristic diffusion times, requirement (4.6) becomes:

$$\left(\frac{R_f}{R_c}\right)^2 < \frac{D_{T,f}}{D_{m,c}}. \tag{4.11}$$

Whether or not a 1-dimensional approximation is justified for a given conductor can now be judged straightforwardly. Suppose two monofilament MgB_2 conductors that have $R_c = 0.5$ mm and $R_f = 0.3$ mm (filling factor f=36 %) and that operate at 20 K. Conductor 1 is stabilised with a Fe matrix while conductor 2 is stabilised with Cu. In appendix B the thermal and electrical properties of relevant materials are presented. The electrical resistivities for conductor 1 are $\rho_{\mathrm{Fe}} = 7 \cdot 10^{-9}$ Ωm and $\rho_{\mathrm{MgB_2}} = 64 \cdot 10^{-9}$Ωm, so that its lumped electrical resistivity becomes $\rho_{\mathrm{lumped}} = 10 \cdot 10^{-9}$ Ωm. The volumetric heat capacity and thermal conductivity of MgB_2 at 20 K are $c_{\mathrm{MgB_2}} = 3892$ J/m^{3}K and $\kappa_{\mathrm{MgB_2}} = 5$ W/mK. This leads to:

$$\frac{D_{T,f}}{D_{m,c}} = 0.16,$$

while the ratio of filament and composite radii is:

$$\left(\frac{R_f}{R_c}\right)^2 = 0.36.$$

Clearly, the requirement is not met with this combination of materials and filling factor and a significant radial temperature gradient is present. For conductor 2, which has a Cu matrix with a resistivity of $\rho_{\mathrm{Cu}} = 0.2 \cdot 10^{-9}$ Ωm (at $B = 0$ T and a residual resistivity ratio RRR=100), the criterion is clearly met since the lumped electrical resistance is reduced to $\rho_{\mathrm{lumped}} = 0.3 \cdot 10^{-9}$ Ωm. The ratio of thermal and magnetic diffusivities now becomes:

$$\frac{D_{T,f}}{D_{m,c}} = 5.8,$$

while the ratio of filament and composite radii is not changed.

In this example the matrix resistivity is the decisive factor for the fulfilment of requirement (4.6). However, reducing the radius of the filament (left hand side of inequality (4.11)) can also help to justify the 1-dimensional assumption.

It should be noted that this analysis is rather crude in the sense that it neglects that filaments are for some time during the diffusion in the superconducting state. Current diffusion is then described by equation (4.5) and the diffusion "constant" can no longer simply be written as $D_m = \rho/\mu_0$, but effectively depends on the current density itself. Since equation (4.5) is non-linear, a full validation of the 1-dimensional approximation requires a 2-dimensional numerical model that also accounts for the superconducting state of the filaments.

4.3 Minimum Quench Energy and Normal Zone Propagation

As discussed in §4.2.1, a normal conducting zone in which the current is distributed over both filaments and matrix can only continue to exist if its initial volume

–induced by Q_{initial}– is large enough so that the total heat generation is larger than the cooling. The minimum value of Q_{initial} required to initiate such a zone is the MQE. When $Q_{\text{initial}} \geq \text{MQE}$, an "avalanche" effect occurs since the imbalance between heat generation and cooling increases the temperature even further and the normal zone grows with a velocity v_{nz}.

In §4.3.1 a straightforward analytical model that provides a clear understanding of MQE and the v_{nz} is discussed.

The simple model assumes temperature- and field independent material properties and an abrupt diffusion of all the transport current from the filaments into the matrix. These are rather crude assumptions that can lead to a significant disagreement with the measurements, especially in the case of MgB_2, where a smooth transition from lossless transport to Ohmic heat generation can occur. Furthermore, the large temperature margin in MgB_2 ($T_c \sim 40$ K) requires that one takes into account the temperature dependence of the relevant material properties. Therefore, a 1-dimensional numerical model was developed that accounts for: 1) the continuous temperature dependence of I_c; 2) the detailed voltage-current transition of the filaments; and 3) the temperature- and field dependence of the material properties. The details of the refinements are discussed in §4.3.2, while their implications on the heat generation, MQE and v_{nz} are presented in §4.3.3.

4.3.1 Analytical Description

Minimum Quench Energy

An instructive analytical approximation for the magnitude of MQE was presented by Wilson [28]. The basis of this analytical description is that for a normal zone to propagate, Q_{initial} must be large enough so that: 1) the temperature increases above T_c [2], all the current I_0 flows in the matrix (with current density $J_m = I_0/A_m$) and Ohmic heat is generated ($p_{\text{diss}} = J_m^2 \rho_m$); and 2) the length of this region must be large enough so that the total Ohmic heat generation integrated over the entire length exceeds the cooling[3]. Figure 4.2 schematically shows a conductor that initially carries a current density J_0 in the filaments and in which a thermal disturbance Q_{initial} induces a temperature rise above T_c over a length l. If this length is too short, the heat will simply diffuse and the temperature will drop again below T_c. The minimum length that is needed for this normal zone to propagate (for heat generation to exceed cooling) is defined as the "minimum propagation zone" l_{MPZ}. Equating Ohmic heat generation and

[2] The choice of T_c as the temperature at which current "switches" from the filaments to the matrix [205] is rather arbitrary. Other possible choices are discussed in §4.3.3.

[3] These assumptions ($T > T_c$ and sharp current redistribution) are rather crude and will be refined later (§4.3.2). However, they provide a clear understanding about the physics without complicating the issue with second order effects.

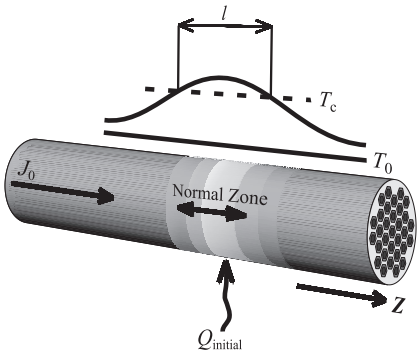

Figure 4.2: A normal zone that is created in a current-carrying wire by a small thermal disturbance. l indicates the length where the temperature exceeds T_c, and heat is generated.

cooling, l_{MPZ} can be written as:

$$\begin{aligned} J_m^2 \rho_m A_m l_{\mathrm{MPZ}} &= \frac{2\kappa_m A_m (T_c - T_0)}{l_{\mathrm{MPZ}}} \\ &\Leftrightarrow \\ l_{\mathrm{MPZ}} &= \left\{ \frac{2\kappa_m (T_c - T_0)}{J_m^2 \rho_m} \right\}^{1/2}, \end{aligned} \tag{4.12}$$

with ρ_m the resistivity of the matrix; κ_m the thermal conductivity of the matrix; and A_m the cross-sectional area of the matrix. Once l_{MPZ} is known, MQE becomes simply the heat needed to raise the temperature above T_c over a length l_{MPZ}:

$$\mathrm{MQE} = A \int_{l_{\mathrm{MPZ}}} \int_{T_0}^{T_c} c(T) dT dz, \tag{4.13}$$

with A the cross-section of the whole conductor.

Normal Zone Propagation Velocity

Once a normal zone is established that propagates along the conductor with a velocity v_{nz}, two regions can be distinguished: 1) the normal conducting part of the wire ($T > T_c$) in which Ohmic heat is generated; and 2) the part of the wire that is still superconducting ($T < T_c$) but which drains heat from the normal conducting zone (see figure 4.3). The two regions are separated by a moving interface at z_s where the temperature is equal to T_c and current I_0 is assumed to diffuse instantly into the matrix. Following Iwasa [47], an expression for v_{nz} can be derived by formulating two separate diffusion equations for the normal- and

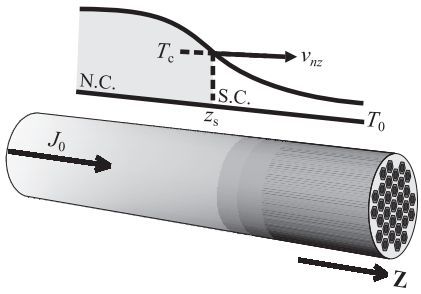

Figure 4.3: A current carrying conductor in which a normal zone propagates with velocity v_{nz}. T_s is the transition temperature above which heat is generated and z_s indicates the position of the normal-superconducting interface.

superconducting zone, which are coupled by the heat flow across the interface:

$$\begin{aligned} c_n \frac{\partial T}{\partial t} &= \frac{\partial}{\partial z}\left(\kappa_n \frac{\partial T}{\partial z}\right) + p_{\text{diss}} \quad \text{(n.c.)}; \\ c_s \frac{\partial T}{\partial t} &= \frac{\partial}{\partial z}\left(\kappa_s \frac{\partial T}{\partial z}\right) \qquad\qquad \text{(s.c.)}, \end{aligned} \tag{4.14}$$

where the indices n and s of c and κ refer to the volumetric heat capacity and thermal conductivity in the normal- and superconducting state, respectively; p_{diss} is the Ohmic heat generation.

The two heat balance equations (4.14) are solved in a moving frame of reference that follows the normal-superconducting interface (z_s) with a velocity v_{nz} in the $+z$ direction. Thus, a coordinate transformation $z' = z - z_s = z - v_{nz}t$ is applied to (4.14). Furthermore, only the area adjacent to the interface needs to be considered, so that the material properties c and κ can be assumed constant. This leaves the following ordinary differential equations:

$$\begin{aligned} v_{nz} c_n \frac{dT}{dz'} + \kappa_n \frac{d^2T}{dz'^2} + p_{\text{diss}} &= 0 \quad \text{(n.c.)}; \\ v_{nz} c_s \frac{dT}{dz'} + \kappa_s \frac{d^2T}{dz'^2} &= 0 \qquad\qquad \text{(s.c.)}. \end{aligned} \tag{4.15}$$

Using the boundary conditions that the heat flux across the interface is continuous and that the temperature at the interface equals T_c, the two heat balance equations leave the following expression for v_{nz}:

$$v_{nz} = \left\{ \frac{p_{\text{diss}} \kappa_n}{c_n c_s (T_c - T_0)} \right\}^{1/2} = \left\{ D_{T,n} \frac{p_{\text{diss}}}{c_s (T_c - T_0)} \right\}^{1/2}, \tag{4.16}$$

with $D_{T,n}$ the thermal diffusion constant of the normal conducting zone.

Thus v_{nz} is determined by p_{diss}, the rate of Ohmic heat generation in the normal zone; by $D_{T,n}$, the speed of heat diffusion from the normal zone into the superconducting zone; and by $c_s(T_c - T_0)$ the amount of heat required to maintain the temperature gradient in the superconducting region.

It should be noted that most authors ([28, 201]) use one single value of c and κ for the superconducting and normal conducting regions, i.e. $c_n = c_s = c$ and $\kappa_n = \kappa_s = \kappa_m$, with κ_m the matrix' thermal conductivity. Using the Wiedemann-Franz law $\rho_m \kappa_m = L_0 T_c$ (4.16) becomes:

$$v_{nz} = \frac{J_m}{c} \left\{ \frac{\rho_m \kappa_m}{(T_c - T_0)} \right\}^{1/2} = \frac{J_m}{c} \left\{ \frac{L_0 T_c}{(T_c - T_0)} \right\}^{1/2}, \tag{4.17}$$

where the Lorentz number $L_0 = 2.45 \cdot 10^{-8}$ WΩ/K^2.

4.3.2 Numerical Models

Although equations (4.13) and (4.16) provide a good qualitative insight in the parameters that influence MQE and v_{nz}, serious simplifications were applied in their derivation that can lead to a quantitative discrepancy with the measured values. Arguably the most serious simplification is the assumption that the complete transport current I_0 instantly diffuses into the matrix as soon as the temperature reaches T_c. This assumption disregards the fact that I_c is a continuous function of the temperature (that I_c does not become infinite at $T < T_c$) and also that the voltage-current transition has a finite n-value. Significant deviation between the model and the measurements may result, especially in the case of MgB_2 that exhibits relatively low n-values at high magnetic field. Furthermore, when accounting for the continuous $I_c(T)$ function and a finite n-value, the temperature dependence of the heat capacity, thermal conductivity and the electrical resistivity must be included.

To include all these effects, a 1-dimensional numerical model was developed, based on the explicit finite difference scheme of equation (4.1)[4]. In the remainder of this paragraph, several refinements are discussed. As a first refinement step the continuous temperature dependence of I_c is implemented in the numerical model, which leads to the concept of "current sharing" between filaments and matrix [207]. As a second refinement step, the voltage-current relation of the filaments is included in the model by considering filaments and matrix as an electrical parallel circuit. As a last step, the field- and temperature dependence of the thermal- and electrical properties are taken into account. The actual implications of the refinements on MQE and v_{nz} are discussed separately in §4.3.3.

[4]For a thorough discussion on numerical finite difference solutions of partial differential equations, see for example [206]. The details of this particular numerical model are discussed in [199, 200].

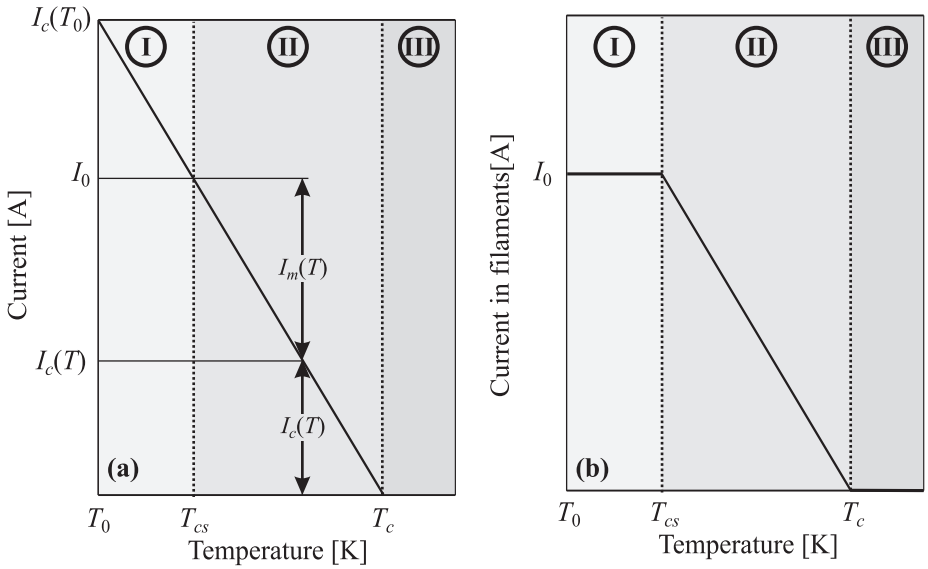

Figure 4.4: (a) shows the $I_c(T)$ line of MgB_2. Due to a thermal disturbance $I_c(T)$ drops below the transport current I_0. As a consequence, I_0 is shared between the matrix, carrying a current I_m and the filaments that carry a current $I_c(T)$. (b) shows how the current in the filaments decreases with increasing temperature. Region **(I)** indicates the region where I_0 is transported lossless by the filaments; **(II)** indicates the region where current is shared between the matrix and filaments; and **(III)** the region where all the transport current flows in the matrix.

Current Sharing Model

When a conductor is operating at its nominal temperature T_0 –with a critical current $I_c(T_0)$–, the transport current I_0 is carried lossless by the filaments (region (I) in figures 4.4a and b). If the temperature of the conductor is raised by a thermal disturbance I_c will drop, following the $I_c(T)$ line in figure 4.4a. At the current sharing temperature T_{cs}, the critical current equals the transport current I_0. When this temperature is exceeded (region (II)), the filaments cannot carry all the transport current anymore. Instead, current is shared between the filaments and matrix. The filaments continue to carry a part $I_c(T)$ of the current lossless, while the excess current $I_m(T) = I_0 - I_c(T)$ is carried Ohmic by the matrix. At the moment where the temperature exceeds T_c, I_c has become zero and the transport current is carried only by the matrix.

It has to be stressed that in this current sharing model only the excess current $I_m(T)$ generates Ohmic heat. This assumption is reasonable as long as a conductor has a sharp voltage-current transition and when the electrical resistivity of its matrix is much lower than the normal state resistivity of its filaments. This is the case for Nb-Ti and Nb_3Sn conductors that usually have high n-values and a low

resistive Cu matrix. Accordingly, this straightforward current sharing concept works very well for these materials [208], but not necessarily for MgB_2.

Parallel-Paths Model

Presently some MgB_2 conductors suffer from relatively low n-values. Furthermore, since MgB_2 reacts strongly with low-resistive materials such as Cu or Al other metals are commonly used with a resistivity that is often similar to that of the filaments. The heat generation in the partly normal conducting filaments can therefore not be neglected anymore. To account for this, the current sharing concept described above is further refined by including also the voltage current relation of the superconducting filaments:

$$E = E_c \left(\frac{J_{sc}}{J_c} \right)^n . \tag{4.4}$$

E_c is the voltage criterium at which the critical current density J_c is defined and J_{sc} is the current density in the superconductor. Furthermore, an electric field $E_{c,\mathrm{onset}}$ and current density $J_{c,\mathrm{onset}} (= I_{c,\mathrm{onset}}/A_{sc})$ are defined at which dissipation in the normal- and superconducting state of the filaments become equal:

$$E_{c,\mathrm{onset}} = E_c \left(\frac{J_{c,\mathrm{onset}}}{J_c} \right)^n = \rho_{sc} J_{c,\mathrm{onset}}, \tag{4.18}$$

with ρ_{sc} the normal-state resistivity of the filaments. The temperature at which $I_{c,\mathrm{onset}} = I_0$ is defined as the current dependent normal state temperature T_{ns}.

Figure 4.5a shows the $I_c(T)$ line on which the voltage-current transition (4.4), (4.18) is projected, while figure 4.5b shows how the current in the filaments reduces with increasing temperature in the case of a low- and a high n-value. Considering a conductor with a high n-value, the voltage-current relation is sharp and the current in the filaments starts to decrease when $T \approx T_{cs}$, following the $I_c(T)$ line, just like in the current sharing model. However it should be stressed that with this model, the current in the filaments *does* generate heat, which was not the case in the simpler current sharing model. When the temperature has reached T_{ns}, the filaments switch to Ohmic behaviour (4.18). Furthermore, due to the finite resistance of the filaments, the current in the filaments does not reduce to zero when $T > T_{ns}$ but continues to be distributed between the filaments and matrix. In a conductor with a low n-value, on the other hand, the relatively "smooth" voltage-current transition causes most of the current I_0 to be carried by the filaments up to a temperature that is significantly higher than T_{cs}.

Overall, by including the voltage-current relation and in the case that $\rho_{sc} \sim \rho_m$, the clear boundaries (I)-(II) and (II)-(III) in the current sharing model (figure 4.4a and b) become poorly defined.

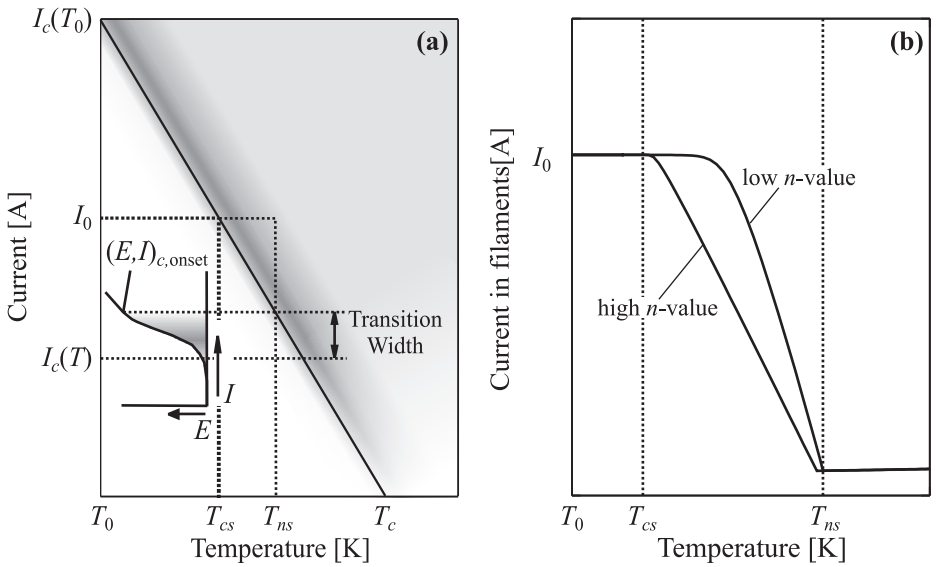

Figure 4.5: (a) shows the $I_c(T)$ line of MgB_2. The shaded area around the $I_c(T)$ line represents the transition width (it is the voltage-current transition projected on the $I_c(T)$ line (**inset**)). (b) shows how the current in the filament reduces with increasing temperature in the case of a low- and a high n-value.

The detailed distribution of I_0 during the transition from lossless to Ohmic current transport is defined by considering the filaments and matrix as parallel-paths:

$$J_0 = \begin{cases} (1-f)\dfrac{E}{\rho_m} + f\left[J_c\left(\dfrac{E}{E_c}\right)^{1/n}\right] & E < E_{c,\text{onset}}; \\ (1-f)\dfrac{E}{\rho_m} + f\dfrac{E}{\rho_{sc}} & E > E_{c,\text{onset}}, \end{cases} \tag{4.19}$$

where f is the superconductor filling factor, ρ_m is the electrical resistivity of the matrix and ρ_{sc} is the normal state resistivity of the superconductor. The accompanying ohmic heat generation term becomes:

$$p_{\text{diss}} = EJ_0. \tag{4.20}$$

A comparison of the heat generation terms in the parallel-paths model (4.20); the current sharing model; and the analytical approximation as well as the implications for MQE and v_{nz} are discussed in §4.3.3.

Temperature- and Field Dependence of the Thermal- and Electrical Properties

The heating function (4.19), (4.20) requires knowledge of the temperature- and field dependence of J_c as well as the n-value. Therefore equations (3.1) and (4.21) are used to describe the $J_c(B,T)$ and $n(B,T)$ surfaces [94]:

$$\frac{J_c(B,T)}{J_{c,0}} = \left(1 - \frac{T}{T_{c,0}}\right) \exp\left[-\frac{B}{B_{p,0}\left(1 - \frac{T}{T_c}\right)}\right]; \tag{3.1}$$

$$\frac{n(B,T)}{n_0} = \left(1 - \frac{T}{T_{c,0}}\right) \exp\left[-\frac{B}{B_{n,0}\left(1 - \frac{T}{T_c}\right)}\right]. \tag{4.21}$$

The transition from lossless- to Ohmic current transport can become a very gradual function of temperature, especially at low n-vales and highly resistive matrices. Therefore the temperature dependence of the material properties –c, κ and ρ– must be accounted for. Indeed, these material properties can be strong functions of the temperature. For example, the electrical- and thermal conductivities in pure metals such as Cu undergo a transition from electron-impurity scattering to electron-phonon scattering. This is reflected in a strong deflection of their temperature dependence below 50 K [5]. Furthermore c, κ and ρ can be a strong function of the magnetic field as well, not only in the superconducting filaments but also in the metallic matrix materials.

Output of the Numerical Model

The principle output of the numerical model is the time evolution of the temperature profile along the conductor. Two examples of such profiles are plotted in figures 4.6a and b. Figure 4.6a shows how the normal zone collapses in time when the thermal disturbance Q_{initial} is lower than MQE. Figure 4.6b shows the opposite case, in which the normal zone propagates along the conductor.

Similar to the actual experiment (§4.4.5), the value of MQE is found by varying Q_{initial} and searching for the boundary between a collapsing and a propagating normal zone. The search routine is truncated when the difference between the values of Q_{initial} at a propagating- and collapsing normal zone is smaller than ~ 1 %.

Once the normal zone is propagating (figure 4.6b), the numerical code calculates v_{nz} following:

$$v_{nz} = \frac{z_2 - z_1}{t_2 - t_1}. \tag{4.22}$$

[5] In fact, for pure metals the Wiedemann-Franz law used in equation (4.17) is not valid in the temperature range from 10 to 250 K due to the different effect of the electron-phonon scattering on ρ and κ ([209]).

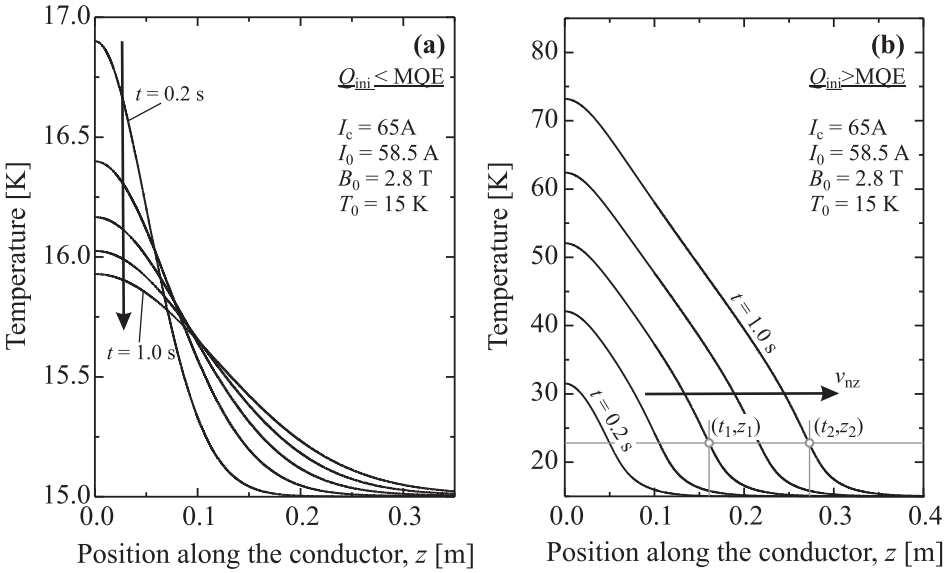

Figure 4.6: Calculated time evolution of the temperature profile along sample HTR1 (see table 4.1) for (a) a collapsing normal zone and (b) a propagating normal zone. (t_1, z_1) and (t_2, z_2) are the time-space coordinates from which v_{nz} is determined using equation (4.22). MQE of this sample 10 mJ

The position on the temperature profile at which z_1 and z_1 are determined is the average of the "classical" T_{cs} and the temperature T_{ns} at which $I_{c,\text{onset}}$ meets the transport current I_0.

4.3.3 Comparison Between the Models

The main refinement of the parallel-paths model with respect to the current sharing model and to the analytical approximations (4.12) and (4.16) is that the filaments can also generate heat. Furthermore, compared to the analytical approximations, the current sharing- and parallel-paths models account for the temperature- and field dependence of the material properties (c, κ and ρ). The refinements mainly influence the heat generation during a transition. In this paragraph it will be shown how the heat generation varies from one model to another and how this influences the prediction of MQE and v_{nz}.

Heat Generation

Figure 4.7a shows the heat generation in the analytical approximations (4.12) and (4.16) as a function of temperature. The approximations are represented by three step-like heating functions that are labeled by the authors that proposed them

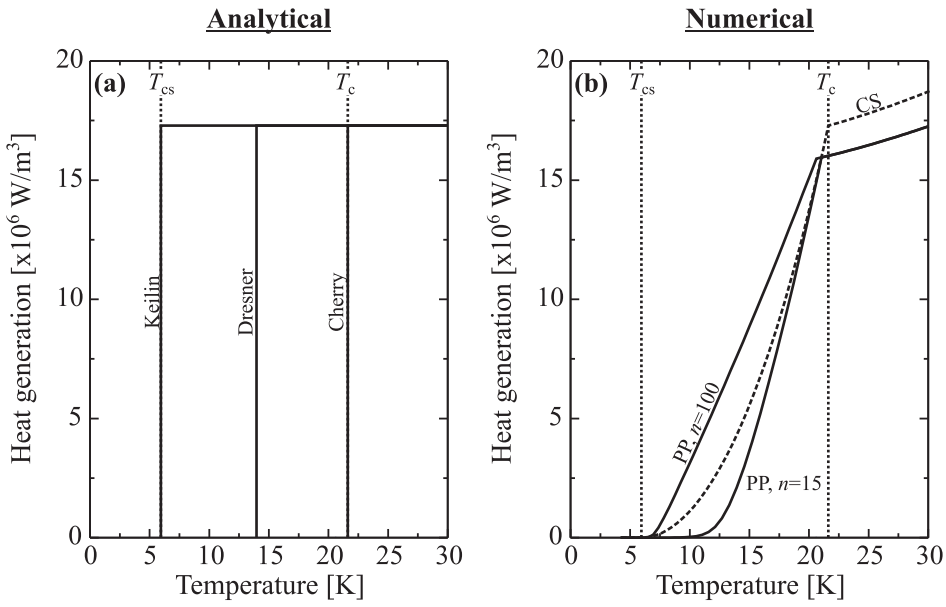

Figure 4.7: (a) compares the heat generation as a function temperature of the analytical approximation (Keilin at T_{cs}, Dresner at $\frac{1}{2}(T_{cs}+T_c)$ and Cherry at T_c [88]). Note that here T_c is an effective critical temperature and is thus B-dependent. (b) shows the heating function of the current sharing- and of the parallel-paths model at an n-value of 15 and 100. In this example, a MgB_2/Fe conductor is assumed with $f = 42$ %, operating at $B_0 = 8$ T, $T_0 = 4.2$ K and $I_c = 40$ A.

(Cherry, Keilin and Dresner [88]). As already discussed in §4.3.2, current diffusion –and therefore heat generation– starts at T_{cs}. Therefore the assumption of Cherry that current abruptly diffuses into the matrix at $T = T_c$ (the assumption used in (4.12) and (4.16)) results in an underestimation of the heat generation. As an alternative, Keilin replaced T_c with the current sharing temperature, so that all the current abruptly diffuses into the matrix at $T = T_{cs}$. This clearly leads to an overestimation of the heat generation, since at T_{cs} the critical current of the filaments does not become zero and the filaments still carry a sizeable fraction of the current. As a compromise, Dresner used the intermediate temperature $\frac{1}{2}(T_{cs}+T_c)$ as the temperature where heat generation starts. Although Dresner's choice might seem a reasonable compromise, compared to both the current sharing and the parallel-paths model it is still a crude approximation that does not account for the detailed distribution of the current between the filaments and the matrix.

Figure 4.7b compares the heat generation in the parallel-paths model in the case of an n-value of either 15 or 100 with that in the current sharing model. For a conductor with $n = 15$, the current sharing model overestimates the heat generation with respect to the parallel-paths model. In contrast, the current

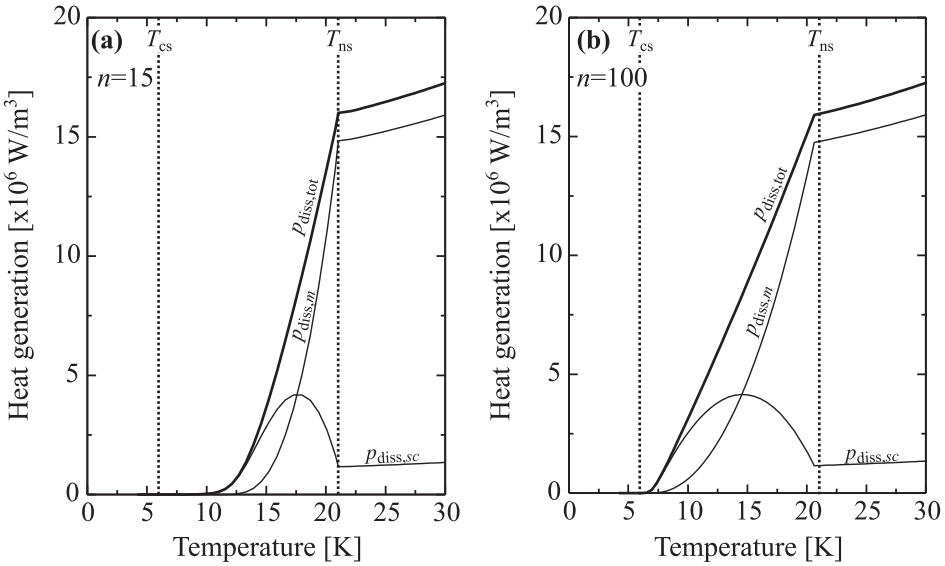

Figure 4.8: Heating function of the parallel-paths model, showing the individual contributions of the filaments and matrix. (a) shows the case for a n-value of 15, while (b) shows the case for a n-value of 100.

sharing model underestimates dissipation for a conductor with a high n-value.

To clarify the differences, the heating function of the parallel paths model is re-plotted in figure 4.8a ($n = 15$) and b ($n = 100$), this time also showing the separate contributions of the filaments and the matrix. The heat generation in the matrix simply follows $p_{\mathrm{diss},m}(T) = J_m(T)^2\rho_m(T)$. Heat generation in the filaments, on the other hand, follows $p_{\mathrm{diss},sc}(T) = J_{sc}(T)E(J_{sc}(T))$, which results in a peaked curve between T_{cs} and T_c. As defined before, T_{cs} is the temperature at which the voltage starts to rise, which causes the current to diffuse into the matrix. The maximum in the curve $p_{\mathrm{diss},sc}$ corresponds to the temperature at which the effective resistance of the filaments equals that of the matrix. When the temperature increases further, the effective resistance becomes higher than that of the matrix and the current in the filaments decreases fast. Above the normal state temperature T_{ns}, the filaments are normal conducting and current continues to be shared between filaments and matrix according to the parallel-paths connection between two Ohmic resistances. As a consequence even in this regime, dissipation in the filaments is not zero since in typical MgB_2 conductors the normal state resistivity of the filaments and matrix are comparable.

As shown in figure 4.5b, the "smooth" voltage-current relation of the filaments for low n-values causes the transport current to be carried virtually lossless by the filaments well above T_{cs}. Accordingly, significant heating starts at a higher temperature than in the case of the current sharing model. For $n = 100$, on the

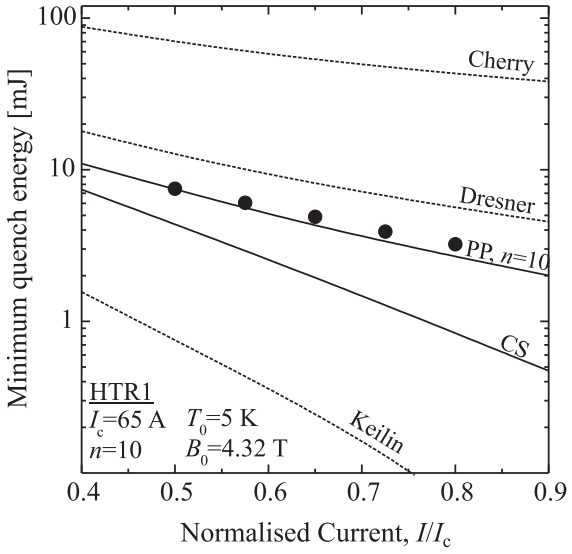

Figure 4.9: Comparison of measured MQE(I/I_c) values for conductor HTR1 (**data points**) with the analytical (**dashed lines**) and the numerical models (**solid lines**). Further details of sample HTR 1 can be found in table 4.1. Note that for the analytical approximations κ and ρ are taken at $T = \frac{1}{2}(T_{cs} + T_c)$.

other hand, the sharp voltage-current relation causes the current in the filaments to decrease almost linearly with temperature, just like in the current sharing model (see figures 4.4b and 4.5b). The reason that the heating function of the parallel-paths model does not converge with that of the current sharing model at high n-values is the heat generation in the filaments, which is neglected in the current sharing model. In fact, the heat generation in the filaments causes the total heat generation to become an almost linear function of temperature that, within the range $T_{cs} < T < T_c$, is higher than in the current sharing model.

Minimum Quench Energy

Figure 4.9 compares experimental MQE data as a function of current with different model calculations. Comparing the different models, it becomes clear that the details of current redistribution –and the associated heating functions– are very important as they lead to results that differ two orders of magnitude. As shown by equation (4.12), l_{MPZ} and MQE depend on $p_{\mathrm{diss}}^{-1/2}$. As a result, the underestimation of p_{diss} following from Cherry's assumption (no heat generation below T_c) leads to a seriously overestimation of MQE. The opposite is true for Keilin's assumption, which results in predicted values of MQE that are too low. In fact, by assuming T_{cs} as the temperature at which current diffuses abruptly into the matrix, MQE →

0 when I_0 approaches I_c. This is caused by the fact that for $I \rightarrow I_c$, T_{cs} approaches the baseline temperature T_0 and the temperature margin vanishes.

The overestimation of p_{diss} (see figure 4.7a and b) of Dresner's assumption with respect to the parallel-paths model results in a predicted MQE value that is too low. The reason that MQE is in fact overestimated is the assumption of a relatively simple "block" shaped temperature profile in the minimum propagation zone ($T(z) = \frac{1}{2}(T_{cs} + T_c)$ over l_{MPZ}). Furthermore, equation (4.12) requires the choice of κ and ρ at some "appropriate" temperature, which introduces an extra uncertainty.

Just like the parallel-paths model, the current sharing model does account for the strong temperature dependence of c. The underestimation of MQE in the current sharing model is a direct result of neglecting the voltage-current relation of the filaments. As shown by figure 4.7b, a low n-value causes significant heating to start at a higher temperature than in the current sharing model.

Normal Zone Propagation Velocity

In figure 4.10a measurements of v_{nz} as a function of current for sample HTR1 are compared with the model calculations. Clearly, by including the details of current distribution the parallel-paths model results in a good agreement with the experimental data.

With the analytical approximation, using Cherry's assumption results in an underestimation of v_{nz}, due to the omission of heat generation for $T < T_c$. In contrast, the overestimation of p_{diss} in Keilin's approximation results in a seriously overestimated v_{nz}. Similar to MQE, by assuming T_{cs} as the temperature at which *all* the current diffuses in the matrix, the temperature margin vanishes as $I_0 \rightarrow I_c$, which in this case results in $v_{nz} \rightarrow \infty$.

Figures 4.7a and b show that with Dresner's assumption, the total Ohmic heat generation over the temperature range T_{cs} to T_c is slightly overestimated with respect to the current sharing and parallel-paths model. On first sight, this would suggest that also the predicted values of v_{nz} would be too high. The reason that v_{nz} is actually underestimated is the assumption that all material properties are temperature independent. Clearly, in order to get a better agreement, an "appropriate" temperature has to be chosen at which c, κ and ρ are taken. However, in the case of MgB_2, this leads to the problem that c increases by two orders of magnitude in the range between 5 and 40 K, which causes the results of the analytical predictions to depend strongly on the choice of this "appropriate" temperature.

Similar to MQE, the overestimation of v_{nz} in the current sharing model is a direct result of neglecting the voltage-current relation of the filaments. The relatively low n-value of this conductor under these operating conditions causes significant heat generation to start at a higher temperature than in the current sharing model (see figure 4.7b).

For comparison, v_{nz} measurements as a function of current for a Nb_3Sn/Cu conductor with an n-value of 50 are presented in figure 4.10b. As expected from

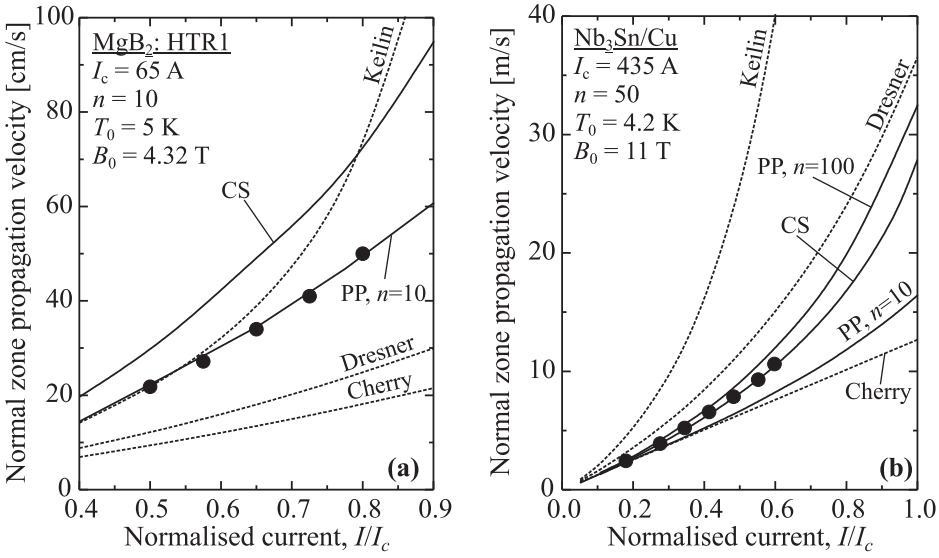

Figure 4.10: Comparison of the measured $v_{nz}(I/I_c)$ (**data points**) with the analytical (**dashed lines**) and the numerical models (**solid lines**). (a) shows the results of MgB_2 conductor HTR1 (table 4.1) and (b) of a Nb_3Sn/Cu conductor. Note that for the analytical approximations c, κ and ρ are taken at $T = \frac{1}{2}(T_{cs}+T_c)$.

the heating functions parallel-paths model calculations with n-values of 10 and 100 result in an under- and overestimated v_{nz} respectively. Interestingly, however, the conductor's intermediate n-value (compared to 10 and 100) causes the results of current sharing model to agree rather well with the measurements. Contrary to MgB_2, the normal state resistivity of Nb_3Sn filaments is significantly higher than the matrix resistivity, so that in this material the current sharing approximation (absence of dissipation in filaments) is justified.

4.4 Experiment

As discussed in section 4.3, prediction of v_{nz} and MQE can be inaccurate due to the 1-dimensional approach of most models, uncertainties in the boundary conditions (liquid helium cooling, thermal contacts) and uncertainties in the thermal and electrical properties of the conductors. Moreover, the electrical and thermal properties vary with magnetic field and temperature. To verify the predictive value of the numerical model, it is necessary to measure v_{nz} and MQE not only as a function of transport current but also of magnetic field and temperature.

In §4.4.1 the principle of the voltage-time-of-flight method with which v_{nz} is measured is explained. Furthermore, some details of the quench heater that ini-

tiates the normal zone are treated.

It is useful to measure v_{nz} and MQE under adiabatic conditions. This yields the intrinsic properties of the conductor, avoiding complicated cooling terms –that depend on the detailed boundary conditions– and straightforwardly simulates the cryogen-free operation of MgB_2 conductors. In order to perform such measurements a quasi-adiabatic set-up was constructed, which is described in §4.4.2.

With the quasi-adiabatic set-up it is possible to measure v_{nz} and MQE as a function of temperature. Measurements at elevated temperature require a careful thermal design of the experiment in order to ensure a homogeneous baseline temperature along the sample. The thermal design of the experimental set-up is therefore discussed separately in §4.4.3.

In §4.4.4 the instrumentation is discussed that is used to accurately measure v_{nz} and MQE data under different operating conditions (I_0,T_0,B_0).

Lastly, v_{nz} and MQE depend on the cross-sectional layout of the conductors (thermal/electrical conductivity, heat capacity, filling factor, number of filaments, etc.). Therefore, conductors with various layouts were selected to study v_{nz} and MQE. In §4.4.6 an overview is given of their relevant properties and the main differences between them are discussed.

4.4.1 Measurement Technique

The voltage-time-of-flight method is a widely used technique to measure the normal zone propagation velocity v_{nz} [208,210,211]. A conductor sample is equipped with a quench-heater (in this case a manganin wire wound around the sample) and with several voltage taps that are spaced a distance Δz apart and connected to an oscilloscope (figure 4.11). The conductor is biased with a steady current and a propagating normal zone is initiated with a block shaped heat pulse Q_{initial} ($= P_{\text{initial}}\Delta t$). The propagating normal zone front passes the voltage contact at position z_{V_1+} at time t_{V_1+} and the voltage signal V_1 starts to rise. At t_{V_1-} the volume between z_{V_1+} and z_{V_1-} is completely in the normal state. For $t > t_{V_1-}$ any further voltage rise is only due to the increase of electrical resistance with temperature. The same process holds for voltage signal V_2. The normal zone propagation velocity v_{nz} is then calculated from the time lag Δt between voltage signals $V1$ and $V2$:

$$v_{nz} = \frac{\Delta z}{\Delta t} = \frac{z_{V_2+} - z_{V_1+}}{t_{V_2+} - t_{V_1+}} = \frac{z_{V_2-} - z_{V_1-}}{t_{V_2-} - t_{V_1-}}. \tag{4.23}$$

An alternative method, uses pick-up coils rather than voltage taps to trace the position of the normal zone front [212,213]. Current diffusion from the filaments to the matrix around the normal zone front causes a change in flux distribution, which induces a voltage signal in the pick-up coils. Similarly to the previous method, the normal zone propagation velocity is calculated from the time lag between the voltage signals of two consecutive pick-up coils.

With the voltage-time-of-flight method it is in principle possible to measure also the minimum quench energy MQE, simply by varying Q_{initial} and searching

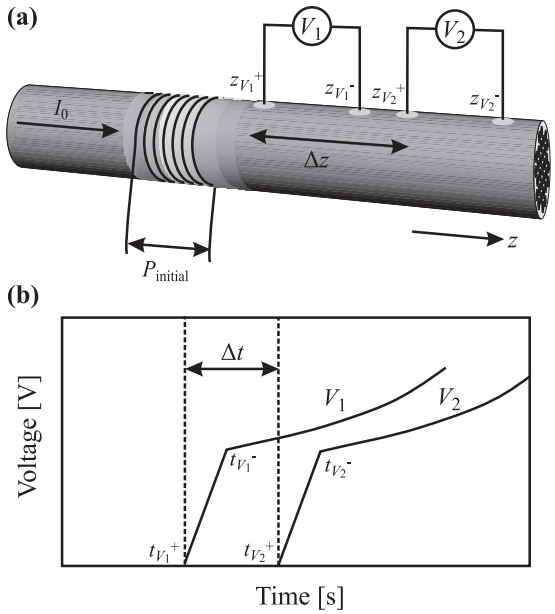

Figure 4.11: Principle of the Voltage-Time-of-Flight method. (a) shows a conductor that carries a transport current density J_0. The thermal disturbance P_{initial} is injected into the conductor with a wire wound heater to initiate a normal zone. Voltage taps V_1 and V_2 are soldered to the wire, a distance Δz apart. They are connected to an oscilloscope to measure the time dependent voltage signal that is associated with the normal zone propagation. (b) shows a typical voltage signal of a propagating normal zone. The signal between t_{V_1+} and t_{V_1-} (or t_{V_2+} and t_{V_2-}) are associated with the normal zone growth in-between z_{V_1+} and z_{V_1-} (z_{V_2+} and z_{V_2-}). The voltage rise for $t > t_{V_1-}$ ($t > t_{V_2-}$) is associated with the increase of resistance with temperature.

for the transition point between a collapsing- and a propagating normal zone. The main uncertainty in this kind of measurements is the amount of heat that is actually transferred to the conductor itself. In this respect, three requirements are important for heater design: 1) the enthalpy of the heater itself (the temperature integral of the volumetric heat capacity over the heater's volume) needs to be small compared to MQE. If this is not the case, the generated heat is distributed over both sample and heater, which leads to a significant overestimation of MQE; 2) the thermal conductivity between heater and sample needs to be high so that the generated heat does not remain localised in the heater itself, which would again lead to an overestimation of MQE; 3) thermal contacts between heater and other parts of the experimental set-up (heat conduction through heater wiring) should be kept minimal, since once more this heat loss would lead to a significant overestimation of MQE.

An optimised heater for MQE measurements that fulfills all of the design requirements above is presented in [214]. A small tip-heater ($d \sim 0.6$ mm) is pressed against the sample with a clamping system. Heating takes place at the point where the tip-heater is presses against the sample via the electrical resistance of the heater-sample contact. Control of the heater-sample resistance is achieved by using graphite paste between heater and sample and by the use of a clamping system that allows to control the force with which the heater is pressed on the sample. Furthermore, the tip-heater is made with a low thermal conductivity material (graphite or machinable glass (Macor)) that is coated with several micrometers of silver paint or Ti/Ag to provide electrical conductance. With this method, heat diffusion into the tip heater is limited, thus minimising the overestimation of MQE.

Although the heater enabled accurate MQE measurements in Nb-Ti samples, the similar design was not adopted here, since its use seriously limits sample throughput as for each sample shape (wire or tape) a different clamping system would have to be used. Moreover, the size of the clamping system makes it difficult to mount the whole in a vacuum can, limiting the ability to vary the temperature of the sample in a controllable manner.

A relatively simple manganin wire-wound heater is used. The total length of the manganin wire is about ~ 45 cm, its diameter ~ 0.1 mm and its resistance $\sim 25\ \Omega$. The heater wire is tightly wrapped around the sample into a bifilar winding to minimise self-induction. It is then fixed to the sample with GE varnish. Clearly, this heater design leads to an overestimation of MQE, since its enthalpy is large compared to that of the average sample. The enthalpy of the manganin heater is approximately ~ 0.3 mJ [32] in the range between 4 and 40 K, whereas the MQE of the MgB_2/Fe conductor from table 1.1 for example is about 0.04 mJ at 4.2 K. The generated heat will thus be distributed over both the sample and the heater. Nevertheless, this type of heater was used in all experiments described below, mainly because of its ease of handling and flexibility. Similarly to [215], the intrinsic MQE values are estimated by comparing the experimentally obtained values with the results of the numerical calculations, thus estimating the effective heat transfer from the quench-heater to the the sample. The corresponding heat "loss" is typically about 80 % of the total heat input. The MQE values presented in the corresponding figures are 20 % of the measured ones.

4.4.2 Design

If the normal zone propagation velocity and minimum quench energy are measured in LHe, an extra cooling term would have to be added to the heat balance equation (4.1). This cooling term seriously complicates the analysis of v_{nz} and MQE, since transient effects of LHe film boiling at the sample's wetted perimeter have to be accounted for. These transient effects are caused by the relatively slow formation and decay of He vapour films[6]. Moreover, as explained in §4.1, direct LHe cooling

[6]The influence of transient effects on the stability of superconductors is extensively discussed in [201]

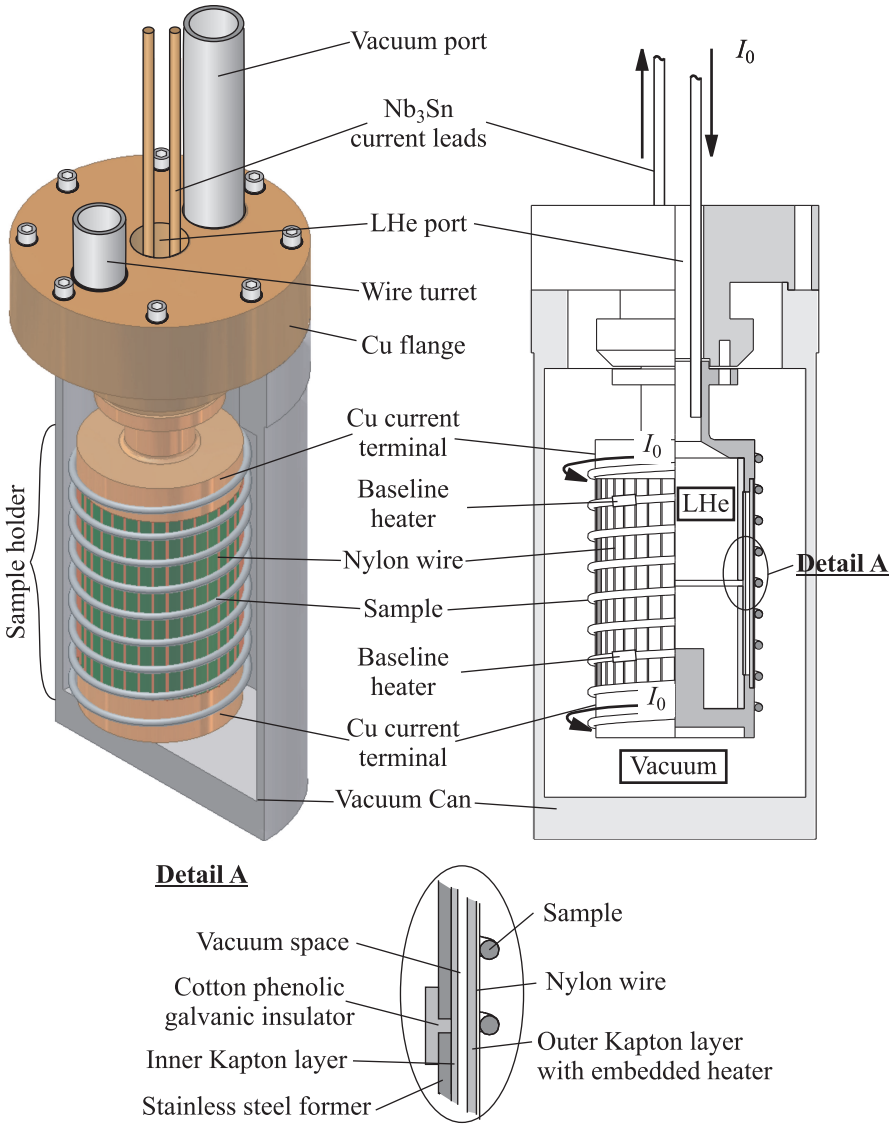

Figure 4.12: Overview of the quasi-adiabatic setup to measure the normal zone propagation velocity. The sample is placed in a vacuum can and the normal conducting Cu current terminals to which the sample is soldered are cooled with liquid helium that is allowed inside the sample holder through the LHe port. In order to change the baseline temperature, two resistors are positioned at the ends of the sample and a third wire-wound heater (manganin) is embedded in the outer Kapton layer. To limit heat conduction from this embedded heater to the LHe reservoir inside the holder the outer- and inner Kapton layers are separated with a vacuum space. The nylon wire thermally detaches the sample from the outer Kapton layer.

might not be the most relevant operating condition for MgB_2 conductors. To avoid complications of transient heat-transfer effects and to simulate cryogen-free operation of MgB_2, the sample is isolated from LHe by placing it in a vacuum can. A schematic overview of the experimental set-up is given in figure 4.12.

An as-deformed sample is wound on a reaction holder and subsequently sintered (ex-situ) or reacted (in-situ) at the required temperature. After heat treatment, the helically shaped sample is transferred to the sample holder and soldered to the Cu current terminals. The transport current is fed to the current terminals with two Nb_3Sn current leads. To provide additional cooling of the normal conducting current terminals, LHe is allowed inside the hollow central core of the sample holder through a LHe port. The sample is equipped with a quench-heater and voltage taps to trace the position of the normal zone front (as described in the previous paragraph). Additional voltage taps monitor the voltage over the whole sample, while two background heaters and three Cernox thermometers regulate the operating temperature of the sample. The wiring for the instrumentation is fed through the wire turret, which is vacuum sealed with Stycast 2850FT.

The sample holder consists of an upper and lower stainless steel former, which are galvanically separated with a piece of cotton phenolic. The galvanic separation prevents current from flowing through the steel former during the superconducting to normal transition. To prevent LHe from leaking out of the hollow core into the vacuum can, Kapton foil (inner Kapton layer) is wound around the former and glued with Stycast 2850FT. A vacuum space is left between the inner and outer Kapton layers to decrease the heat transfer from the embedded heater in the outer Kapton layer to the LHe. The outer Kapton layer is also made of coiled Kapton foil, and a manganin wire heater is co-wound to provide additional baseline heating. More details on the thermal design are presented in §4.4.3. Nylon spacer wires minimise the mechanical contact area between the sample and the outer Kapton layer. This limits heat leak from the sample to the outer Kapton layer during the propagation of the normal zone, which otherwise would result in an underestimation of v_{nz}. Lastly, the mechanical connection between the Cu flange and the vacuum can and sample holder assembly is provided with a pressed In wire seal ($d \sim 1$ mm), which is impermeable for LHe.

4.4.3 Controlling Heat Flows

To measure v_{nz} and MQE of MgB_2 conductors at elevated temperatures, temperature regulation had to be added to the set-up. In a first attempt the temperature of the MgB_2 sample was regulated by two baseline heaters, P_{h1} and P'_{h1}, and two temperature sensors, T_1 and T'_1, which were directly mounted on the sample near the top- and bottom Cu current leads respectively. To reduce the lateral heat leak, the sample was not fixed with Stycast 2850FT, but loosely wound on the Kapton layer. The temperature profile over the sample was then monitored with sensors T_1 and T'_1 on both ends of the sample, a central sensor T_2 in the middle of the sample and with two extra auxiliary thermometers between T_1 and T_2. The resulting temperature profiles over the sample at different heater powers is

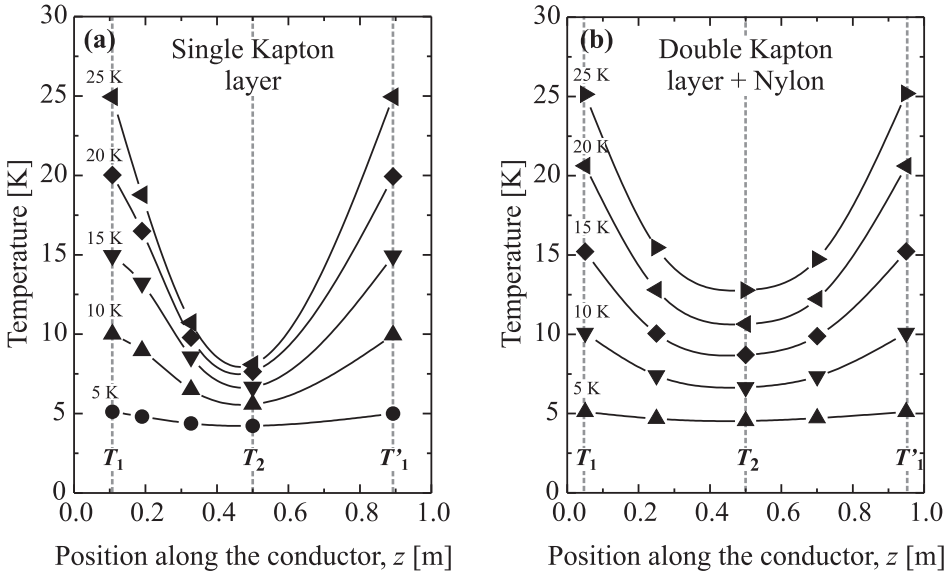

Figure 4.13: Temperature profiles over the sample with (a) the original sample holder (with a single Kapton layer) and (b) with the second version of the sample holder with Nylon wires and a vacuum space between the inner and outer Kapton layer. The different profiles in each graph represent the different baseline temperatures to which T_1 and T_1' are regulated with heaters P_{h1} and P_{h1}' respectively.

depicted in figure 4.13a. Clearly, a large lateral heat leak between sample and holder resulted in a temperature gradient that can be as large as ~ 70 % (when $T_1 = 25$ K). This is too large for v_{nz} and MQE measurements, since I_c over a typical MgB_2 conductor tested at a nominal temperature of 25 K and 1 T would vary about 300 % along its length. For an acceptable I_c gradient over the sample of ~ 5 %, the maximum temperature gradient should be about ~ 1 %.

To decrease the lateral heat leak, a new holder was made in which the single Kapton layer was replaced by an inner- and outer Kapton layer with a vacuum space in-between. Furthermore, Nylon spacer wires were mounted on the outer Kapton layer, further minimising the thermal contact between sample and holder. This layout was similar to the final version of the sample holder, depicted in 4.12. Increasing the temperature of the sample in a similar manner as before resulted in the temperature profiles shown in figure 4.13b. Although the homogeneity of the temperature over the sample was improved with these measures, the gradient over the sample at 25 K remained still about ~ 50 %, i.e. still too large.

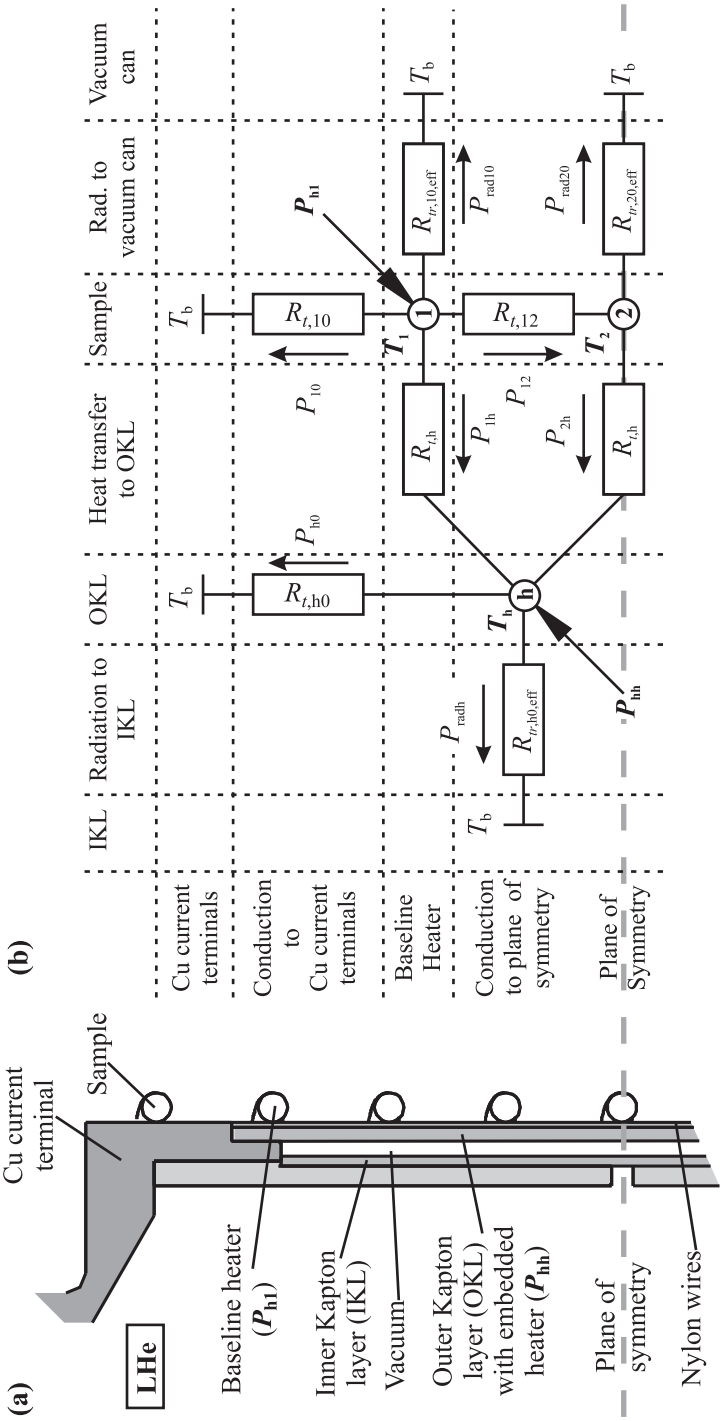

Figure 4.14: (a) Shows part of the cross-section of the sample holder, while (b) shows its equivalent thermal network.

To solve this problem, a careful thermal analysis of the sample holder assembly was made, as summarised in the next two paragraphs. For more details, the reader is referred to appendix C.

Thermal Analysis

The thermal analysis is performed by modeling the holder as an equivalent thermal network (see figure 4.14). It is assumed that the problem is symmetric around the midplane of the sample holder (designated as the plane of symmetry) and that the outer Kapton layer is isothermal at temperature $T_{\rm h}$. Also the Cu current leads, the inner Kapton layer and the vacuum can are assumed to be at a fixed temperature of $T_{\rm b} = 4.2$ K. The assumptions leave three nodes at which the temperature needs to be solved as a function of the baseline heater input $P_{\rm h1}$:

node 1: the point on the sample where heater $P_{\rm h1}$ is mounted, close to the Cu current terminal and at a temperature T_1;

node 2: the point on the sample at the plane of symmetry, with temperature T_2;

node h: the outer Kapton layer with temperature $T_{\rm h}$.

At each node the heat fluxes are balanced, yielding three equations. The heat fluxes themselves are determined by:

$$P = \frac{\Delta T}{R_t}. \tag{4.24}$$

ΔT and R_t are the temperature drop and the effective thermal resistance ([K/W]), in each branch of the thermal network. In principle, all the thermal resistances can be estimated using the relevant thermal properties of each branch (thermal conductivity κ, cross-sectional area A and length l for conductivity and emissivity ϵ, Stefan-Boltzmann constant $\sigma_{\rm SB}$ and surface area A for radiation). Overall, this leaves a set of three linear equations, expressing heat balances at each node and three unknown temperatures (T_1, T_2 and T_h). The only thermal resistance which is a-priori unknown is that of the sample to the outer Kapton layer ($R_{t,\rm h}$), because of the poorly defined thermal contact between the sample and the Nylon wires. Instead, $R_{t,\rm h}$ is determined by fitting the linear equations to the measured temperature profile in figure 4.13b.

With this model, two possible strategies to minimise the thermal gradient over the sample were explored: 1) increasing $R_{t,\rm h}$ further; and 2) minimising the lateral heat leak by increasing temperature $T_{\rm h}$ of the outer Kapton layer.

Results

Figure 4.15a shows the calculated temperature gradient between T_1 and T_2 as a function of both the power of the baseline heater at node 1 ($P_{\rm h1}$) and $R_{t,\rm h}$. The data-points in the graph are the measured temperature gradients from the profiles in figure 4.13b. The best fit between data and calculations corresponds to a value

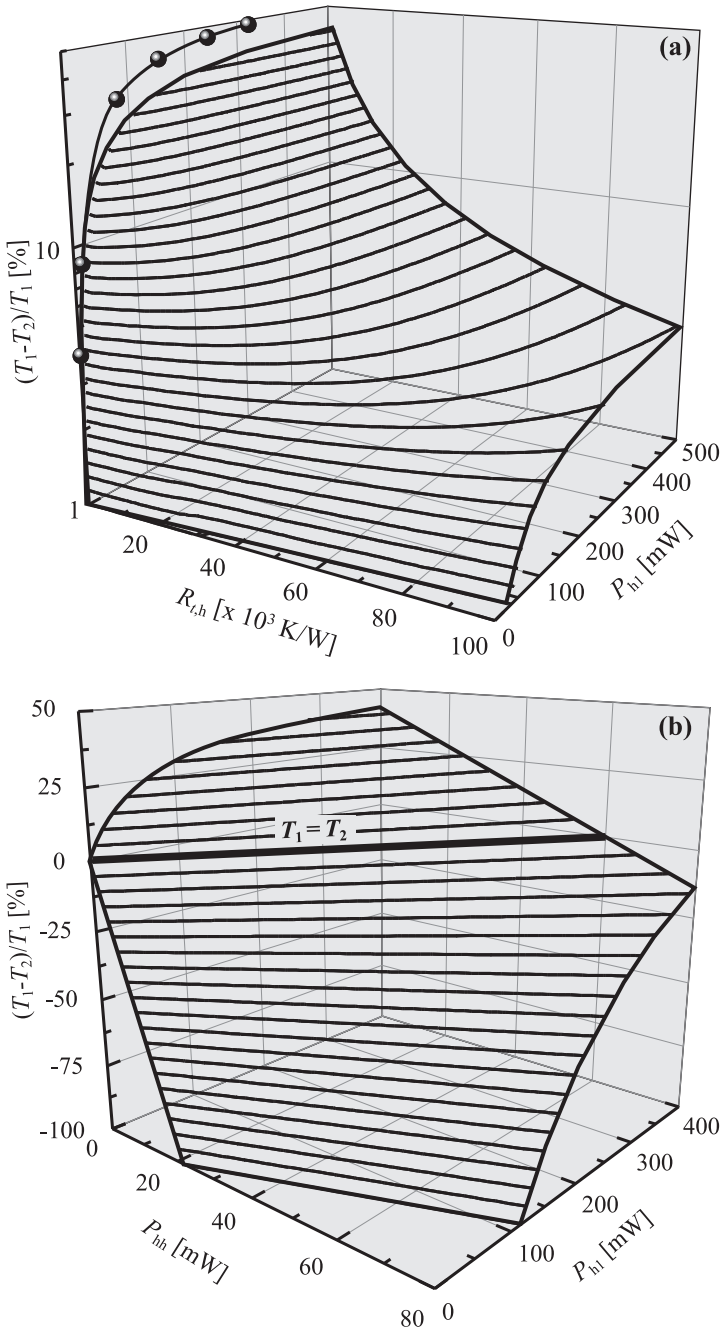

Figure 4.15: (a) Calculation of the relative temperature difference as a function of the heater power P_{h1} and the thermal resistance between sample and outer Kapton layer ($R_{t,\mathrm{h}}$). The data points indicate the measurements (see figure 4.13b) at an assumed $R_{t,\mathrm{h}}$ of 1000 K/W. Note the logarithmic scale of the $(T_1 - T_2)/T_1$-axis. (b) Calculation of the relative temperature difference as a function of the embedded heater power in the outer Kapton layer (P_{hh}) and the heater power at node 1 (P_{h1}).

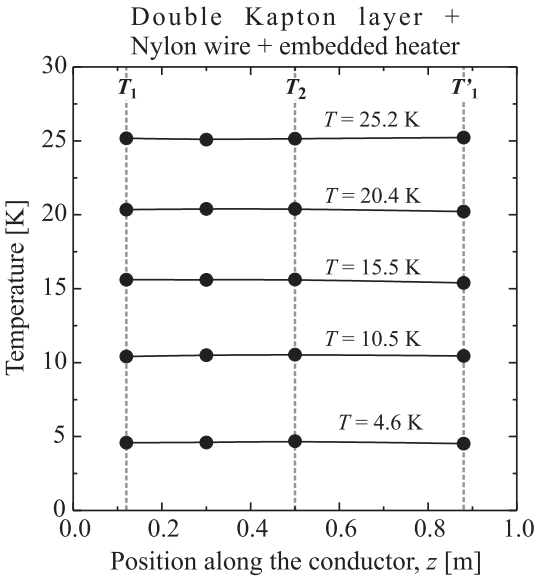

Figure 4.16: Measured temperature profiles along the sample in the final thermal design of the sample holder. The various profiles represent the different temperatures to which T_1, T_2 and T_1' are regulated to by P_{h1}, P_{hh} and P_{h1}' respectively.

for $R_{t,\mathrm{h}}$ of about 1000 K/W. If this value could be increased to $1 \cdot 10^5$ K/W, the maximum temperature gradient would be about 3 %. This corresponds to an I_c gradient of about 14 %. Although this would be a clear improvement of the temperature homogeneity, it is still too high. Moreover, $R_{t,\mathrm{h}} \sim 1 \cdot 10^5$ K/W corresponds to a free-hanging sample with only radiation as a lateral heat loss mechanism. In conclusion, increasing $R_{t,\mathrm{h}}$, even to an unrealistically high level, would not lead to an acceptable temperature gradient.

The second option –implemented in the final design– is to increase the temperature of the outer Kapton layer with a third heater P_{hh} on the outer Kapton layer so that the lateral heat leak is minimised. The model calculations in figure 4.15b show that with this third heater it is possible to invert the temperature gradient, such that $T_2 > T_1$. This means that the temperature gradient can be regulated to zero. As discussed in §4.4.2, this concept is implemented by embedding a manganin heater in the outer Kapton layer across its full length. The measured temperature profiles in figure 4.16 show that with this design the gradient has indeed reduced significantly to about ~ 0.5 % at 25.2 K, corresponding to an I_c gradient of ~ 2 %, which is only limited by the waiting time acceptable for full temperature stabilisation.

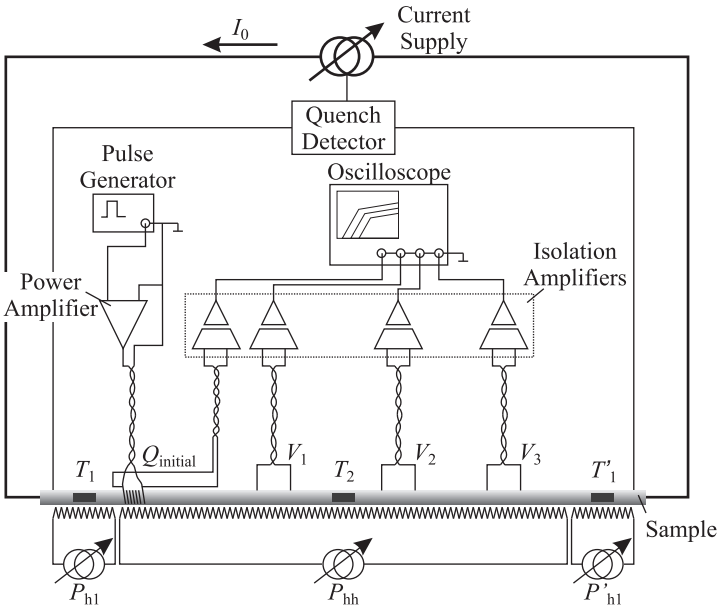

Figure 4.17: Schematic view of the instrumentation. Note that the instrumentation for the magnet field is not included.

4.4.4 Instrumentation

The instrumentation used to measure MQE and v_{nz} as a function of temperature, field and transport current is described. Figure 4.17 shows a schematic overview.

As discussed in the previous section, 3 heaters ($P_{\text{h1}}, P'_{\text{h1}}$ and P_{hh}) are used to increase the baseline temperature of the sample above 4.2 K. Each heater has its own current source so that residual temperature gradients across the sample can be minimised. The temperature of the sample is monitored with three Cernox thermometers (T_1, T'_1 and T_2).

The current source providing the sample current I_0 is connected to a quench detector that monitors the voltage over the whole sample. If the voltage exceeds 50 mV while a normal zone is propagating through the sample, the quench detector switches the current supply off, preventing the sample from burning out.

The quench heater that initiates the normal zone (P_{initial}) is a wire-wound heater with a resistance of $\sim 25\ \Omega$. The heater envelops a sample length of about ~ 15 mm. The heat pulse has a block shape and is generated by a programmable function generator that controls a power amplifier. The typical length of the heat pulse is about ~ 0.5 s depending on the operating conditions (I_0, T_0, B_0).

In order to increase the resolution of the voltage traces of the propagating normal zone (see figure 4.11b), the voltage signals V_1 through V_3 are amplified before they are fed into the oscilloscope. The amplifiers also galvanically isolate

the oscilloscope from the sample to prevent ground loops, which might otherwise cause artefacts in the voltage traces.

4.4.5 Measurement Procedure

As explained in §4.4.1, the minimum quench energy (MQE) is determined by varying Q_{initial} and finding the transition point between a collapsing- and a propagating normal zone. The maximum difference between the value of Q_{initial} at which the normal zone collapses and the value at which the normal zone propagates is chosen in such a way that the uncertainty in the measured value of MQE (as opposed to the absolute uncertainty in MQE, discussed in §4.4.1) is about ~ 5 %. Once the normal zone is propagating, v_{nz} is also measured.

Both v_{nz} and MQE depend on the operating conditions (I_0, T_0, B_0). I_0 determines the value of the heating term in (4.16), while T_0 and B_0 influence the material properties c, κ and ρ. Moreover, all three parameters together determine the temperature margin in (4.16) through:

$$T_s - T_0 \approx [I_0 - I_c(B_0, T_0)] \left(\frac{\mathrm{d}I_c(B_0, T)}{\mathrm{d}T} \right)^{-1} . \tag{4.25}$$

Ideally, v_{nz} and MQE should therefore be characterised as a function of all three parameters. This, however, requires a prohibitively large amount of data-points to be measured, which is time consuming especially in view of the MQE search routine. In order to keep the measurement time reasonable, a strategy is chosen in which the parameters B_0 and T_0 are coupled in such a way that the critical current I_c is kept constant. This procedure is schematically illustrated in figure 4.18. At each (B_0,T_0) setting, v_{nz} and MQE are measured as a function of the transport current I_0.

To adjust B_0 in such a way that I_c remains constant when T_0 is changed, the critical surface of a conductor should first be measured over the relevant (B_0,T_0) range. The initial I_c measurements also serve to verify whether handling damage has occured during the preparation of the normal zone experiment. Since the adiabatic nature of the experimental set-up makes it less suited for I_c measurements at elevated temperatures (thermal runaways), $I_c(B)$ is only measured at 4.2 K, directly cooled with LHe and without vacuum can. In order to estimate the whole critical surface, T_c is also measured by applying a transport current of 1 mA to the sample during the cool-down of the set-up (with the vacuum can installed). The resistive transition is determined by monitoring the voltages V_1, V_2 and V_3 together with temperatures T_1-T_3 [7]. The cool-down of the sample is slow and homogeneous enough to measure T_c within ~ 2 K accuracy. With the measured $I_c(B)$ curve at 4.2 K and critical temperature T_c the two remaining parameters $I_{c,0}$ and $B_{p,0}$ in the approximate descriptions of the critical surface

[7] See §5.2.3 for a more thorough discussion on T_c measurements.

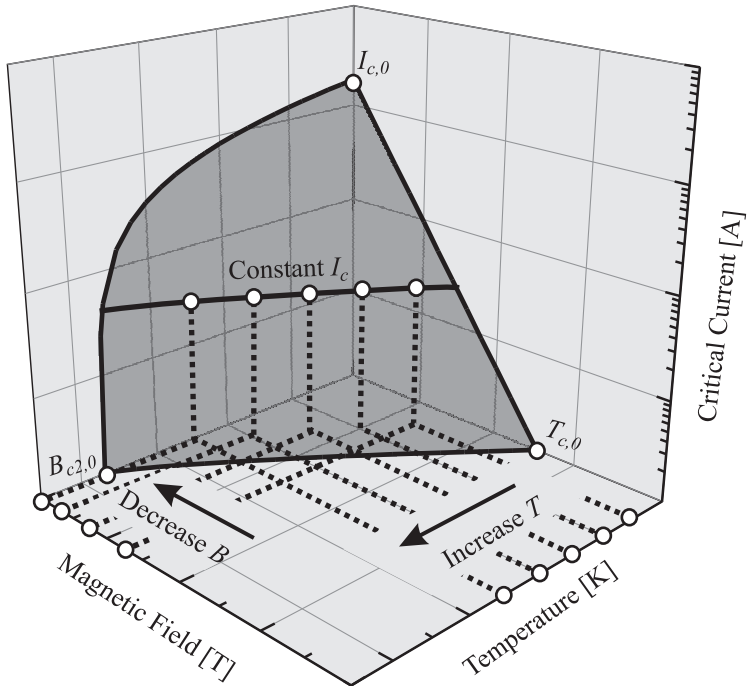

Figure 4.18: Overview of the measurement procedure. To keep the critical current I_c constant while T is increased, the magnetic field B has to be decreased accordingly.

(3.1) can be determined:

$$I_{c,0} = I_c(0\ \mathrm{T}, 4.2\ \mathrm{K}) \left(1 - \frac{4.2\ \mathrm{K}}{T_c}\right)^{-1} \quad \text{and}$$
$$B_{p,0} = B_p(4.2\ \mathrm{K}) \left(1 - \frac{4.2\ \mathrm{K}}{T_c}\right)^{-1}. \tag{4.26}$$

$I_c(0\ \mathrm{T}, 4.2\ \mathrm{K})$ is determined via the extrapolation of $\ln(I_c(B))$ to 0 T, while the slope of the $\ln(I_c(B))$ curve determines $B_p(4.2\ \mathrm{K})$. An example of such an $I_c(B)$ curve measured at 4.2 K and is fitted with equation (3.1) is plotted in figure 4.19a.

Knowledge of the critical surface in the relevant temperature-field range is not only important for the v_{nz} and MQE measurement procedure, but also serves as input data for the numerical model. For modeling, the n-value as a function of T and B also needs to be known. Equation (4.21) can be used in an analogous

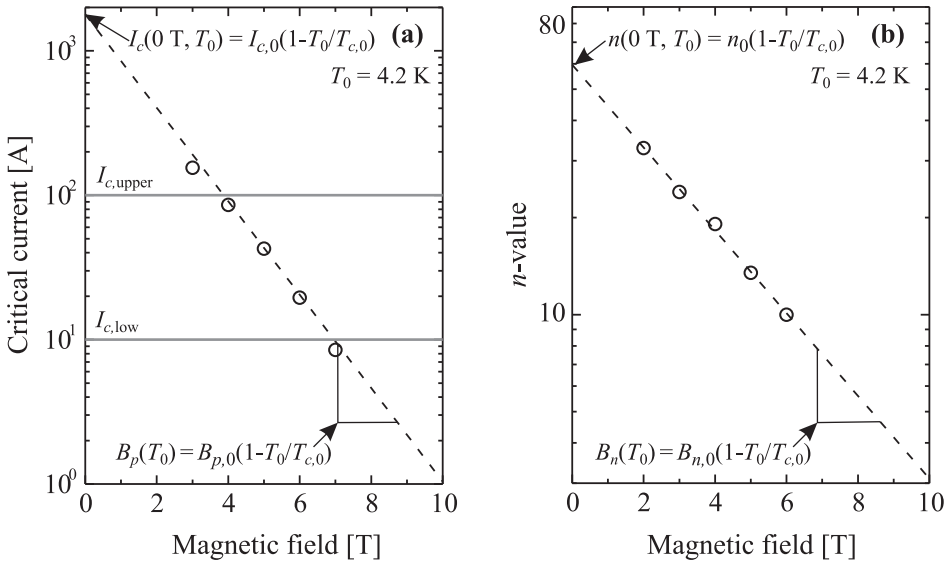

Figure 4.19: (a) shows an $I_c(B)$ measurement at 4.2 K for sample HTR1 (see §4.4.6) from which $I_{c,0}$ and $B_{p,0}$ are determined with equation (3.1*) (**dashed line**). The **gray lines** show the upper and lower I_c limits for the v_{nz} and MQE measurements. (b) shows an $n(B)$ curve for sample FZK from which n_0 and $B_{n,0}$ are determined.

manner to obtain n_0 and $B_{n,0}$:

$$\begin{aligned} n_0 &= n(0\ \mathrm{T}, 4.2\ \mathrm{K}) \left(1 - \frac{4.2\ \mathrm{K}}{T_c}\right)^{-1} \quad \text{and} \\ B_{n,0} &= B_n(4.2\ \mathrm{K}) \left(1 - \frac{4.2\ \mathrm{K}}{T_c}\right)^{-1}. \end{aligned} \tag{4.27}$$

An example of a fitted $n(B)$ curve at 4.2 K is shown in figure 4.19b.

Figure 4.19a also shows a minimum and maximum value for the critical current. This is the I_c range in which v_{nz} and MQE are measured. The upper value is the point where the I_c data start to deviate from the exponential dependence (3.1). As explained in chapter 3, this is assumed to be the point where the sample heats up due to intrinsic thermal instability. The lower value for I_c corresponds to the practical maximum value MQE ($\approx$ 5 J) that can be measured with the set-up. Measurements at lower $I_c(B_0,T_0)$ values would require heat pulses MQE $>$ 5 J, which might burn out the quench-heater.

4.4.6 Samples

As discussed in §4.2 and §4.3, both v_{nz} and MQE are influenced by the conductors cross-sectional layout (number, shape and size of the filaments), the heat capacity and the electrical/thermal conductivity of the materials in the composite conductor. The n-value and the critical current density also plays a significant role. The samples studied here are different but representative. Their cross-sections are depicted in figure 4.20a-d, while table 4.1 lists their layout properties as well as the parameters describing their critical surface and $n(B,T)$ dependence.

The design of a superconductor is, amongst other considerations, a trade-off between thermal stability and the requirement that the filaments should be sufficiently dense to obtain a high J_c (see chapter 2 and §4.1). Sufficient stability requires the incorporation of a high conductivity material in the matrix, such as Cu or Al. On the other hand, as discussed in chapter 2, to obtain a high filament density a high strength matrix material is required, which is usually poorly conducting. Another trade-off arises since high conductivity materials tend to react with MgB_2 while chemically compatible materials are usually relatively poor conductors. The necessity to include poorly conducting materials in the matrix will influence the diffusion of current and heat and thus v_{nz} and MQE. In the conductors studied here different strategies are applied to ensure sufficient filament density and to prevent reaction between filament and matrix, while providing at the same time thermal stability. Consequently the conductors will react differently to thermal instabilities. In order to obtain a high densification, the filaments of sample CLM are embedded in a hard, but compared to Cu poorly conducting, Ni matrix. The Ni matrix, together with the Fe, also serves as a reaction barrier between the filaments and the Cu stabiliser that is placed at the center of the sample. Thus, in conductor CLM filament densification and stability are provided by using multiple materials in the matrix. In contrast, in sample FZK, both filament densification and stability are provided by the relatively poorly conducting, but high strength, CuNi18Zn20 alloy. Reaction between Cu and MgB_2 is prevented by a Nb reaction barrier. Similarly to tape CLM in the HTR wires filament densification and stability are provided by using different materials in the matrix. In HTR1 the high conductivity Cu directly surrounds the filaments (with a Nb reaction barrier in-between) to provide stability, while sufficient filament density is attained by using a Monel (Cu-Ni) outer tube. The same strategy is applied in sample HTR2, but in this case the Monel outer tube is replaced by Glidcop, which is a dispersion strengthened Cu [216]. This material has significant advantages over Cu alloys, since Cu is strengthened by Al_2O_3 particles rather than alloyed with other metals. The inter-particle distance is large enough to preserve largely the high conductivity of the Cu.

The variety of layouts allows to study the predictive value of the 1D model. For example, in §4.2 the limits of the 1D model were discussed by comparing the radial diffusion with the longitudinal diffusion (v_{nz}) of current and heat. Radial diffusion can be relatively slow if the filaments are thick compared to the matrix or if they are surrounded by a relatively thick diffusion barrier, since the resistivity of

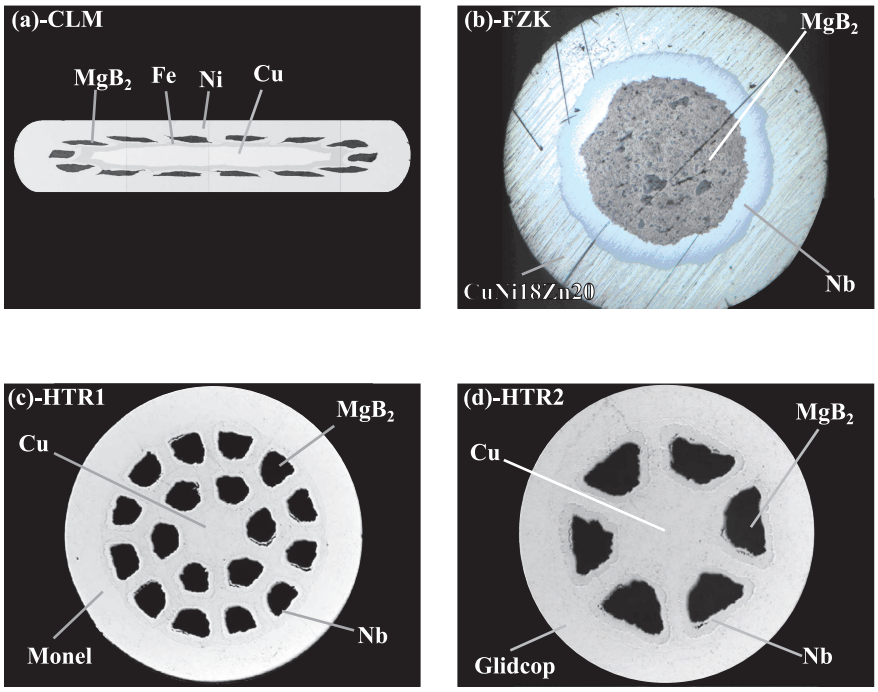

Figure 4.20: Cross-sections of the investigated conductors. (a) sample CLM, a 14-filaments ex-situ tape by Columbus Superconductors (Genova, Italy). (b) sample FZK, a monofilament in-situ wire by Forschungzentrum Karlsruhe (Karlsruhe, Germany). (c) sample HTR1, an 18-filaments in-situ wire by Hypertech Research (Columbus, Ohio, USA). (d) sample HTR2, a 6-filaments in-situ wire also fabricated by Hypertech Research. Details on dimensions and compositional layout of the conductors are given in table 4.1.

barrier materials is typically relatively high. This will lead to an inhomogeneous distribution of the current and temperature in the cross-section of the sample. The samples CLM and HTR1 form two extremes. Sample HTR1 has a relatively straightforward layout, with finely distributed filaments. Thus current and heat are distributed relatively fast and homogeneous over the cross-section. In this case the 1D model can be expected to describe v_{nz} and MQE relatively good. On the other hand, sample CLM has from a diffusion point of view a more "complicated" layout. Although it also has relatively small filaments, its tape form and the fact that the filaments are cooled only from one side by the Cu stabiliser leads to asymmetric current and heat distributions, so that deviations between the 1D model and the measurements are expected to be larger. Similarly, sample FZK has a single, relatively thick, filament. Since cooling occurs through CuNi18Zn20, rather than copper, this will lead to a relatively slow radial diffusion.

Table 4.1: Overview of the samples with their layout properties, parameters describing their critical surface and parameters describing $n(B,T)$.

		CLM	FZK	HTR1	HTR2
Shape		Tape	Wire	Wire	Wire
Powder		Ex-situ	In-situ	In-situ	In-situ
d	[mm]	-	0.9	0.83	0.83
w	[mm]	0.7	-	-	-
h	[mm]	3.6	-	-	-
A	[mm^2]	2.5	0.6	0.5	0.5
f	[%]	9	26	17	16
Matrix		Ni/Cu/Fe	Nb/CuNiZn	Nb/Cu/Monel	Nb/Cu/GC[a]
f_i	[%]	67/14/10	19/55	19/22/41	18/28/39
# Filaments		14	1	18	6
$T_{c,0}$	[K]	38	35	40	40
$J_{c,0}$	[A/mm^2]	$1.3{\cdot}10^3$	$0.9{\cdot}10^3$	$21.7{\cdot}10^3$	$5.0{\cdot}10^3$
$B_{p,0}$	[T]	1.4	1.9	1.4	2.2
n_0		40	67	34	97
$B_{n,0}$	[T]	8.3	3.4	5.5	3.1

[a] GC stands for Glidcop.

Finally, the samples differ significantly in critical current density and n-value, which leads to a quantitatively different heat generation process during a thermal instability (see §4.3.2).

4.5 Results

The results of the MQE and v_{nz} experiments are presented together with the parallel-paths model calculations.

In §4.5.1 the MQE and v_{nz} behavior of the conductors under study at varying transport current, baseline temperature and magnetic field are compared. It shows how the different matrix materials and cross-sectional layouts result in a different response to a thermal disturbance.

In order to demonstrate the predictive value of the parallel-paths model, the experimental MQE and v_{nz} data are compared with the model calculations in §4.5.2. In this paragraph also the limits of the 1-dimensional model are analysed and it is shown how uncertainties in the relevant parameters such as c, κ and ρ can lead to discrepancies between measurements and model.

Since the matrix materials in MgB_2 conductors vary widely (from highly conducting Cu matrices to poorly conducting Fe matrices) and also their n-values can vary significantly, the parallel-paths model is used to investigate the influence

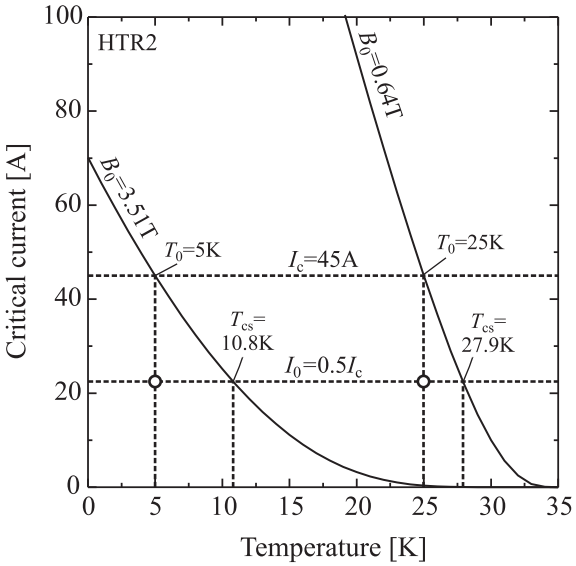

Figure 4.21: $I_c(T)$ lines of sample HTR2 according to equation (3.1) at B_0 =3.51 T and B_0 =0.64 T. The critical current for both cases is set to I_c =45 A so that the (B_0, T_0) settings are (3.51 T, 5 K) and (0.64 T, 25 K). In this example sample HTR2 operates at $I_0 = 0.5I_c$ and the operating points (I_0,B_0,T_0) are indicated by the **open circles**.

of these parameters on the response of a thermal disturbance of a hypothetical conductor. In this analysis, not only the variation of MQE and v_{nz} are calculated but also the time evolution of the hot spot temperature since its time evolution will decide whether a given conductor will burn out.

As mentioned in §4.4.1, the quench heater used in this study has a rather limited efficiency of about 20 %, which will be derived in §4.5.2. Throughout this paragraph, the "corrected" value of the measured MQE will be used unless stated otherwise.

4.5.1 Temperature- and Field Dependence

The measurement procedure as presented in §4.4.5 is used. In order to compare MQE and v_{nz} of samples CLM, FZK, HTR1 and HTR2 (see table 4.1) under similar conditions, the critical current of all conductors is kept constant at 45 A. Thus, to study the behaviour of the conductors at elevated temperatures, the baseline temperature is increased from 5 to 25 K whilst the magnetic field is reduced in such a way that I_c remains constant. To illustrate this, figure 4.21 shows two $I_c(T)$ lines at $B_0 = 3.51$ T and 0.64 T of sample HTR2. These magnetic field values are chosen so that I_c remains constant at 45 A at $T_0 = 5$ K and 25 K.

Minimum Quench Energy

The minimum quench energy as a function of transport current at different (B_0,T_0) settings of samples CLM, HTR1 and HTR2 are displayed in figures 4.22a, c and e.

As a first observation, the minimum quench energies range from ~ 2 to 250 mJ, which is a factor ~ 1000 times higher than typical values measured in low-T_c conductors [214]. These differences are mainly caused by the fact that temperature margins are generally larger than in low-T_c conductors.

Considering the temperature dependence of MQE in more detail, figures 4.22(b), (d) and (f) show a clear non-monotonic behaviour. Since not just the temperature, but also the field B_0 is varied, all four parameters (κ, ρ, c and temperature margin) in equations (4.12) and (4.13) are affected. With reference to the lumped material properties presented in appendix B, the following can be observed:

1. The volumetric heat capacity c increases by approximately two orders of magnitude when the temperature is increased from 5 to 25 K.

2. κ increases by a factor 3 to 10, depending on the sample, when temperature is increased from 5 to 25 K. Furthermore, due to the inclusion of pure Cu in samples CLM, HTR1 and HTR2, the lumped κ-value depends on magnetic field and increases a factor 2 when B_0 is reduced from 5 to 0 T. Sample FZK, on the other hand, only contains "dirty" materials (materials with a low mean free paths for electron transport) and therefore κ is not affected by a changing magnetic field.

3. In contrast to the thermal conductivity, ρ is virtually temperature independent in the range from 5 to 25 K. However, since samples CLM, HTR1 and HTR2 contain pure Cu, their electrical resistivity depends on B_0 and decreases a factor of 2 when B_0 is reduced from 5 to 0 T.

4. Increasing the temperature T_0 whilst decreasing B_0 to keep I_c constant results in steeper $\partial I_c/\partial T|_{B=B_0}$ curves (figure 4.21) and therefore smaller temperature margins (equation (4.25)). Using for instance Dresner's assumption (see §4.3.3) that heat generation starts at $T_s = \frac{1}{2}(T_{cs} + T_c)$, the temperature margin typically reduces by a factor of ~ 2 between 5 and 25 K.

It is now possible to gauge the influence of the various temperature dependencies on the measured temperature dependence of MQE. As discussed in §4.3.1, the value of MQE can be estimated analytically with:

$$l_{\mathrm{MPZ}} = \left\{ \frac{2\kappa_m (T_c - T_0)}{J_m^2 \rho_m} \right\}^{1/2} \quad \text{and} \tag{4.12}$$

$$\mathrm{MQE} = A \int_{l_{\mathrm{MPZ}}} \int_{T_0}^{T_c} c(T) \mathrm{d}T \mathrm{d}z. \tag{4.13}$$

ρ and κ enter the expression for l_{MPZ} only as a square root. The temperature margin also appears in this square-root expression, but furthermore influences

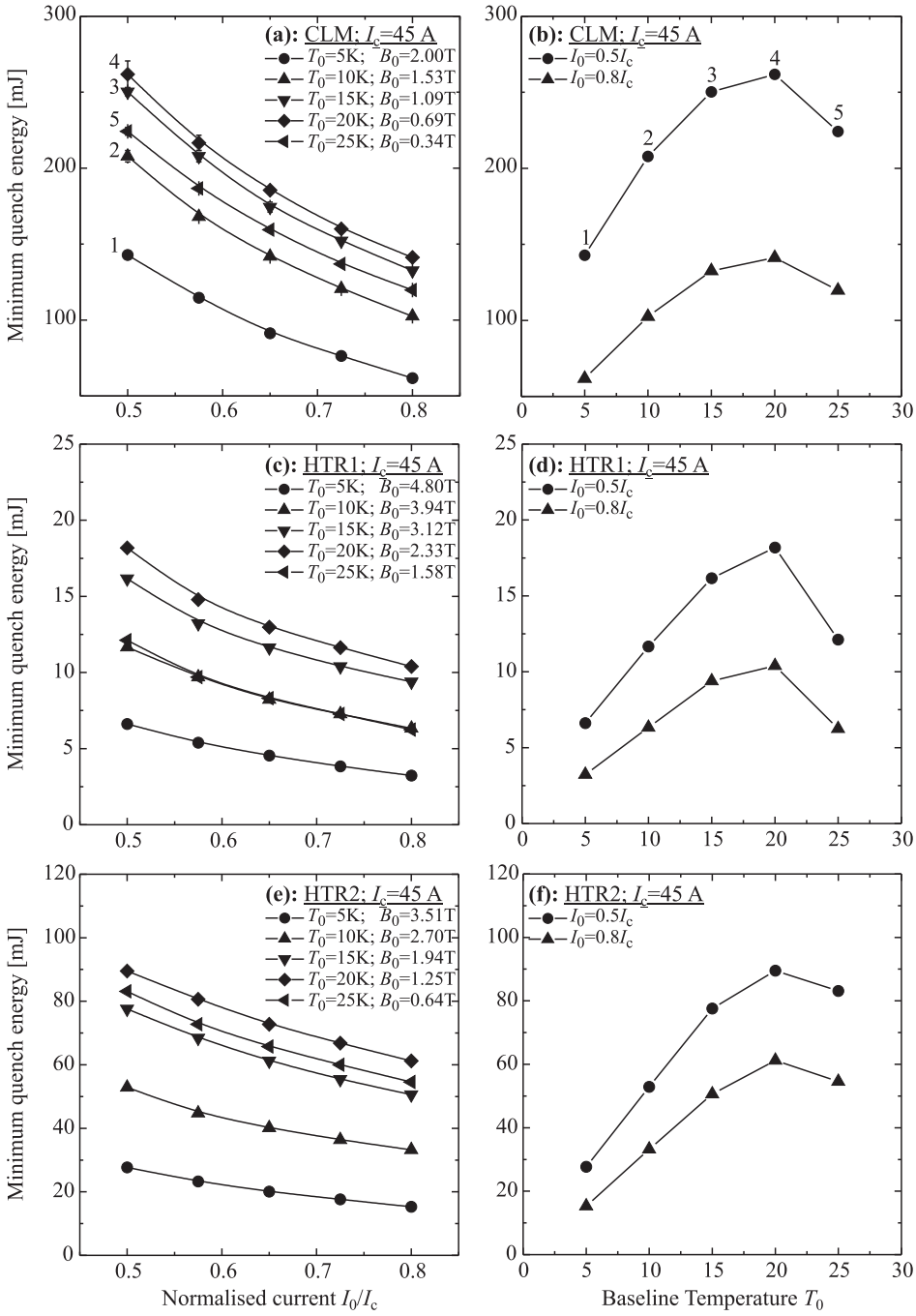

Figure 4.22: (a), (c) and (e) show MQE measurements of samples CLM, HTR1 and HTR2 as a function of the normalised current at an I_c of 45 A and at different temperature- and field combinations. (b), (d) and (f) show the same data, this time plotted as a function of the baseline temperature T_0 at $I_0 = 0.5I_c$ and $I_0 = 0.8I_c$. Note that with changing T_0 also B_0 changes. The **solid lines** are a guide to the eye.

the value of MQE through the integration boundaries in (4.13). The volumetric heat capacity c enters (4.13) directly. From this, it is clear that the temperature dependence of MQE will be determined mainly by the balance between the decreasing temperature margin and the strongly increasing heat capacity.

Between 5 K and 20 K, it turns out to be the latter effect that is dominant in all 3 conductors and MQE is an increasing function of temperature. Above 20 K, on the other hand, it is the decreasing temperature margin that dominates and in all 3 samples MQE decreases again going from $T_0 = 20$ K to 25 K (figures 4.22b, d, f).

Comparing the individual conductors shows that sample CLM is the most stable conductor with MQE values ranging from 100 to 300 mJ, which is 3 to 10 times higher than MQE in samples HTR1 and HTR2. Similar values for the same conductor have also been measured and calculated by other authors [211,215,217], although under different operating conditions. The high MQE values are mainly caused by the relatively small filling factor of this conductor ($\sim$ 9 %), which causes the overall current density to be relatively small ($J_e \sim 20$ A/mm^2 at an I_c of 45 A) and thus significantly reduces Ohmic heat generation.

Samples HTR1 and HTR2 only differ in matrix materials, while their filling factor is approximately the same. The matrix of sample HTR1 contains the relatively poor conductor Monel, which is replaced by the relatively highly conducting Glidcop in sample HTR2. The effect of this replacement is reflected in MQE values that are a factor ~ 5 higher than in sample HTR1. Clearly, using Glidcop significantly enhances MQE, while still providing enough strength for wire deformation.

Normal Zone Propagation Velocity

Figures 4.23a-d show the v_{nz} measurements of samples CLM, FZK, HTR1 and HTR2 as a function of transport current at several (B_0,T_0) settings and a constant critical current of 45 A.

The same reasons that cause MQE values in these MgB_2 conductors to be significantly higher than in low-T_c conductors, also cause the v_{nz} values to be significantly lower. The v_{nz} values fall in the range from 1 to 50 cm/s, compared to 10 to 100 m/s in low-T_c conductors [48, 199, 208, 214]. Just like with MQE, this difference originates mainly from higher temperature margins and also higher c at elevated temperatures. The temperature dependence of v_{nz} is governed by similar considerations. The analytical approximation

$$v_{nz} = \frac{J_m}{c} \left\{ \frac{\rho_m \kappa_m}{(T_c - T_0)} \right\}^{1/2} \tag{4.17}$$

shows that there is a competition between the increasing heat capacity and the decreasing temperature margin. Between 5 K and 20 K, the temperature dependence of c dominates and v_{nz} decreases with temperature. Approaching T_c, however, this balance changes and when the baseline temperature T_0 is increased further from 20 to 25 K, v_{nz} ceases to decrease. Again similarly to MQE, the

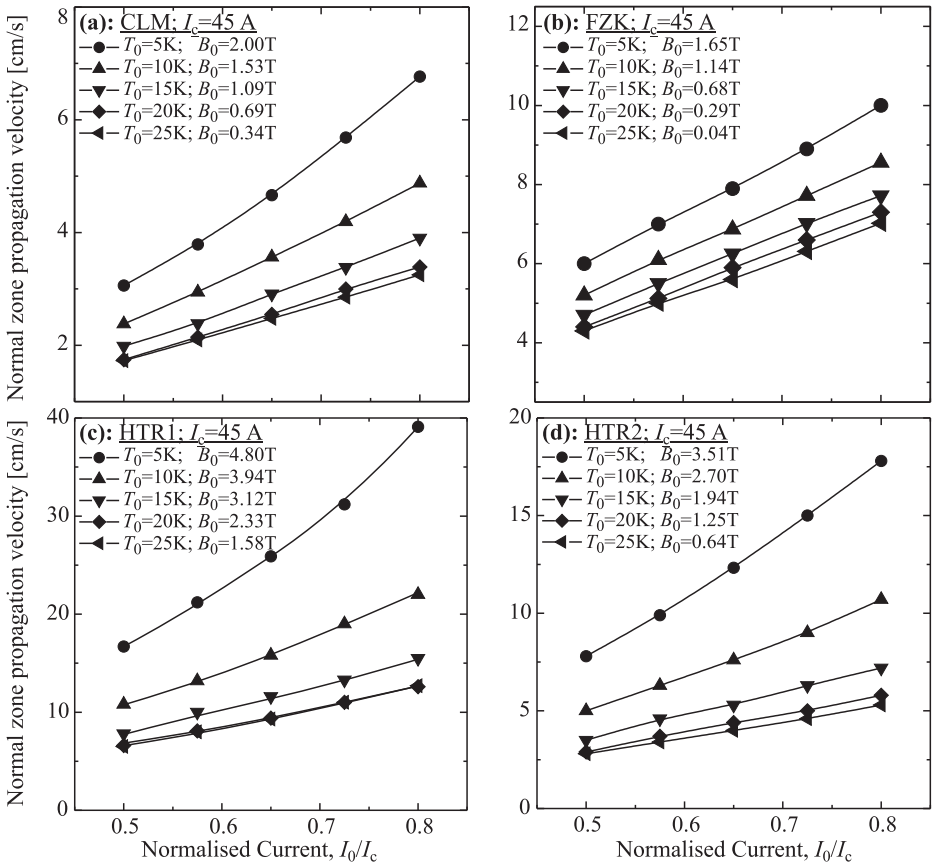

Figure 4.23: $v_{nz}(I_0/I_c)$ measurements at an I_c of 45 A and at different (B_0,T_0) combinations of samples CLM (a); FZK (b); HTR1 (c); and HTR2 (d). The **solid lines** are a guide to the eye.

temperature margin decreases and in this range starts to dominate over the temperature dependence of the heat capacity.

Comparing the four samples, it is clear that sample CLM, which is the most stable one in terms of MQE, also has the lowest v_{nz}. Again, it is the relatively low filling factor of this conductor that results in relatively low current densities and consequently relatively low heat generation. In contrast, sample FZK has a cross-section that is almost a factor 4 lower than of sample CLM, so that v_{nz} can be expected to be significantly higher. The reason that v_{nz} of the two samples are nevertheless rather similar is that even when the lumped resistivity of sample FZK is a factor of 4 higher than that of sample CLM, its lumped thermal conductivity is a factor 40 lower (see figures B.3b and B.2b in appendix B). Equation (4.17) then shows that v_{nz} in sample FZK is suppressed by the poor thermal diffusivity of

the matrix material. Accordingly, since heat remains localised it can be expected that the temperature at the point of disturbance (hot spot temperature) will rise faster than in sample CLM. In §4.5.3 this will be verified with model calculations.

Comparing samples HTR1 and HTR2, it can be seen that their v_{nz} values differ by a factor ~ 2. Clearly, the replacement of Monel with Glidcop reduces v_{nz}, since both current densities as well as temperature margin of the two samples are similar. However, based on the available thermal conductivity and electrical resistivity data of Glidcop this reduction is unexpected. Due to the presence of a pure Cu core in both conductors, the changes in the overall ρ and κ values are limited. The lumped electrical resistivity of sample HTR2 is approximately a factor 3 lower (figure B.3b), while the lumped thermal conductivity is factor of 3 higher (figure B.2) than in sample HTR1 at a temperature $T_s = \frac{1}{2}(T_{cs} + T_c)$. Furthermore, at this temperature the heat capacities of the two conductors are about the same. Equation (4.17) then predicts similar propagation velocities. The discrepancy between analytical prediction and observed data is likely due to the rather high uncertainty in the thermal conductivity and electrical resistivity data of Glidcop. As discussed in appendix B, data of Glidcop is found only for temperatures above 100 K [216] and data below 100 K is extrapolated, which causes significant uncertainties.

4.5.2 Comparing Measurement and Model

In order to demonstrate the predictive value of the parallel-paths model calculations, the experimentally determined MQE- and v_{nz} values are compared with the a-priori model calculations.

It is also shown that for the mono-filamentary conductor FZK the 1-dimensional model is unable to predict v_{nz} and MQE accurately, since this conductor does not fulfill requirement (4.6) and a significant radial temperature gradient occurs across the superconducting core.

Finally, it is shown by how far uncertainties in the material properties influence the model predictions of MQE and v_{nz}.

Normal Zone Propagation Velocity

In figures 4.24a-d, the parallel-paths model calculations for v_{nz} with the measured data of samples CLM, FZK, HTR1 and HTR2 are compared.

For samples CLM, FZK and HTR1 the model results are a-priori calculations, involving no free parameters. Even so, satisfactory agreement between measurements and calculations is generally observed. For sample HTR2 initial attempts to model v_{nz} with extrapolated data proved unsatisfactory (typically deviating ~ 10 %). Therefore κ of this conductor was used as an adjustable parameter. The final thermal conductivity of Glidcop was set to 75 % of that of Cu with an RRR of 100 at 5 T. Compared to the published data of Glidcop above 100 K, this is about 15 % lower.

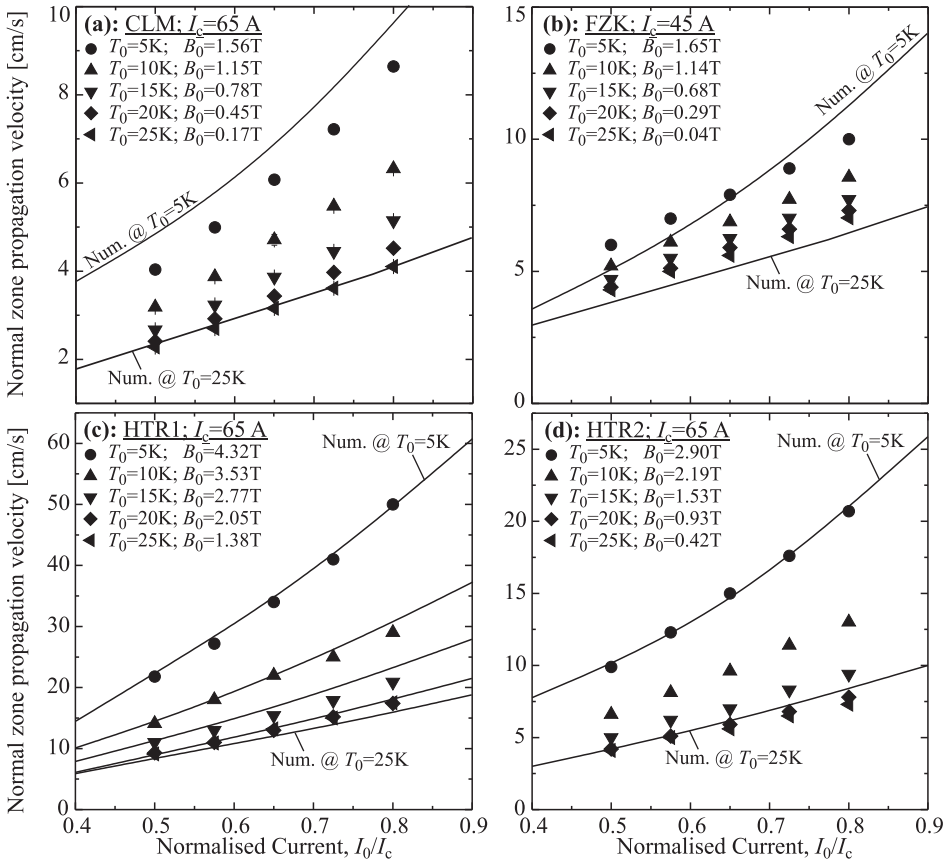

Figure 4.24: Comparison of $v_{nz}(I_0/I_c)$ measurements (**data points**) with parallel-paths model calculations (**solid lines**) at several (B_0,T_0) settings for samples CLM (a); FZK (b); HTR1 (c); and HTR2 (d).

For sample CLM, the measured data at lower temperatures are systematically ~ 10 % lower than the a-priori calculations. This indicates a lower Ohmic heating than expected. As shown in figure 4.20a, sample CLM has a Cu stabiliser in the center of the composite, while the filaments are directly surrounded by the poor conducting Ni and Fe. This relatively complicated lay-out can cause a different distribution of current- and heat fluxes than assumed in the simple 1-dimensional parallel paths approximation.

For the mono-core sample FZK, the measured data at $T_0 = 5$ K shows a different trend than the calculations. As will be shown below, sample FZK does not satisfy requirement (4.6) for 1-dimensional modeling and a temperature gradient is expected to exist within the superconducting core. In this case the 1-dimensional parallel-paths model no longer fully describes the thermal stability. Furthermore,

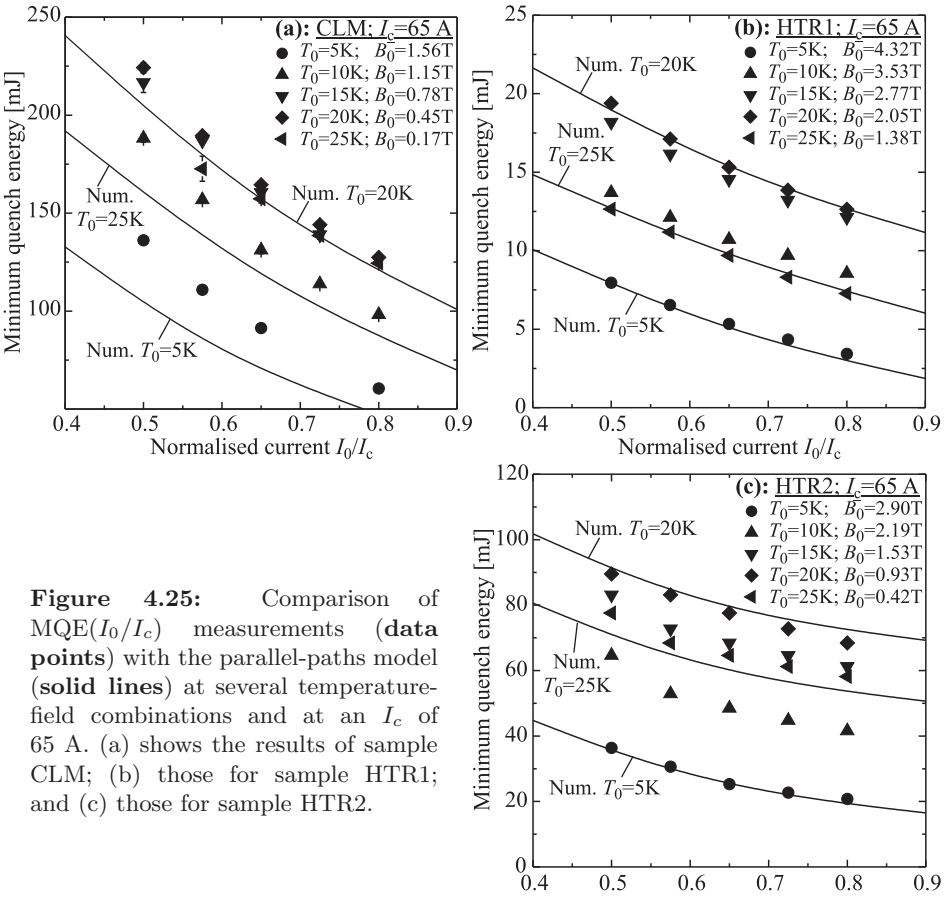

Figure 4.25: Comparison of MQE(I_0/I_c) measurements (**data points**) with the parallel-paths model (**solid lines**) at several temperature-field combinations and at an I_c of 65 A. (a) shows the results of sample CLM; (b) those for sample HTR1; and (c) those for sample HTR2.

in the absence of the relevant material properties of its CuNi18Zn20 matrix, these properties are estimated based on the available data for a CuNi30 alloy.

Minimum Quench Energy

In figures 4.25a-c MQE(I_0/I_c) measurements on samples CLM, HTR1 and HTR2 with the corresponding model calculations at several (B_0,T_0) settings are compared.

As explained in §4.4.1, the quench heater that is used is a relatively simple wire-wound heater. The main uncertainty therefore is the amount of heat that is actually transferred from the heater to the sample: a large amount of heat remains localised in the heater itself since it has a similar enthalpy as the sample. A comparison between measured data and model calculations of MQE can therefore also serve as a determination of the "efficiency" of the quench heater.

For all three conductors the calculated MQE values fall within 20 ± 5 % of

the measured ones. Thus, despite the uncertainties caused by the mounting of the quench heater (how tight the heater wire is wound and the amount of GE varnish used), the efficiency of the heat transfer from quench heater to sample is relatively constant.

Taking into account this 20 % efficiency, it follows from figures 4.25a-c that the calculated and measured results for MQE of sample HTR1 agree within ~ 5 % over the whole measured (I_0,B_0,T_0) range.

The calculated MQE results for sample CLM tend to be systematically lower than the measured data. Not only may this be caused by the uncertainty in the heat transfer from quench heater to sample but, just as with the v_{nz} calculations, it is also possible that the heat flux- and current distribution in the relative complex cross-section are not fully described by a simple 1-dimensional model.

In contrast to samples CLM and HTR1, the numerical results of HTR2 are not based on a-priori calculations, but are generated by fitting the calculated- to measured v_{nz}, using κ of Glidcop as a fitting parameter. Nevertheless, when this fitted κ is used together with the 20 ± 5 % efficiency of the heater this leads to satisfactory agreement between measured- and calculated MQE values over the measured (I_0,B_0,T_0) range.

Validity of the 1D Model

In §4.2.2 it was discussed that for 1-dimensional modeling to be accurate (assuming lumped values for the composite volumetric heat capacity, thermal conductivity and electrical resistivity) the thermal diffusion time of the filaments ($\tau_{T,f}$) must be smaller than the magnetic diffusion time of the whole composite ($\tau_{m,c}$), see equation (4.6). If this is not the case, significant radial temperature gradients occur across the filaments so that J_c and heat generation become radially inhomogeneous. Assuming round filaments- and conductors, this requirement was written as:

$$\eta(T,B) = \left(\frac{R_f}{R_c}\right)^2 \left(\frac{D_{m,c}(T,B)}{D_{T,f}(T,B)}\right) < 1, \tag{4.11}$$

with $\eta(T,B)$ a temperature- and field dependent factor. The T and B dependence originates from the fact that c, κ and ρ all depend on temperature and field.

Figure 4.26 shows the factor η as a function of temperature for the four samples. The relevant material properties of sample FZK are field independent, while the presence of high-purity Cu in samples CLM, HTR1 and HTR2 causes a significant field dependence of η. As a worst case, the plotted values of η for these samples are taken at 5 T, which is outside the field-range that is applied to the samples. For the magnetic diffusivity, the lumped electrical resistivity is taken with the MgB_2 filaments in the normal state.

Clearly, sample FZK does not fulfill the requirement for 1-dimensional modeling, mainly due to the poor electrical- and thermal conductivity of its matrix material. It should be noted, however, that the deviation between measurements

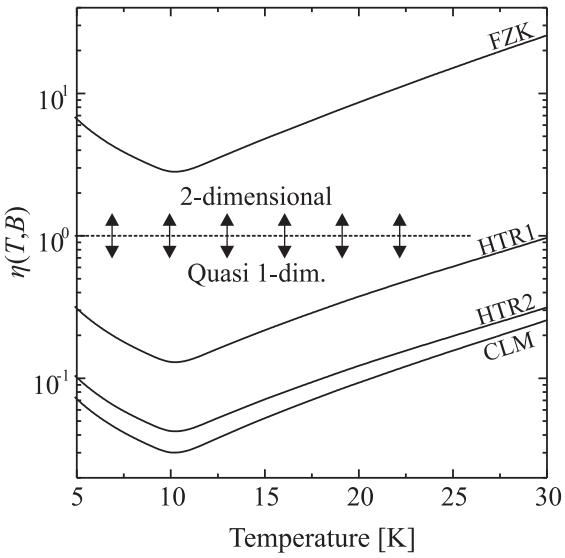

Figure 4.26: Temperature dependence of requirement (4.11) for 1D approximation of MQE and v_{nz} for the four samples. Data of samples CLM, HTR1 and HTR2 are taken at $B_0 = 5$ T.

and model calculations is still rather small (see figure 4.24d), especially considering the uncertainties in the relevant material properties of its CuNi18Zn20 matrix.

The figure also shows that sample CLM does fulfill requirement (4.11), despite the fact that the comparison between measurements and model calculations show some discrepancy (figures 4.24a and 4.25a). As argued above, the deviations might well be due to the relatively complex cross-section and corresponding current- and heat flux distribution in this conductor. The magnetic diffusivity $D_{m,c}$ in requirement (4.11) accounts for the lumped ρ of the whole composite, while it is not excluded that electrical field gradients occur across the sample. To verify such a scenario, a 2 or 3-dimensional model [217] needs to be used to simulate these MQE and v_{nz} measurements.

Uncertainties in Materials Properties

The main uncertainties originate in the unknown thermal conductivity and electrical resistivity of some matrix materials. In this paragraph, the influence of uncertainties in the lumped volumetric heat capacity c, in the matrix thermal conductivity κ_m and in the matrix electrical resistivity ρ_m on the calculated MQE and v_{nz} values are compared. As an example, model calculations of sample HTR1, which show a good agreement with the measurements, are used to study the effects. Figures 4.27a and b show how the predictions for MQE and v_{nz} change

when c, κ and ρ of the matrix are estimated 20 % too high with respect to the literature values.

When MQE is calculated with values for c that are estimated too high, the calculated value of MQE is also $\sim$ 20 % higher than measured. This can be expected, since in such a case 20 % more heat is needed to bring the temperature of a length l_{MPZ} of the conductor above T_c (equation (4.13)). When κ_m is estimated 20 % too high, the longitudinal cooling at both ends of the normal zone is overestimated. This results in a $\sim$ 9 % overestimation of MQE. For a 20 % higher ρ_m, the heat generation is overestimated, resulting in a 9 % underestimation of MQE. Using the analytical approximations (4.12) and (4.13) the influence of the uncertainty in c, κ_m and ρ_m can also be deduced analytically:

$$\frac{\Delta\mathrm{MQE}}{\mathrm{MQE}} = \frac{\Delta c}{c} + \frac{\Delta\kappa_m}{2\kappa_m} - \frac{\Delta\rho_m}{2\rho_m}\,, \tag{4.28}$$

with ΔMQE, Δc, $\Delta\kappa_m$ and $\Delta\rho_m$ the absolute uncertainty of the corresponding parameters. Using the 20 % overestimated properties in (4.28), it can be seen that this equation describes the influence on the model calculations rather well, despite the fact that it neglects the detailed heating function.

Uncertainties of 20 % in the thermal conductivity and electrical resistivity of MgB_2 (rather than the matrix resistivity ρ_m) have in this example only a negligible influence on MQE, mainly because of the relatively low fill factor and the presence of highly-conducting Cu in the matrix.

A calculation of v_{nz} with a c-value that is 20 % too high leads to a 15 % underestimation of v_{nz}, which is expected since c directly influences the diffusion of heat. In contrast, the overestimation of κ leads to an expected diffusivity that is too high and v_{nz} is overestimated by $\sim$ 9 %. As expected from equation (4.17) a similar effect occurs when the matrix resistivity ρ_m is estimated too high, also leading to a $\sim$ 9 % overestimation of v_{nz}. Using the analytical expression for v_{nz} (4.17), the influence of uncertainty in the material properties becomes:

$$\frac{\Delta v_{nz}}{v_{nz}} = -\frac{\Delta c}{c} + \frac{\Delta\kappa_m}{2\kappa_m} + \frac{\Delta\rho_m}{2\rho_m}\,, \tag{4.29}$$

with Δv_{nz} the absolute uncertainty of v_{nz}. Similar as with equation (4.28), the observed uncertainty is described rather well with (4.29).

For similar reasons as with MQE, an uncertainty in the thermal conductivity and electrical resistivity of MgB_2 has, for this specific conductor, negligible influence on v_{nz}.

A further factor introducing uncertainty is the lateral heat leak from the conductor to the sample-holder during the experiments, which can lead to a higher MQE and lower v_{nz} than one would expect from an ideal adiabatic case. As discussed in §4.4.3 and in appendix C, the thermal resistance from sample to the sample-holder is relatively low ($R_{t,\mathrm{h}} \approx 1000$ K/W), compared to the longitudinal thermal resistance of the sample itself ($R_{t,12} \approx 2750$ K/W). Figures 4.27a and b show also how this lateral heat leak influences MQE and v_{nz}.

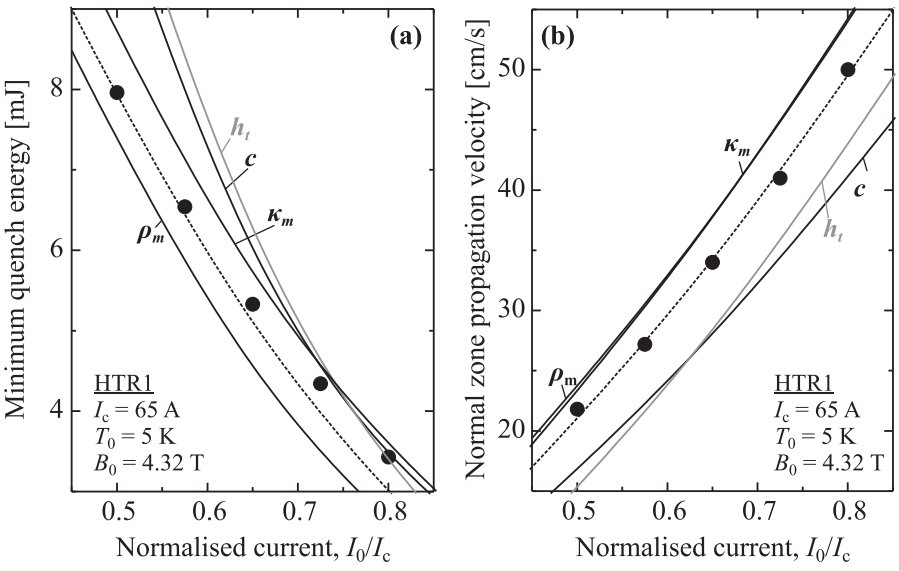

Figure 4.27: Calculated influence on MQE (a) and v_{nz} (b) of estimating the volumetric heat capacity c, thermal conductivity of the matrix κ_m and electrical resistivity of the matrix ρ_m 20 % too high. Also shown is the influence of a lateral heat leak from sample to sample-holder with a heat transfer coefficient h_t of 40 W/m^{2}K (**curves labeled as "h_t"**). The **dashed lines** are the simulations as presented in figures 4.24c and 4.25b. The **data points** show the measured MQE and v_{nz}.

The assumed heat transfer coefficient is $h_t = 40$ W/m^{2}K, which leads to a 17 % increase in MQE and a 18 % reduction of v_{nz} compared to the adiabatic situation. It should be noted, however, that the measured thermal resistance between sample and sample-holder of $R_{t,\mathrm{h}} \approx 1000$ K/W corresponds to a heat transfer coefficient of only $h_t = 2$ W/m^{2}K, so that the actual experimentally realised differences with the MQE and v_{nz} in the ideal adiabatic case are negligible.

4.5.3 Influence of Matrix Material and n-value

Having established the reliability of the 1-dimensional numerical model by directly comparing it to the experimental results, the model can now be used to study the influence of various parameters on the stability in an explicit way, i.e. varying only one parameter while keeping all others constant.

Clearly, the choice of matrix material significantly influences the conductor's response to a thermal disturbance, with highly conducting materials significantly enhancing thermal stability in terms of MQE. In the experimental results presented above however, direct comparison between different matrix materials is some-

what complicated, since the matrix materials also influence the J_c- and n-value of a conductor. In this paragraph parallel-paths model simulations are presented on an "imaginary" conductor, keeping the $J_c(B,T)$ and $n(B,T)$ performance as well as the filling factor constant but assuming two different matrix materials, namely relatively poorly conductive Fe and highly conducting Cu. For the simulations the $J_c(B,T)$, $n(B,T)$ surfaces and filling factor of sample HTR1 are adopted.

Furthermore, sample HTR1 shows relatively low n-values of ~ 10, which is not uncommon in MgB_2 conductors. However, very high n-values of ~ 100 can also occur [119]. To study the influence of the n-value on both MQE and v_{nz}, two hypothetical samples are modeled, one with a constant n-value of 10 and one with an n-value of 100. Both conductors are assumed to have a matrix and $J_c(B,T)$ surface identical to sample HTR1.

In the experiments temperature and field were set in such a way that the critical currents were relatively low. Experimentally, one of the limiting factors is the intrinsic thermal instability of the samples at currents larger than ~ 100 A, which at low temperature and field results in a reduction of the measured "$I_c(B)$-curve" below the exponential behaviour (3.1). It is assumed that the conductors follow the $J_c(B,T)$ and $n(B,T)$ dependence of equations (3.1) and (4.21) up to higher currents. This idealised hypothetical case allows to study the response to a thermal instability of a MgB_2 conductor at relatively high currents.

Influence of Matrix Conductivity

Figures 4.28a and b show how the replacement of a relatively poorly conducting Fe matrix with a Cu one affects MQE at an applied field of 2 T and $T_0 = 5$ K ($I_c = 381$ A) or $T_0 = 15$ K ($I_c = 148$ A). For both temperatures, replacing Fe with Cu increases MQE by more than an order of magnitude and thus significantly enhances the thermal stability of the conductor.

Note that in the case of the Fe-stabilised conductor, the calculated MQE values are significantly lower than the values measured for sample HTR1 (figure 4.25b), which is caused by the higher current as well as by the lower conductivity of the Fe matrix with respect to the Nb/Cu/Monel matrix of HTR1. Interestingly, the Cu-stabilised conductor has significantly higher MQE values than those measured on sample HTR1, even if the assumed currents are 3 to 6 times higher.

In contrast to MQE, v_{nz} is hardly affected by replacing the Fe matrix with Cu, as shown in figures 4.28c and d. This can be understood from the analytical approximations (4.13) and (4.17), since a decrease in electrical resistivity is combined with an increase in thermal conductivity. As a result, the reduced heat generation ($p_{\mathrm{diss}} = J^2\rho$) is counterbalanced by the increased thermal diffusivity ($D_{T,n} = \kappa/c$), see equation (4.16). Thus, provided that c remains constant (as is roughly the case with Fe and Cu at these temperatures), replacing a poorly conducting matrix material with a highly conducting one does not automatically imply that v_{nz} increases. For MQE on the other hand, the decrease in ρ and the corresponding increase in κ reinforce each other (4.12).

Compared to the v_{nz} measurements on sample HTR1 (figure 4.24b), the cal-

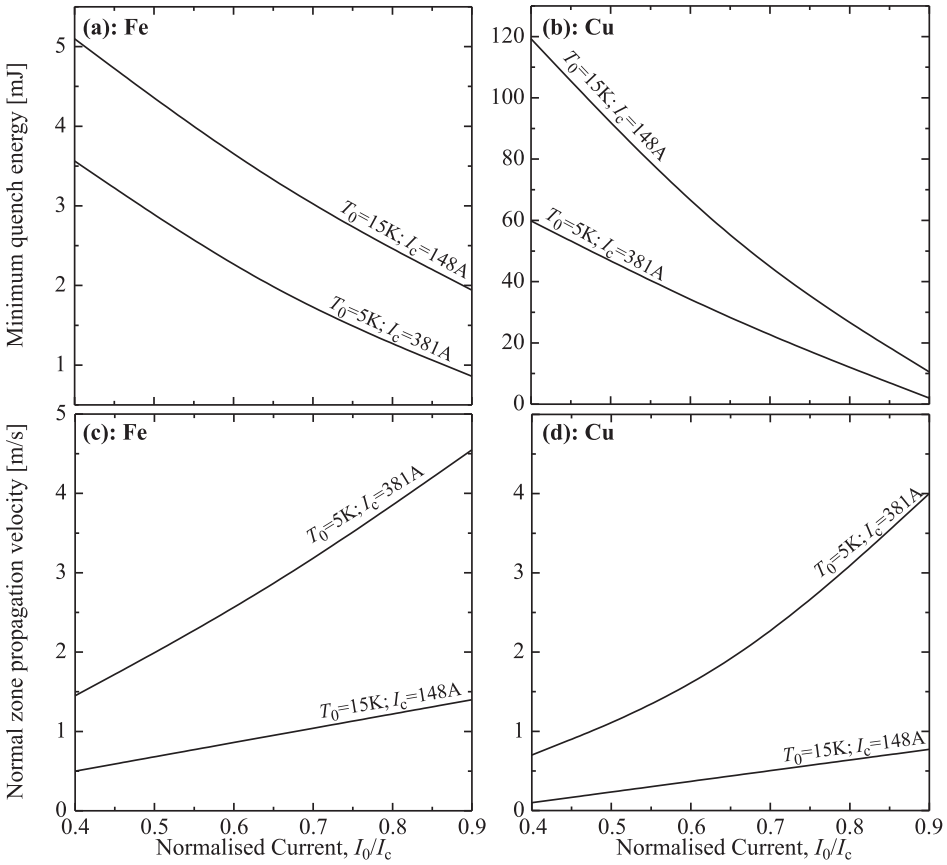

Figure 4.28: Comparison of MQE and v_{nz} for a Fe stabilised MgB_2 conductor ((a) and (c)) and a Cu stabilised MgB_2 conductor ((b) and (d)).

culated v_{nz} values at relatively high current increased to about $\sim$ 1 m/s rather than $\sim$ 10 cm/s. Clearly, a higher current causes a higher heat generation, so that v_{nz} increases.

The fact that v_{nz} in a Fe- or a Cu-stabilised conductor are similar has immediate consequences for the hot spot temperature. Since the propagation velocity remains similar, at any given time the volume in which heat is generated will also be similar, but the amount of heat generated itself will be almost two orders of magnitude higher in the Fe-stabilised conductor than in the Cu stabilised one. The time evolution of the hot spot temperature is presented in figures 4.29a-d.

Note that the time scales of the plots showing the Fe stabilised ((a) and (c)) and the Cu ((b) and (d)) stabilised conductors differ by more than two orders of magnitude. This means that the time lag between a thermal instability and a possible burnout is significantly increased by replacing Fe with Cu.

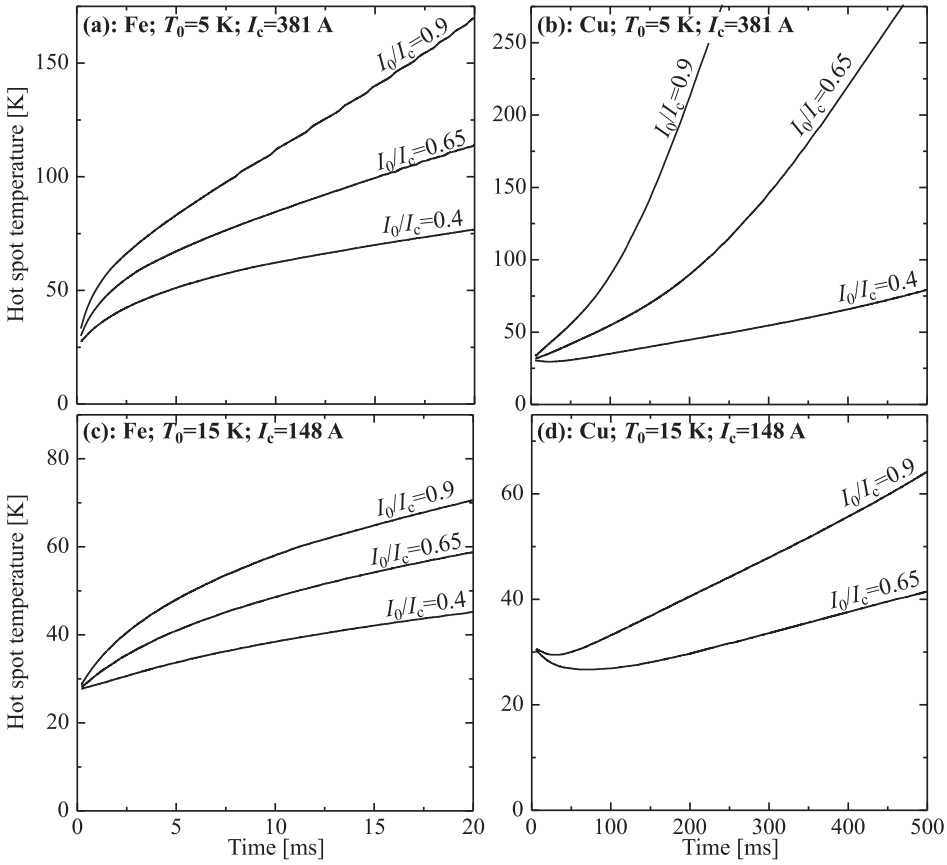

Figure 4.29: Comparison of the time evolution of the hot spot temperature of an Fe stabilised MgB_2 conductor at 5 K and 15 K (a) and (c) and that of a Cu stabilised one (b) and (d). Note the different time scales between Fe and Cu.

When the baseline temperature T_0 is increased from 5 to 15 K, the hot spot temperature increase becomes slower due to the reduced transport current as well as the increased heat capacity.

Influence of the Superconductors' n-value

In figures 4.30a and b it is shown how the n-value influences both MQE and v_{nz}.

Figure 4.8 showed how in conductors with a higher n-value, significant heating starts already at a lower temperature than with a relatively low n-value. Due to the higher heating of the conductor with $n = 100$, the MQE of this conductor is about a factor 2 lower than that of the conductor with $n = 10$ at $T_0 = 5$ K. However its v_{nz} at this temperature is a factor 4 higher. At $T_0 = 15$ K, MQE for the

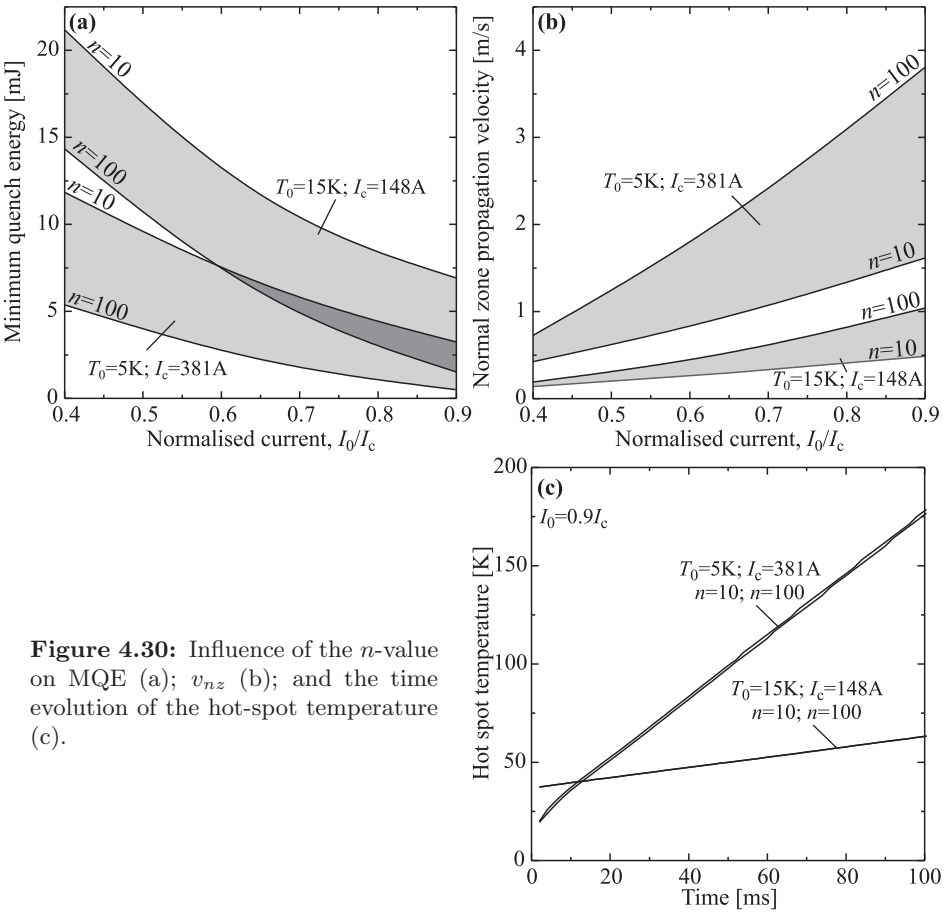

Figure 4.30: Influence of the n-value on MQE (a); v_{nz} (b); and the time evolution of the hot-spot temperature (c).

conductor with $n = 100$ is about 25 % lower, while its v_{nz} is about 2 times higher. Thus, with increasing n-value v_{nz} increases twice as fast than MQE decreases.

Figure 4.30c shows the time evolution of the hot spot temperature for both $n = 10$ and $n = 100$. Clearly, the two n-values result in virtually identical hot spot temperature increase. Indeed, different n-values only have an effect on the heat generation in the region immediately adjacent to the normal-superconducting interface. For larger times, the hot spot is relatively far from this interface and it is the normal state resistivity of the filaments that determines heat generation.

4.6 Conclusion

The influence of material properties and operating temperature on the normal zone behaviour in MgB_2 conductors was studied both experimentally and with a numerical parallel-paths model.

Representing a composite superconductor as electrical parallel-paths between superconducting filaments and normal conducting matrix makes it explicitly clear that the driving force of current diffusion during a thermal instability is the electric field. Moreover, the parallel-paths model accounts for the heat generation in all parts of the composite conductor, including the superconducting filaments.

Compared to analytical approximations and the "classical" current sharing model, this new model leads to a more detailed heating function in which the n-value of the superconductor becomes an important parameter. This is especially relevant for MgB_2 conductors, since their n-values vary widely depending on the fabrication route and operating conditions. In combination with a poorly conducting matrix material, heat generated in the MgB_2 filaments becomes a significant contribution to the overall heat generation.

In order to measure intrinsic MQE and v_{nz} values, a new quasi-adiabatic experimental set-up was developed, which is unique in the sense that three relevant operating parameters, current, magnetic field and temperature can be varied.

MQE measurements on three different MgB_2 conductors yield values ranging between 2 and 300 mJ, which is a factor ~ 1000 higher than typical values observed for low-T_c conductors. This difference is mainly caused by the larger thermal margin of the MgB_2 conductors and indicates that MgB_2 conductors are more stable than low-T_c conductors.

Increasing the baseline temperature (while decreasing the magnetic field to keep I_c constant) reveals a non-monotonic temperature dependence of MQE, due to a competition between increasing heat capacity and decreasing temperature margin. Between 5 and 20 K, all conductors show an increase of MQE with temperature due to the rapid increase of c. Between 20 and 25 K, the reduced thermal margin dominates and MQE starts to decrease in all samples. Thus, MgB_2 conductors tend to be the most stable around 20 K, with MQE values ranging between 20 and 300 mJ.

v_{nz} measurements on four different samples yield values between 1 and 100 cm/s, which is a factor 100 lower than those observed in low-T_c conductors. This indicates that it will be more difficult to detect a normal zone in MgB_2 conductors than in low-T_c conductors. Similar to MQE, this is caused by the larger thermal margin. When the baseline temperature is increased (and B_0 decreased), v_{nz} decreases even further due to the increasing heat capacity, but reaches a minimum at 20 K with typical v_{nz} values of ~ 50 cm/s.

Parallel-paths model calculations of MQE and v_{nz} generally show a good agreement with the measurements. For wires with a poorly conducting matrix or conductors that have a relatively complex lay-out, the 1-dimensional model results deviates somewhat from the measurements. This is likely due to radial thermal- or electric field gradients, so that a 2-dimensional model is expected to yield more accurate predictions.

Uncertainties in the model calculations are mainly caused by the absence of relevant data for some matrix materials. Ideally, the properties of these materials should be measured. This is especially the case for Glidcop, which is an interesting material that shows relatively good stabilising properties (high κ and low ρ) and

is at the same time strong enough for powder densification.

With the 1-dimensional model, the influence of varying matrix properties can be separated from possible variations in $J_c(B,T)$ and $n(B,T)$. It turns out that the matrix conductivity has a strong influence on MQE but hardly changes v_{nz}. A direct consequence of this latter observation is that the temperature in a wire with a relatively poorly conducting matrix will rise much faster than when a high-conductivity material is used. Thus, just like with any other technical superconductor, a highly conducting matrix is not only beneficial for stability but also reduces the risk of conductor burnout

The parallel-paths model predicts also that a high n-value of about 100 results in a higher Ohmic heat generation in the filaments than in a similar conductor with an n-value of about 10. At 15 K, this causes ~ 25 % lower MQE values and a factor ~ 2 higher v_{nz}. However, the time evolution of the hot spot temperature is not affected the n-value since only the normal state resistivity causes heat generation at the centre of the normal zone. Thus at the expense of somewhat reduced stability, the detection of a normal zone becomes easier in conductors with high n-values.

Although MQE and v_{nz} are important factors in the normal zone behaviour of a superconductor, the time evolution of the hot spot temperature is also of significant practical importance. It can be readily studied with parallel-paths calculations, but to verify the calculated hot spot temperature it should also be measured experimentally.

Chapter 5

Mechanical Behaviour

Knowledge of the strain dependence of the critical surface is important for the design of MgB_2-based magnets. The strain dependence of the critical current is studied experimentally and shows two distinct regions. Just like Nb_3Sn, MgB_2 in compressive and moderate tensile strain shows a reversible behaviour and, just like $Bi_2Sr_2Ca_2Cu_3O_x$, above a conductor-dependent reversible strain limit a steep and irreversible degradation of the critical current sets in. The reversible strain limit strongly depends on the degree of pre-compression that the matrix exerts on the filaments. In the reversible regime, the strain dependence of the critical current seems to have an electronic origin since also the critical temperature and the irreversibility field vary with strain. It is shown that the reversible strain dependence of the critical surface can be described with the strain dependence of just three critical parameters: the zero-field, zero-temperature extrapolation of the critical current density, the critical temperature and the zero-temperature extrapolation of the irreversibility field.

5.1 Introduction

Understanding the behaviour of superconductors subjected to mechanical strain is of fundamental as well as technical relevance. Among the first measurements of the behaviour of strained MgB_2 conductors were those by Kitaguchi *et. al.* [218] and by Kováč *et. al.* [219]. A typical result of the critical current dependence on strain is shown in figure 5.1a. At sufficiently low strain the critical current depends linearly and reversibly on strain. Above a certain strain level called the reversible strain limit $\varepsilon_{\mathrm{rev}}$, the critical current degrades steeply and this decrease is irreversible.

Comparing these observations to the well-studied strain dependence of I_c of other technical superconductors, i.e. Nb_3Sn, $Bi_2Sr_2Ca_2Cu_3O_x$ and $YBa_2Cu_3O_x$ (figures 5.1b to d), three remarks can be made: 1) All these materials show a reversible-to-irreversible crossover at a strain level $\varepsilon_{\mathrm{rev}}$. Indeed, they are all brittle materials and at high strain will develop microstructural cracks. In the ceramic $Bi_2Sr_2Ca_2Cu_3O_x$ this was shown indirectly with an ultrasonic fracturing technique [220, 221], or through microscopic investigations of strained tapes [222]. Later, Van Der Laan [223] confirmed this cracking process in both strained $Bi_2Sr_2Ca_2Cu_3O_x$ and $YBa_2Cu_3O_x$ tapes with an in-situ magneto-optical technique (figure 5.1e and f). Similar cracks were observed with electron microscopy in Nb_3Sn conductors subjected to sufficiently high axial strain [224]. 2) just like MgB_2, Nb_3Sn shows a reversible $I_c(\varepsilon)$ dependence below $\varepsilon_{\mathrm{rev}}$, which is believed to have an electronic origin [45,46] and can be described by Ekin's scaling law [42] or later refinements (for an overview of such models see [12]). The strain scaling refinement by Ten Haken [44] is displayed as the solid line in figure 5.1b. In contrast, I_c appears to be virtually strain independent below $\varepsilon_{\mathrm{rev}}$ in $Bi_2Sr_2Ca_2Cu_3O_x$ [225], while in $YBa_2Cu_3O_x$ coated conductors sometimes modest [226,227], but recently also a strong [228] reversible strain dependence is reported. 3) it was shown, e.g. by Passerini *et. al.* [222], that the value of $\varepsilon_{\mathrm{rev}}$ in $Bi_2Sr_2Ca_2Cu_3O_x$ conductors is closely related to the pre-compressive strain that the matrix exerts on the filaments due to differential thermal contraction during cool-down. For Nb_3Sn, on the other hand, the thermal pre-compression is not related to $\varepsilon_{\mathrm{rev}}$, but rather to the position of the peak in the $I_c(\varepsilon)$ curve, while it is believed that microstructural cracks start to occur when the $I_c(\varepsilon)$ data starts to deviate from its scaling [229]. As a further interesting observation, figures 5.1b to d also illustrate how the two ceramic conductors show an abrupt and steep degradation with strain, while the Nb_3Sn conductor merely slowly deviates from its scaling curve.

The strain dependence of the critical current in MgB_2 appears to be between that of Nb_3Sn and that of the ceramic conductors. Like Nb_3Sn, MgB_2 has a clear reversible $I_c(\varepsilon)$ regime, presumably indicating an electronic origin; and, just like the ceramic conductors, it has an abrupt degradation of I_c above $\varepsilon_{\mathrm{rev}}$.

This chapter will focus on two issues: the factors determining the value of $\varepsilon_{\mathrm{rev}}$ will be explored; and the reversible $I_c(\varepsilon)$ regime will be mapped out in detail, leading to a scaling law for this regime. In §5.2, the experimental techniques to apply axial strain to a conductor and measure the critical parameters are discussed

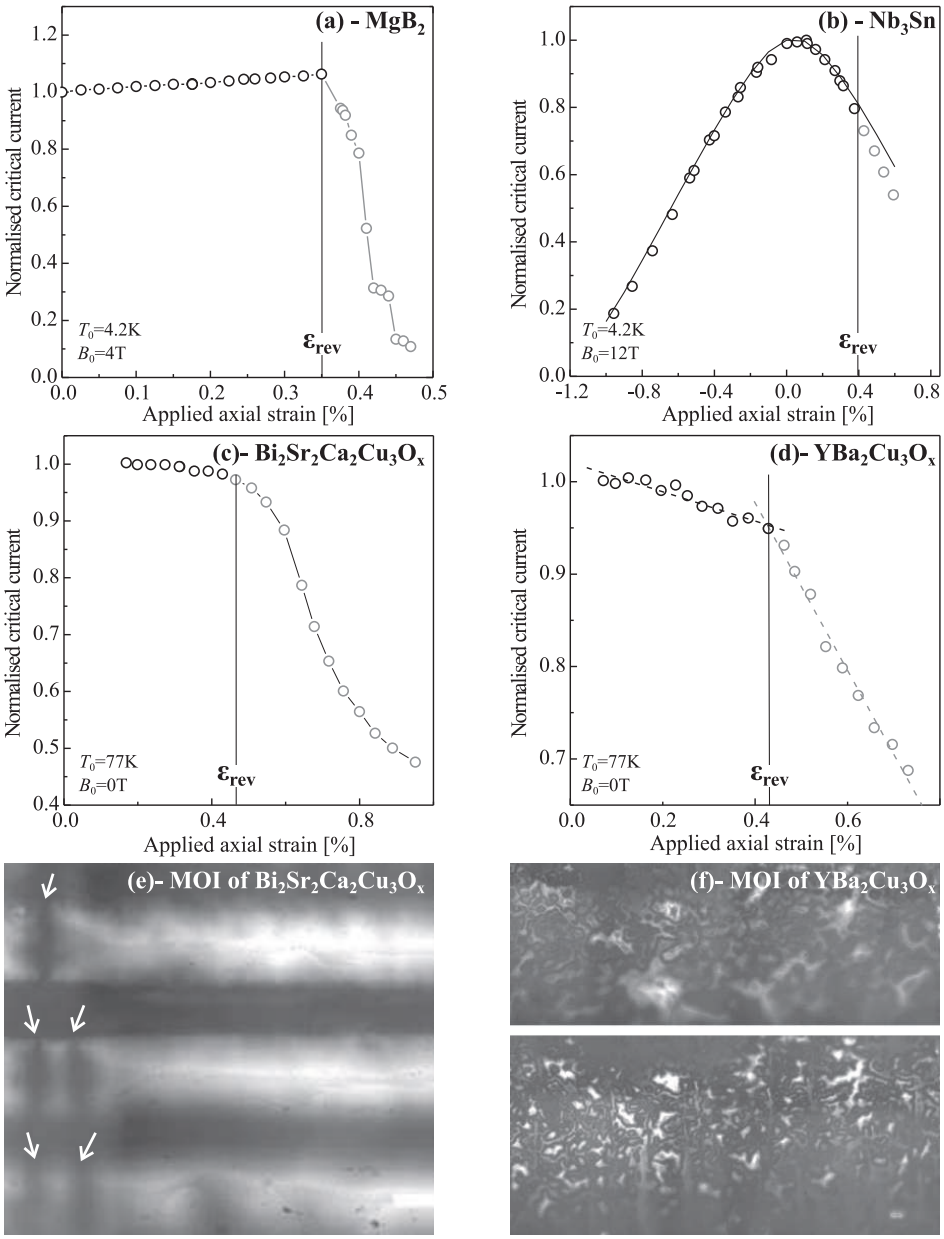

Figure 5.1: Comparison between the strain response of the critical current in MgB_2 (a), Nb_3Sn (b), $Bi_2Sr_2Ca_2Cu_3O_x$ (c) and $YBa_2Cu_3O_x$ (d), after [49,219,223]. The solid line in (b) is calculated with a scaling relation for the $I_c(\varepsilon)$ data. All the conductors display irreversible behaviour when a composite-dependent reversible strain limit $\varepsilon_{\rm rev}$ is exceeded. The figures at the bottom are magneto optical images (MOI): (e) reveals cracks in strained $Bi_2Sr_2Ca_2Cu_3O_x$ filaments on the left part of the image, indicated by the arrows. The upper image of (f) shows an unstrained $YBa_2Cu_3O_x$ coated conductor and the bottom image shows a strained sample in which cracks occur. Both MO images are adapted from [223].

and the samples selected for this study are described. §5.3 presents in detail the strain dependence of the critical current. Here the origin of the reversible strain limit is investigated and a general scaling of the reversible strain regime is introduced. Next the strain dependence of the critical temperature T_c and the irreversibility field B^* are described in §5.4 and §5.5 respectively. Combining the strain dependence of the critical current, the critical temperature and the irreversibility field, a scaling relation of the reversible strain response of the entire critical surface is developed in §5.6.

5.2 Experiment

As indicated above, the strain dependence of the critical parameters of MgB_2 conductors can have either a microstructural or an electronic origin. In order to study this, strain has to be applied to a MgB_2 conductor both in the compressive and tensile regime. Moreover, tensile stress needs to be high enough to be able to reach the reversible strain limit. In §5.2.1 several techniques are discussed that are used to apply strain to superconductors and to measure the critical parameters as a function of strain. It concludes with the U-shaped bending spring set-up used in this study.

It is explained in §5.2.2 how with this U-spring experiment incomplete current transfer to the MgB_2 filaments can lead to an anomalous ohmic contribution in the voltage-current characteristic. A procedure to obtain the correct value of critical current and n-value is introduced.

In §5.2.3 the procedure is described to extract the variation of the critical temperature T_c and the irreversibility field B^* data with strain from the resistive transition as function of temperature and magnetic field respectively.

Lastly, the critical parameters may depend on the geometry and precursor powder of the conductor (i.e. tape/wire, matrix material, number of filaments). Therefore, several conductors have been selected to study the strain behaviour of the critical parameters. §5.2.4 describes the samples and the properties that are investigated.

5.2.1 Experimental Set-Up

Several experimental methods to characterise the strain response of superconductors can be employed. In the first and most straightforward technique, the sample is clamped at both ends and an axial pulling force is applied (see for example [42]). The main advantages of this method are that it does not require a special sample shape, that the stress needed to reach a given strain level in the sample can be measured directly and that the experiment introduces no extra thermal pre-strain in the conductor. However, the sample can only be strained in tension and not in compression, limiting the experimental strain window considerably. A second type of device is the so called Walter's spring. A sample is mounted on a spiraled substrate and is subjected to axial strain by applying a torsion force to the sub-

strate [230]. The main advantage of this probe is the relatively long sample length (~ 1 m), which enables measurements at low electric field to be performed relatively easy. By soldering the sample over its full length on the substrate, it can easily be brought into the compressive strain regime. Moreover, the temperature can be varied by positioning the sample in a flow cryostat or a vacuum can. A drawback of this method is its complex mechanical structure, causing sample preparation and temperature regulation to be relatively difficult. The temperature response is relatively slow so that care has to be taken to avoid thermal runaways. Consequently, at elevated temperatures the maximum current that can be applied to the sample is limited [12]. To overcome this problem Godeke [49] recently developed a probe that has the same functionality as the Walter's spring, but with a structure that is "simplified" by reducing the amount of turns to one, limiting the sample length to ≈ 10 cm. Due to its shape, this device is referred to as the "Pacman". The simplified mechanical structure of the Pacman, in comparison with the Walter's spring, allows a relatively fast temperature regulation so that the risk of thermal runaways is limited. Both the Walter's spring and the Pacman device require the sample to be heat treated in a specific shape to avoid initial straining (bending) of the sample during mounting of the experiment.

To avoid this complication, in this study a fourth method is used based on a straight beam section as part of a U-shaped bending spring [44, 231, 232]. This probe has been used for over a decade at the University of Twente. The major advantages are the simple sample layout, the relative ease with which the sample can be compressed, and the ease of temperature regulation. A disadvantage is the fact that the maximum length of the sample is limited by the bore of the magnet. The typical sample length of ≈ 4 cm so that current entrance can have a significant influence, depending on the matrix material of the studied sample. Moreover, due to the limited sample length the electric field resolution is low compared to the Walters' spring or the Pacman-device. Nevertheless, this device is used for its fast temperature regulation (thermal response time ~ 1 s), which is especially important for characterising MgB_2 conductors as typical temperatures are relatively high (up to 50 K).

A schematic overview of the U-shaped bending spring and its components is depicted in figure 5.2. The device is made of Ti-6Al-4V, which allows to apply high strain levels due to its high elastic strain limit of about 1.2 % [12]. Moreover, this material introduces a small thermal pre-compression of -0.05 % to typical MgB_2 samples [219]. The sample is mounted by soldering it over its full length onto a copper buffer layer on top of the straight beam section of the device. In this way, the sample can be brought into the compressive regime without buckling. Force is applied to the legs of the U-spring by an H-shaped lever system, which legs are adjusted by a left- and right threaded rod and wormgear. This bends the straight beam section of the U-spring so that the sample is axially strained in the compressive or in the tensile regime, depending on the direction of the rotation. In order to measure a superconducting transition (i.e. voltage-current for I_c, voltage-temperature for T_c or voltage-field for B_{c2}), a pair of voltage taps are soldered to the sample, approximately 10 mm apart. To monitor the strain state of

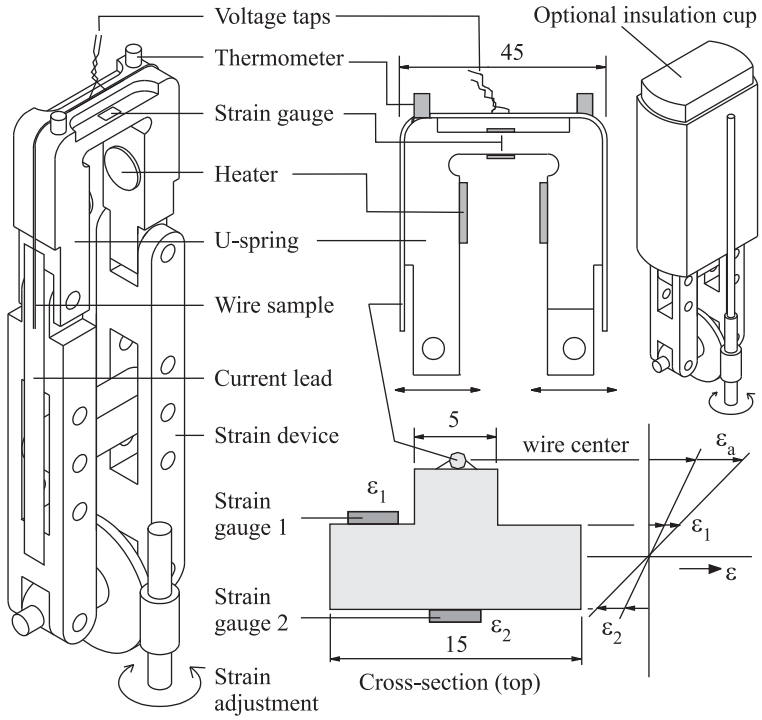

Figure 5.2: U-shaped bending spring. Strain is applied by a rotating wormgear that drives a left- and right threaded rod pushing the legs of the device apart. A helium gas environment is created by placing the insulator cup over the device so that temperature can be regulated through a set of heaters and thermometers. Strain in the sample is monitored by extrapolating the readings of the two strain gauges.

the sample, two strain gauges are mounted on the U-spring so that their readings can be extrapolated to the wire axis position. Measurements above 4.2 K can be performed by covering the entire device with a polyamide cup creating a helium gas environment. The devices' mechanical structure causes the heat leaks and heat generation paths to be nearly symmetric. Residual temperature gradients along the sample can be minimised by using two thermometers and two heaters. For current transport to the sample, etched $Ag/Bi_2Sr_2Ca_2Cu_3O_x$ current leads are used to limit the the heat leak from the sample to the helium bath (4.2 K), while allowing enough transport current to be able to measure critical currents. Turbulent convection of the helium gas in the polyamide cup plays a significant role at higher temperatures, increasing temperature fluctuations and thus rendering measurements of the critical parameters less precise. The sample is therefore isolated with a piece of neoprene foam to minimise the effect of temperature fluctuations to about 30 mK in the range of 4.2 K to 60 K operating temperature.

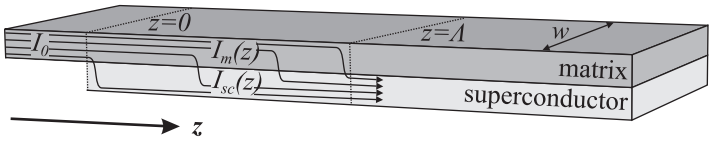

Figure 5.3: Current transfer in a superconductor-normal conductor composite, modeled in a "coated conductor" layout. The transport current I_0 first enters the matrix at $z = 0$ at which current is only flowing in the matrix. Along the entrance length, from $z = 0$ to $z \approx \Lambda$, current is diffusing from the matrix into the superconductor (i.e. I_m decreases while I_{sc} increases). Within the entrance length an electric field is generated even for $I_0 < I_c$. For $z \gg \Lambda$ nearly all the current is flowing in the superconductor so that no electric field is generated.

The total response time of the thermal system of the U-spring device is ~ 1 s, allowing compensation for dissipation in the sample itself during the measurement of a voltage-current transition. With this method, critical currents up to 200 A have been measured at temperatures up to 20 K in MgB_2 conductors [142] and up to 60 K in $Bi_2Sr_2Ca_2Cu_3O_x$ samples.

5.2.2 Critical Current and n-value

Determination of the critical current and the n-value from voltage-current data obtained with the U-spring requires a correction procedure. The short sample length together with the presence of a solder layer all along the sample cause current transfer effects to have a significant influence on the voltage-current transition.

Transfer effects are caused by current that passes non-uniformly through the matrix before it is carried by the superconducting filaments, generating an ohmic electric field. Schematically this process is depicted in figure 5.3. A composite conductor is modeled in a quasi 1-dimensional layout with width w. At the point of current injection at $z = 0$ the transport current I_0 is flowing in the matrix so that an Ohmic electric field is generated. Then, for $z > 0$, the current gradually diffuses from the matrix into the superconductor, dividing the total transport current I_0 into $I_m(z)$ and $I_{sc}(z)$. Across this length an electric field is generated by $I_m(z)$ even when the total transport current I_0 is lower than I_c of the superconductor. At distances much larger than the characteristic transfer length $z \gg \Lambda$ nearly all the transport current has diffused into the superconductor so that no electric field is generated. A simplified model for current transfer that allows to calculate the characteristic entrance length is presented by Wilson [28]. Recently Dhallé [233] extended this model to include the non-linearity of the voltage-current transition of the superconductor (the power law $E \propto J^n$). Typical results are depicted in figure 5.4. Figure 5.4a shows the voltage-current relations of the components in the composite. E_{m0} is the voltage-current relation of purely the matrix ($\propto I_0$)

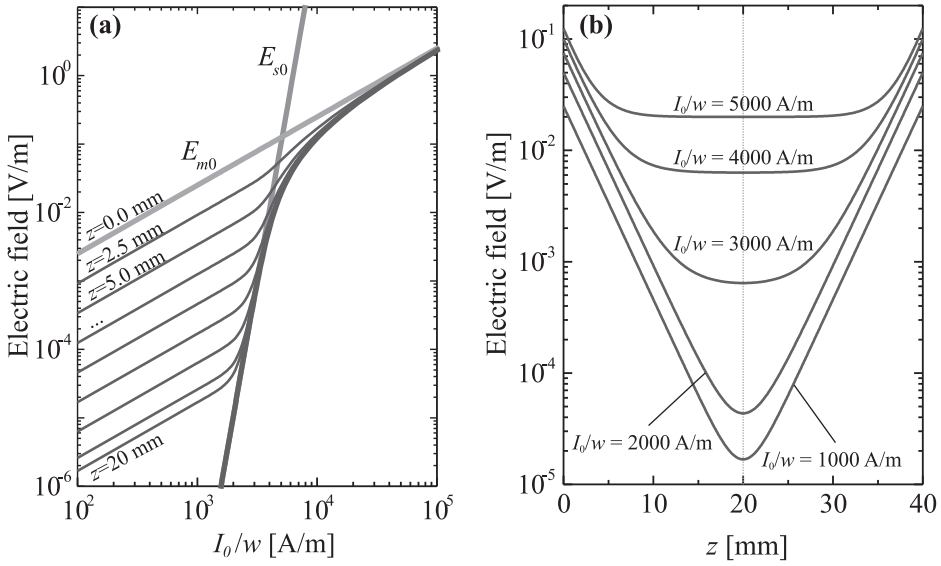

Figure 5.4: (a) Calculations of the electric field in a parallel superconductor-normal conductor composite when a current is applied. E_{m0} and E_{s0} represent the electric field in the matrix ($E_{m0} \propto I_0$) and a "pure" superconductor ($E_{s0} \propto I_0^n$). The thin lines represent the electric field close to the point where current is injected. E_∞ represents the "intrinsic" voltage-current transition of the composite superconductor. In (b) the electric field profile along the conductor is displayed at various currents. Note that samples on the U-spring are indeed about 40 mm long, thus an ohmic contribution can be expected when the voltage-current transition is measured. A transfer length of $\Lambda = 2.5$ mm is assumed.

and E_{s0} is the voltage-current relation of the bare superconductor ($\propto I_0^n$). The thin lines represent the electric field in the matrix of a composite, such as the one depicted in figure 5.3, at various distances from the injection point. E_∞ is the electric field in the matrix of the composite far away from the injection point ($z \to \infty$). As mention before, all the transport current at the injection point ($z = 0$) is flowing in the matrix so that the electric field in the matrix of the composite corresponds with that of a "pure" normal conductor. With increasing distance from the injection-point, the amount of current flowing in the matrix ($I_m(z)$) decreases, whilst current in the superconductor $I_{sc}(z)$ increases, so that the ohmic contribution decreases along the conductor. At sufficiently large distances ($z \gg \Lambda$), the ohmic contribution disappears for $I_0 \ll I_c$ as all the transport current is carried by the superconductor (E_∞). When the total current I_0 is increased and I_c is exceeded the electric field approaches E_{m0} since current diffuses back into the matrix, similarly to the current sharing process described in chapter §4.3.2.

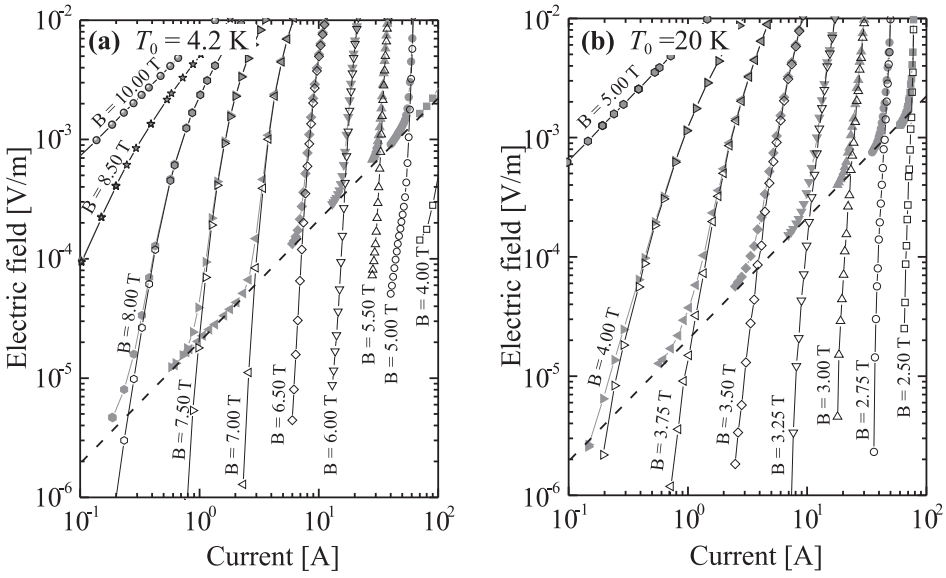

Figure 5.5: Voltage-current characteristics of a MgB_2/Fe tape from University of Geneva at various magnetic fields and at temperature 4.2 K (a) and 20 K (b) measured on the U-spring sample holder (**solid symbols**). The ohmic contribution of the entrance effect is indicated by the **dashed line**, which is subtracted from the data to obtain the intrinsic voltage-current characteristic of the conductor (**open symbols**). These characteristics are fitted with the second order polynomial of (5.1) in order to obtain I_c and the n-value.

A profile of the electric field in the matrix along the length of the composite at different currents is depicted by 5.4b. The sample length that is assumed in this plot is approximately the length of a typical sample measured with the U-spring. The voltage-taps are placed at about $z = 15$ mm and 25 mm, but even at the center of the sample at low currents a significant contribution of the entrance effect in the measured voltage-current transition can be expected. Indeed, when a reasonable value of E_c (e.g. 10^{-4} V/m) is chosen, the data has be corrected in order to determine I_c and the n-values that are representative for long length samples.

An example of a voltage-current transition at various magnetic fields of a MgB_2/Fe tape measured with the U-spring is indicated by the solid data points in figure 5.5. Similarly to figures 5.4a and b, a significant ohmic contribution (indicated by the dashed line) is measured that is caused by current flow in the matrix. Strikingly, the same ohmic limit acts as a lower boundary for all voltage-current curves irrespective of the external magnetic field or of the temperature. This is easily understood when considering that the matrix material is pure Fe, which has a resistivity virtually independent of temperature and field

in the range under consideration. The value of the corresponding resistance (in this case $\sim 20\mu\Omega/\mathrm{m}$) thus depends only on the resistivity of Fe and on geometrical factors. Consequently, this point of the voltage-current characteristics is not representative for the intrinsic properties of the superconductor. In order to determine the intrinsic J_c and n-value, first the ohmic contribution is linearly fitted and the corresponding line is subtracted from the raw data, yielding the intrinsic voltage-current transition (i.e. E_∞) of the superconductor indicated by the open symbols. This (double logarithmic) intrinsic voltage-current curve is then written as a Taylor expansion around $\ln(E) = \ln(E_c)$:

$$\ln J = a_0 + a_1 \left(\ln(E) - \ln(E_c)\right) + \frac{a_2}{2} \left(\ln(E) - \ln(E_c)\right)^2 . \tag{5.1}$$

A second-order expansion is used to take into account the curvature of the transition that is caused by the diffusion of current back into the matrix at currents $J \gg J_c$. The critical current density is obtained by fitting the second-order polynomial (5.1) to the data and taking $J_c = \exp(a_0)$, while its uncertainty can be found from $\Delta J_c = J_c \Delta a_0$. The n-value (the local slope of the voltage-current characteristic on a log-log plot) is simply given by $n = a_1$; $\Delta n = \Delta a_1$.

5.2.3 Resistive Transition

If the critical current density in MgB_2 shows a reversible strain dependence, it might well be of an electronic origin. This suggests that not only I_c changes reversibly, but also the critical temperature T_c and the irreversibility field B^*. To verify if this is the case, in this study T_c and B^* are probed by resistive transition measurements, of which two examples are displayed in figure 5.6a and b (R-T and R-B, respectively). Both plots can roughly be separated into three parts: first there is the superconducting region at temperature (or field) below T_{offset} (B_{offset}); secondly, above T_{offset} (B_{offset}) the resistivity starts to rise towards the normal state (the resistive transition itself); and thirdly above T_{onset}(B_{onset}) the superconductor is in the normal state. In other words, T_{onset} is defined as the temperature at which, during cool-down, the resistivity starts to drop below its normal-state value, while T_{offset} is the temperature at which the resistive transition is "complete" and the resistivity becomes zero. It should be noted that the resistive transition is not infinitely sharp. Not only are T_{onset} and T_{offset} well-separated temperatures, the on- and offset points are also "rounded" in such a way that their determination depends to some extent on the precision of the resistivity measurement. There are essentially three mechanisms that can determine the width of the transitions: thermal fluctuations, magnetic flux motion and sample inhomogeneity.

Even in the absence of any significant magnetic field and in pure samples such as for instance single crystals, thermal fluctuations will cause "smearing out" of both T_{onset} and T_{offset}. Above T_c, the paired electron state has a higher energy than unpaired ones. However, when the temperature is sufficiently close to T_c, this energy difference becomes comparable to $k_B T$ so that there is a non-zero

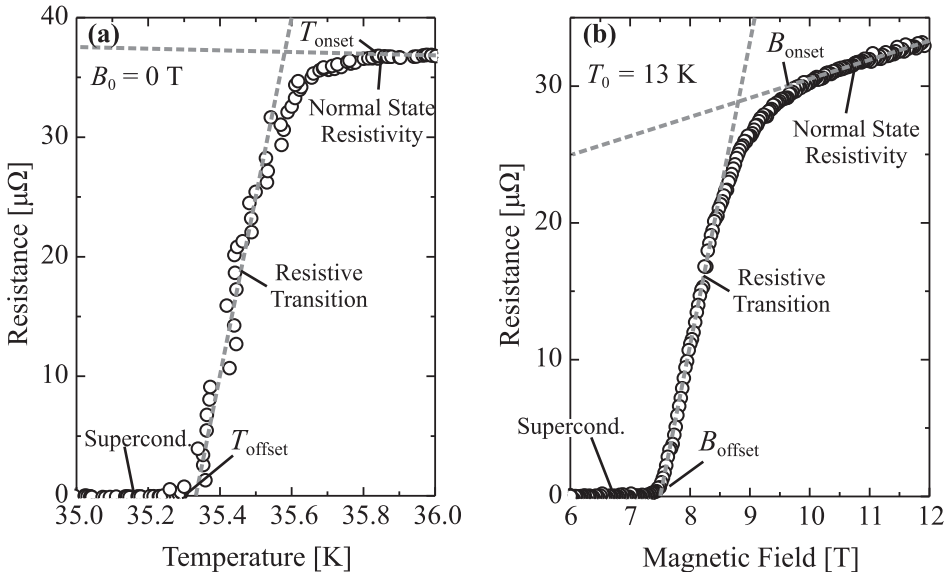

Figure 5.6: Example of the resistive transitions as function of temperature (a) and magnetic field (b) for an ex-situ MgB_2 conductor fabricated at the Institute of Electrical Engineering in Bratislava, Slovakia.

probability for electrons to pair already. This so-called fluctuation conductivity can start to contribute already well above T_c and thus determines the value of T_{onset} [234]. Vice versa, the appearance of resistance at T_{offset} can occur well below T_c since thermal fluctuations can already break up electron-pairs.

The first occurrence of resistance at B_{offset}, well below the second critical field B_{c2}, in figure 5.6b is assumed to be caused by the motion of flux-lines, which is a dissipative process. The motion of flux lines is hampered by flux pinning [67] with a corresponding pinning energy. In general, this pinning energy is a decreasing function of temperature, field and current, which can become zero well below the $B_{c2}(T)$ line. When this happens, the critical current becomes zero and a finite resistivity will be measured irrespective of the transport current. The corresponding magnetic field is called the irreversibility field B^*. When measured with a sufficiently low current density, the offset field in a $R(B)$ curve such as the one in figure 5.6b will approximately correspond to this irreversibility field, $B_{\text{offset}} \approx B^*$. Due to the dissipative nature of the flux motion the exact position of B_{offset} depends on the transport current and if the transport current is too high, B_{offset} will be lower than B^*. For the same reason B_{onset} also depends on the transport current. But, when the current is sufficiently low, B_{onset} will approximate the point where the value of the superconductivity gap reduces to zero (when the field is ramped up) and thus approximates B_{c2}, $B_{\text{onset}} \approx B_{c2}$ [234].

A third factor influencing the shape of the $R(T)$ and $R(B)$ curves is sample ho-

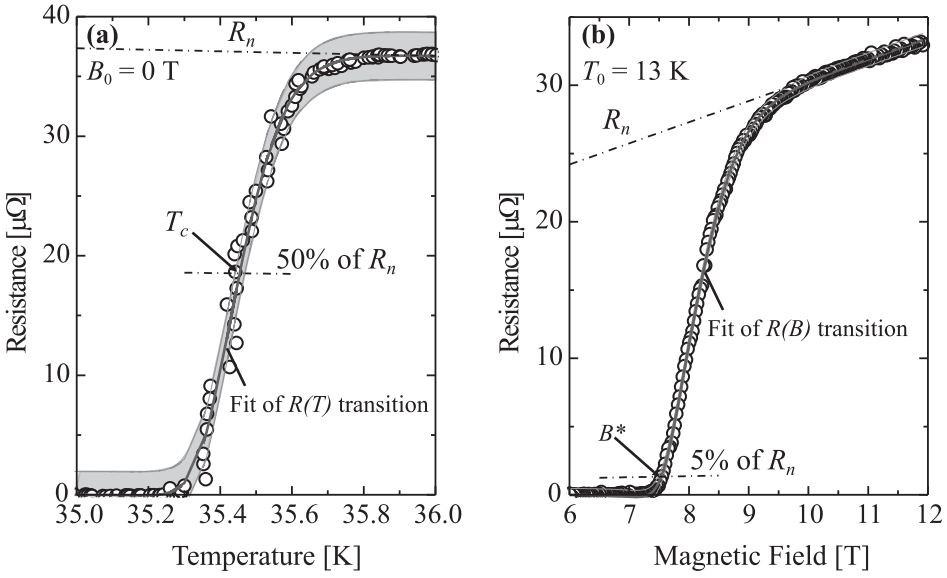

Figure 5.7: The same R-T and R-B transitions as shown in figure 5.6, but indicating the points where the critical temperature T_c and irreversibility field B^* are defined. It also indicates the fit (**solid line**) of the measured data with expression (5.2) and the 99 % prediction band (**gray area**) from which the uncertainty in T_c and B^* are determined.

mogeneity. The filaments in a practical MgB_2 superconductor are polycrystalline with the crystallites randomly ordered. Since the critical parameters of MgB_2 in the direction of the *ab*-plane differ from those in the *c*-axis direction [235], crystallites will display a different behaviour depending on the (local) direction of field and current. Consequently, the width of the transitions can also be caused by distributed critical temperatures, critical fields and irreversibility fields [236]. Furthermore, inevitable non-superconducting impurities in the filaments can induce resistance developing before the intrinsic critical parameters are crossed. For example, Godeke [12] reported a significant reduction of the R-B transition width in Nb_3Sn-PIT conductors when the reaction time is increased, which is attributed to a more homogeneous Sn distribution throughout the cross-section of the filament.

In order to characterise the strain dependence of the resistive transitions first T_c is defined at the 50 % intersection of the normal state resistivity with the R-T transition. Secondly, B^* is defined as the field at which the $R(B)$ curve intersects with the 5 % of the normal state resistivity curve. Figure 5.7a and b show the same resistive transitions as in figure 5.6 but include T_c and B^* with the 50 and 5 % normal state resistivities at which they are defined.

The measured transitions with temperature are obtained by applying a DC

current of 100 mA that toggles polarity at each data point, to compensate for offset or inductive voltages. While applying this current, the temperature is varied and magnetic field is fixed to obtain the *R-T* curves such as that shown in figure 5.7a. In order to avoid apparent hysteresis between increasing- and decreasing temperature, a relatively low temperature ramp rate of 50 mK/min is used. Vice versa, to obtain the *R-B* curve (figure 5.7b) the temperature is fixed while the magnetic field is varied at a ramp rate of about 0.2 T/min. This ramp rate is low enough to avoid a measurable hysteresis between ramping the magnetic field up and down.

In order to estimate T_c and B^* from the measured transitions, they are fitted with the following function:

$$R(x) = (a_1 x + a_2)\frac{1}{2} \quad \left\{1 - \frac{w_1}{x_{c1} - x_{c2}} \ln\left[2\cosh\left(\frac{x - x_{c1}}{w_1}\right)\right] + \frac{w_2}{x_{c1} - x_{c2}} \ln\left[2\cosh\left(\frac{x - x_{c2}}{w_2}\right)\right]\right\} \tag{5.2}$$

with,

$x = T$ or $x = B$.

This expression is essentially a step function that can be asymmetric, in which $(a_1 x + a_2)$ is the linear normal state resistivity, and x_{c1} and x_{c2} are centered at the offset and onset of the transition, respectively. Moreover, equation (5.2) allows the offset and onset to have a certain width (in contrast to a sudden increase of the resistance), which are proportional to w_1 and w_2 respectively. Then, T_c and B^* are the intersections of this fit with 50 % and 5 % of their normal state resistivities, respectively ($0.5 \times (a_1 x + a_2)$ and $0.05 \times (a_1 x + a_2)$). The uncertainty of T_c and B^* are obtained through the 99 % prediction band of equation (5.2), indicated by the gray area in figure 5.7a.

5.2.4 Samples

As pointed out before, type and uniformity of matrix materials can be of great influence on the critical parameters (see also §2.3.2) as well as the thermal stability (§4.5). The samples listed in table 5.1 have different matrix materials that are chosen either to provide enough strength to obtain a high densification of the filaments during deformation (using Ni, Fe or the alloys CuNiZn and AgMg) or to obtain sufficient thermal stabilisation (Cu). As will be shown below, the choice of matrix material also influences the strain response of the critical current. This is not unusual, already in the introduction (§5.1) it was mentioned that in A15 and ceramic superconductors the thermal expansion coefficient of the matrix material influences the point where the strain-dependence of the critical parameters switches from reversible to irreversible behaviour ($\varepsilon_{\mathrm{rev}}$).

Another parameter that varies from sample to sample and that can influence the strain response of the critical parameters is the powder itself, which can be either ex-situ/in-situ or doped/non-doped. For example, both B^* and B_{c2} are

Table 5.1: Overview of the investigated samples and their layout properties. f and f_i are the filling factor and the fraction of the i^{th} component in the matrix.

Sample	Powder	f[%]	Matrix	f_i[%]	# Filaments	Shape	Dimensions
CLM[a]	ex-situ	9	Ni/Cu/Fe	67/14/10	14	Tape	A=0.7 × 3.6 mm^2
FZK1[b]	in-situ	50	Fe	50	Mono	Wire	$\varnothing = 1.2$ mm
FZK2[b]	in-situ	13	Cu/CuNiZn/Nb	56/24/7	7	Wire	$\varnothing = 0.9$ mm
HTR[c]	in-situ	16	Nb/Cu/Monel	15/29/40	7	Wire	$\varnothing = 0.8$ mm
IEE1[d]	ex-situ	25	Fe	75	4	Square	$A = 1.2 \times 1.2$ mm^2
IEE2[d]	in-situ+SiC	26	AgMg/Nb	44/30	4	Square	$A = 1.1 \times 1.1$ mm^2
UG1[e]	ex-situ	30	Fe	70	Mono	Tape	$A = 0.4 \times 3.9$ mm^2
UG2[e]	in-situ	29	Fe	71	Mono	Wire	$\varnothing = 1.1$ mm

[a] Columbus Superconductors, Genova (Italy)
[b] Forschungszentrum Karlsruhe, Karlsruhe (Germany)
[c] HyperTech Research, Columbus, Ohio (USA)
[d] Institute of Electrical Engineering, Bratislava (Slovakia)
[e] University of Geneva, Geneva (Switserland)

enhanced by SiC addition so that their strain dependence might well be different from that in non-doped samples.

Also the geometry of the conductors will influence their strain response. The investigated samples are either rolled to tapes, drawn into wires or two-axially-rolled into square wires. The different deformation processes affect the texture of the MgB_2 grains [156] thus influencing the effective critical parameters (see also §5.2.3) and so the strain dependence. Moreover, when axial strain is applied to a conductor, also a transverse strain will be built up, as described by an effective Poisson ratio of the composite. The influence of the transverse strain components on the critical parameters of the superconducting filaments will depend on the geometry of the conductor [44] and thus the number of filaments.

5.3 Strain Dependence of the Critical Current

Figures 5.8a, c and d show the strain dependence of the critical current of samples CLM, FZK1 and HTR from table 5.1.

The sequence of the measurements is indicated by the numbers next to the data-points in figure 5.8a. The critical current is first measured at zero applied strain (data-point 1). Then, the applied strain is stepwise decreased into the compressive regime down to a minimum of approximately -0.6 %. At each step the critical current is measured (data-points 2 to 4). Next, the applied strain is stepwise increased back into the tensile regime (data-points 3 to 18). Finally, the strain is decreased again to 0 % (data-points 19 to 21).

The samples all show a similar behaviour in the sense that they all exhibit reversible linear strain response for compressive and sufficiently low tensile strain (data-points 1 to 13), while, when the tensile strain is increased above a certain reversible strain limit $\varepsilon_{\mathrm{rev}}$ (indicated by the gray band), the critical current decreases abruptly (data-points 13 to 18). When the applied strain is finally released again (data-points 19 to 21), the critical current does not recover. This behaviour is general for MgB_2 conductors and is also observed by other authors [218, 237]. These observations do not only hold for the critical current, but also for the n-value as indicated by figure 5.8b.

Comparing figures 5.8a, c and d shows that the reversible strain limit $\varepsilon_{\mathrm{rev}}$ is sample dependent ($\varepsilon_{\mathrm{rev}} \approx$ 0.23 %, 0.18 % and 0.30 % for sample CLM, FZK1 and HTR respectively), while the two different measurements of sample FZK1 (figure 5.8c, taken from two different pieces of the same wire) show that the value of $\varepsilon_{\mathrm{rev}}$ seems to be independent of temperature and magnetic field. Taken together with the irreversible $I_c(\varepsilon)$ and $n(\varepsilon)$ behaviour above $\varepsilon_{\mathrm{rev}}$, the fact that the value of $\varepsilon_{\mathrm{rev}}$ does not depend on T or B suggests that, just like in ceramic superconductors, $\varepsilon_{\mathrm{rev}}$ is strongly related to the degree of thermal pre-compression of the filaments by the matrix. In §5.3.1 this will be further investigated.

Although $\varepsilon_{\mathrm{rev}}$ does not seem to depend on the operating conditions, the strain response of the critical current in the reversible regime clearly does (figure 5.8c). This is reminiscent of the strain response of A15 materials as discussed in §1.3.2

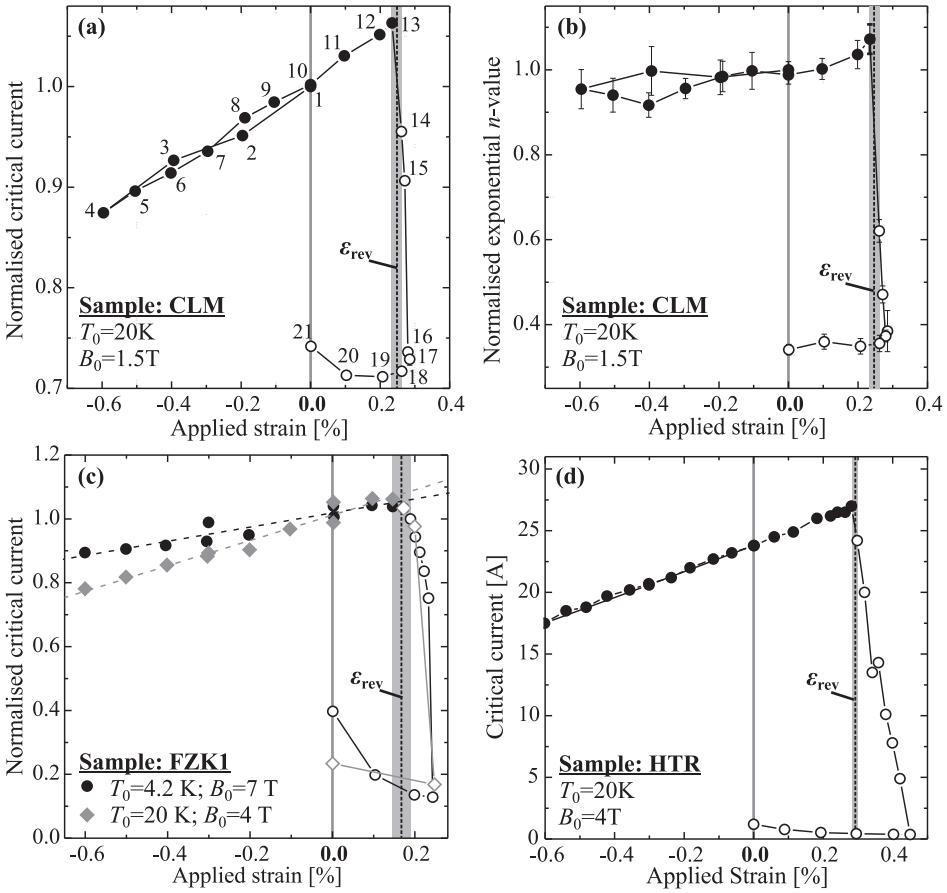

Figure 5.8: General observations of the strain dependence of the critical current (a, c and d) and the n-value (b). The dashed lines indicate the reversible strain limit $\varepsilon_{\mathrm{rev}}$ at which reversible strain response changes to irreversible behaviour. The corresponding gray bands indicate the uncertainty of $\varepsilon_{\mathrm{rev}}$, which is the window described by the last data-point in the reversible regime and the first data-point in the irreversible regime. (a) Strain response of the normalised critical current of sample CLM. The numbers indicate the order in which the critical current is measured as function of applied axial strain. (b) n-value as function of strain of sample CLM. (c) Strain dependence of the normalised critical current of sample FZK1 at two combinations of field and temperature. (d) Strain dependence of the critical current of sample HTR.

and §5.1 and suggests an electronic origin of the reversible strain response also for MgB_2. A detailed study of the reversible strain response of I_c as a function of T and B will be presented in §5.3.2.

5.3.1 Reversible Strain Limit

In order to verify the correlation between the reversible strain limit and the thermal pre-compression in the superconducting filaments (like in BSCCO/Ag composites), the thermal strain exerted by the matrix on the MgB_2 filaments has to be estimated. This is done by considering the different thermal expansion coefficients α of the constituent materials:

$$\alpha \equiv \frac{1}{l}\left(\frac{dl}{dT}\right), \quad l(T) \approx l(T_0)[1+\alpha(T-T_0)]. \tag{5.3}$$

In a simple 1-dimensional approach, if two materials A and B with different thermal expansion coefficients α_A and α_B are welded at a temperature T_0 and subsequently cooled down to temperature $T = T_0 + \Delta T$, they will each be constrained in their thermal contraction by the other material and therefore each be subjected to a thermal strain $\varepsilon_{A,B}$:

$$\begin{aligned} \varepsilon_A &= \frac{l(T)-l_A(T)}{l_A(T)}, \quad l_A(T) \approx l(T_0)[1+\alpha_A \Delta T] \\ \varepsilon_B &= \frac{l(T)-l_B(T)}{l_B(T)}, \quad l_B(T) \approx l(T_0)[1+\alpha_B \Delta T], \end{aligned} \tag{5.4}$$

with $l(T)$ the length of the composite at temperature T and $l_{A,B}(T)$ the length of either material if they were allowed to contract freely. The actual length of the composite can then be calculated by demanding that the forces exerted by the two materials on one another must be balanced:

$$\begin{aligned} &f_A \sigma_A(T) + f_B \sigma_B(T) = 0 \\ &f_A E_{Y,A} \varepsilon_A(T) + f_B E_{Y,B} \varepsilon_B(T) = 0, \end{aligned} \tag{5.5}$$

with $f_{A,B}$ the volume fractions, $\sigma_{A,B}$ the thermal stresses and $E_{Y,A,B}$ the Youngs' moduli of materials A and B. Substituting equation (5.4) into (5.5) and considering $\alpha_{A,B}\Delta T \ll 1$, the actual length change of the whole composite and the thermal strain in each component can be expressed as function of their mechanical- and thermal properties:

$$\begin{aligned} l(T) &\approx l(T_0)\left[1 + \frac{f_A E_{Y,A}\alpha_A + f_B E_{Y,B}\alpha_B}{f_A E_{Y,A} + f_B E_{Y,B}} \Delta T\right], \\ \varepsilon_A &\approx \frac{f_B E_{Y,B}}{f_A E_{Y,A} + f_B E_{Y,B}} (\alpha_B - \alpha_A)\Delta T, \\ \varepsilon_B &\approx \frac{f_A E_{Y,A}}{f_A E_{Y,A} + f_B E_{Y,B}} (\alpha_A - \alpha_B)\Delta T. \end{aligned} \tag{5.6}$$

As indicated in table 5.1, some conductors have more than two components. To account for this, (5.6) can be readily expanded to N components:

$$\begin{aligned} &\sum_{i=1}^{N} f_i E_{Y,i} \varepsilon_i(T) = 0, \\ &l(T) \approx l(T_0) \left[1 + \frac{\sum f_i E_{Y,i} \alpha_i}{\sum f_i E_{Y,i}} \Delta T \right], \\ &\varepsilon_i(T) \approx \frac{\sum f_i E_{Y,i} (\alpha_i - \alpha_j)}{\sum f_i E_{Y,i}} \Delta T. \end{aligned} \tag{5.7}$$

Note that equations (5.6) and (5.7) provide only rough estimates for temperature variations ΔT of a few hundreds of Kelvin. Properties such as α and E_Y are temperature dependent, so that equations (5.3), (5.4), (5.6) and (5.7) need to be integrated over the relevant temperature range. Furthermore, the thermal constraints can become so important that for some materials (e.g. Cu) they may exceed the elastic limit, so that the temperature dependent yield strength needs to be taken into account. Unfortunately, the temperature dependence of the Youngs' modulus E_Y and the yield strength σ_y are not available in the literature for all the materials that are analysed in this study. Therefore, (5.7) is used to estimate the thermal pre-compression. An example of a more thorough approach for $Bi_2Sr_2Ca_2Cu_3O_x$/Ag conductors can be found in [222].

The values of the thermal expansion coefficient α and Youngs' modulus E_Y that are used are listed in table 5.2 and the estimates of the thermal pre-compression are listed in table 5.3. The estimation of the thermal pre-compression is separated into $\varepsilon_{\text{pre I}}$ and $\varepsilon_{\text{pre II}}$. The former is the pre-compression that builds up during cool-down from the heat treatment- to room temperature, whereas the latter is the extra thermal strain building up during the cryogenic cool-down to 4.2 K. The reason for this separation is that α tends to zero between $T \approx 100 - 150$ K for most materials [80]. If its room temperature value were used throughout this low-temperature range, the thermal contraction would by strongly overestimated. Instead, for the cryogenic cool down the "integrated" thermal contraction $\varepsilon_{293 \to 4.2\ \text{K}} = (l(4.2\ \text{K}) - l(293\ \text{K}))/l(293\ \text{K})$ is used. For the samples that are soldered on a U-shaped bending, spring $\varepsilon_{\text{pre I}}$ is further split into the cool-down from heat treatment to the soldering temperature of 220 °C and from soldering temperature to room temperature. When the sample is soldered to a spring, the thermal contraction is nearly completely determined by the spring, since the cross-sectional area of the spring is much larger than the one of the sample: $A_{\text{spring}} (\approx 100\ \text{mm}^2) \gg A_{\text{sample}} (\approx 1\ \text{mm}^2)$.

The pre-compression estimates for the samples that are measured in this study and those measured by others, listed in table 5.3, are shown as a function of the measured reversible strain limit ε_{rev} in figure 5.9. Clearly ε_{rev} and ε_{pre} are related, since all data lie grouped around the line $\varepsilon_{\text{rev}} = -\varepsilon_{\text{pre}}$. So, to first order, the reversible strain limit of MgB_2/metal composites is determined by the level of thermal pre-compression. Just like in ceramic superconductors, the filaments

Table 5.2: Thermal and mechanical properties that are used in the estimation of the thermal pre-strain that the matrix exert on the filaments. α_{273K} and $E_{Y,273K}$ are the thermal expansion coefficient and the Youngs' modulus at 273 K respectively. $\varepsilon_{293\rightarrow4.2K}$ is the relative change in length during a cool down from room temperature to 4.2 K. $\Delta\alpha_{273K}$ and $\Delta\varepsilon_{293\rightarrow4.2K}$ are the differences in the values of α_{273K} and $\varepsilon_{293\rightarrow4.2K}$ between the given material and MgB_2.

Material	α_{273K} $[10^{-6}K^{-1}]$	$\varepsilon_{293\rightarrow4.2K}$ [%]	$E_{Y,273K}$ [GPa]	$\Delta\alpha_{273K}$ $[10^{-6}K^{-1}]$	$\Delta\varepsilon_{293\rightarrow4.2K}$ [%]	Source
MgB_2	8.0 ± 0.2	-0.14 ± 0.01	151 ± 10	-	-	[238, 239]
AgMg	11.7 ± 0.2	-0.40 ± 0.05	100 ± 10	10.9 ± 0.4	-0.26 ± 0.02	[240]
Cu	16.0 ± 0.2	-0.32 ± 0.01	121 ± 10	8.0 ± 0.4	-0.18 ± 0.02	[80]
CuNi18Zn20	16.0 ± 0.2	-0.25 ± 0.05	128 ± 10	8.0 ± 0.4	-0.11 ± 0.02	[241]
CuZn30	19.0 ± 0.3	-0.39 ± 0.01	125 ± 10	11.0 ± 0.5	-0.25 ± 0.02	[80]
Fe	12.0 ± 0.2	-0.24 ± 0.01	180 ± 10	4.0 ± 0.4	-0.10 ± 0.02	[242]
Monel-400	13.0 ± 0.2	-0.22 ± 0.01	186 ± 10	5.0 ± 0.4	-0.06 ± 0.02	[243]
Ni	12.0 ± 0.2	-0.22 ± 0.01	200 ± 10	4.0 ± 0.4	-0.08 ± 0.02	[80]
Nb	6.7 ± 0.2	-0.14 ± 0.01	105 ± 10	-1.3 ± 0.4	-0.00 ± 0.02	[80]
SS	15.0 ± 0.3	-0.30 ± 0.01	190 ± 10	7.0 ± 0.5	-0.16 ± 0.02	[80]
Ti6AlV4	8.9 ± 0.2	-0.17 ± 0.01	115 ± 10	0.9 ± 0.4	-0.03 ± 0.02	[80]

Table 5.3: Estimates of the thermal pre-strain in the MgB_2 filaments of the samples listed in table 5.1 and of samples measured by Kováč [219], Kitaguchi [151, 218] and Goldacker [108, 237]. $\varepsilon_{\text{pre I}}$ is the thermal strain building up between sintering- and room temperature. It is split in two ranges; cool down from heat treatment (HT)- to soldering temperature (ST) and from soldering- to room temperature (RT). The heat treatment temperatures are typically 700 °C for in-situ and 950 °C for ex-situ conductors. $\varepsilon_{\text{pre II}}$ is the strain building up from the cool down from room temperature to 4.2 K. (CuZn), (SS) and (Ti) indicate a brass, stainless steel or titanium bending spring, respectively.

Sample	Composition	f_i[%]	$\varepsilon_{\text{pre I(HT}\rightarrow\text{RT)}}$ [%]		$\varepsilon_{\text{pre II(293}\rightarrow\text{4.2K)}}$ [%]	$\varepsilon_{\text{pre, total}}$ [%]
			(HT → ST)	(ST → RT)		
CLM	MgB_2/Fe/Cu/Ni(Ti)	9/10/14/66	-0.30 ± 0.06	-0.02 ± 0.01	-0.03 ± 0.02	-0.35 ± 0.09
FZK1	MgB_2/Fe(Ti)	50/50	-0.16 ± 0.03	-0.02 ± 0.01	-0.03 ± 0.02	-0.21 ± 0.06
FZK2	MgB_2/Nb/Cu/CNZ(Ti)[a]	13/7/56/24	-0.30 ± 0.06	-0.02 ± 0.01	-0.03 ± 0.02	-0.35 ± 0.09
HTR	MgB_2/Nb/Cu/Monel(Ti)	16/15/29/40	-0.20 ± 0.04	-0.02 ± 0.01	-0.03 ± 0.02	-0.25 ± 0.07
IEE1	MgB_2/Fe(Ti)	25/75	-0.23 ± 0.05	-0.02 ± 0.01	-0.03 ± 0.02	-0.28 ± 0.06
IEE2	MgB_2/Nb/AgMg(Ti)	26/30/44	-0.08 ± 0.02	-0.02 ± 0.01	-0.03 ± 0.02	-0.13 ± 0.06
UG1	MgB_2/Fe(Ti)	30/70	-0.21 ± 0.05	-0.02 ± 0.01	-0.03 ± 0.02	-0.26 ± 0.06
UG2	MgB_2/Fe(Ti)	29/71	-0.22 ± 0.05	-0.02 ± 0.01	-0.03 ± 0.02	-0.27 ± 0.06
Kováč.	MgB_2/Fe(CuZn)	47/53	-	-0.22 ± 0.01	-0.25 ± 0.02	-0.47 ± 0.09
	MgB_2/Fe(Ti)	47/53	-0.17 ± 0.05	-0.02 ± 0.01	-0.03 ± 0.02	-0.22 ± 0.08
	MgB_2/Fe(Ti)	25/75	-0.22 ± 0.06	-0.02 ± 0.01	-0.03 ± 0.02	-0.27 ± 0.09
Kitag.	MgB_2/SS(SS)	0.4/0.6	-	-0.14 ± 0.01	-0.16 ± 0.02	-0.30 ± 0.06
	MgB_2/Fe/Cu/Ni(SS)[b]	9/10/14/66	-0.30 ± 0.06	-0.14 ± 0.01	-0.16 ± 0.02	-0.60 ± 0.09
Gold.	MgB_2/Fe	49/51	-0.20 ± 0.04		-0.06 ± 0.02	-0.26 ± 0.06
	MgB_2/Fe/SS	30/33/37	-0.39 ± 0.12		-0.09 ± 0.03	-0.48 ± 0.15
	MgB_2/Fe/SS	22/24/54	-0.46 ± 0.13		-0.11 ± 0.04	-0.57 ± 0.17
	MgB_2/Fe	58/42	-		-0.05 ± 0.02	-0.05 ± 0.02
	MgB_2/Fe	58/42	-0.17 ± 0.06		-0.05 ± 0.02	-0.22 ± 0.08

[a] CNZ stands for CuNi18Zn20

[b] Note that this sample is in fact sample CLM measured on a stainless steel U-shaped bending spring.

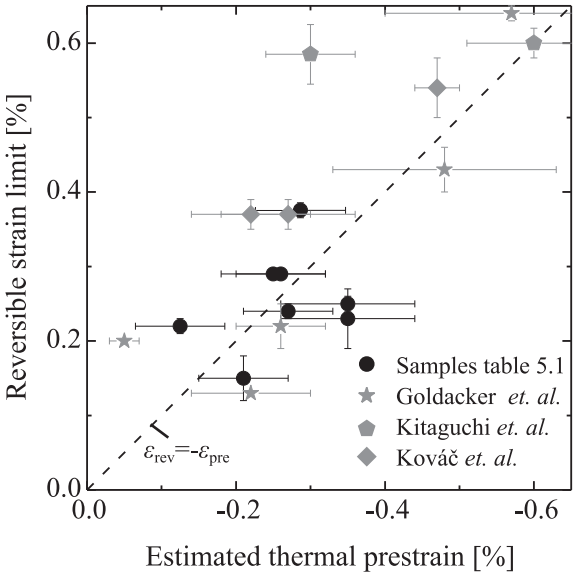

Figure 5.9: Measured reversible strain limit $\varepsilon_{\mathrm{rev}}$ of MgB_2/metal composites, versus the estimated thermal pre-compression strain $\varepsilon_{\mathrm{pre}}$.

will not be damaged by an applied tensile stress as long as this stress does not fully compensate the thermally induced compressive stress (as long as the internal strain state of the filaments remains compressive).

However, note that the thermal pre-compression alone cannot fully explain the sample dependence of the reversible strain limit. Kováč *et al.* [59] measured the strain response of the critical current of samples with the same matrix materials and fill factors, but different in layout (aspect ratio and number of filaments). If thermal pre-compression alone would determine the reversible strain limit, $\varepsilon_{\mathrm{rev}}$ should be similar for these samples. Instead, they found significantly different reversible strain limits ($\varepsilon_{\mathrm{rev}} \approx 0.20 - 0.35$ %) depending on the shape of the samples. Experimental artefacts such as a strain gradient across the sample could be excluded. The value of such a strain gradient would be ≈ 7 % of the mean strain value, which cannot explain the observed difference. Similarly, also samples UG1 and UG2, with $\varepsilon_{\mathrm{rev}} \approx 0.29$ and 0.23 % respectively, differ significantly. They both have a Fe matrix with approximately the same filling factor but UG1 is an ex-situ tape, whereas UG2 is an in-situ wire. A similar discrepancy between in- and ex-situ conductors was also observed by Kováč [244]. A possible explanation for these deviations is a difference in filament density, which results in differences in the effective Youngs' modulus. For example, as discussed in chapter 2, MgB_2/Fe ex-situ samples that are rolled into tapes have a significantly higher filament density than similar samples that are drawn into wires. Also softer materials in the precursor powder (Pb additions such as discussed in §2.3.2 or Mg in

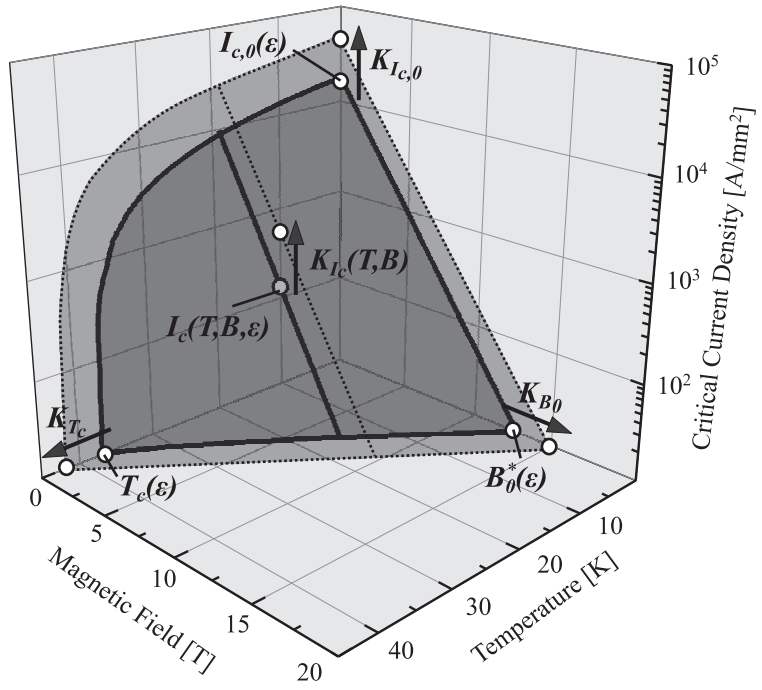

Figure 5.10: Schematic representation of the strain response of the critical surface of a MgB_2 conductor. $I_c(B,T,\varepsilon)$ is the temperature-, field- and strain-dependent critical current with $K_{I_c}(B,T)$ its strain response as described by equation (5.9). $I_{c,0}(\varepsilon)$, $T_c(\varepsilon)$ and $B_0^*(\varepsilon)$ are the strain dependent "corner points" of the critical surface and $K_{I_{c,0}}$, K_{T_c} and K_{B_0} are their corresponding strain responses. Note that the strain response of the critical surface is exaggerated for clarity.

the in-situ route) lead to higher effective densities. To verify if indeed the filament density influences the level of pre-compression, a more systematic study on the variation of the Youngs' modulus as a function of filament density is needed.

5.3.2 Reversible Regime

The linear strain response of the critical current in the reversible regime can be described as:

$$I_c(B,T,\varepsilon) = I_c(B,T,0)[1 + K_{I_c}(B,T)\varepsilon], \tag{5.8}$$

with $K_{I_c}(B,T)$ the normalised slope of the reversible strain response:

$$K_{I_c}(B,T) \equiv \frac{1}{I_c(B,T,0)} \left(\frac{\partial I_c(B,T,\varepsilon)}{\partial \varepsilon} \right)_{B,T}. \tag{5.9}$$

In §5.1 the electronic origin of the reversible strain dependence in Nb_3Sn was briefly discussed. If the strain response of I_c also has an electronic origin in MgB_2, then the critical temperature T_c and the irreversibility field B_0^* might be expected to be similarly strain dependent. Indeed, Lorenz [245] and Tang [246] reported a T_c suppression in MgB_2 bulk samples when applied to hydrostatic pressure. Kitaguchi [247] also observed similar effects in axially strained MgB_2 tapes. At the University of Twente it was found that the irreversibility field B_0^* is also strain dependent [142]. The aim of the remainder of this chapter is to show that the reversible strain response of the critical current K_{I_c} at any field and temperature can be expressed in terms of just three scaling parameters: 1) the zero field-, zero temperature-limit of the strain response of the critical current $K_{I_{c,0}}$; 2) the strain response of the critical temperature K_{T_c}; and 3) the strain response of the irreversibility field at zero temperature K_{B_0}. In fact, these three parameters describe the reversible strain behaviour of the three "corner points" $I_{c,0}$, T_c and B_0^* of the critical surface, as displayed in figure 5.10. Mathematically, they are defined as:

$$\begin{aligned} I_{c,0}(\varepsilon) &\equiv I_c(B=0, T=0, \varepsilon); \\ T_c(\varepsilon) &\equiv T(I_c=0, B=0, \varepsilon); \\ B_0^*(\varepsilon) &\equiv B(I_c=0, T=0, \varepsilon), \end{aligned} \tag{5.10}$$

where $T_c(B, I_c, \varepsilon)$, $B(I_c, T, \varepsilon)$ and $I_c(B, T, \varepsilon)$ are three equivalent descriptions of the strain-dependent critical surface. Analogous to the strain response of the critical current at any T and B (expression (5.9)), the strain responses of the three "corner points" of the critical surface can be described with the normalised strain derivative:

$$\begin{aligned} K_{I_{c,0}} &\equiv \frac{1}{I_{c,0}(0)} \frac{\mathrm{d}I_{c,0}(\varepsilon)}{\mathrm{d}\varepsilon} = \frac{1}{I_c(0,0,0)} \left(\frac{\partial I_c(B, I_c, \varepsilon)}{\partial \varepsilon} \right)_{T=0;B=0}; \\ K_{T_c} &\equiv \frac{1}{T_c(0)} \frac{\mathrm{d}T_c(\varepsilon)}{\mathrm{d}\varepsilon} = \frac{1}{T(0,0,0)} \left(\frac{\partial T(B, I_c, \varepsilon)}{\partial \varepsilon} \right)_{B=0;I_c=0}; \\ K_{B_0} &\equiv \frac{1}{B_0^*(0)} \frac{\mathrm{d}B_0^*(\varepsilon)}{\mathrm{d}\varepsilon} = \frac{1}{B(0,0,0)} \left(\frac{\partial B(I_c, T, \varepsilon)}{\partial \varepsilon} \right)_{I_c=0;T=0}. \end{aligned} \tag{5.11}$$

In §5.6 it will be shown how to construct a relation of the form

$$K_{I_c}(B,T) = g\left(\frac{B}{B_0^*}, \frac{T}{T_c(0)}; K_{I_{c,0}}; K_{T_c}; K_{B_0} \right), \tag{5.12}$$

that describes the strain dependence of the entire critical surface in terms of these three partial derivatives, reflecting the behaviour of its corner points. However, first the reversible strain dependence of the critical temperature and the irreversibility field, i.e. the second and third partial derivatives in (5.11), will be examined in detail.

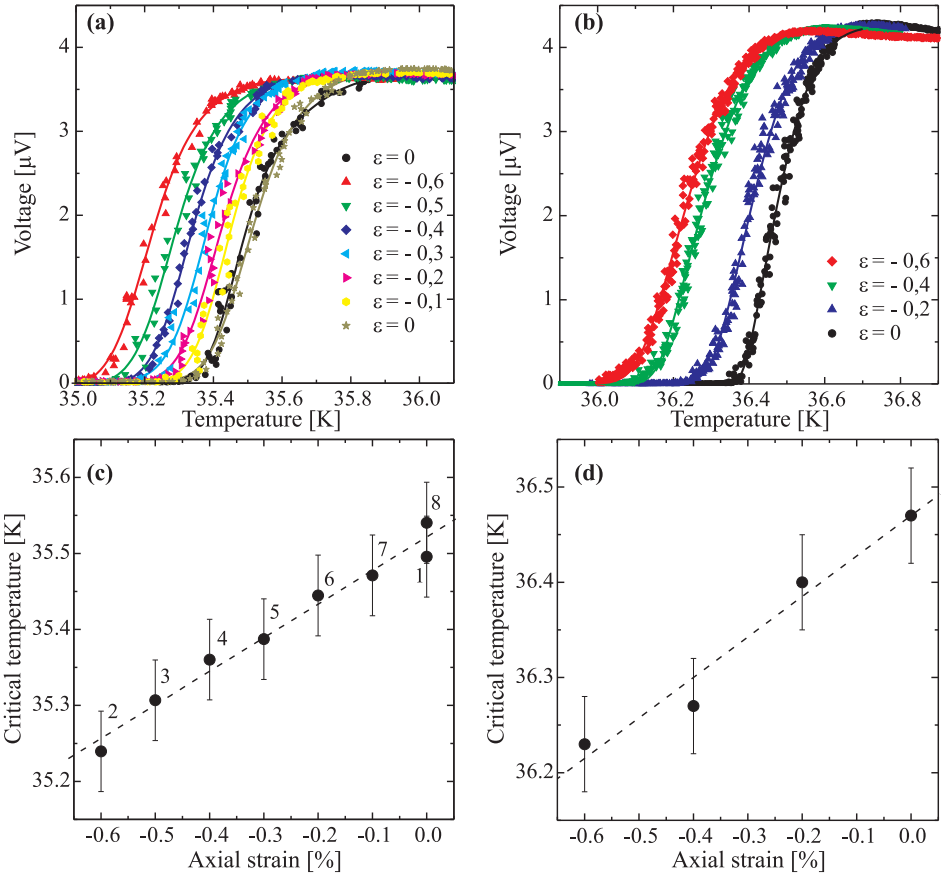

Figure 5.11: Reversible variation of T_c with axial strain. (a) and (c) are measured on sample IEE1 and (b) and (d) are measured on sample FZK1.

5.4 Strain Dependence of the Critical Temperature

To verify the validity the scaling relation (5.12), samples IEE1 and FZK1 were fully characterised in terms of the strain dependence of the critical current, -temperature and the irreversibility field. The latter will be treated in §5.5. In this paragraph the behaviour of T_c is described.

The resistive transitions as a function of axial strain for both samples are displayed in figures 5.11a and b. Clearly, the transitions shift when strain is applied to those samples. Plotting the critical temperature against axial strain (figures 5.11c and d) reveals a linear $T_c(\varepsilon)$ dependence. Moreover, the numbers next to the data-points in figure 5.11c indicate the order in which strain is applied. It is clear

that the T_c variation with strain is also reversible. The linear strain response of the critical temperature allows to determine K_{T_c} through linear regression. Since the transitions shift as a whole, the strain response does not depend on the exact criterion used to determine T_c. In figures 5.11c and d, a criterion of 50 % of the normal resistivity is used, while the uncertainty of T_c is determined with the 99 % prediction band as discussed in §5.2.3.

For sample IEE1, an ex-situ multi-filamentary square wire, K_{T_c} is 1.3, whereas for sample FZK1, an in-situ mono-filamentary wire, K_{T_c}=1.2. The K_{T_c} values found here are comparable to those found by Kitaguchi [247] who found a value of K_{T_c}=1.4 for an ex-situ MgB_2/Fe tape. These observed values of K_{T_c} correspond to a relatively small effect, since a 1 % change in strain induces a change in T_c of only $\approx$ 1.3 % ($\Delta T_c \approx 0.5$ K). Note that the similarity between the K_{T_c} values measured for samples FZK1, IEE1 and for the sample reported by Kitaguchi is quite remarkable, since the conductors differ substantially. For example, in-situ and ex-situ conductors differ significantly in homogeneity and purity, which can influence the electron-phonon coupling, so that the strain response of T_c of these conductors can be expected to differ. Furthermore, as discussed in §5.2.3, the superconducting properties of a polycrystalline MgB_2 conductor are for a large part determined by distributed properties of the individual crystallites. Since MgB_2 grains in tapes tend to exhibit more texturing [156], this would cause the "overall" strain response of T_c to behave differently in these conductors. Lastly, the fact that these conductors vary in layout (number of filaments, dimensions and shape) causes the transversal Poisson contraction to deform the conductors differently. Again, this can affect the strain response of T_c.

5.5 Strain Dependence of the Irreversibility Field

Analogous to the determination of K_{T_c}, K_{B_0} is found by measuring the magnetoresistive transitions at different levels of applied strain. The data are shown in figure 5.12a and b, for samples IEE1 and FZK1. Each family of $V(B)$ curves corresponds to a constant temperature and represents a set of selected compressive strain values. Next, the irreversibility field is determined using the criterion 5 % of the normal state resistivity. In this way the temperature dependence of the irreversibility field at selected strain levels is obtained. The curves are depicted in figures 5.12c and d for samples IEE1 and FZK1 respectively. The irreversibility field at zero temperature B_0^* is found through linear extrapolation of the $B^*(T)$ curves, obtaining the strain dependence of B_0^* shown in figures 5.12e and f (samples IEE1 and FZK1 respectively).

Just like T_c, B_0^* turns out to be linearly dependent on strain, so that K_{B_0} can readily be obtained through linear regression. Furthermore, K_{B_0} is also surprisingly similar for both conductors, being $K_{B_0} = 5.5$ for both samples. The strain response of B_0^* is stronger than that of T_c, since a 1 % change in strain induces a change of $\approx$ 5 % in B_0^* (for sample FZK1, this corresponds to 1 T).

Also plotted in figures 5.12c and d is the magnetic field at the onset of su-

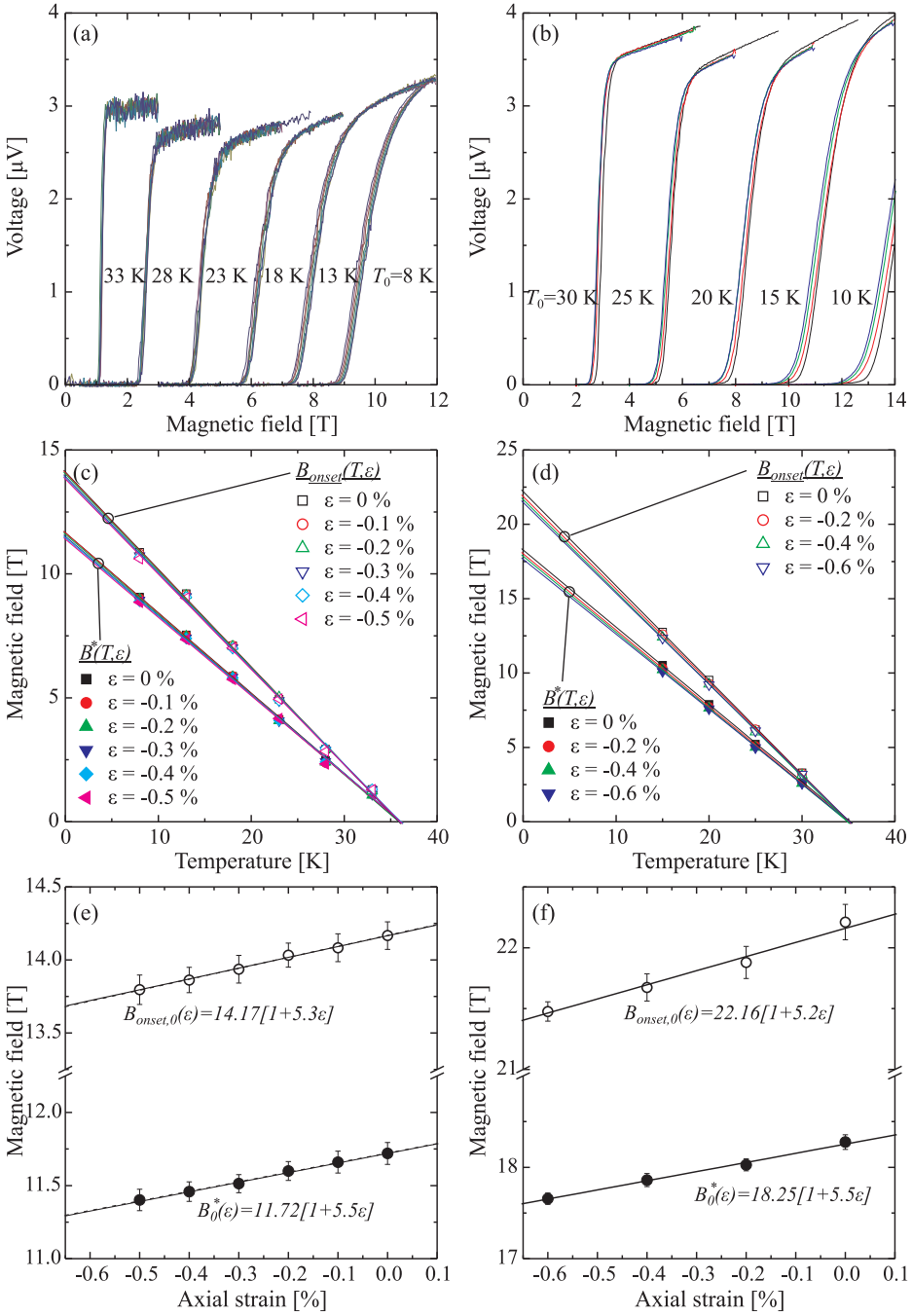

Figure 5.12: Reversible variation of the irreversibility field with axial strain. (a),(c) and (e) correspond to sample IEE1; (b)(d)(f) to sample FZK1. (a) and (b) are the magneto-resistive transition at selected temperatures and strains. (c) and (d) are the corresponding temperature dependent irreversibility- and onset fields. (e) and (f) are the strain dependence of the zero-temperature extrapolation of the irreversibility field and onset field

perconductivity B_{onset} as a function of temperature at different strain states. Extrapolating these data to zero temperature results in the strain dependence of $B_{\text{onset},0}$, plotted in figures 5.5e and f. Clearly, strain shifts the magneto-resistive transition as a whole, so that the strain response of $B_{\text{onset},0}$ is similar to that of B_0^* for both samples, just like the resistive transition with temperature shown in figure 5.11. A-priori, this is rather unexpected.

As discussed in §5.2.3, the measured $B_{\text{onset},0}$ approximates the second critical field $B_{c2,0}$, while $B_{\text{offset},0}$ should correspond to irreversibility field B_0^*. If this is indeed the case then $B_{\text{onset},0}$ should also be proportional to the thermodynamic critical field $B_c(0)$. As suggested by several experiments [2,248], MgB_2 is a BCS-like material with $B_c(0)$ proportional to the gap energy $\Delta(0)$. Summarising this mathematically, one would expect

$$B_{\text{onset},0} \approx B_{c2,0} = \sqrt{2}\kappa B_c(0) = \sqrt{8\pi N(0)}\kappa\Delta(0), \tag{5.13}$$

in which κ is the Ginzburg-Landau parameter, defined as the ratio of the London penetration depth to the coherence length; and $N(0)$ is the density of states. The irreversibility field B_0^* , on the other hand, can be seen as a crude measure of the effective pinning potential. As such, in a first approximation it is expected to be proportional to the condensation energy [67]. The latter is proportional to to the square of $\Delta(0)$, leading to the expectation

$$B_0^* \propto \Delta^2(0). \tag{5.14}$$

Combining (5.13) and (5.14) shows that B_0^* is proportional to the square of $B_{\text{onset},0}$, i.e.

$$B_0^* \propto B_{\text{onset},0}^2. \tag{5.15}$$

Consequently, when strain is applied to a sample, a-priori the variation of B_0^* is expected to be twice that of $B_{\text{onset},0}$:

$$\frac{1}{B_0^*}\left(\frac{\mathrm{d}B_0^*(\varepsilon)}{\mathrm{d}\varepsilon}\right) = \frac{2}{B_{\text{onset},0}}\left(\frac{\mathrm{d}B_{\text{onset},0}(\varepsilon)}{\mathrm{d}\varepsilon}\right). \tag{5.16}$$

As suggested before, this clearly is not the case in the conductors under study, since the measured slopes of $B_0^*(\varepsilon)$ and $B_{\text{onset},0}(\varepsilon)$ are virtually equal.

In order to understand the discrepancy between the first order approximation described above and the actual measurements, it would be insightful to study the strain or pressure dependence of B_0^* and $B_{\text{onset},0}$ in MgB_2 single crystals. In this way any "averaging" of the anisotropic superconducting properties of the individual crystallites over the whole polycrystalline filaments [236] can be ruled out. These conditions will allow, for example, to verify the assumption that B_{c2} and B_c indeed respond similar to strain, which is implicitly assumed in expression (5.13) and is not necessarily the case, for instance if the Ginzburg-Landau parameter κ itself is strain dependent.

5.6 Scaling the Strain Dependence of the Critical Current

With both the strain dependence of the critical temperature T_c and the zero-temperature extrapolation of the irreversibility field B_0^* determined, it is now possible to see whether the strain response of the critical current can indeed be scaled, i.e. whether a relation of the form (5.12) can be found. Such scaling implies that the critical current at any field and temperature can be described according to

$$\frac{I_c(B,T,\varepsilon)}{I_{c,0}(\varepsilon)} = f\left(\frac{B}{B_0^*(\varepsilon)}, \frac{T}{T_c(\varepsilon)}\right), \tag{5.17}$$

with f a function that does not depend explicitly on ε. Combining with (5.9) yields

$$\begin{aligned} &K_{I_c}(B,T) = K_{I_{c,0}} - \frac{1}{f}\left(\frac{\partial f}{\partial t}\right)_b tK_{Tc} - \frac{1}{f}\left(\frac{\partial f}{\partial b}\right)_t bK_{B_0} \\ &\text{with } t \equiv \frac{T}{T_c}; b \equiv \frac{B}{B_0^*}. \end{aligned} \tag{5.18}$$

This expression has the form of (5.12) and describes the strain response of the entire critical surface in terms of the variations of its three "corner points" only. In order to verify if (5.18) indeed describes the observed strain behaviour of the critical current at any field and temperature, three possible cases are considered:

1. The field-temperature scaling relation f of the critical current (5.17) is known analytically;
2. The field-temperature scaling relation f of the critical current (5.17) is only known numerically;
3. The field-temperature scaling relation f of the critical current (5.17) is known analytically *and* the three scaling parameters $K_{I_{c,0}}$, K_{T_c} and K_{B_0} are known.

5.6.1 Scaling Relation is known Analytically

In §3.2.1, an analytical expression (equation (3.1)) was introduced that approximates the experimentally observed critical surface of bulk MgB_2, as well as that of most MgB_2 composite conductors:

$$\begin{aligned} &\frac{I_c(B,T)}{I_{c,0}} = \left(1 - \frac{T}{T_c}\right) \exp\left[-\frac{B}{B_p(T)}\right], \\ &\text{with } B_p(T) = B_{p,0}\left(1 - \frac{T}{T_c}\right). \end{aligned} \tag{3.1}$$

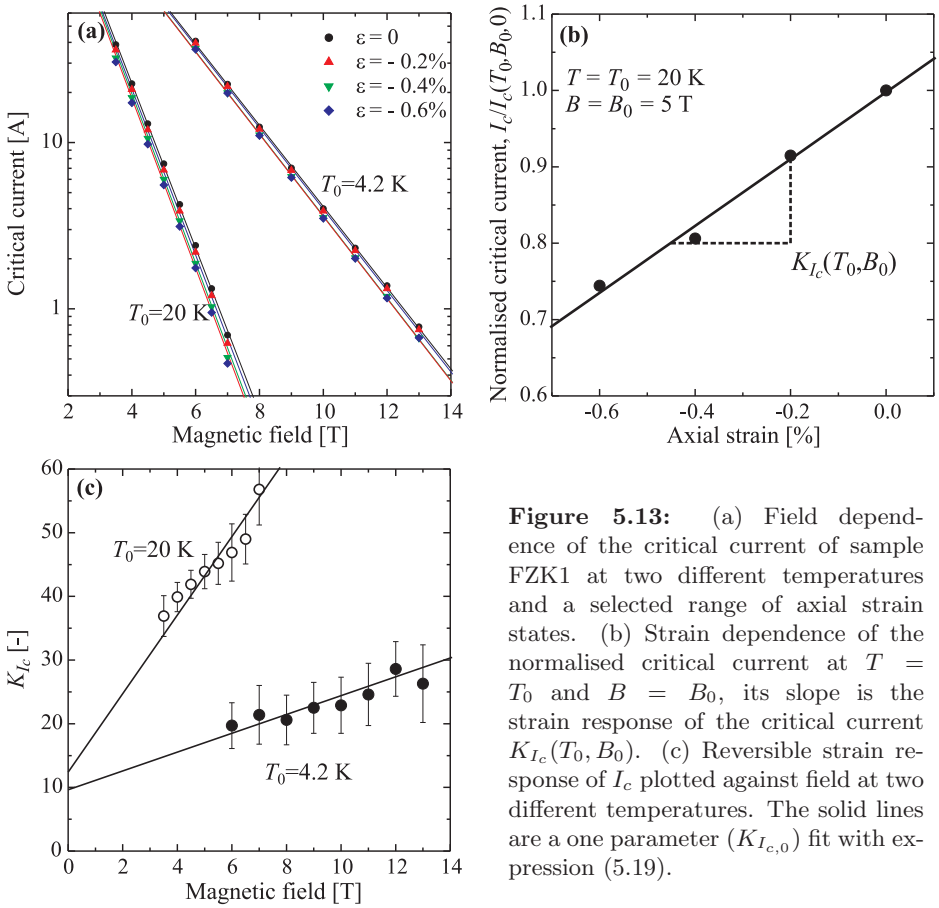

Figure 5.13: (a) Field dependence of the critical current of sample FZK1 at two different temperatures and a selected range of axial strain states. (b) Strain dependence of the normalised critical current at $T = T_0$ and $B = B_0$, its slope is the strain response of the critical current $K_{I_c}(T_0, B_0)$. (c) Reversible strain response of I_c plotted against field at two different temperatures. The solid lines are a one parameter ($K_{I_{c,0}}$) fit with expression (5.19).

Indeed, (3.1) has the form of (5.17). Moreover, as shown in figure 5.13a, the scaling relation (3.1) satisfactory describes the critical current data of the unstrained sample FZK1 using $I_{c,0} \approx 5100$ A, $T_c = 35.3$ K and $B_{p,0} = 2.02$ T.

So with expression (3.1) as a satisfactory scaling relation, equation (5.18) can be written as:

$$K_{I_c}(B,T) = K_{I_{c,0}} + \frac{T}{T_c - T}\left(1 + \frac{B}{B_p(T)}\right) K_{Tc} + \left(\frac{B}{B_p(T)}\right) K_{B_0}. \qquad (5.19)$$

Also plotted in figure 5.13a are the $I_c(B,T)$ data measured at four different levels of compressive strain. Linear regression of $I_c(\varepsilon)$ at constant temperature and field yields the strain response of the critical current K_{I_c}, which as an example is plotted in figure 5.13b for $T = 20$ K and $B = 5$ T. As already noted in §5.3, it is clear that the K_{I_c} depends on both magnetic field and temperature. Knowing $K_{T_c}(=1.2)$ and $K_{B_0}(=5.5)$ from §5.4 and §5.5 respectively, expression (5.19) can be fit to the measured data with only one remaining free parameter $K_{I_{c,0}}$. The

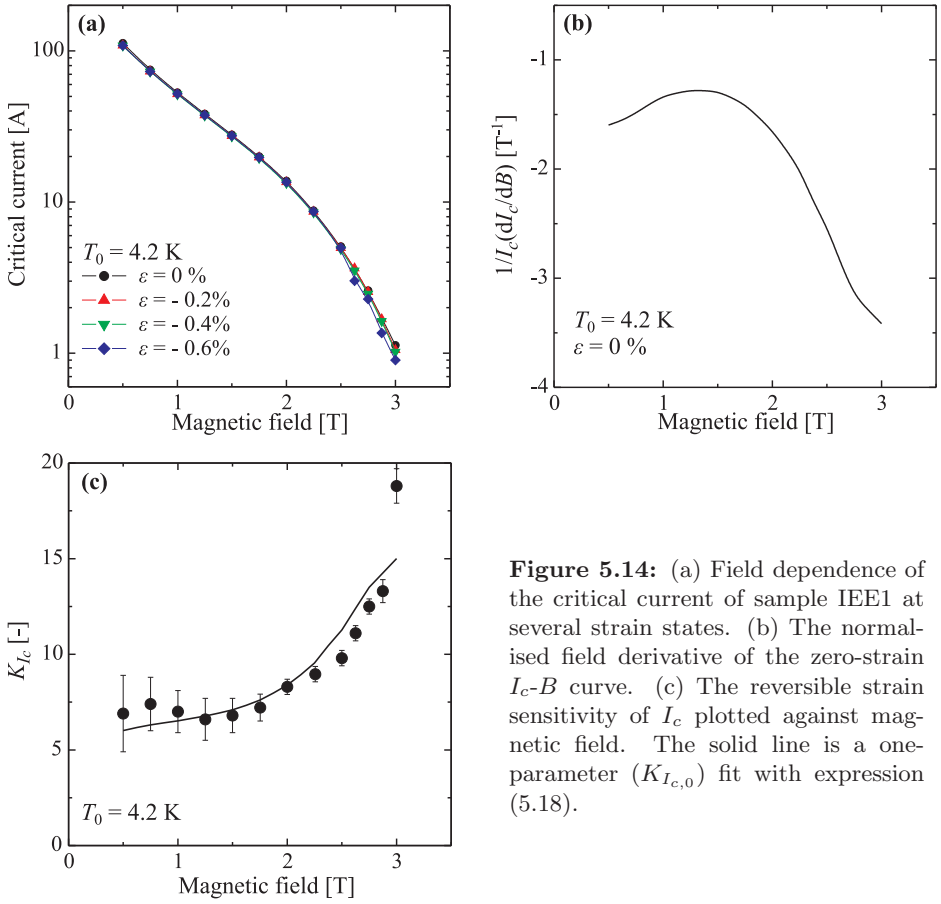

Figure 5.14: (a) Field dependence of the critical current of sample IEE1 at several strain states. (b) The normalised field derivative of the zero-strain I_c-B curve. (c) The reversible strain sensitivity of I_c plotted against magnetic field. The solid line is a one-parameter ($K_{I_{c,0}}$) fit with expression (5.18).

solid lines in figure 5.13c are the result of a least squares fit of expression (5.19) to the measured K_{I_c} data, yielding a value of $K_{I_{c,0}}$ of 9.3. It is clear that expression (5.19) is indeed able to describe the field and temperature dependence of the strain response of the critical current.

5.6.2 Scaling Relation is known Numerically

In contrast to sample FZK1, figure 5.14a shows that sample IEE1 does not exhibit an exponential dependence of the critical current with magnetic field. In fact, it shows a poor performance in magnetic field with a strong downturn of $I_c(B)$ at 4.2 K for fields above 2 T (see also figure 5.14b), probably caused by handling damage during sample mounting. Consequently, it is difficult to describe the field-temperature dependence of the critical current analytically. This data are presented to show that also for this case, expression (5.18) can still be used to describe the strain response of the critical current, using numerical data.

The second term on the right hand side in (5.18) (the temperature dependence) can be estimated to be of the order 0.1 at 4.2 K, while the strain dependence of the critical current K_{I_c} is measured to be of the order 10 (figure 5.14c), so that this second term can be neglected at $T = 4.2$ K. The normalised field derivative of the critical current is calculated numerically from the measured $I_c(B)$ dependence and is plotted in figure 5.14b.

Knowing that $K_{B_0} = 5.5$ and $B_0^* = 11.7$ T from §5.5, expression (5.18) can again be fit to the $K_{I_c}(B)$ data with $K_{I_{c,0}}$ as a single free parameter. Using $K_{I_{c,0}} = 5.3$ results in the solid line in figure 5.14c. Clearly, also in this case expression (5.18) describes the measured $K_{I_c}(B)$ data well. It can be seen that $K_{I_c}(B)$ does not show a linear behaviour like sample FZK1, which is a direct reflection of the downturn in the $I_c(B)$ curve.

5.6.3 Scaling Relation is known Analytically and the Scaling Parameters are known

In §5.6.1 and §5.6.2 it was shown how (5.18) indeed applies to the measured strain response of $I_c(B,T)$ of samples FZK1 and IEE1, respectively. Of course, the practical use of a scaling relation such as (5.18) lies in its predictive value. This is demonstrated in this paragraph.

When a (hypothetical) conductor is considered of which function (5.17) is known, as well as the three scaling parameters $K_{I_{c,0}}$, K_{T_c} and K_{B_0}, then expression (5.18) can readily be used to *predict* the strain response of the critical surface. Using expression (3.1) as the analytical description of the critical surface, so that expression (5.18) can be written in the form of (5.19), and taking $K_{I_{c,0}} = 10$, $K_{T_c} = 5$ and $K_{B_0} = 1$ for the three scaling parameters (similar to sample FZK1), results in a strain response of the critical surface K_{I_c} as depicted in figure 5.15.

Interestingly, the strain response of the critical current can show relatively high values ($K_{I_c} \sim 50$ or even higher) compared to the values of the strain responses of T_c, B_0^* and $I_{c,0}$, especially close to the line $B^*(T)$. This is a direct result from the strong field dependence of I_c, together with the fact that the current decay field B_p is strongly dependent on the temperature (i.e. $B_p \to 0$ when $T \to T_c$), which causes the last term in (5.18) to dominate.

5.7 Conclusion

The strain response of the critical current is found to exhibit two distinct regimes: 1) in the compressive strain regime or for moderate tensile strains, the critical current shows a linear and reversible dependence on strain; and 2) when a certain sample-dependent reversible strain limit $\varepsilon_{\mathrm{rev}}$ is exceeded, the critical current shows a steep and irreversible degradation.

By estimating the thermal pre-compression $\varepsilon_{\mathrm{pre}}$ that the matrix and sample holder exert on the MgB_2 filaments, it was found that the reversible strain limit is, to first order, determined by this thermal pre-compression strain.

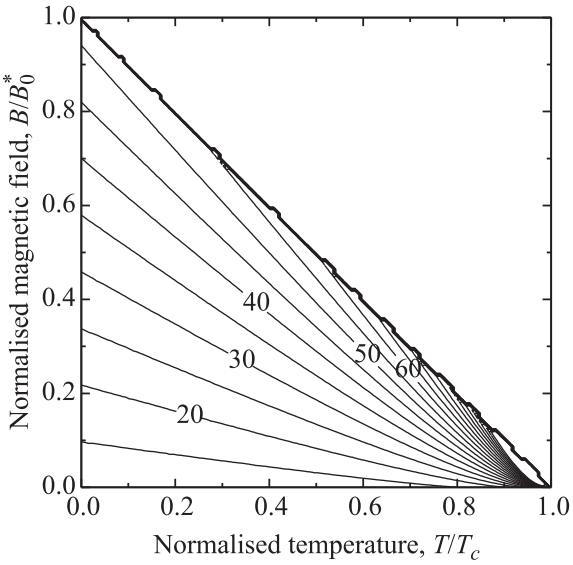

Figure 5.15: Calculated strain response K_{I_c} of a hypothetical conductor as a function of the normalised field and -temperature, of which the field-temperature scaling of I_c is known as well as the three scaling parameters $K_{I_{c,0}}$, K_{T_c} and K_{B_0}. The parameters are chosen such that this hypothetic conductor is similar to sample FZK1. The magnetic field is normalised to the zero-temperature extrapolation of the irreversibility field B_0^*, while the temperature is normalised to the critical temperature T_c.

Measurements of the resistive and magneto-resistive transitions of strained samples shows that both the critical temperature T_c and the irreversibility field B^* are strain dependent. Just like the critical current, they depend linearly and reversibly on axial strain.

The studied conductors show a remarkably similar strain dependence in both the T_c and B^*, despite the fact that these conductors are inherently different trough their precursor powder (in-situ versus ex-situ), matrix material and layout (shape, dimensions and number of filaments). All these aspects can influence texture, homogeneity and purity of the filaments, but apparently they do not affect the effective strain dependence of T_c and B^*.

It is also found that the strain dependence of the magneto-resistive transitions does not follow the expected behaviour based on simple BCS-like arguments, which would predict the strain sensitivity of B_0^* to be twice that of $B_{c2,0}$. The reason for this is at present unclear and further studies of strained single crystals or single crystals under hydrostatic pressure are suggested to clarify this issue.

Combining the strain dependence of I_c, T_c and B^*, it was found that the slope $K_{I_c}(B,T)$ of the linear and reversible $I_c(\varepsilon)$ regime at any temperature and mag-

netic field can be described with the strain sensitivities of the zero-temperature, zero-field extrapolation of the critical current ($K_{I_{c,0}}$), the critical temperature (K_{T_c}) and the zero-temperature extrapolation of the irreversibility field (K_{B_0}).

Chapter 6

Conclusion

In the previous chapters several aspects related to the application of technical MgB_2 conductors in magnets were studied. These include whether the $J_c(B,T)$ performance is suitable for magnet operation; prospects for further development of the material; and how MgB_2 conductors respond to thermal instabilities and electro-mechanical forces. The main findings and conclusions are brought together in this chapter and are used to address the general suitability of MgB_2 superconductors for magnet applications.

This thesis work was motivated by the discovery of superconductivity in MgB_2, a material with several attractive features that, taken together, make it a useful and practical superconductor. At an estimated materials cost of about 0.80 €/m for filaments and matrix together MgB_2 constitutes a relative low-cost superconductor, provided that the manufacturing cost can be kept low. Furthermore, with a critical temperature of 40 K it can be operated at a higher temperature than Nb-Ti and Nb_3Sn. Compared to high-T_c conductors MgB_2 is a relatively simple compound. Lastly, MgB_2 conductors can be made with the powder-in-tube technology already used for Nb_3Sn and high-T_c conductors.

In order to gauge the applicability of MgB_2 conductors in magnets, three areas of attention were defined: 1) cost-efficient fabrication of MgB_2 conductors with suitable $J_c(B,T)$ performance; 2) the possibility to protect MgB_2-based magnets from thermal instabilities; and 3) the influence of mechanical deformations in magnets on the superconducting properties of MgB_2 conductors. These issues were formulated as questions in the introductory chapter 1 and will be answered here.

1) Is the $J_c(B,T)$ performance of MgB_2 conductors suitable for magnet applications?

Experience with previously developed practical superconductors learns that the $J_c(B,T)$ performance of a conductor depends on the degree of electrical connectivity that can be obtained between the crystallites in the filament and on the field retention of J_c, which is determined by flux-line pinning and the value of B_{c2}. In MgB_2 these factors depend strongly on the deformation technique, mechanical strength of the matrix material and the precursor powder (in- and ex-situ, pure MgB_2 or doped). The literature study in chapter 3 on the $J_c(B)$ performance of reported conductors in the years 2003-2006 reveals that the top 50 % of the conductors have self-field extrapolated critical current density values falling in a relatively narrow range of $J_{c,0}^T = 10^4 - 10^5$ A/mm^2 at 4.2 K. The self-field extrapolation of J_c appears to be a purely connectivity determined parameter as it is not correlated with its field retention, i.e. pinning or changes in the second critical field B_{c2}. Thus, the upper limit of J_c seems to be $10^4 - 10^5$ A/mm^2 at 4.2 K and is imposed by an upper limit in the connectivity.

Less clear to quantify at present is an upper limit of the in-field performance, i.e. the field retention of J_c. First, the field retention of J_c has continued to improve between 2003 and 2006. The median value of technical upper field limit B_{100} above which J_c drops below 100 A/mm^2 has increased by 25 % over the four years to a present value of 7 T. Related to this is a general shift of focus towards in-situ conductors in which low level doping is better controlled and the field retention has increased accordingly. A second reason that a possible upper limit in the field retention is still difficult to gauge is the fact that the mechanism of carbon-based doping is at present unclear. Comparison of non-carbon and carbon based dopants shows that the latter tends to increase the field retention by $\sim$ 50 % compared to undoped conductors, while non-carbon based dopants tends to increase the field retention by only $\sim$ 15 %. This could suggest that

carbon based dopants improve both pinning and B_{c2}, while the non-carbon based dopants only increase pinning. Further study of the effect of carbon-based dopants will reveal the mechanism of the enhancement and might well open possibilities to improve the field retention even further. At the time of writing this thesis, the conductor with the best field retention showed a B_{100} value of 13 T.

Literature data concerning higher temperatures is sparse, a point which could be addressed better in future work. Nevertheless, generally speaking both $J_{c,0}^{T}$ and B_{100} decrease with a factor of ~ 2 when going from 4.2 to 20 K. High-temperature applications at 20 K with still sufficient current density at fields of 3-5 T are thus already feasible with state-of-the-art conductors, while also here ongoing development is likely to push this field limit up.

In view of the $J_c(B,T)$ performance, this work addresses the question which combination of deformation techniques, matrix materials and precursor powders is the most successful. In chapter 2 the fabrication of ex-situ PIT conductors using different matrix- materials and layout and different deformation techniques is described. It was found that with wire drawing alone using either a Fe or a bi-metal Cu/Fe matrix insufficient powder densification is reached to obtain high J_c values. Significantly better J_c performance was found by using after wire drawing also the flat-rolling technique with a Fe matrix.

Critical current density values of the ex-situ conductors enhances significantly after a heat treatment at 950 °C, by a factor of ~ 10 in drawn wires and ~ 100 in flat rolled tapes. The MgB_2 grains show the neck growth behaviour typical for sintering, causing the grain-to-grain connectivity to increase. Another way to enhance the apparent $J_c(B,T)$ performance is the addition of soft metals such as Pb. The mechanism behind this improved performance is an increase in thermal stability at higher currents, i.e. at low magnetic field. Also, Pb acts as a lubricant during drawing so that powder flow is improved, allowing for a higher overall area reduction compared to Pb-free conductors. However, the grain-to-grain connectivity is compromised with Pb additions.

These observations together indicate that for the ex-situ route with pure MgB_2 powder, the most suitable technique is flat-rolling. The fact that drawing alone leads to insufficient powder density is mainly caused by the poor flow characteristics of hard particles at higher density. Also in the literature study it is found that most successful ex-situ conductors are fabricated with rolling techniques (i.e. flat-rolling or two-axial rolling), in contrast to the in-situ route where the relatively soft Mg facilitates powder flow and wires are successfully fabricated with drawing. For applications at low magnetic field, Pb-containing ex-situ conductors can be useful, in which Pb serves not only as lubricant during deformation but also as an internal stabiliser especially when a high strength and therefore usually poorly conducting matrix material is required. The effect of Pb can be further optimised by investigating lower concentrations between 1 and 5 %.

2) Given the conductors matrix materials and operating temperature, can a MgB_2 magnet be protected against thermal instabilities?

The key parameters needed to answer this question are the propagation velocity of the normal conducting zone v_{nz} and the minimum quench energy MQE. A high v_{nz} value implies that the heat generated in the normal zone is distributed over a large volume and that the temperature rise remains limited. Also, a higher normal zone voltage is generated, detection becomes easier so that appropriate measures can be taken faster. As described in chapter 4, these parameters were studied both experimentally and numerically. Since MgB_2 is particularly beneficial for applications in conduction-cooled magnet systems operating at a temperature of ~ 20 K, it is important to characterise and model the normal zone development under relevant conditions. For this purpose a versatile quasi-adiabatic experimental set-up is developed with which intrinsic normal zone development can be measured as function of temperature, magnetic field and transport current.

Typical propagation velocities of the normal zone in MgB_2 conductors range from 1 to 100 cm/s, depending on the conductors' matrix layout, filament properties and experimental boundary conditions. Compared to high-T_c conductors, in which normal zone development can be described as static heating, detection is relatively simple. Compared to low-T_c conductors, on the other hand, v_{nz} is typically a factor 100 lower, mainly due to the higher temperature margin. At a higher operating temperature v_{nz} decreases further due to the increased heat capacity. Even for samples with very different matrix materials and tested at a wide range of current densities v_{nz} reaches a minimum value ranging from 1 to 50 cm/s at $T \approx 20$ K. Thus, normal zone detection in MgB_2 conductors is certainly possible but will require more care than in low-T_c conductors.

On the other hand, the probability that a normal zone occurs, which is inversely proportional to MQE, is a factor ~ 1000 lower than in low-T_c conductors. Again this is mainly due to the higher thermal margin. Similarly to v_{nz}, MQE increases with temperature due to the increasing heat capacity and typically reaches a maximum at 20 K. At higher temperatures MQE decreases again due to the decreasing thermal margin. The maximum MQE values range from 20 to 300 mJ, depending on the conductors' matrix material and current densities. Thus, MgB_2 tends to be the most stable at an operating temperature of 20 K.

As a tool for magnet design, classical analytical models fail to predict v_{nz} and MQE accurately, mainly because they fail to take into account the filament behaviour in detail and the temperature dependence of the material properties. These factors affect the heating function during the super- to normal-conducting transition strongly and should be included. Including the voltage-current relation (n-value) and the temperature dependence a new numerical algorithm was developed that predicts the experimental data with ~ 5 % accuracy. This model is not just a valuable aid for magnet design, but also allows to calculate v_{nz} and MQE of hypothetical conductors, so that selected parameters can be optimised in the very first stage of conductor design.

Compared to conductors with relatively low n-values of about 10, the ones

that have high n-values of about 100 show MQE values that are $\sim$ 25 % lower, while their v_{nz} is a factor of $\sim$ 2 higher. Thus, at the expense of somewhat reduced stability, the detection of a normal conducting zone becomes easier. The conductivity of the matrix material mainly influences MQE: a conductor with a Fe matrix, for example, shows a factor 20 lower MQE value than one with a Cu matrix at a similar current density. At the same time v_{nz} and thus the ease of protection is hardly influenced due to the competing effects of resistivity (heat generation) and thermal conductivity (heat drainage). Thus, further development of MgB_2 conductors should continue to focus also on the implementation of highly conducting matrix materials.

3) Given a MgB_2 conductor with a certain matrix, does it support the electromagnetic forces acting on a magnet?

Also the answer to this question depends largely on the choice of matrix material. In chapter 5 it is described that the strain dependence of the critical current has two distinct regions. For compressive and moderate tensile strains, the critical current depends linearly and reversibly on strain. When a certain sample-dependent reversible strain limit is exceeded, the critical current degrades steeply and irreversibly. The reversible strain limit is, to first order, determined by the thermal pre-compression that the matrix exerts on the filaments. The maximum strain that a conductor can tolerate can thus be increased by choosing a matrix material that has a relatively large thermal expansion coefficient compared to the filaments.

The reversible linear regime is also important since strain-induced reversible changes in the current carrying capability can become significant, especially at higher magnetic field and temperature. It is shown that in this regime not only J_c changes linearly with strain but also the critical current T_c and the irreversibility field B^*. The strain dependence of J_c has a clear electronic origin, of which the exact mechanism is still unclear. Nevertheless, it was shown that the strain dependence of the whole critical surface for a given conductor can be predicted with only three parameters: the strain sensitivity of the zero-temperature, zero-field extrapolation of I_c; that of the critical temperature; and that of the zero-temperature extrapolation of the irreversibility field.

In summary, the answer to our initial questions is that present-day MgB_2 already constitutes a practical material for magnet applications requiring a peak magnetic field of 7-10 T at 4.2 K or 3-5 T at 20 K and these field limits are likely to increase further. From a technical point of view, thermal stability and electro-mechanical issues will, just like with other technical superconductors, require careful design which is best addressed already in the stage of material development. It is my hope that the tools and insights laid down in this thesis will form a useful contribution to these developments.

Appendix A

Properties of Published Magnesium Diboride Conductors

In chapter 3 a literature survey of the transport $J_c(B)$ performance of MgB_2 conductors published over the years 2003 to 2006 is presented. Selected properties of the conductors are tabulated in this appendix. The conductors are categorised by year, shape, precursor powder, number of filaments, final deformation, matrix material and additions. The values of the figures of merit, B_{100}, B_p and $J_{c,0}^T$ at 4.2 K, with which the statistical analysis in chapter 3 is conducted are also tabulated.

Table A.1: Overview of references and selected properties of published MgB_2 conductors. The **shape** of the conductor can be a Wire, Tape or Other; **MgB_2 precursor** can be Ex-situ, In-situ or Other; the **number of filaments** can be either Mono or MUlti in which case the number of filaments is also listed; **final deformation** is DRawn, Extruded, Swaged, FlatRolled, GrooveRolled, 4Rolled or Other. In the columns **matrix** and **additions** the elements are denoted by their usual symbols. Other materials that occur in these columns are Monel Steel, Stainless Steel and Carbon Nano Tubes. Irradiated samples are also noted as additions.

									Perpendicular field			**Parallel field**		
First Author	**Ref**	**Year**	**Shp.**	**Prc.**	**# Fil.**	**Fin. Def.**	**Mat.**	**Add.**	B_{100} **[T]**	B_p **[T]**	$J_{c,0}^T$ **[A/mm^2]**	B_{100} **[T]**	B_p **[T]**	$J_{c,0}^T$ **[A/mm^2]**
Arda	[139]	2005	W	I	M	DR	Fe/Mon.		12.7	1.4	7000000			
Bhatia	[122]-1	2004	W	I	M	DR	Cu		1.5	1.1	400			
Bhatia	[122]-2	2004	W	I	M	DR	Cu		4.2	1.7	1100			
Bhatia	[122]-3	2004	W	I	M	DR	Fe		7.7	1.9	6200			
Bhatia	[122]-4	2004	W	I	M	DR	Cu		6.4	3.2	700			
Braccini	[8]	2006	T	E				C				13.6	3.2	7200
Chen	[141]-1	2005	W	I	M	DR	Fe					5.1	1.6	2700
Chen	[141]-2	2005	W	I	M	DR	Fe					4.7	1.5	2000
Chen	[141]-3	2005	W	I	M	DR	Fe					5.8	1.5	5500
Chen	[141]-4	2005	W	I	M	DR	Fe					4.2	1.4	1900
Chen	[141]-5	2005	W	I	M	DR	Fe	CNT				6.5	1.5	6800
Chen	[141]-6	2005	W	I	M	DR	Fe	CNT				6.4	1.7	5100
Chen	[141]-7	2005	W	I	M	DR	Fe	CNT					1.7	6500
Chen	[141]-8	2005	W	I	M	DR	Fe	CNT					1.7	5800
Chen	[141]-9	2005	W	I	M	DR	Fe	SiC				7.0	2.3	2400
Chen	[141]-10	2005	W	I	M	DR	Fe	SiC				5.9	2.0	1700
Chen	[141]-11	2005	W	I	M	DR	Fe	SiC					2.1	2800
Chen	[141]-12	2005	W	I	M	DR	Fe	SiC				6.2	2.0	2000
Civale	[97]-1	2003	W	E	M	DR	SS		1.5	1.5	300			
Civale	[97]-2	2003	W	E	M	DR	SS			1.7	< 100			
Civale	[97]-3	2003	W	E	M	DR	SS		6.0	1.5	6200			
Collings	[92]-1	2003	W	I	M	DR	Fe/Mon.		5.3	1.8	2000			
Collings	[92]-2	2003	W	I	M	DR	Fe/Mon.		5.2	1.0	15300			
Dhalle	[142]-1	2005	W	I	M	DR			5.3	1.8	1100			
Dhalle	[142]-2	2005	W	E	MU	4R			1.3	0.5	1300			
Dou	[98]-1	2003	W	I	M	DR	Fe		7.8	1.5	15700			
Dou	[98]-2	2003	W	I	M	DR	Fe	SiC	12.0	2.8	7300			

Continued on next page

First Author	Ref	Year	Shp.	Prc.	# Fil.	Fin. Def.	Mat.	Add.	Perpendicular field			Parallel field		
									B_{100} [T]	B_p [T]	$J_{c,0}^T$ [A/mm^2]	B_{100} [T]	B_p [T]	$J_{c,0}^T$ [A/mm^2]
Eisterer	[143]-1	2005	W	I	M	DR	Fe/SS					7.2	1.4	16400
Eisterer	[143]-2	2005	W	I	M	DR	Fe/SS	Irr.				8.8	1.7	16300
Eisterer	[144]-1	2005	W	I	M	DR	Fe/SS					7.2	1.4	16400
Eisterer	[144]-2	2005	W	I	M	DR	Cu					3.4	0.8	6500
Eisterer	[144]-3	2005	W	I	M	DR	Cu	Irr.				5.6	1.2	10800
Eyidi	[99]-1	2003	T	E	M	FR	Fe					5.8	1.2	12500
Eyidi	[99]-2	2003	W	E	M	DR	SS/Fe		5.4	1.9	1800			
Fabbric.	[100]	2003	T	E	MU4	4R	Fe		2.5	0.5	11100			
Fang	[101]	2003	T	E	M	FR	Fe							
Fang	[145]-1	2005	T	I	M	FR	Fe		2.9	0.7	7100			
Fang	[145]-2	2005	T	I	M	FR	Fe					5.6	2.2	1500
Fang	[146]	2005	W	I	M	GR	Cu							
Feng	[102]	2003	W	I	M	DR	Fe		7.6	1.4	26600			
Feng	[103]	2003	W	I	M	DR	Fe		6.1	0.9	76100			
Feng	[123]-1	2004	W	I	M	DR	Fe		9.5	2.7	3400			
Feng	[123]-2	2004	W	I	M	DR	Fe		10.5	3.0	3500			
Feng	[123]-3	2004	W	I	M	DR	Fe		8.2	1.9	6600			
Feng	[123]-4	2004	W	I	M	DR	Fe		6.8	1.7	5600			
Fischer	[104]-1	2003	T	E	M	FR	Fe					9.1	1.8	15700
Fischer	[104]-2	2003	T	E	M	FR	Fe					7.7	2.0	4700
Fischer	[104]-3	2003	T	E	M	FR	Fe					8.0	2.0	5135
Fischer	[104]-4	2003	T	E	M	FR	Fe					9.0	1.2	133200
Fischer	[124]-1	2004	T	E	M	FR	Cu					3.3	2.1	500
Fischer	[124]-2	2004	T	E	M	FR	Cu					2.2	2.9	200
Fischer	[124]-3	2004	T	E	M	FR	Cu					2.0	2.2	300
Fischer	[124]-4	2004	T	E	M	FR	Fe					9.1	1.8	16600
Fischer	[124]-5	2004	T	E	M	FR	Fe					7.7	1.9	5400
Fischer	[124]-6	2004	T	E	M	FR	Fe					8.9	1.3	87300
Fischer	[124]-7	2004	T	E	M	FR	Fe					9.2	1.8	17000
Fischer	[124]-8	2004	T	E	M	FR	Fe					9.2	1.6	29600
Fischer	[124]-9	2004	T	E	MU19	FR	Fe					10.0	2.1	11700
Fischer	[124]-10	2004	T	E	M	FR	Fe					6.6	2.0	2700
Fischer	[124]-11	2004	T	E	M	FR	Fe					10.1	2.0	16900
Fischer	[124]-12	2004	T	E	M	FR	Fe					8.3	1.9	7300
Fischer	[124]-13	2004	T	E	M	FR	Fe					9.9	1.8	21500
Flukiger	[55]-1	2003	T	E	M	FR	Fe					6.7	1.1	42000

Continued on next page

First Author	Ref	Year	Shp.	Prc.	# Fil.	Fin. Def.	Mat.	Add.	Perpendicular field			Parallel field		
									B_{100} [T]	B_p [T]	$J_{c,0}^T$ [A/mm^2]	B_{100} [T]	B_p [T]	$J_{c,0}^T$ [A/mm^2]
Flukiger	[55]-2	2003	T	E	M	FR	Fe					1.4	1.6	200
Flukiger	[55]-3	2003	T	E	M	FR	Fe					5.2	0.9	38400
Flukiger	[55]-4	2003	T	E	MU7	FR	Fe					4.6	0.7	59600
Fu	[105]-1	2003	W	I	M	DR	Fe		6.1	1.1	33300			
Fu	[105]-2	2003	W	I	M	DR	Ta/Cu		2.0	0.6	3300			
Fu	[125]	2004	T	E	M	FR	CuNi		0.1	1.9	100			
Fuji	[106]-1	2003	T	I	M	FR	Fe	WB				7.5	1.6	12500
Fuji	[106]-2	2003	T	I	M	FR	Fe	WB				8.8	1.7	15500
Fuji	[106]-3	2003	T	I	M	FR	Fe	WB				8.3	1.7	14500
Fuji	[107]-1	2003	T	I	M	FR	St.					1.8	1.5	300
Fuji	[107]-2	2003	T	I	M	FR	St.					5.2	1.8	1900
Fuji	[107]-3	2003	T	I	M	FR	St.					7.1	1.6	8600
Fuji	[107]-4	2003	T	I	M	FR	St.					5.6	1.5	3800
Fuji	[107]-5	2003	T	I	M	FR	St.					6.1	1.4	9200
Fuji	[107]-6	2003	T	I	M	FR	St.					6.2	1.3	10700
Fuji	[107]-7	2003	T	I	M	FR	St.						0.3	100
Fuji	[107]-8	2003	T	I	M	FR	St.					3.1	1.4	900
Fuji	[107]-9	2003	T	I	M	FR	St.					3.3	1.2	1700
Fuji	[107]-10	2003	T	I	M	FR	St.					2.9	1.1	1300
Fuji	[107]-11	2003	T	I	M	FR	St.					2.3	1.2	600
Fuji	[107]-12	2003	T	I	M	FR	St.					7.1	1.6	9500
Fuji	[107]-13	2003	T	I	M	FR	St.					8.2	1.5	19600
Fuji	[107]-14	2003	T	I	M	FR	St.					6.7	1.5	7600
Fuji	[107]-15	2003	T	I	M	FR	St.		7.5	1.4	18300	8.1	1.6	18200
Fuji	[107]-16	2003	T	E	M	FR	St.		5.3	0.6	1007600	6.1	1.1	22900
Fuji	[107]-17	2003	T	E	M	FR	St.		6.0	0.7	958200	7.4	1.6	10100
Giunchi	[53]-1	2003	W	O	M	DR	St./Nb		6.0	1.1	26700			
Giunchi	[53]-2	2003	W	O	MU7	S	St./Nb		6.1	1.2	15900			
Goldacker	[108]-1	2003	W	E	M	DR	Fe		5.2	1.0	18800			
Goldacker	[108]-2	2003	W	E	M	DR	Fe/SS		4.0	1.1	3400			
Goldacker	[108]-3	2003	W	E	M	DR	Fe/SS		3.9	0.9	9700			
Goldacker	[108]-4	2003	W	E	M	DR	Fe/SS		3.7	0.9	6000			
Goldacker	[126]	2004												
Goldacker	[127]-1	2004	W	I	M	DR	Fe/SS			1.5	< 100			
Goldacker	[127]-2	2004	W	I	M	DR	Fe/SS		1.2	1.5	200			
Goldacker	[127]-3	2004	W	I	M	DR	Fe/SS		3.0	1.4	900			

Continued on next page

First Author	Ref	Year	Shp.	Prc.	# Fil.	Fin. Def.	Mat.	Add.	Perpendicular field			Parallel field		
									B_{100} [T]	B_p [T]	$J_{c,0}^T$ [A/mm^2]	B_{100} [T]	B_p [T]	$J_{c,0}^T$ [A/mm^2]
Goldacker	[127]-4	2004	W	I	M	DR	Fe/SS		1.4	0.8	600			
Goldacker	[127]-5	2004	W	I	M	DR	Fe/SS		2.6	0.9	2200			
Goldacker	[127]-6	2004	W	E	M	DR	Fe/SS		1.1	1.0	300			
Goldacker	[127]-7	2004	W	E	M	DR	Fe/SS		4.9	1.2	5400			
Goldacker	[127]-8	2004	W	I	M	DR	Fe/SS		5.6	1.2	9700			
Goldacker	[127]-9	2004	W	I	M	DR	Fe/SS		5.6	1.2	12500			
Goldacker	[127]-10	2004	W	I	M	DR	Fe/SS		5.8	1.3	7500			
Goldacker	[127]-11	2004	W	I	M	DR	Fe/SS		7.8	1.6	14200			
Goldacker	[128]-1	2004	W	I	M	DR	Fe		5.8	1.2	12900			
Goldacker	[128]-2	2004	W	E	M	DR	Fe		5.5	1.0	19400			
Goldacker	[128]-3	2004	W	E	M	DR	Fe		3.1	1.7	600			
Goldacker	[129]-1	2004	W	I	M	DR	Fe/SS		7.3	1.5	13600			
Goldacker	[129]-2	2004	W	I	M	DR	Fe/SS		8.0	1.5	21200			
Grasso	[58]-1	2003	T	E	M	FR	Ni		2.6	1.7	500			
Grasso	[58]-2	2003	T	E	M	FR	Ni		5.4	2.4	1000			
Grasso	[58]-3	2003	T	E	M	FR	Ni		6.9	1.7	5200			
Grasso	[58]-4	2003	T	E	M	FR	Ni		5.7	1.1	17800			
Grasso	[58]-5	2003	T	E	M	FR	Ni		4.0	0.8	17000			
Grasso	[65]	2004												
Hascicek	[130]	2004												
Hassler	[109]-1	2003	T	E	M	FR	Cu					3.3	2.0	500
Hassler	[109]-2	2003	T	E	MU16	FR	Cu					2.1	2.3	300
Hassler	[109]-3	2003	T	E	M	FR	Cu					2.2	2.6	200
Hassler	[165]-1	2006	T	E	M	FR	Fe					9.3	1.5	52100
Hassler	[165]-2	2006	T	E	M	FR	Fe					9.7	1.6	49800
Hassler	[165]-3	2006	T	E	M	FR	Fe					9.7	1.6	49800
Hassler	[165]-4	2006	T	E	M	FR	Fe					3.1	1.1	1600
Hassler	[165]-5	2006	T	E	M	FR	Fe					9.6	2.0	13600
Hata	[166]-1	2006	T	I	M	FR	Fe					7.9	1.5	23000
Hata	[166]-2	2006	T	I	M	FR	Fe	SiC				10.4	2.3	9600
Hata	[166]-3	2006	T	I	M	FR	Fe	SiC				11.0	2.5	7800
Hishinuma	[167]-1	2006	W	I	M	O	Fe	$MgCu_2$	8.2	1.7	11600			
Hishinuma	[167]-2	2006	W	I	M	O	Fe	$MgCu_2$	7.8	1.6	15000			
Hishinuma	[167]-3	2006	W	I	M	O	Fe	$MgCu_2$	6.3	1.2	23400			
Hishinuma	[167]-4	2006	W	I	M	O	Fe	$MgCu_2$	6.1	1.1	23500			
Holubek	[147]	2005	T	E	M	4R	Fe		4.5	0.9	14500			

Continued on next page

First Author	Ref	Year	Shp.	Prc.	# Fil.	Fin. Def.	Mat.	Add.	Perpendicular field B_{100} [T]	Perpendicular field B_p [T]	Perpendicular field $J_{c,0}^T$ [A/mm^2]	Parallel field B_{100} [T]	Parallel field B_p [T]	Parallel field $J_{c,0}^T$ [A/mm^2]
Jiang	[91]-1	2005	T	I	M	FR	Fe					8.3	1.4	36100
Jiang	[91]-2	2005	T	I	M	FR	Fe					8.6	1.4	42500
Jiang	[91]-3	2005	T	I	M	FR	Fe					9.2	1.4	60200
Jiang	[91]-4	2005	T	I	M	FR	Fe					6.4	1.4	8900
Jiang	[91]-5	2005	T	I	M	FR	Fe					8.2	1.4	30800
Jiang	[91]-6	2005	T	I	M	FR	Fe					9.1	1.5	50700
Jiang	[91]-7	2005	T	I	M	FR	Fe					5.0	1.6	2400
Jiang	[91]-8	2005	T	I	M	FR	Fe	SiC				9.7	2.0	11500
Jiang	[91]-9	2005	T	I	M	FR	Fe	SiC				10.2	2.2	10400
Jiang	[91]-10	2005	T	I	M	FR	Fe	SiC				11.0	2.1	18000
Jiang	[91]-11	2005	T	I	M	FR	Fe	SiC				7.2	2.4	2100
Jiang	[91]-12	2005	T	I	M	FR	Fe	SiC				9.2	2.1	7900
Jiang	[91]-13	2005	T	I	M	FR	Fe	SiC				9.7	2.1	10600
Jiang	[91]-14	2005	T	I	M	FR	Fe	SiC				6.1	2.5	1100
Jiang	[148]-1	2005	T	I	M	FR	Fe					8.2	1.5	23800
Jiang	[148]-2	2005	T	I	M	FR	Fe	Si_3N_4				8.5	1.7	17700
Jiang	[148]-3	2005	T	I	M	FR	Fe	Si_3N_4				8.7	1.7	16000
Jiang	[148]-4	2005	T	I	M	FR	Fe	Si_3N_4				8.7	1.7	16000
Jiang	[148]-5	2005	T	I	M	FR	Fe	Si_3N_4				8.3	1.7	13400
Jiang	[148]-6	2005	T	I	M	FR	Fe	Si_3N_4				7.8	1.7	11100
Jiang	[148]-7	2005	T	I	M	FR	Fe	Si_3N_4				7.2	1.6	10300
Jiang	[149]-1	2005	T	I	M	FR	Fe					7.9	1.4	25000
Jiang	[149]-2	2005	T	I	M	FR	Fe	MgO				8.2	1.4	30900
Jiang	[149]-3	2005	T	I	M	FR	Fe	MgO				8.5	1.5	32600
Jiang	[149]-4	2005	T	I	M	FR	Fe	MgO				8.3	1.5	26000
Jiang	[149]-5	2005	T	I	M	FR	Fe	MgO				8.0	1.5	22300
Jiang	[168]-1	2006	T	I	M	FR	Fe					8.2	1.5	23600
Jiang	[168]-2	2006	T	I	M	FR	Fe	SiC				9.7	1.9	15400
Jiang	[168]-3	2006	T	I	M	FR	Fe	SiC				10.2	2.1	13600
Jiang	[168]-4	2006	T	I	M	FR	Fe	SiC				10.8	2.3	11500
Jiang	[168]-5	2006	T	I	M	FR	Fe	Si_3N_4				8.5	1.7	17200
Jiang	[168]-6	2006	T	I	M	FR	Fe	Si_3N_4				8.7	1.7	15900
Jiang	[168]-7	2006	T	I	M	FR	Fe	Si_3N_4				8.7	1.7	15900
Jiang	[168]-8	2006	T	I	M	FR	Fe	Si_3N_4				8.2	1.7	12700
Jiang	[168]-9	2006	T	I	M	FR	Fe	Si_3N_4				7.8	1.7	10700
Kikuchi	[131]	2004	W	I	M	O	Fe		2.4	0.8	2400			

Continued on next page

First Author	Ref	Year	Shp.	Prc.	# Fil.	Fin. Def.	Mat.	Add.	Perpendicular field			Parallel field		
									B_{100} [T]	B_p [T]	$J_{c,0}^T$ [A/mm^2]	B_{100} [T]	B_p [T]	$J_{c,0}^T$ [A/mm^2]
Kikuchi	[150]	2005	W	I	M	DR	Fe		4.1	1.1	4400			
Kim	[169]-1	2006	W	I	M	DR	Fe		6.6	1.3	19700			
Kim	[169]-2	2006	W	I	M	DR	Fe	CNT	9.2	2.0	9400			
Kim	[170]-1	2006	W	I	M	DR	Fe		6.8	1.4	15000			
Kim	[170]-2	2006	W	I	M	DR	Fe		6.8	1.2	33200			
Kim	[170]-3	2006	W	I	M	DR	Fe	CNT	8.8	1.7	17400			
Kim	[170]-4	2006	W	I	M	DR	Fe	CNT	9.2	1.9	14000			
Kim	[170]-5	2006	W	I	M	DR	Fe	CNT	7.9	1.5	20100			
Kim	[170]-6	2006	W	I	M	DR	Fe	CNT	7.0	1.4	17000			
Kim	[170]-7	2006	W	I	M	DR	Fe	CNT	8.7	1.6	27000			
Kim	[170]-8	2006	W	I	M	DR	Fe	CNT	10.1	1.9	21700			
Kitaguchi	[132]-1	2004	T	I	M	FR	Fe	SiC				10.7	2.3	11900
Kitaguchi	[132]-2	2004	T	I	M	FR	Fe					7.9	1.5	18900
Kitaguchi	[249]-1	2005	T	E	MU	FR	Ni/Fe/Cu					4.3	1.0	9100
Kitaguchi	[249]-2	2005	T	E	MU	FR	Ni/Fe/Cu					3.7	0.7	18900
Ko	[110]-1	2003	T	E	M	FR	SS					4.7	1.0	9300
Ko	[110]-2	2003	T	E	M	FR	SS	Cu				4.2	1.1	5100
Ko	[110]-3	2003	T	E	M	FR	SS	Cu				4.2	1.1	5100
Ko	[110]-4	2003	T	E	M	FR	SS	Cu				4.3	1.2	3600
Ko	[110]-5	2003	T	E	M	FR	SS						2.9	100
Ko	[110]-6	2003	T	E	M	FR	SS	Cu				3.4	2.4	400
Kondo	[152]-1	2005	T	I	M	FR	Fe	SiC		2.0	100			
Kondo	[152]-2	2005	T	I	M	FR	Fe	SiC	2.9	1.4	800			
Kondo	[152]-3	2005	T	I	M	FR	Fe	SiC	1.2	1.4	200			
Kondo	[152]-4	2005	T	I	M	FR	Fe	SiC	7.7	2.0	4500			
Kondo	[152]-5	2005	T	I	M	FR	Fe	SiC	7.6	1.7	8800			
Kondo	[152]-6	2005	T	I	M	FR	Fe	SiC	5.5	1.6	2900			
Kondo	[152]-7	2005	T	I	M	FR	Fe	SiC	6.9	2.1	2700			
Kondo	[152]-8	2005	T	I	M	FR	Fe	SiC	5.1	2.2	1100			
Kondo	[152]-9	2005	T	I	M	FR	Fe	SiC	5.5	1.5	3900			
Kovac	[74]-1	2004	T	E	M	4R	NiFe	SiC	5.3	1.2	8500			
Kovac	[74]-2	2004	T	E	M	4R	NiFe	Hf	5.6	1.0	22900			
Kovac	[74]-3	2004	T	E	M	4R	NiFe	W	5.3	1.2	8500			
Kovac	[74]-4	2004	T	E	M	4R	NiFe	Nb	5.5	1.0	28000			
Kovac	[74]-5	2004	T	E	M	4R	NiFe	Zr	5.3	0.9	37900			
Kovac	[74]-6	2004	T	E	M	4R	NiFe	Nb_2O_5	5.0	1.0	14700			

Continued on next page

First Author	Ref	Year	Shp.	Prc.	# Fil.	Fin. Def.	Mat.	Add.	Perpendicular field B_{100} [T]	Perpendicular field B_p [T]	Perpendicular field $J_{c,0}^T$ [A/mm^2]	Parallel field B_{100} [T]	Parallel field B_p [T]	Parallel field $J_{c,0}^T$ [A/mm^2]
Kovac	[74]-7	2004	T	E	M	4R	NiFe	Ti	5.0	1.0	16000			
Kovac	[74]-8	2004	T	E	M	4R	NiFe		4.3	1.1	5300			
Kovac	[74]-9	2004	T	E	M	4R	NiFe	Ti_2O_5	3.3	0.9	3400			
Kovac	[74]-10	2004	T	E	M	4R	NiFe	BN	0.4	1.9	100			
Kovac	[74]-11	2004	T	E	M	4R	NiFe	V_2O_5	0.2	1.6	100			
Kovac	[74]-12	2004	T	E	M	4R	NiFe	$SrCO_3$		2.3	< 100			
Kovac	[153]-6	2005	T	E	MU	4R	FeNiCo		4.7	0.9	20800			
Kovac	[153]-7	2005	W	E	MU	DR	FeNiCo		3.6	0.8	7300			
Kovac	[153]-8	2005	T	E	MU	4R	FeNiCo		4.1	0.7	25100			
Kovac	[153]-9	2005	T	E	MU	4R	FeNiCo					4.3	0.9	12400
Kovac	[153]-10	2005	T	E	M	4R	FeNiCo		6.3	0.9	104800			
Kovac	[154]-1	2005	T	I	M	4R	FeNiCo		2.4	1.2	700			
Kovac	[154]-2	2005	T	I	M	4R	FeNiCo		4.8	1.0	10400			
Kovac	[154]-3	2005	T	I	M	4R	FeNiCo		4.7	0.9	14800			
Kovac	[154]-4	2005	T	I	M	4R	FeNiCo		3.5	1.0	3400			
Kovac	[154]-5	2005	T	I	M	4R	FeNiCo		0.5	1.1	200			
Kovac	[154]-6	2005	T	I	M	4R	FeNiCo			1.2	< 100			
Kovac	[154]-7	2005	T	I	M	4R	Fe		2.9	0.8	4800			
Kovac	[154]-8	2005	T	I	M	4R	Fe		5.1	0.9	27900			
Kovac	[154]-9	2005	T	I	M	4R	Fe		4.9	0.8	33800			
Kovac	[154]-10	2005	T	I	M	4R	Fe		5.0	0.8	35200			
Kovac	[171]-1	2006	T	E	MU4	4R	Fe		4.9	0.9	29400			
Kovac	[171]-2	2006	T	E	MU4	4R	Fe		4.3	0.9	15100			
Kovac	[171]-3	2006	T	E	MU4	4R	Fe		3.6	0.8	7300			
Kovac	[171]-4	2006	T	I	MU4	4R	Nb/AgMg	SiC	6.5	1.8	3800			
Kovac	[171]-5	2006	T	I	MU4	4R	Nb/AgMg	SiC	6.5	1.7	5000			
Kovac	[171]-6	2006	T	I	MU4	4R	Nb/AgMg	SiC	5.5	1.7	2700			
Kovac	[172]-1	2006	T	E	MU6	4R	Fe		6.5	1.4	9200			
Kovac	[172]-2	2006	T	E	MU6	4R	Fe		6.7	1.4	10800			
Kovac	[172]-3	2006	T	E	MU6	4R	Fe		6.7	1.4	11400			
Kovac	[172]-4	2006	T	E	MU6	4R	Fe		6.2	1.3	10100			
Kovac	[172]-5	2006	T	E	M	4R	Fe		5.9	1.3	10800			
Kovac	[173]-1	2006	T	I	M	4R	Nb		5.4	1.0	22800			
Kovac	[173]-2	2006	T	I	M	4R	Ta		5.2	1.0	18500			
Kovac	[173]-3	2006	T	I	M	4R	Fe		4.9	0.9	21000			
Kovac	[173]-4	2006	T	E	M	4R	Fe/Cu		6.3	1.0	48800			

Continued on next page

First Author	Ref	Year	Shp.	Prc.	# Fil.	Fin. Def.	Mat.	Add.	Perpendicular field			Parallel field		
									B_{100} [T]	B_p [T]	$J_{c,0}^T$ [A/mm^2]	B_{100} [T]	B_p [T]	$J_{c,0}^T$ [A/mm^2]
Kovac	[173]-5	2006	T	E	M	4R	Ta/Fe		4.1	1.0	5100			
Kovac	[173]-6	2006	T	E	M	4R	Nb/Fe			1.5	100			
Kumakura	[111]-1	2003	T	E	M	O	SS					5.2	1.2	6800
Kumakura	[111]-2	2003	T	E	M	O	FeC					3.7	1.5	1300
Kumakura	[111]-3	2003	T	E	M	O	Cu-Ni					1.2	1.7	200
Kumakura	[111]-4	2003	T	E	M	O	Cu					0.2	1.6	100
Kumakura	[111]-5	2003	T	E	M	GR	SS		4.2	0.7	28700	3.9	1.5	1400
Kumakura	[111]-6	2003	T	E	M	O	SS		5.6	0.7	267600	6.3	1.1	27800
Kumakura	[111]-7	2003	T	E	M	O	Fe						1.4	100
Kumakura	[111]-10	2003	T	E	M	O	Fe					5.6	1.2	13300
Kumakura	[111]-11	2003	T	E	M	O	Fe-C					7.4	1.5	12800
Kumakura	[111]-12	2003	T	E	M	O	SS					6.3	1.8	3200
Kumakura	[133]-1	2004	T	I	M	FR	Fe					7.9	1.5	17200
Kumakura	[133]-2	2004	T	I	M	FR	Fe	SiC				11.0	2.0	22500
Kumakura	[133]-3	2004	T	I	M	FR	Fe	SiC				11.0	2.4	8900
Kumakura	[155]-1	2005	T	I	M	FR	Fe					8.0	1.6	16700
Kumakura	[155]-2	2005	T	I	M	FR	Fe					7.3	1.3	22600
Kumakura	[155]-3	2005	T	I	M	FR	Fe					7.1	1.4	16500
Kumakura	[155]-4	2005	T	I	M	FR	Fe	SiC				10.6	2.2	12000
Kumakura	[155]-5	2005	T	I	M	FR	Fe	SiC				10.6	2.2	12000
Kumakura	[155]-6	2005	T	I	M	FR	Fe	SiC				10.6	2.2	12000
Kuroda	[174]-1	2006	T	E	M	FR	Fe					0.1	1.3	100
Kuroda	[174]-2	2006	T	E	M	FR	Fe	Fe					1.3	100
Kuroda	[174]-3	2006	T	E	M	FR	Fe	Fe					1.3	100
Kuroda	[174]-4	2006	T	E	M	FR	Fe						1.9	100
Kuroda	[174]-5	2006	T	E	M	FR	Fe	Fe					1.6	< 100
Kuroda	[174]-6	2006	T	E	M	FR	Fe	Fe					1.9	< 100
Kuroda	[174]-7	2006	T	I	M	FR	Fe					8.0	1.6	13800
Kuroda	[174]-8	2006	T	I	M	FR	Fe	Fe				6.2	1.7	3900
Kuroda	[174]-9	2006	T	I	M	FR	Fe	Fe				3.6	1.8	800
Kuroda	[174]-10	2006	T	I	M	FR	Fe	Fe				2.1	1.8	300
Kuroda	[174]-11	2006	T	I	M	FR	Fe	Fe				0.1	1.8	100
Lezza	[90]-1	2004	T	E	M	FR	Fe					6.1	1.1	25800
Lezza	[90]-2	2004	T	E	M	FR	Fe					6.8	1.4	14300
Lezza	[90]-3	2004	T	E	M	FR	Fe					7.0	1.2	29000
Lezza	[156]-1	2005	T	E	M	FR	Fe		5.2	0.6	431000		1.4	11100

Continued on next page

First Author	Ref	Year	Shp.	Prc.	# Fil.	Fin. Def.	Mat.	Add.	Perpendicular field			Parallel field		
									B_{100} [T]	B_p [T]	$J_{c,0}^T$ [A/mm^2]	B_{100} [T]	B_p [T]	$J_{c,0}^T$ [A/mm^2]
Lezza	[156]-2	2005	T	E	M	FR	Fe			0.6	1042000		1.3	16000
Lezza	[156]-3	2005	T	E	M	FR	Fe		5.5	0.8	70600	6.9	1.4	13900
Lezza	[156]-4	2005	T	E	M	FR	Fe			0.9	31500		1.2	17000
Lezza	[175]-1	2006	W	I	M	DR	Fe		7.2	1.5	11400			
Lezza	[175]-2	2006	W	I	M	DR	Fe		6.7	1.3	21600			
Lezza	[175]-3	2006	W	I	M	DR	Fe		6.2	1.0	57000			
Lezza	[175]-4	2006	W	I	M	DR	Fe	B_4C	6.4	2.2	1700			
Lezza	[175]-5	2006	W	I	M	DR	Fe	B_4C	7.9	2.1	4000			
Lezza	[175]-6	2006	W	I	M	DR	Fe	B_4C	9.1	1.8	14700			
Lezza	[175]-7	2006	W	I	M	DR	Fe	B_4C	6.9	1.6	7600			
Lezza	[175]-8	2006	W	I	M	DR	Fe	B_4C	6.4	1.5	8100			
Lezza	[175]-9	2006	W	I	M	DR	Fe	B_4C	9.3	1.7	28100			
Lezza	[175]-10	2006	W	I	M	DR	Fe	B_4C	8.6	1.8	13300			
Lezza	[175]-11	2006	W	I	M	DR	Fe	B_4C						
Ma	[112]-1	2003	T	I	M	FR	Fe	$ZrSi_2$				7.7	1.8	6600
Ma	[112]-2	2003	T	I	M	FR	Fe	WSi_2				6.7	2.0	2800
Ma	[112]-3	2003	T	I	M	FR	Fe	ZrB_2				6.7	1.8	3900
Ma	[112]-4	2003	T	I	M	FR	Fe					5.6	1.8	2300
Ma	[134]-1	2004	T	I	M	FR	Fe					5.6	1.8	2200
Ma	[134]-2	2004	T	I	M	FR	Fe	WSi_2				6.6	2.0	2600
Ma	[20]-1	2006	T	I	M	FR	Fe					5.0	1.2	6900
Ma	[20]-2	2006	T	I	M	FR	Fe	$ZrSi_2$				6.7	2.0	2500
Ma	[20]-3	2006	T	I	M	FR	Fe	SiC				10.8	1.9	27000
Ma	[176]-1	2006	T	I	M	FR	Fe					5.7	1.6	3700
Ma	[176]-2	2006	T	I	M	FR	Fe					6.0	1.7	3100
Ma	[177]-1	2006	T	I	M	FR	Fe					6.1	1.2	18700
Ma	[177]-2	2006	T	I	M	FR	Fe	C				9.3	1.8	16000
Ma	[177]-3	2006	T	I	M	FR	Fe	C				9.3	2.0	9700
Ma	[177]-4	2006	T	I	M	FR	Fe	C				8.8	2.2	5200
Ma	[177]-5	2006	T	I	M	FR	Fe	C				8.1	2.3	3600
Ma	[177]-6	2006	T	I	M	FR	Fe	C				7.9	2.5	2500
Ma	[177]-7	2006	T	I	M	FR	Fe	C				10.1	2.0	14900
Ma	[177]-8	2006	T	I	M	FR	Fe					8.0	1.4	33700
Ma	[177]-9	2006	T	I	M	FR	Fe	C				10.6	1.9	26900
Ma	[177]-10	2006	T	I	M	FR	Fe	C				11.3	2.2	17700
Malagoli	[113]-1	2003	T	E	M	FR	Ni		5.5	0.8	122500	7.5	1.7	7800

Continued on next page

First Author	Ref	Year	Shp.	Prc.	# Fil.	Fin. Def.	Mat.	Add.	Perpendicular field			Parallel field		
									B_{100} [T]	B_p [T]	$J_{c,0}^T$ [A/mm^2]	B_{100} [T]	B_p [T]	$J_{c,0}^T$ [A/mm^2]
Malagoli	[113]-2	2003	T	E	MU7	FR	Ni		8.5	2.3	3800			
Matsumoto	[114]-1	2003	T	I	M	FR	Fe					4.6	1.8	1200
Matsumoto	[114]-2	2003	T	I	M	FR	Fe	SiO_2				7.4	1.9	5300
Matsumoto	[114]-3	2003	T	I	M	FR	Fe	SiO_2				5.8	1.9	2200
Matsumoto	[114]-4	2003	T	I	M	FR	Fe	SiO_2				2.7	1.2	1000
Matsumoto	[114]-6	2003	T	I	M	FR	Fe	SiC				4.7	1.4	2500
Matsumoto	[114]-7	2003	T	I	M	FR	Fe	SiC				5.5	1.5	4300
Matsumoto	[114]-8	2003	T	I	M	FR	Fe	SiC				6.6	1.8	4100
Matsumoto	[114]-9	2003	T	I	M	FR	Fe					7.6	1.2	51300
Matsumoto	[114]-10	2003	T	I	M	FR	Fe	SiO_2				5.2	1.3	4700
Matsumoto	[114]-11	2003	T	I	M	FR	Fe	SiC				9.4	1.7	22600
Matsumoto	[114]-12	2003	T	I	M	FR	Fe					8.1	1.2	89400
Matsumoto	[114]-13	2003	T	I	M	FR	Fe	SiC				8.2	1.3	55600
Matsumoto	[114]-14	2003	T	I	M	FR	Fe	SiC				8.2	1.3	55600
Matsumoto	[114]-15	2003	T	I	M	FR	Fe	SiC				8.5	1.5	35500
Matsumoto	[114]-16	2003	T	I	M	FR	Fe	SiC				7.3	1.7	7500
Matsumoto	[114]-17	2003	T	I	M	FR	Fe					8.2	1.4	28300
Matsumoto	[114]-18	2003	T	I	M	FR	Fe	SiC				10.6	2.3	9600
Matsumoto	[115]-1	2003	T	E	M	FR	SS					5.9	0.9	73300
Matsumoto	[115]-2	2003	T	E	M	FR	SS					6.3	1.0	57100
Matsumoto	[115]-3	2003	T	E	M	FR	SS					4.4	0.9	11700
Matsumoto	[115]-4	2003	T	E	M	FR	SS					6.0	1.5	5300
Matsumoto	[115]-5	2003	T	E	M	FR	SS					7.2	1.7	6800
Matsumoto	[115]-6	2003	T	E	M	FR	SS					6.4	2.1	2100
Matsumoto	[115]-7	2003	T	E	M	FR	SS					5.8	0.7	312200
Matsumoto	[115]-8	2003	T	E	M	FR	SS					5.9	0.8	139100
Matsumoto	[115]-9	2003	T	E	M	FR	SS					6.3	0.9	128900
Matsumoto	[115]-10	2003	T	E	M	FR	SS					5.7	1.4	5900
Matsumoto	[115]-11	2003	T	E	M	FR	SS					6.4	1.6	5100
Matsumoto	[115]-12	2003	T	E	M	FR	SS					6.1	3.1	700
Matsumoto	[135]-1	2004	T	I	M	FR	Fe					7.9	1.5	18500
Matsumoto	[135]-2	2004	T	I	M	FR	Fe	WSi_2				7.8	1.7	11400
Matsumoto	[135]-3	2004	T	I	M	FR	Fe	$ZrSi_2$				8.4	1.6	17600
Matsumoto	[135]-4	2004	T	I	M	FR	Fe	Mg_2Si				8.4	1.6	17500
Matsumoto	[135]-6	2004	T	I	M	FR	Fe	SiC				10.4	2.3	9700
Matsumoto	[135]-7	2004	T	I	M	FR	Fe	SiO_2				6.4	1.7	4200

Continued on next page

First Author	Ref	Year	Shp.	Prc.	# Fil.	Fin. Def.	Mat.	Add.	Perpendicular field B_{100} [T]	Perpendicular field B_p [T]	Perpendicular field $J_{c,0}^T$ [A/mm^2]	Parallel field B_{100} [T]	Parallel field B_p [T]	Parallel field $J_{c,0}^T$ [A/mm^2]
Matsumoto	[135]-8	2004	T	I	M	FR	Fe	SiC				11.6	2.4	13500
Matsumoto	[135]-9	2004	T	I	M	FR	Fe	SiC				10.9	2.1	18500
Matsumoto	[135]-10	2004	T	I	M	FR	Fe					8.2	1.4	28200
Matsumoto	[21]-1	2005	T	I	M	FR	Fe						1.8	1300
Matsumoto	[21]-2	2005	T	I	M	FR	Fe					6.2	1.6	5400
Matsumoto	[21]-3	2005	T	I	M	FR	Fe					7.4	1.8	6500
Matsumoto	[21]-4	2005	T	I	M	FR	Fe					8.0	1.6	14500
Matsumoto	[21]-5	2005	T	I	M	FR	Fe					7.3	1.4	18600
Matsumoto	[21]-6	2005	T	I	M	FR	Fe					8.2	1.5	23600
Matsumoto	[21]-7	2005	T	I	M	FR	Fe	SiC				8.0	2.4	3000
Matsumoto	[21]-8	2005	T	I	M	FR	Fe	SiC				9.6	2.4	5300
Matsumoto	[21]-9	2005	T	I	M	FR	Fe	SiC				10.2	2.4	6300
Matsumoto	[21]-10	2005	T	I	M	FR	Fe	SiC				8.9	2.4	4000
Matsumoto	[21]-11	2005	T	I	M	FR	Fe	SiC				7.8	2.0	4900
Matsumoto	[21]-12	2005	T	I	M	FR	Fe	SiC				9.7	2.2	7700
Matsumoto	[21]-13	2005	T	I	M	FR	Fe	SiC				8.3	2.2	4000
Nakane	[22]-1	2006	T	I	M	FR	Fe					8.4	1.6	17600
Nakane	[22]-2	2006	T	O	M	FR	Fe					7.1	2.3	2400
Nakane	[22]-3	2006	T	O	M	FR	Fe					8.8	2.3	4400
Nakane	[178]-1	2006	T	E	M	FR	Fe					0.5	2.2	100
Nakane	[178]-2	2006	T	O	M	FR	Fe					7.4	2.2	3000
Nakane	[178]-3	2006	T	O	M	FR	Fe					7.9	2.6	2100
Nakane	[179]-1	2006	T	I	M	FR	Fe					8.3	1.6	18200
Nakane	[179]-2	2006	T	O	M	FR	Al					4.8	2.1	1000
Nakane	[179]-3	2006	T	O	M	FR	Al					4.5	1.2	4300
Nakane	[179]-4	2006	T	E	M	FR	Al					1.6	1.1	400
Pachla	[157]-1	2005	W	E	M	E	Cu/Fe		4.1	0.9	9900			
Pachla	[157]-2	2005	W	E	M	E	Fe	SiC	5.4	1.0	17700			
Pachla	[157]-3	2005	W	E	M	E	Fe	SiC	2.8	1.6	600			
Pachla	[157]-4	2005	T	E	M	4R	Fe		3.2	1.5	900			
Pachla	[157]-5	2005	T	E	M	4R	Cu/Fe		4.6	0.9	17000			
Pachla	[157]-6	2005	T	E	M	4R	Fe	SiC	5.1	1.1	9000			
Pachla	[180]-1	2006	W	I	M	E	Fe			1.0	5700			
Pachla	[180]-2	2006	W	I	M	E	Fe	SiC	4.9	2.1	1100			
Pachla	[180]-3	2006	W	I	M	E	Fe	SiC		2.6	300			
Pachla	[180]-4	2006	W	I	M	E	Fe	SiC	4.2	1.8	1100			

Continued on next page

First Author	Ref	Year	Shp.	Prc.	# Fil.	Fin. Def.	Mat.	Add.	Perpendicular field			Parallel field		
									B_{100} [T]	B_p [T]	$J_{c,0}^T$ [A/mm^2]	B_{100} [T]	B_p [T]	$J_{c,0}^T$ [A/mm^2]
Pachla	[180]-5	2006	W	I	M	4R	Fe		3.8	1.0	5700			
Pachla	[180]-6	2006	W	I	M	4R	Fe	SiC	5.1	2.0	1200			
Pachla	[180]-7	2006	W	I	M	4R	Fe	SiC	3.5	2.6	400			
Pachla	[180]-8	2006	W	I	M	4R	Fe	SiC		1.8	700			
Pachla	[180]-9	2006	W	I	M	4R	Fe		5.2	1.1	9900			
Perner	[158]-1	2005	T	I	M	FR	Fe					9.2	1.7	23500
Perner	[158]-2	2005	T	I	M	FR	Fe					7.7	2.0	5200
Perner	[158]-3	2005	T	I	M	FR	Fe					8.1	1.9	6400
Perner	[158]-4	2005	T	I	M	FR	Fe					8.8	1.3	104000
Ruan	[116]-1	2003	T	I	M	FR	Fe					6.1	1.2	17800
Ruan	[116]-2	2003	T	I	M	FR	Fe					6.1	1.5	6200
Schlachter	[89]-1	2003	W	E	M	S	Fe		0.5	1.3	100			
Schlachter	[89]-2	2003	W	E	M	S	Fe		4.7	1.0	9500			
Schlachter	[89]-3	2003	W	I	M	S	Fe		4.5	0.9	15700			
Schlachter	[89]-4	2003	W	I	M	S	Fe		4.6	0.9	21200			
Schlachter	[89]-5	2003	W	I	M	S	Fe		5.1	0.9	22900			
Schlachter	[89]-6	2003	W	I	M	S	Fe		3.6	0.9	4900			
Schlachter	[89]-7	2003	W	I	M	S	Fe		3.4	0.9	4800			
Schlachter	[89]-8	2003	W	I	M	S	Fe		3.0	0.8	3900			
Schlachter	[89]-9	2003	W	I	M	S	Fe		2.6	0.8	2700			
Schlachter	[89]-10	2003	W	I	M	S	Fe		2.1	0.8	1300			
Schlachter	[95]-1	2006	W	I	M	S	Cu		5.2	0.9	32000			
Schlachter	[95]-2	2006	W	I	MU7	S	Cu		4.7	1.0	10900			
Schlachter	[95]-3	2006	W	I	MU7	S	Cu		4.4	0.9	11300			
Schlachter	[95]-4	2006	W	I	MU7	S	Cu		3.5	1.0	2900			
Schlachter	[95]-5	2006	W	I	MU7	S	Fe		8.3	1.8	9900			
Schlachter	[95]-6	2006	W	I	MU19	S	Fe		8.4	1.6	17800			
Schlachter	[95]-7	2006	W	I	MU31	S	Fe		7.1	1.4	16600			
Schlachter	[95]-8	2006	W	I	MU19	S	Cu		3.8	1.0	4100			
Schlachter	[95]-9	2006	W	I	MU19	S	CuAg		3.5	1.0	3800			
Schlachter	[95]-10	2006	W	I	MU19	S	CuSn		4.4	1.3	3200			
Schlachter	[95]-11	2006	W	I	MU19	S	CuSn		3.6	1.2	1900			
Schlachter	[95]-12	2006	W	I	MU19	S	CuSn		4.3	1.3	2900			
Schlachter	[95]-13	2006	W	I	M	S	Nb/Cu/SS		7.8	1.8	7600			
Schlachter	[95]-14	2006	W	I	M	S	Nb/CuNiZn		7.4	1.8	6400			
Schlachter	[95]-15	2006	W	I	M	S	Cu		5.2	0.9	31300			

Continued on next page

First Author	Ref	Year	Shp.	Prc.	# Fil.	Fin. Def.	Mat.	Add.	Perpendicular field B_{100} [T]	Perpendicular field B_p [T]	Perpendicular field $J_{c,0}^T$ [A/mm^2]	Parallel field B_{100} [T]	Parallel field B_p [T]	Parallel field $J_{c,0}^T$ [A/mm^2]
Schlachter	[95]-16	2006	W	I	M	S	Nb/Cu		0.5	1.9	100			
Schlachter	[181]-1	2006	W	I	M	S	SS		7.9	1.3	37300			
Schlachter	[181]-2	2006	W	I	M	S	Nb/Cu/SS		9.1	1.7	23700			
Serquis	[117]-1	2003	W	E	M	DR	SS		6.0	1.1	30600			
Serquis	[117]-2	2003	W	E	M	DR	SS		7.4	1.2	41600			
Shcherbak.	[182]-1	2006	W	I	M	DR/GR	Fe		7.7	1.4	25300			
Shcherbak.	[182]-2	2006	W	I	M	DR/GR	Fe	SiC	10.3	1.8	29100			
Shcherbak.	[182]-3	2006	W	I	M	DR/GR	Fe	SiC	11.1	2.4	9700			
Shcherbak.	[182]-4	2006	W	I	M	DR/GR	Fe	SiC	9.6	2.1	9200			
Shcherbak.	[182]-5	2006	W	I	M	DR/GR	Fe	SiC	10.4	2.2	12000			
Shcherbak.	[182]-6	2006	W	I	M	DR/GR	Fe	SiC	10.2	1.8	30700			
Soltanian	[159]-1	2005	W	I	M	DR	Fe		7.1	1.1	59900			
Soltanian	[159]-2	2005	W	I	M	DR	Fe	SiC	12.0	2.5	11200			
Soltanian	[159]-3	2005	W	I	M	DR	Fe	SiC	12.0	2.6	11000			
Soltanian	[159]-4	2005	W	I	M	DR	Fe	SiC	11.4	2.1	22300			
Soltanian	[159]-5	2005	W	I	M	DR	Fe	SiC	11.3	2.1	21200			
Song	[118]	2003	T	E	M	FR	SS							
Sumption	[160]	2005	W	I	MU	DR	Nb/Cu/Mon.		7.3	2.1	3500			
Sumption	[19]-1	2006	W	I	M	DR	NbCu		3.7	2.0	800			
Sumption	[19]-2	2006	W	I	M	DR	NbCu		5.6	2.3	1200			
Sumption	[19]-3	2006	W	I	MU6	DR	Mon/NbCu		8.4	2.0	7300			
Sumption	[19]-4	2006	W	I	MU6	DR	Mon/NbCu		7.9	2.0	5200			
Sumption	[19]-5	2006	W	I	MU18	DR	Mon/NbCu		7.9	2.0	5300			
Sumption	[19]-6	2006	W	I	MU18	DR	Mon/NbCu		7.9	1.8	7600			
Sumption	[19]-7	2006	W	I	MU36	DR	Mon/NbCu		9.5	1.9	14600			
Sumption	[19]-8	2006	W	I	MU6	DR	Mon/NbCu		8.6	1.9	10100			
Sumption	[19]-9	2006	W	I	MU6	DR	Mon/NbCu		9.0	1.8	15500			
Sumption	[19]-10	2006	W	I	MU18	DR	Mon/NbCu		8.8	1.9	11000			
Sumption	[19]-11	2006	W	I	MU6	DR	Mon/NbCu		8.4	2.1	5600			
Sumption	[19]-12	2006	W	I	MU6	DR	Mon/NbCu		6.3	1.7	3500			
Sumption	[19]-13	2006	W	I	MU6	DR	Mon/NbCu		7.1	1.6	8400			
Sumption	[19]-14	2006	W	I	MU6	DR	Mon/NbCu		7.7	1.8	8200			
Sumption	[19]-15	2006	W	I	MU6	DR	Mon/NbCu		7.3	1.3	19000			
Sumption	[19]-16	2006	W	I	MU6	DR	Mon/NbCu		6.6	1.8	4000			
Sumption	[19]-17	2006	W	I	MU6	DR	CuNi/NbCu		9.5	1.8	20000			
Sumption	[19]-18	2006	W	I	MU6	DR	CuNi/NbCu		9.3	1.8	17000			

Continued on next page

First Author	Ref	Year	Shp.	Prc.	# Fil.	Fin. Def.	Mat.	Add.	Perpendicular field			Parallel field		
									B_{100} [T]	B_p [T]	$J_{c,0}^T$ [A/mm^2]	B_{100} [T]	B_p [T]	$J_{c,0}^T$ [A/mm^2]
Sumption	[19]-19	2006	W	I	MU6	DR	Mon/NbCu		9.1	2.0	12000			
Sumption	[19]-20	2006	W	I	MU6	DR	Mon/NbCu		9.0	1.8	13000			
Sumption	[19]-21	2006	W	I	MU18	DR	Mon/NbCu		7.8	1.8	10000			
Sumption	[19]-22	2006	W	I	MU18	DR	Mon/NbCu		6.1	1.8	4300			
Sumption	[19]-23	2006	W	I	MU18	DR	Mon/NbCu		2.8	1.8	600			
Sumption	[19]-24	2006	W	I	MU18	DR	Mon/NbCu			1.8	13000			
Sumption	[19]-25	2006	W	I	MU18	DR	Mon/NbCu			1.4	2300			
Sumption	[19]-26	2006	W	I	MU6	DR	Mon/NbCu		8.9	1.6	21300			
Suo	[119]-1	2003	T	E	M	FR	Fe					6.7	1.1	38200
Suo	[119]-2	2003	T	E	M	FR	Fe					6.3	1.1	29800
Suo	[119]-3	2003	T	E	M	FR	Fe					1.6	1.5	300
Suo	[119]-4	2003	T	E	M	FR	Fe					3.0	1.5	700
Suo	[119]-5	2003	T	E	M	FR	Fe					5.1	0.9	32400
Suo	[119]-6	2003	T	E	M	FR	Fe					5.9	1.2	12400
Suo	[119]-7	2003	T	E	M	FR	Fe					5.4	1.2	9200
Suo	[119]-8	2003	T	E	M	FR	Fe					4.4	1.7	1400
Suo	[119]-9	2003	T	E	M	FR	Fe					6.3	1.3	13600
Suo	[119]-10	2003	T	E	M	FR	Fe					5.9	1.2	12800
Suo	[119]-11	2003	T	E	M	FR	Fe					5.7	1.1	14900
Suo	[119]-12	2003	T	E	MU7	FR	Fe					4.6	0.7	59800
Suo	[119]-13	2003	T	E	MU9	FR	Fe					3.7	1.1	2900
Tachikawa	[120]-1	2003	T	E	M	FR	Ni	In				2.2	1.0	800
Tachikawa	[120]-2	2003	T	E	M	FR	Ni	In				2.5	1.1	1000
Tachikawa	[120]-3	2003	T	E	M	FR	Ni	In				3.1	1.4	1000
Tachikawa	[120]-4	2003	T	E	M	FR	Ni					0.8	0.8	300
Tachikawa	[120]-5	2003	T	E	M	FR	Ni	Sn				1.5	1.0	400
Tachikawa	[120]-6	2003	T	E	M	FR	Ni	Sn				1.7	1.2	400
Tachikawa	[120]-7	2003	T	E	M	FR	Ni	Sn				2.0	1.1	600
Tachikawa	[120]-8	2003	T	E	M	FR	Ni	Cu				1.2	1.6	200
Tachikawa	[120]-9	2003	T	E	M	FR	Ni					0.9	1.0	< 100
Tachikawa	[136]	2004												
Takahashi	[183]	2006	W	I	M	DR	Cu		8.9	1.9	10900			
Tanaka	[137]-1	2004	W	E	MU6	DR	SS/Cu		3.0	0.9	2700			
Tanaka	[137]-2	2004	W	E	MU6	DR	SS/Cu		3.4	1.0	2800			
Tanaka	[137]-3	2004	W	E	MU6	DR	SS/Cu		3.4	1.0	3000			
Tanaka	[137]-4	2004	W	E	MU6	DR	SS/Cu		3.8	1.1	2800			

Continued on next page

First Author	Ref	Year	Shp.	Prc.	# Fil.	Fin. Def.	Mat.	Add.	Perpendicular field			Parallel field		
									B_{100} [T]	B_p [T]	$J_{c,0}^T$ [A/mm^2]	B_{100} [T]	B_p [T]	$J_{c,0}^T$ [A/mm^2]
Tanaka	[161]	2005	W	I	M	DR	Fe/Cu		7.4	1.3	30800			
Tanaka	[162]	2005	W	I	M	DR	Fe/Cu		7.5	1.3	33500			
Xu	[163]-1	2005	W	I	M	DR	St.		4.0	0.9	8719			
Xu	[163]-2	2005	W	I	M	DR	St.		3.9	0.9	9762			
Xu	[163]-3	2005	W	I	M	DR	St.		3.7	0.9	6230			
Xu	[163]-4	2005	W	I	M	DR	St.		3.7	0.9	6230			
Xu	[163]-5	2005	W	I	M	DR	St.		3.1	0.7	7395			
Xu	[184]-1	2006	W	I	M	DR	Fe		4.1	1.0	5100			
Xu	[184]-2	2006	W	I	M	DR	Fe		4.1	0.9	8100			
Xu	[184]-3	2006	W	I	M	DR	Fe		4.4	1.0	7100			
Xu	[184]-4	2006	W	I	M	DR	Fe		3.8	1.2	2600			
Xu	[185]-1	2006	W	I	M	DR	St.	TiB_2	3.7	1.2	2500			
Xu	[185]-2	2006	W	I	M	DR	St.	TiB_2	4.3	1.2	4100			
Xu	[185]-3	2006	W	I	M	DR	St.	TiB_2	4.2	1.2	2900			
Xu	[185]-4	2006	W	I	M	DR	St.	TiB_2	4.1	1.1	3800			
Yamada	[164]-1	2005	T	I	M	FR	Fe					9.8	1.7	30000
Yamada	[164]-2	2005	T	I	M	FR	Fe	SiC				11.8	2.2	21000
Yamada	[164]-3	2005	T	I	M	FR	Fe	SiC				12.1	2.3	19000
Yamada	[164]-4	2005	T	I	M	FR	Fe	SiC				11.8	2.7	7800
Yamada	[11]-1	2004	T	I	M	FR	Fe	SiC				12.2	2.3	18200
Yamada	[11]-2	2004	T	I	M	FR	Fe	SiC				11.7	2.2	21400
Yamada	[11]-3	2004	T	I	M	FR	Fe					9.8	1.8	22700
Yamada	[11]-4	2004	T	I	M	FR	Fe	SiC				8.0	2.4	2900
Yamada	[11]-5	2004	T	I	M	FR	Fe					5.8	1.6	3800
Yamada	[186]-1	2006	T	I	M	FR	Fe					8.4	1.4	32000
Yamada	[186]-2	2006	T	I	M	FR	Fe	Thioph.				10.1	2.1	12000
Yamada	[186]-3	2006	T	I	M	FR	Fe	Napth.				9.9	1.9	16700
Yamada	[186]-4	2006	T	I	M	FR	Fe	Benz.				10.1	1.8	26500
Yamada	[186]-5	2006	T	I	M	FR	Fe	SiC				10.9	2.3	11000
Yamada	[186]-6	2006	T	I	M	FR	Fe	Benz.				10.6	2.1	15400
Yamam.	[121]-1	2003	W	E	M	GR	Fe		5.3	0.9	34200			
Yamam.	[121]-2	2003	W	E	M	GR	Fe		5.7	0.8	92300			
Yamam.	[121]-4	2003	W	E	M	GR	Fe		5.3	0.7	207500			
Yamam.	[121]-5	2003	W	E	M	GR	Fe		3.4	1.1	2500			
Yamam.	[121]-6	2003	W	E	M	GR	Fe		5.1	1.2	7900			
Yamam.	[121]-7	2003	W	E	M	GR	Fe		5.3	1.0	19600			

Continued on next page

First Author	Ref	Year	Shp.	Prc.	# Fil.	Fin. Def.	Mat.	Add.	Perpendicular field			Parallel field		
									B_{100} [T]	B_p [T]	$J_{c,0}^T$ [A/mm^2]	B_{100} [T]	B_p [T]	$J_{c,0}^T$ [A/mm^2]
Yamam.	[121]-8	2003	W	E	M	GR	Fe		7.0	0.8	435600			
Yamam.	[121]-9	2003	W	E	M	GR	Fe		5.5	0.8	71900			
Yamam.	[121]-10	2003	W	E	M	GR	Fe		5.3	0.8	81000			
Yamam.	[121]-11	2003	W	E	M	GR	Fe		1.1	1.2	300			
Zhan	[187]-1	2006	T	I	M	FR	Fe					6.2	1.1	27600
Zhan	[187]-2	2006	T	I	M	FR	Fe	$MoSi_2$				7.2	1.4	19200
Zhan	[187]-3	2006	T	I	M	FR	Fe	$MoSi_2$				6.9	1.3	20500
Zhan	[187]-4	2006	T	I	M	FR	Fe	$MoSi_2$				6.9	1.3	21800
Zhan	[187]-5	2006	T	I	M	FR	Fe	$MoSi_2$				6.2	1.5	6800
Zhan	[187]-6	2006	T	I	M	FR	Fe	$MoSi_2$				5.9	1.4	6300
Zhan	[187]-7	2006	T	I	M	FR	Fe					5.8	1.1	15700
Zhan	[187]-8	2006	T	I	M	FR	Fe	$MoSi_2$				7.0	1.5	10600
Zhan	[187]-9	2006	T	I	M	FR	Fe	$MoSi_2$				6.5	1.5	8700
Zhan	[187]-10	2006	T	I	M	FR	Fe	$MoSi_2$				6.1	1.4	7100
Zhan	[188]-1	2006	T	I	M	FR	Fe					5.8	1.1	15700
Zhan	[188]-2	2006	T	I	M	FR	Fe	ZrB_2				7.4	1.5	13400
Zhan	[188]-3	2006	T	I	M	FR	Fe	ZrB_2				7.8	1.5	16400
Zhan	[188]-4	2006	T	I	M	FR	Fe	ZrB_2				8.2	1.7	14000
Zhan	[188]-5	2006	T	I	M	FR	Fe	ZrB_2				7.4	1.5	13400
Zhan	[189]-1	2006	T	I	M	FR	Fe					6.2	1.1	26000
Zhan	[189]-2	2006	T	I	M	FR	Fe	SiC				9.6	2.0	12000
Zhan	[189]-3	2006	T	I	M	FR	Fe	SiC				8.6	1.6	24200
Zhan	[189]-4	2006	T	I	M	FR	Fe	Si/N/C				7.9	1.6	12700

Appendix B

Heat Capacity, Thermal Conductivity and Electrical Resistivity

The temperature- and field dependence of the volumetric heat capacity, thermal conductivity and electrical resistivity of the materials present in the samples studied in chapter 4 are presented in this appendix. The data are collected from literature and from the commercial database Cryocomp [32]. For some materials the properties were not found in the available literature. This is typically the case for specific alloys, in which case data is used of a similar alloy.

Volumetric Heat Capacity

Figure B.1a shows the temperature dependence of the volumetric heat capacity of all the materials present in samples CLM, FZK HTR1 and HTR2.

The volumetric heat capacities of Cu, CuNi30, Nb, Ni and Monel are taken from Cryocomp. The database not only provides the temperature dependence of the heat capacity but also the field dependence when the material is a superconductor, such as Nb. It should be noted that data for CuNi30 are used for sample FZK, since there are no data available for the CuNi18Zn20 alloy in this sample. It can be seen that the data for CuNi30 follow those of Cu above ~ 20 K, while below this temperature they follow the data for Ni. Comparing the heat capacity of CuNi30 and Cu80Zn20 (brass, not shown in the figure), which does not contain Ni, it follows that alloying with Zn has a limited effect on the total heat capacity as the data of Cu80Zn20 follow those of Cu even below ~ 20 K [1]. Therefore it is assumed that the temperature dependence of CuNi30 approaches that of CuNi18Zn20.

[1] For clarity volumetric heat capacity data of Cu80Zn20 is not presented here, but is available in [32, 80].

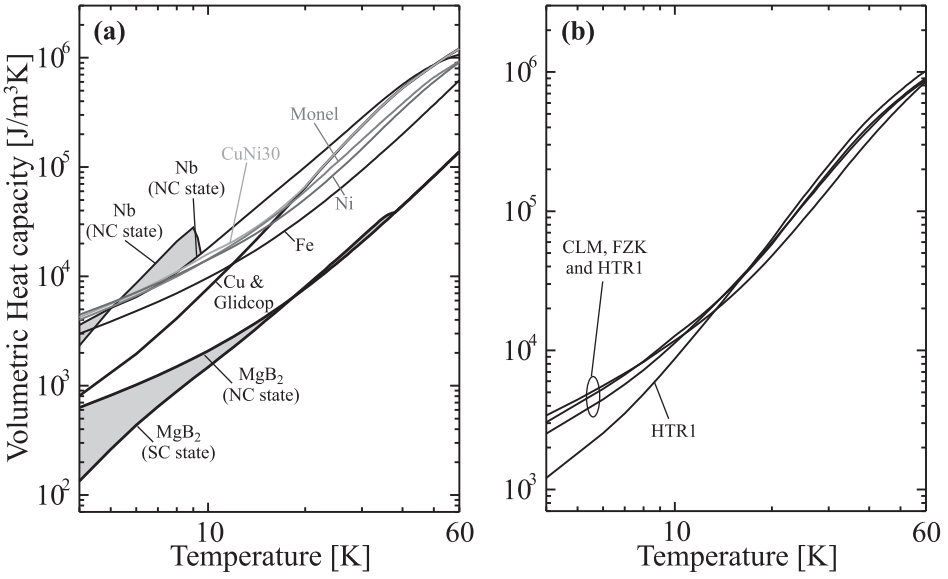

Figure B.1: (a) shows the volumetric heat capacity of the materials that are used in the samples in chapter 4. (b) shows the "lumped" volumetric heat capacity of those samples.

The presented heat capacity of Fe is that of Armco, which is a high purity Fe ($\geq$ 99.8 % [241]) and the data are obtained from [250].

Heat capacity data for Glidcop are acquired from [216]. However, data below 100 K are not presented in this publication and not found in other papers. However, it is shown in [216] that above 100 K the heat capacity of Glidcop is only about 2 % higher than of Cu. Since Glidcop is a Al_2O_3 dispersion-hardened copper, it can be expected that its heat capacity remains similar to that of Cu also below 100 K. Therefore the Glidcop data in the range between 4 and 60 K used in this study are taken to be identical to those for Cu.

The heat capacity data for MgB_2 used here are those published by [31], which agree within 10 % with data published by other authors [251, 252].

Figure B.1b shows the "lumped" volumetric heat capacity of samples CLM, FZK, HTR1 and HTR2 studied in chapter 4. The lumped data are calculated by taking the weighted averages of the volumetric heat capacities of the individual materials that constitute the conductors:

$$c_{\text{lumped}} = \sum_i f_i c_i, \tag{B.1}$$

with f_i and c_i the volume fraction and heat capacity of the i^{th} component in the sample. The fractions of each component in the four samples are listed in table 4.1 in chapter 4. It should be noted that due to the relatively small fraction

of MgB_2 or Nb in the composites, the differences in their heat capacity in the superconducting and normal states are neglected in the lumped heat capacity.

Thermal Conductivity

Figure B.2a shows the thermal conductivity of the materials used in samples CLM, FZK, HTR1 and HTR2.

Similar to the volumetric heat capacity c, the thermal conductivities κ of Cu (RRR = 100), CuNi30, Nb, Ni and Monel are obtained from Cryocomp. Also the thermal conductivity data for CuNi18Zn20 are not found in literature. Therefore the data for CuNi30 are substituted to estimate the temperature dependence of the thermal conductivity of CuNi18Zn20 in sample FZK. For comparison, also the thermal conductivity of Cu80Zn20 is plotted in figure B.2a. Clearly, alloying Cu with Ni has a stronger effect on the thermal conductivity than alloying it with Zn. Therefore it is assumed that the thermal conductivity of CuNi18Zn20 resembles that of CuNi30. Nevertheless, to improve the predictive value of the parallel-paths model in chapter 4, the thermal conductivity should ideally be measured.

The thermal conductivity of Fe is taken to be that of the high purity Armco. The data are obtained from [80].

Just like with c, the temperature dependence of κ for Glidcop is taken from [216], in which data are only given above 100 K. Compared to Cu, the thermal conductivity of Glidcop is approximately 10 % lower above 100 K. In figure B.2a, it is assumed that it continues to be 10 % lower than the thermal conductivity of Cu with RRR = 100 at 5 T down to 4 K. Nevertheless, as discussed in §4.5.2, it was necessary to use the thermal conductivity of Glidcop as a fitting parameter in order to have a good agreement between the model calculations of MQE and v_{nz} and the experiments, due to the large uncertainty involved in this extrapolation. For example, the peak in the thermal conductivity of Cu that results from the transition from electron-phonon to electron-impurity scattering [209] is now also included in the thermal conductivity of Glidcop. In reality, it is unsure how strong this peak will be present in Glidcop. Also, it is unknown to what extent the strong field dependence of the thermal conductivity of Cu is also present in Glidcop. The magnitude of this peak and the field dependence of the thermal conductivity of Cu are strongly related to the purity of Cu (RRR value). For Glidcop no data are available on how the thermal conductivity relates to the purity of the Cu of which it is made of. In order to improve the predictive value of the parallel-paths model in chapter 4, the thermal conductivity of Glidcop should ideally also be measured in the range from 4 to 100 K.

The thermal conductivity data for MgB_2 are obtained from [30]. Compared to measurements by [253], the values are about 20 % lower. The discrepancies are presumably caused by differences in the samples or by measurement uncertainties [30]. The differences in published results are typical for the uncertainty in the estimation of the thermal conductivity of the filaments, since different preparation routes (in-situ or ex-situ and densification) can result in different thermal conductivities.

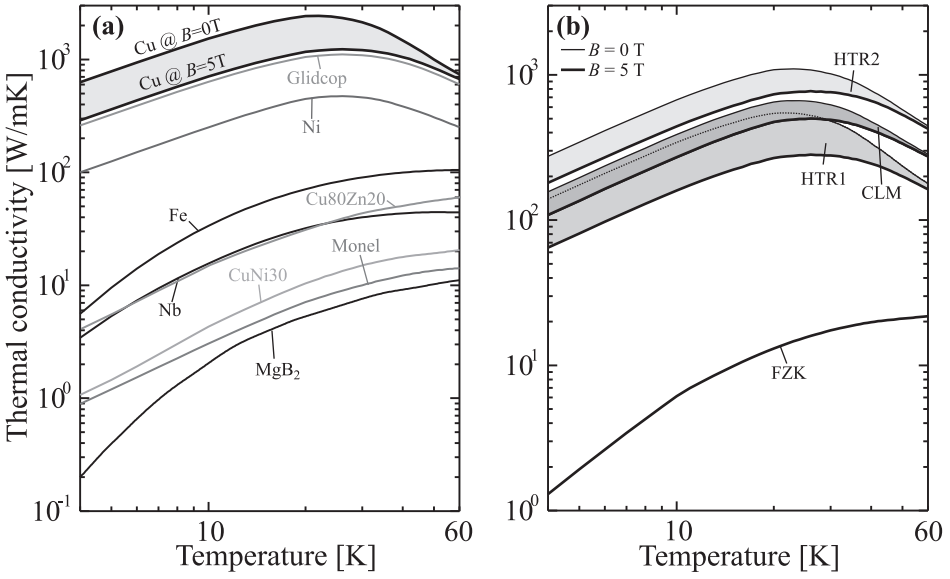

Figure B.2: (a) shows the thermal conductivity of the materials used in the samples studied in chapter 4. (b) shows the "lumped" thermal conductivity of the samples.

Figure B.2b shows the lumped thermal conductivity of the samples CLM, FZK, HTR1 and HTR2. Similar to the heat capacity, the lumped values of the thermal conductivity are calculated as the weighted average of the data for the individual components:

$$\kappa_{\text{lumped}} = \sum_i f_i \kappa_i, \tag{B.2}$$

with κ_i the thermal conductivity of the i^{th} component. Due to the relatively large fraction of Cu in samples CLM, HTR1 and HTR2, the field dependence of the lumped thermal conductivity becomes significant. This field dependence is accounted for in the numerical model discussed in chapter 4.

Electrical Resistivity

Figure B.3a displays the electrical resistivity of the materials used in samples CLM, FZK, HTR1 and HTR2.

Data for Cu (RRR = 100), CuNi30, Nb, Ni and Monel are obtained from Cryocomp. Once more, the electrical resistivity of CuNi30 is used to characterise that of CuNi18Zn20. Comparing the CuNi30 data with that of Cu80Zn20 it can be seen that, just like for the thermal conductivity, Ni has a much stronger effect

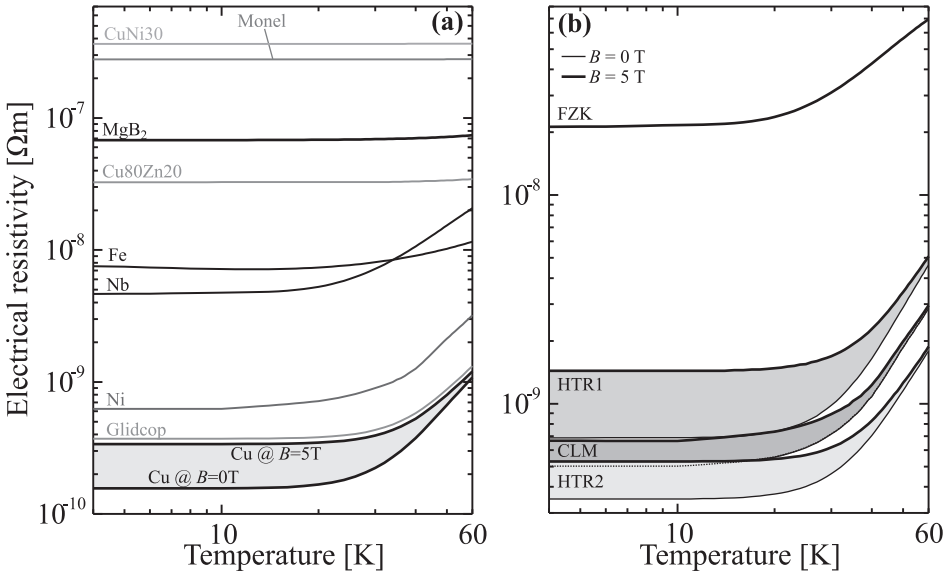

Figure B.3: (a) shows the electrical resistivity of the materials used in the samples studied in chapter 4. (b) shows the "lumped" electrical resistivity of those samples.

on the resistivity of Cu alloys than Zn. Therefore it is assumed that the electrical conductivity of CuNi18Zn20 resembles that of CuNi30.

Electrical resistivity data for Fe (Armco) are obtained from [80].

The temperature dependence of the electrical resistivity of Glidcop is taken from [216]. Just like with the thermal conductivity, electrical resistivity data in this paper are only given above 100 K. Above this temperature the electrical resistivity is approximately 10 % higher than that of Cu and it is assumed that it continues to be so down to 4 K (with respect to Cu with RRR = 100 and at $B = 5$ T). The uncertainty in the electrical resistivity is, similar to the thermal conductivity, the unknown purity of the Cu of which Glidcop is made of; its relation to the overall resistivity of Glidcop; and its response to a magnetic field.

Normal-state electrical resistivity data for MgB_2 are obtained from [30]. Compared to the data from [254] these data are a factor of 3 lower, which can again be attributed to the different preparation routes.

Also the lumped electrical resistivity of the samples is presented here in figure B.3b. It should be noted, however, that the lumped resistivity of the matrix materials and the normal-state electrical resistivity of the filaments are taken separately in the parallel-paths model, since the superconducting-to-normal transition of the filaments is accounted for. The overall lumped resistivity serves as an indication for overall resistivity of a sample in the normal state. They are calculated

through the weighted average of the electrical conductivities $(1/\rho)$:

$$\frac{1}{\rho_{\text{lumped}}} = \sum_i \frac{f_i}{\rho_i}, \tag{B.3}$$

with ρ_i the electrical resistivity of the i^{th} component in the composite conductor. The field dependence of the lumped resistivity of samples CLM, HTR1 and HTR2 is caused by the presence of a relatively large fraction Cu and is accounted for in the numerical model.

Appendix C

Design of the Thermal Stability Experiment

In §4.4.3, the modification of the existing stability set-up –designed for use at 4.2 K only– to higher temperatures is described. The main problem was to minimise lateral heat-leak from the wires sample to the sample holder. A first modification to improve the homogeneity of the temperature over the sample was to minimise the thermal contact with the sample holder using Nylon wires (figure C.1a). Furthermore, the Kapton layer was separated into an inner- and outer Kapton layer with a vacuum space in-between them. With this improvement, the homogeneity of the temperature over the sample was still insufficient. The only way to further improve the homogeneity to an acceptable level turned out to be an embedded heater in the outer Kapton layer. This conclusion is based on an analytical thermal model of the sample holder / sample assembly. In this appendix the thermal model is discussed in detail and it is shown how it led to this conclusion.

Analytical Model

The analytical model is based on an equivalent thermal network of the sample holder / sample assembly. The relation between the actual assembly and the equivalent network is shown in figure C.1. The model makes the following assumptions:

1. The problem is symmetric around the mid-plane of the sample holder, indicated as the "plane of symmetry";

2. The inner Kapton layer, the Cu current terminals and the walls of the vacuum can all have a fixed temperature $T_b = 4.2$ K.

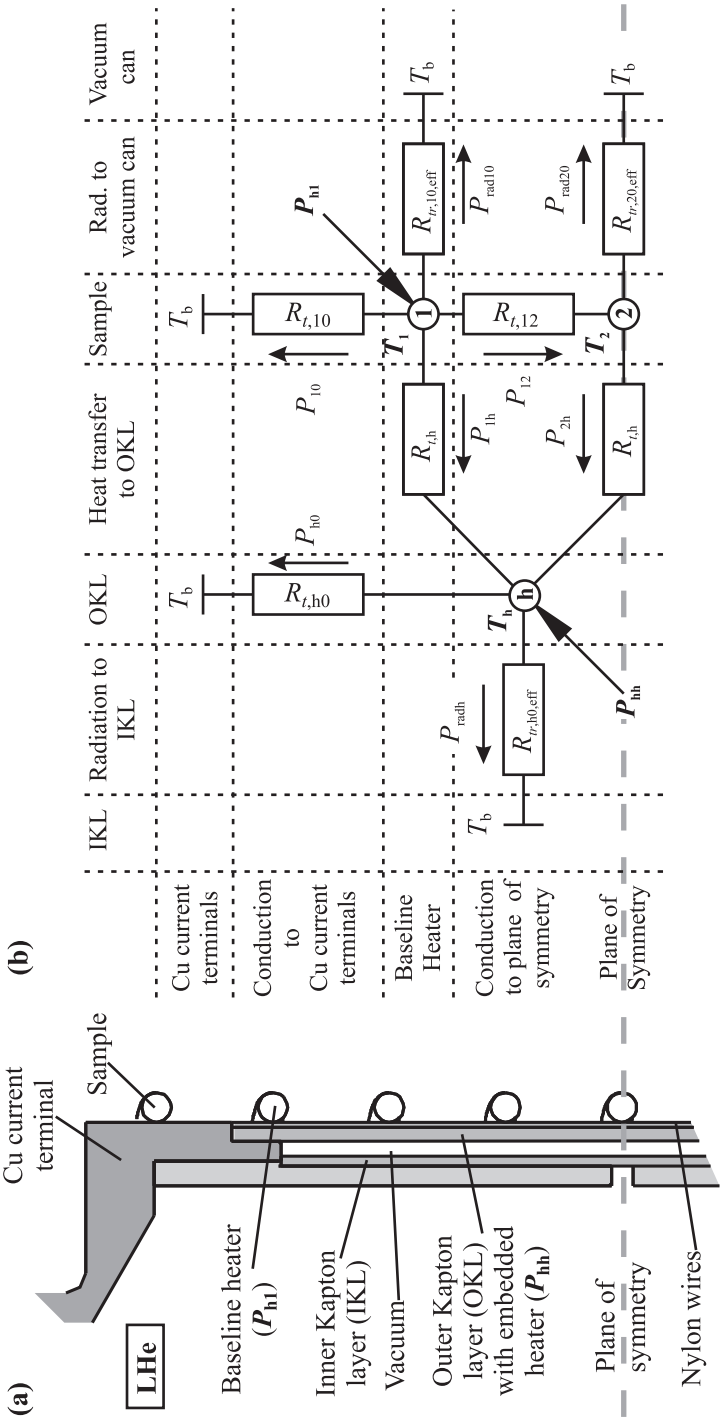

Figure C.1: (a) Shows a part of the cross-section of the sample holder, while (b) shows the equivalent thermal network.

With these assumptions, three nodes are defined at which the temperature is to be solved as a function of the heater inputs P_{h1} on the sample and P_{hh} embedded in the Kapton:

node 1: the point on the sample where the sample heater P_{h1} is mounted, close to the Cu current terminal and at a temperature T_1;

node 2: the point on the sample where it crosses the plane of symmetry, with temperature T_2;

node h: the outer Kapton layer with temperature T_{h}. This is also the location of the embedded heater P_{hh}.

The three unknown temperatures T_1, T_2 and T_{h} are solved by balancing the heat fluxes at these three nodes:

$$\begin{array}{lllllll} P_{\mathrm{h1}} & -P_{10} & -P_{\mathrm{rad1}} & -P_{12} & -P_{1\mathrm{h}} & = 0 & \text{(node 1)} \\ & & -P_{\mathrm{rad2}} & +P_{12} & -P_{2\mathrm{h}} & = 0 & \text{(node 2)} \\ P_{\mathrm{hh}} & -P_{\mathrm{h0}} & -P_{\mathrm{radh}} & +P_{1\mathrm{h}} & +P_{2\mathrm{h}} & = 0 & \text{(node h)} \end{array} \tag{C.1}$$

Node 1 receives heat from heater P_{h1} mounted on the sample. From this node heat is conducted through the sample to the Cu current terminal (P_{10}) and to node 2 (P_{12}). A radiative heat flux goes from node 1 to the vacuum can (P_{rad1}). Furthermore, the lateral cooling of the sample to the outer Kapton layer is represented by $P_{1\mathrm{h}}$. Node 2 receives a conductive heat flux from node 1 (P_{12}). Heat is lost by radiation the vacuum can (P_{rad2}) and via lateral cooling to the outer Kapton layer ($P_{2\mathrm{h}}$). The outer Kapton layer (node h) receives heat from the embedded heater (P_{hh}) and incoming heat fluxes from nodes 1 and 2 ($P_{1\mathrm{h}}$ and $P_{2\mathrm{h}}$ respectively). Furthermore, heat is distributed via conduction to the Cu current terminal (P_{h0}) and via radiation to the inner Kapton layer (P_{radh}).

The heaters P_{h1} and P_{hh} are resistive so that the heat that they generate can be derived from their electrical resistance and from the current with which they are fed.

The conductive heat fluxes, P_{10}, P_{12}, $P_{1\mathrm{h}}$, $P_{2\mathrm{h}}$ and P_{h0}, are estimated using the effective thermal resistances R_t of the corresponding conduction paths:

$$\begin{aligned} P_{\mathrm{cond}} &= \frac{\Delta T}{R_t}, \\ \text{with } R_t &= \frac{l}{A\kappa}. \end{aligned} \tag{C.2}$$

ΔT is the temperature drop across the conduction path; l and A are its length and cross-sectional area, respectively; and κ its thermal conductivity.

Radiative heat flux in this problem always occurs between a surface at a fixed LHe temperature of $T_{\mathrm{b}} = 4.2$ K (inner Kapton layer or vacuum can) and a surface x with a variable –a-priori unknown– temperature (sample temperatures T_1 and T_2 and outer Kapton layer temperature T_{h}). These radiative heat fluxes are

described as:

$$P_{\mathrm{rad}} = c_{\mathrm{rad}} \left[T_x^4 - T_{\mathrm{b}}^4 \right],$$

$$\text{with} \quad c_{\mathrm{rad}} = \frac{\sigma_{\mathrm{SB}}}{\dfrac{1-\epsilon_x}{A_x \epsilon_x} + \dfrac{1}{A_x \nu} + \dfrac{1-\epsilon_{\mathrm{b}}}{A_{\mathrm{b}} \epsilon_{\mathrm{b}}}}. \tag{C.3}$$

T_x is the unknown temperature T_1, T_2 or T_{h}; T_{b} is the LHe temperature; the proportionality constant c_{rad} depends on the Stefan-Boltzmann constant ($\sigma_{\mathrm{SB}} = 5.669 \cdot 10^{-8}$ $\mathrm{Wm^{-2}K^{-4}}$), the surface areas A_x and A_{b}, the emissivity of the two surfaces (ϵ_x and ϵ_{b}) and the geometric view factor ν [255]. Note that for the radiation terms the temperature of the sample between the Cu current lead and node 1 is assumed to be at temperature T_1 and between node 1 and node 2 at temperature T_2.

The view factor ν from the outer- to the inner Kapton layer is assumed to be that of two infinitely long concentric cylinders. In this case, the outer cylinder radiates to the inner cylinder and the view factor takes the form: $\nu = A_{\mathrm{b}}/A_x$ [255]. The view factor from the sample to the vacuum can is rather complicated because of the sample's helical shape. To simplify the problem, the view factor is again assumed to be that of two infinitely long concentric cylinders. In this case the inner cylinder (the sample) radiates to the outer cylinder (the vacuum can) and the view factor $\nu = 1$. Note that with this assumption the view factor (thus P_{rad}) is overestimated.

In order to simplify the solution of (C.1), the radiative heat fluxes are linearised with respect to the unknown temperature T_x by developing (C.3) in a first order Taylor expansion:

$$\begin{aligned} P_{\mathrm{rad}} &\approx c_{\mathrm{rad}} \left(T_{x,0}^4 - T_{\mathrm{b}}^4 \right) + 4 c_{\mathrm{rad}} T_{x,0}^3 \left(T_x - T_{x,0} \right) \\ &= \frac{T_x}{R_{tr,x0}} - \frac{T_{\mathrm{b}}}{R_{tr,0x}}, \end{aligned}$$

with (C.4)

$$R_{tr,x0} = \left[4 c_{\mathrm{rad}} T_{x,0}^3 \right]^{-1};$$

$$R_{tr,0x} = \left[c_{\mathrm{rad}} \left(T_{\mathrm{b}}^3 + 3 \frac{T_{x,0}^4}{T_{\mathrm{b}}} \right) \right]^{-1}.$$

$R_{tr,x0}$ and $R_{tr,0x}$ can be regarded as the "thermal resistances" close to surfaces x and b respectively[1]. $T_{x,0}$ is a temperature that needs to be estimated a-priori and

[1] Note that for ease of representation, the radiative heat transfer in figure C.1 is represented by a single effective resistance, i.e.:

$$\frac{T_x}{R_{tr,x0}} - \frac{T_{\mathrm{b}}}{R_{tr,0x}} \equiv \frac{T_x - T_{\mathrm{b}}}{R_{tr,x0,\mathrm{eff}}}.$$

is taken to be the average estimated temperature of the whole radiation surface under consideration. For example, in table C.1 in the radiation term from the part of the sample between the current terminal and node 1 to the vacuum can (column S1 → vacuum can) $T_{x,0}$ is listed with a value of 15 K, which is an approximate average of the temperature of T_1 at node 1 and the bath temperature T_b.

With equations (C.2) and (C.4), the set of linear equations (C.1) can be written as:

$$\begin{aligned} P_\mathrm{h1} - \left(\frac{T_1 - T_\mathrm{b}}{R_{t,10}}\right) - \left(\frac{T_1}{R_{tr,10}} - \frac{T_\mathrm{b}}{R_{tr,01}}\right) - \left(\frac{T_1 - T_2}{R_{t,12}}\right) - \left(\frac{T_1 - T_\mathrm{h}}{R_{t,\mathrm{h}}}\right) &= 0 \\ - \left(\frac{T_2}{R_{tr,20}} - \frac{T_\mathrm{b}}{R_{tr,02}}\right) + \left(\frac{T_1 - T_2}{R_{t,12}}\right) - \left(\frac{T_2 - T_\mathrm{h}}{R_{t,\mathrm{h}}}\right) &= 0 \\ P_\mathrm{hh} - \left(\frac{T_\mathrm{h} - T_\mathrm{b}}{R_{t,\mathrm{h}0}}\right) - \left(\frac{T_\mathrm{h}}{R_{tr,\mathrm{h}0}} - \frac{T_\mathrm{b}}{R_{tr,0\mathrm{h}}}\right) + \left(\frac{T_1 - T_\mathrm{h}}{R_{t,\mathrm{h}}}\right) + \left(\frac{T_2 - T_\mathrm{h}}{R_{t,\mathrm{h}}}\right) &= 0 \end{aligned} \quad \text{(C.5)}$$

Reorganising (C.5) leaves the following linear equation:

$$\begin{pmatrix} \frac{-1}{R_{t,1\mathrm{tot}}} & \frac{1}{R_{t,12}} & \frac{1}{R_{t,\mathrm{h}}} \\ \frac{1}{R_{t,12}} & \frac{-1}{R_{t,2\mathrm{tot}}} & \frac{1}{R_{t,\mathrm{h}}} \\ \frac{1}{R_{t,\mathrm{h}}} & \frac{1}{R_{t,\mathrm{h}}} & \frac{-1}{R_{t,\mathrm{htot}}} \end{pmatrix} \begin{pmatrix} T_1 \\ T_2 \\ T_\mathrm{h} \end{pmatrix} = \begin{pmatrix} -P_\mathrm{h1} - \frac{T_\mathrm{b}}{R_{t,10}} - \frac{T_\mathrm{b}}{R_{tr,01}} \\ -\frac{T_\mathrm{b}}{R_{tr,02}} \\ -P_\mathrm{hh} - \frac{T_\mathrm{b}}{R_{t,\mathrm{h}0}} - \frac{T_\mathrm{b}}{R_{tr,0\mathrm{h}}} \end{pmatrix},$$

with (C.6)

$$\begin{aligned} R_{t,1\mathrm{tot}} &= \frac{1}{R_{t,10}} + \frac{1}{R_{tr,10}} + \frac{1}{R_{t,12}} + \frac{1}{R_{t,\mathrm{h}}}; \\ R_{t,2\mathrm{tot}} &= \frac{1}{R_{tr,20}} + \frac{1}{R_{t,12}} + \frac{1}{R_{t,\mathrm{h}}}; \\ R_{t,\mathrm{htot}} &= \frac{1}{R_{t,\mathrm{h}0}} + \frac{1}{R_{tr,\mathrm{h}0}} + \frac{2}{R_{t,\mathrm{h}}}. \end{aligned}$$

In this equation, the temperatures T_1, T_2 and T_h are the parameters to be solved; the heater powers P_h1 and P_hh are the independent variables and all the thermal resistances are known through the relevant material properties (see equations (C.2) and (C.4)) and are worked out –as an example– for a given wire in table C.1. The only remaining thermal resistance that is a-priori unknown is the resistance between the sample and the outer Kapton layer $R_{t,\mathrm{h}}$. This resistance consists of poorly defined contacts between the sample and the Nylon wires. Therefore $R_{t,\mathrm{h}}$ is determined by fitting T_1 and T_2 in equation (C.6) to the measured temperature T_1 and T_2, using $R_{t,\mathrm{h}}$ as a free parameter.

Table C.1: Estimate of the thermal resistivities in the sample holder / sample assembly at a baseline temperature of 25 K. The sample is a 19 filament MgB_2/CuSn wire with $d = 0.9$ mm and a filling factor f of 17 %. The data of the material properties are obtained from [30, 32, 255, 256].

		Node 1 ↓ Curr. term.	S1† ↓ Vac. can	Node 1 ↓ Node 2	S2† ↓ Vac. can	Node h (OKL) ↓ Curr. term.	Node h (OKL) ↓ IKL
Conduction							
A	[mm^2]	0.64	-	0.64	-	65	-
l	[mm]	10	-	490	-	3	-
κ	[W/mK]	280	-	280	-	0.1	-
R_t	[K/W]	56	-	2752	-	459	-
Radiation							
$T_{x,0}$	[K]	-	15	-	20	-	12
A_x	[mm^2]	-	304	-	2485	-	3100
A_b	[mm^2]	-	471	-	3847	-	2900
ϵ_x	[-]	-	0.7	-	0.7	-	0.9
ϵ_b	[-]	-	0.8	-	0.8	-	0.9
ν	[-]	-	1	-	1	-	1.1
$R_{tr,x0}$	[$\cdot 10^6$K/W]	-	5.31	-	0.27	-	0.11
$R_{tr,0x}$	[$\cdot 10^6$K/W]	-	1.98	-	0.08	-	0.03

† S1 is the sample between Cu current lead and node 1. S2 is the sample between node 1 and node 2.

Temperature Profile across the Sample

The measurements are performed with a 19 filament MgB_2/CuSn wire with a diameter of 0.9 mm and a filling factor of 17 %. Node 1 with the sample heater P_h1 is located approximately 3 mm from the upper Cu current terminals, which correspond to approximately 10 mm along the conductor. At this point an 80 Ω resistor is mounted on the wire that acts as heater P_h1. Close to this point a Cernox thermometer (T_1) is mounted on the wire. To ensure symmetry around the midplane of the holder, a similar heater (P'_h1) and thermometer (T'_1) are mounted ≈ 3 mm from the bottom Cu current terminal (node 1′). At node 2 a third Cernox thermometer is mounted to monitor T_2. The relevant parameters estimated for this configuration are listed in table C.1.

T_1, T_2 and T'_1 are then measured as a function of the heater powers P_h1 and P'_h1, while P_hh is switched off. In this way the temperature gradient between T_1 and T_2 is representative for the radial heat loss along the sample. The results of

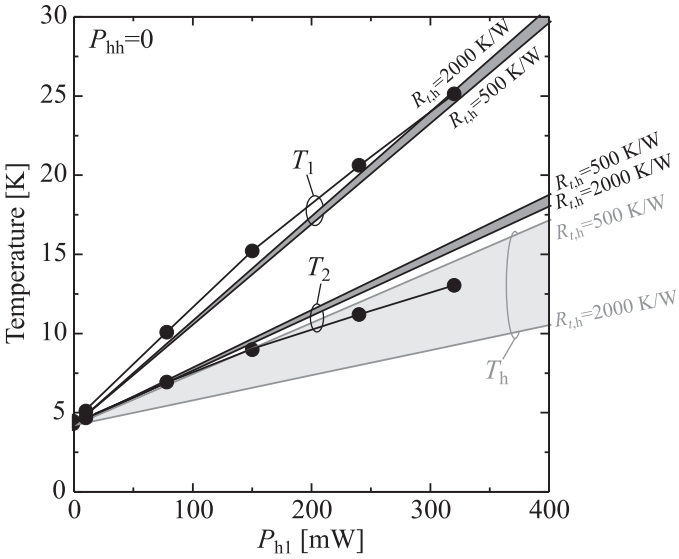

Figure C.2: Measured temperatures T_1 and T_2 as a function of the heater power P_{h1}, with $P_{\mathrm{hh}} = 0$ (**data-points**)). The **dark gray bands** indicate the calculations with $R_{t,\mathrm{h}}$ ranging from 500 to 2000 K/W. Also plotted (**light gray band**) is the corresponding temperature of the outer Kapton layer T_{h}.

the measurements are plotted in figure C.2, along with the model calculations. It can be seen that the model describes both T_1 and T_2 as a function of P_{h1} reasonably well when $R_{t,\mathrm{h}}$ is taken to be in the range between 500 and 2000 K/W. The deviation between the calculations and the data can be attributed to the simplifications that were assumed in the model. For instance, the downward curvature of the measured data is not described by the model. This is likely due to the linearisation of the radiative heat fluxes and to the increasing heat conduction through the wiring at higher temperatures, which is not accounted for in the model.

Note that the resulting value of $R_{t,\mathrm{h}}$, ranging between 500 and 2000 K/W, is relatively low compared to the thermal resistance of the sample between nodes 1 and 2 ($R_{t,12} \approx 2750$ K/W). Consequently, in spite of the Nylon spacers a significant amount of heat is lost to the underlying outer Kapton layer, resulting in a temperature gradient along the sample between nodes 1 and 2. In order to improve the homogeneity of the temperature, either $R_{t,\mathrm{h}}$ should be increased or the outer Kapton layer should be heated (P_{hh}). Both options are considered below.

Results

Figure C.3a displays the calculated effect of increasing $R_{t,\mathrm{h}}$ further. The calculated relative temperature gradient between T_1 and T_2 is plotted as a function of the heater power (P_{h1}) and the thermal resistance between sample and outer Kapton layer ($R_{t,\mathrm{h}}$). Included in the figure (data points) are the measured temperature gradients (from figure C.2) at $R_{t,\mathrm{h}} \approx 1000$ K/W. Increasing the value of $R_{t,\mathrm{h}}$ by a factor $\sim 100 \sim 1 \cdot 10^5$ K/W still leaves a maximum temperature gradient of about 3 %. Although this would be a significant improvement, table C.1 shows that this value of $R_{t,\mathrm{h}}$ would be similar to that of the radiative thermal resistances. In other words, even a free-hanging sample would still show a significant temperature gradient. So increasing $R_{t,\mathrm{h}}$, even to unrealistically high levels, would not result in an acceptable homogeneity over the sample.

Figure C.3b shows the effect of using an embedded heater P_{hh} in the outer Kapton layer instead of increasing $R_{t,\mathrm{h}}$. In this graph, the relative temperature gradient between T_1 and T_2 is plotted against the heater powers P_{h1} and P_{hh} (assuming that $R_{t,\mathrm{h}} \approx 1000$ K/W, as derived from the measurements at $P_{\mathrm{hh}} = 0$). This figure shows that, for sufficiently high P_{hh}-values, the temperature gradient can even be inverted with $T_2 > T_1$. This implies that in principle, P_{h1} and P_{hh} can be adjusted in such a way that $T_1 = T_2$. The model shows that for this particular sample, a homogeneous profile is achieved when $P_{\mathrm{hh}} \approx 0.15 P_{\mathrm{h1}}$. Also worth noting is that using only P_{hh} (along the line $P_{\mathrm{h1}} = 0$), would leave a negative gradient (i.e. $T_2 > T_1$) and would not lead to an acceptable temperature homogeneity. Thus to eliminate the temperature gradient, both the heaters on the sample's ends (P_{h1} and P'_{h1}) and the embedded heater (P_{hh}) have to be used.

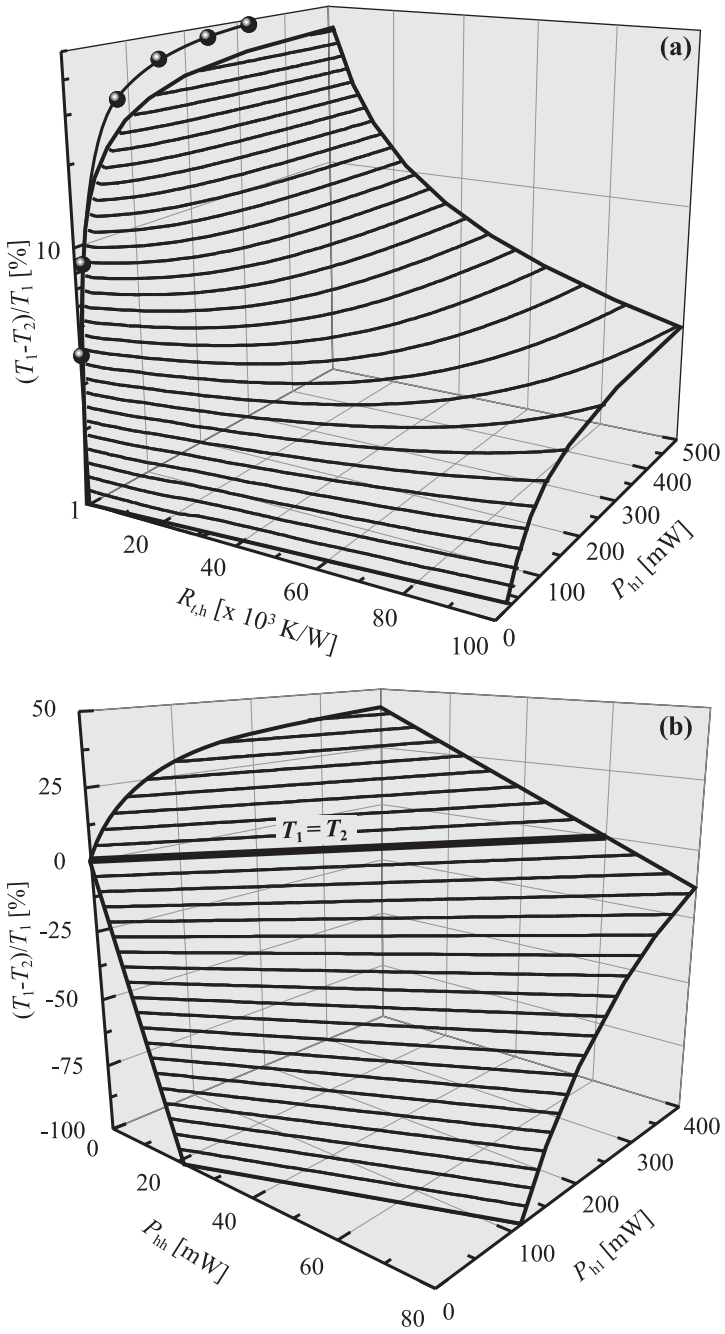

Figure C.3: (a) Calculated relative temperature difference as a function of the heater power P_{h1} and the thermal resistance between sample and outer Kapton layer ($R_{t,\mathrm{h}}$). The data points indicate the measurements (see figure C.2) at an assumed $R_{t,\mathrm{h}}$ of 1000 K/W. Note the logarithmic scale of the $(T_1 - T_2)/T_1$-axis. (b) Calculated relative temperature difference as a function of the heater power at the outer Kapton layer (P_{hh}) and the heater power at node 1 (P_{h1}).

Bibliography

[1] Nagamatsu, J., Nakagawa, N., Muranaka, T., Zenitani, Y., and Akimitsu, J. "Superconductivity at 39 K in Magnesium Diboride". *Nature* **410**, 63 (2001).

[2] Bud'ko, S., Lapertot, G., Petrovic, C., Cunningham, C., Anderson, N., and Canfield, P. "Boron isotope effect in superconducting MgB_2". *Physical Review Letters* **86**, 1877–1879 (2001).

[3] Lima, O., Ribeiro, R., Avila, M., Cardoso, C., and Coelho, A. "Anisotropic superconducting properties of aligned MgB_2 crystallites". *Physical Review Letters* **86**, 5974–5977 (2001).

[4] Suhl, H., Matthias, B., and Walker, L. "Bardeen-Cooper-Schrieffer theory of superconductivity in case of overlapping bands". *Physical Review Letters* **3**, 552–554 (1959).

[5] Choi, H., Roundy, D., H, S., Cohen, M., and Louie, S. "The origin of the anomalous superconducting properties of MgB_2". *Nature* **418**, 758–760 (2002).

[6] Cooley, L., Ghosh, A., and Scanlan, R. "Costs of high-field superconducting strands for particle accelerator magnets". *Superconductor Science and Technology* **18**, R51–R65 (2005).

[7] Tsukamoto, O. "Roads for HTS power applications to go into the real world: Cost issues and technical issues". *Cryogenics* **45**, 3–10 (2005).

[8] Braccini, V., Malagoli, A., Tumino, A., Romano, G., Vignolo, M., Grasso, G., and Siri, A. "Improvement of magnetic field behaviour of ex-situ processed Magnesium Diboride wires and tapes". presented at ASC 2006, Seattle (Wa), USA, August (2006).

[9] Rieger, J. "Siemens activities in superconductivity". Presented at the Workshop on Accelerator Magnet Superconductors (WAMS), Archamps, France, March (2004).

[10] Weijers, H., Trociewitz, U., Marken, K., Meinesz, M., Miao, H., and Schwartz, J. "The generation of 25.05T using a 5.11T $Bi_2Sr_2Ca_1Cu_2O_x$ superconducting insert magnet". *Superconductor Science and Technology* **17**, 636–644 (2004).

[11] Yamada, Y., Muroga, T., Iwai, H., Watanabe, T., Miyata, S., and Shiohara, Y. "Current status of pulsed laser deposition YBCO coated conductors in SRL using buffer layers by ion-beam assisted deposition GZO and self-epitaxy pulsed laser deposition CeO_2". *Superconductor Science and Technology* **17**, S328–S331 (2004).

[12] Godeke, A. *Performance bounderies in Nb_3Sn superconductors*. PhD thesis, University of Twente, (2005).

[13] Bottura, L. "A practical fit for the critical surface of NbTi". *IEEE Transactions on Applied Superconductivity* **10**, 1054 (2000).

[14] Somerkoski, J., Hampshire, D., Jones, H., Toivanen, R., and Lindroos, V. "Structure and superconducting property characterisation of MF Cu/Nb-46.5 w% Ti superconductors". *IEEE Transactions on Magnetics* **23**, 1629 (1987).

[15] `http://www.oxford-instruments.com`.

[16] `http://www.asc.wisc.edu/plot/plot.htm`.

[17] Sumption, M., Bhatia, M., Dou, S., Rindfleisch, M., Tomsic, M., Arda, L., Ozdemir, M., Hascicek, Y., and Collings, E. "Irreversibility field and flux pinning in MgB_2 with and without SiC additions". *Superconductor Science and Technology* **17**, 1180–1184 (2004).

[18] Sumption, M., Bhatia, M., Wu, X., Rindfleisch, M., Tomsic, M., and Collings, E. "Multifilamentary, in situ route,Cu-stabilized MgB_2 strands". *Superconductor Science and Technology* **18**, 730–734 (2005).

[19] Sumption, M., Bhatia, M., Rindfleisch, M., Tomsic, M., and Collings, E. "Transport properties of multifilamentary, in situ route, Cu-stabilized MgB_2 strands: one metre segments and the $J_c(B,T)$ dependence of short samples". *Superconductor Science and Technology* **19**, 155–160 (2006).

[20] Ma, Y., Zhang, X., Xu, A., Li, X., Xiao, L., Nishijima, G., Awaji, S., Watanabe, K., Jiao, Y., Xiao, L., Bai, X., Wu, K., and Wen, H. "The effect of $ZrSi_2$ and SiC doping on the microstructure and $J_c(B)$ properties of PIT processed MgB_2 tapes". *Superconductor Science and Technology* **19**, 133–137 (2006).

[21] Matsumoto, A., Kumakura, H., Kitaguchi, H., Hatakeyama, H., Yamada, H., and Hirakawa, M. "The microstructures and superconducting properties of MgB_2 tapes processed in-situ by a ball-milling method". *IEEE Transactions on Applied Superconductivity* **15**, 3333–3336 (2005).

[22] Nakane, T., Kitaguchi, H., and Kumakura, H. "Improvement in the critical current density of ex situ powder in tube processed MgB_2 tapes by utilizing powder prepared from an in situ processed tape". *Applied Physics Letters* **88**, 22513–1–3 (2006).

[23] Yamada, H., Hirakawa, M., Kumakura, H., Matsumoto, A., and Kitaguchi, H. "Superconducting properties of Powder-in-Tube MgB_2 tapes prepared with fine powders". *IEEE Transactions on Applied Superconductivity* **15**, 3337–3340 (2005).

[24] Dou, S. X., Soltanian, S., Horvat, J., Wang, X. L., Zhou, S. H., Ionescu, M., Liu, H. K., Munroe, P., and Tomsic, M. "Enhancement of the critical current density and flux pinning of MgB_2 superconductor by nanoparticle SiC doping". *Applied Physics Letters* **81**, 3419–3421 (2002).

[25] Tressler, R. "Vehicular fuel cell systems". `http://www.fuelcell-magazine.com/eprints/free/maxwellsept04.pdf`.

[26] `http://www.amsuper.com/products/transmissionGrid/104273034641.cfm`.

[27] Kiyoshi, T., Yoshikawa, M., Sato, A., Itoh, K., Matsumoto, S., Wada, H., Ito, S., Miki, T., Miyazaki, T., Kamikado, T., Ozaki, A., Hase, T., Hamada, M., Hyashi, S., Kawate, Y., and Hirose, R. "Operation of a 920-MHz high-resolution NMR magnet at TML". *IEEE Transactions on Applied Superconductivity* **13**, 1391–1395 (2003).

[28] Wilson, M. N. *Superconducting Magnets*. Oxford University Press, (1987).

[29] Yang, Y., Young, E., Bianchetti, M., Beduz, C., Martínez, E., and Giunchi, G. "Measurements of AC-losses in MgB_2 wire and bulk conductors at different temperatures". *IEEE Transactions on Applied Superconductivity* **15**, 2883–2886 (2005).

[30] Schneider, M., Lipp, D., Gladun, A., Zahn, P., Handstein, A., Fuchs, G., Drechsler, S., Richter, M., Müller, K., and Rosner, H. "Heat and charge transport properties of MgB_2". *Physica C* **363**, 6–12 (2001).

[31] Wang, Y., Plackowski, T., and Junod, A. "Specific heat in the superconducting and normal state (2300 K, 016 T), and magnetic susceptibility of the 38 K superconductor MgB2: evidence for a multicomponent gap". *Physica C* **355**, 179–193 (2001).

[32] Eckels Engineering Inc. "Cryocomp 3.01". Crycomp is a database for thermal properties of materials used in cryogenic engineering.

[33] `http://cryogenics.nist.gov/`.

[34] Castellazzi, S., Cimberle, M., Ferdeghini, C., Giannini, E., Grasso, G., Marré, D., Putti, M., and Siri, A. "Thermal conductivity of a BSCCO(2223) c-oriented tape: a discussion on the origin of the peak". *Physica C* **273**, 314–322 (1997).

[35] Gordon, J., Prigge, S., Collocott, S., and Driver, R. "Specific heat of $(BiPb)_2Sr_2Ca_2Cu_3O_{10-\gamma}$ from 78 to 300K". *Physica C* **185-189**, 1351–1352 (1991).

[36] Dhallé, M., Van der Laan, D., Van Weeren, H., Ten Haken, B. "Signatures of different dissipation mechanisms in the n-value of Bi,Pb(2223) tapes". Presented at the ICMC Topical Conferenence on the Voltage-Current Relation, Enschede, The Netherlands, May (2003).

[37] Müller, C. and Saur, E. "Influence of pressure on the superconductivity of some high-field superconductors". *Reviews of Modern Physics* **36**, 103–105 (1964).

[38] Chu, C. and Vieland, L. "The superconducting transition temperature and its high-pressure behaviour of tetragonal Nb_3Sn". *Journal of Low Temperature Physics* **17**, 25–29 (1974).

[39] Gubser, D. and Webb, A. "High-pressure effects on the superconducting transition temperature of aluminium". *Physical Review Letters* **35**, 104–107 (1975).

[40] Ekin, J., Fickett, F., and Clark, A. "Effect of stress on the critical current of NbTi multifilamentary composite wire". *Advances in Cryogenic Engineering* **22**, 449–452 (1977).

[41] Ekin, J. "Effect of stress on the critical current of Nb_3Sn multifilamentary composite wire". *Applied Physics Letters* **29**, 216–219 (1976).

[42] Ekin, J. "Strain scaling law for flux pinning in practical superconductors. Part 1: Basic relationship and application to Nb_3Sn conductors". *Cryogenic* **20**, 611–624 (1980).

[43] Ekin, J. "Four-dimensional J-B-T-ε critical surface for superconductors". *Journal of Applied Physics* **54**, 303–306 (1983).

[44] Ten Haken, B. *Strain effects on the critical properties of high-field superconductors*. PhD thesis, University of Twente, (1994).

[45] Markiewicz, W. D. "Elastic stiffness model for the critical temperature T_c of Nb_3Sn including strain dependence". *Cryogenics* **44**, 767–782 (2004).

[46] Markiewicz, W. D. "Invariant formulation of the strain dependence of the critical temperature T_c of Nb_3Sn in a three term approximation". *Cryogenics* **44**, 895–908 (2004).

[47] Iwasa, Y. *Case studies in superconducting magnets.* Kluwer Academic Publishers, (2002).

[48] Van den Eijnden, N. C., Nijhuis, A., Ilyin, Y., Wessel, W., and Ten Kate, H. "Axial tensile stress-strain characterization of ITER model coil type Nb_3Sn strands in TARSIS". *Superconductor Science and Technology* **18**, 1523–1532 (2005).

[49] Godeke, A., Dhallé, M., Morelli, A., Stobbelaar, L., Van Weeren, H., Van Eck, H., Abbas, W., Nijhuis, A., Den Ouden, A., and Ten Haken, B. "A device to investigate the axial strain dependence of the critical current density in superconductors". *Review of Scientific Instruments* **75**, 5112–5118 (2004).

[50] Canfield, P., Finnemore, D., Bud'ko, S., Ostenson, J., Lapertot, G., Cunningham, C., and Petrovic, C. "Superconductivity in dense MgB_2 wires". *Physical Review Letters* **86**, 2423–2426 (2001).

[51] Cunningham, C., Petrovic, C., Lapertot, G., Bud'ko, S., Laabs, F., Straszheim, W., Finnemore, D., and Canfield, P. "Synthesis and processing of MgB_2 powders and wires". *Physica C* **353**, 5–10 (2001).

[52] Komori, K., Kawagishi, K., Takano, Y., Fujii, H., Arisawa, S., and Kumakura, H. "Approach for the fabrication of MgB_2 superconducting tape with large in-field transport critical current density". *Applied Physics Letters* **81**, 1047–1049 (2002).

[53] Giunchi, G., Ceresara, S., Ripamonti, G., Zenobio, A, D., Rossi, S., Chiarelli, S., Spadoni, M., Wesche, R., and Bruzzone, P. "High performance new MgB_2 superconducting hollow wires". *Superconductor Science and Technology* **16**, 285–291 (2003).

[54] Togano, K., Nakane, T., Fujii, H., Takeya, H., and Kumakura, H. "An interface diffusion process approach for the fabrication of MgB_2 wire". *Superconductor Science and Technology* **19**, L17–L20 (2006).

[55] Flükiger, R., Lezza, P., Beneduce, C., Musolino, N., and Suo, H. "Improved transport critical current and irreversibility fields in mono- and multifilamentary Fe/MgB_2 tapes and wires using fine powders". *Superconductor Science and Technology* **16**, 264–270 (2003).

[56] Flükiger, R., Suo, H., Musolino, N Beneduce, C., Toulemonde, P., and Lezza, P. "Superconducting properties of MgB_2 tapes and wires". *Physica C* **385**, 286–305 (2003).

[57] Grasso, G., Malagoli, A., Marré, D., Bellingeri, E., Braccini, V., Roncallo, S., Scati, N., and Siri, A. "Transport properties of Powder-In-Tube processed MgB_2 tapes". *Physica C* **378-381**, 899–902 (2002).

[58] Grasso, G., Malagoli, A., Modica, M., Tumino, A., Ferdeghini, C., Siri, A., Vignola, C., Martini, L., Previtali, V., and Volpini, G. "Fabrication and properties of monofilamentary MgB_2 superconducting tapes". *Superconductor Science and Technology* **16**, 271–275 (2003).

[59] Kováč, P., Hušek, I., and Melišek, T. "Transport currents of two-axially-rolled and post-annealed MgB_2/Fe wires at 4.2K". *Superconductor Science and Technology* **15**, 1340–1344 (2002).

[60] Pan, V., Zhou, S., Liu, H., and Dou, S. "Properties of superconducting MgB_2 wires: in-situ versus ex-situ reaction technique". *Superconductor Science and Technology* **16**, 639–644 (2003).

[61] Eisterer, M., Glowacki, B., Weber, H., Greenwood, L., and Majoros, M. "Enhanced transport current in Cu-sheathed MgB_2 wires". *Superconductor Science and Technology* **15**, 1088–1091 (2002).

[62] Glowacki, B., Majoros, M., Vickers, M., Evetts, J., Shi, Y., and McDougal, I. "Superconductivity of Powder-In-Tube MgB_2 wires". *Superconductor Science and Technology* **14**, 193–199 (2001).

[63] Mikheenko, P., Bevan, A., and Abell, J. "Origin of high critical current in bulk MgB_2". presented at ASC 2006, Seattle (Wa), USA, August (2006).

[64] Suo, H., Beneduce, C., Dhallé, Musolino, N., Genoud, J., and Flükiger, R. "Large transport critical currents in dense Fe- and Ni-clad MgB_2 superconducting tapes". *Applied Physics Letters* **79**, 3116–3118 (2001).

[65] Grasso, G., Malagoli, A., Tumino, A., Fanciulli, C., Nardelli, D., Ferdeghini, C., and Siri, A. "Present status and future perspectives for Ni-sheathed MgB_2 superconducting tapes". Institute of Physics Conference Series, Eucas 2003 (2003).

[66] Giunch, G., Ripamonti, G., Raineri, S., Botta, D., Gerbaldo, R., and Quarantiello, R. "Grain size effects on the superconducting properties of high density bulk MgB_2". *Superconductor Science and Technology* **17**, S583–S588 (2004).

[67] Tinkham, M. *Introduction to Superconductivity.* McGraw-Hill, (1996).

[68] Ten Elshof, J. Comminution. Internal Report CT94/482/31, University of Twente, Inorganic Materials Science group, (1994).

[69] Kazakov, S., Karpinski, J., Jun, J., Geiser, P., Zhigadlo, N., Puzniak, R., and Mironov, A. "Single crystal growth and properties of MgB_2 and $Mg(B_{1-x}C_x)_2$". *Physica C* **408-410**, 123–124 (2004).

[70] Dhallé, M, Cuthbert, M and Johnston, M and Everett, J and Flükiger, R and Dou, S and Goldacker, W and Beale, T and Caplin, A. "Experimental assessment of the current-limiting mechanisms in BSCCO/Ag high temperature superconducting tapes". *Superconductor Science and Technology* **10**, 21–31 (1997).

[71] Angadi, M., Caplin, A., Laverty, J., and Shen, Z. "Non-destructive determination of the current-carrying length scale in superconducting crystals and thin films". *Physica C* **177**, 479–486 (1991).

[72] Holcomb, M. "Supercurrents in magnesium diboride/metal composite wire". *Physica C* **423**, 103–118 (2005).

[73] Tachikawa, K., Yamada, Y., Enomoto, M., Aodai, M., and Kumakura, H. "Structure and critical current of Ni-sheathed PIT MgB_2 tapes with In metal powder addition". *Physica C* **392-396**, 1030–1034 (2003).

[74] Kováč, P., Hušek, I., Melišek, T., Grovenor, C., Haigh, S., and Jones, H. "Improvement of the current carrying capability of ex situ MgB_2 wires by normal particle additions". *Superconductor Science and Technology* **17**, 1225–1230 (2004).

[75] Avitzur, B. *Handbook of Metal Forming Porcesses.* John Wiley & Sons, Inc., (1983).

[76] Avitzur, B., Wu, R., Talbert, S., and Chou, Y. "Criterion for the prevention of core fracturing during extrusion of bimetal rods". *Journal of Engineering for Industry* **104**, 293–304 (1982).

[77] Avitzur, B., Wu, R., Talbert, S., and Chou, Y. "Fracture in drawing bimetal rods and wire". *Journal of Engineering for Industry, Series B* **108**, 133–140 (1986).

[78] Shinohara, K. "Relationship between work-hardening exponent and load dependence of Vickers hardness in copper". *Journal of Materials Science* **28**, 5325–5329 (1993).

[79] Wilson, D. "Relationships between microstructure and behaviour in the uniaxial tensile test". *Journal of Physics D: Applied Physics* **7**, 954–968 (1974).

[80] Campbell, J. *Handbook on materials for superconducting machinary.* Batelle, Columbus, Ohio: Metals and Ceramics Information Center, (1974).

[81] Weissbach, W. *Materialenkennis en Materiaalbeproeving.* Technische Uitgeverij De Vey Mestdagh B.V., (1981).

[82] Kováč, P. Private communication, (2004). Sintering at 950 °C for 0.5 hr leaves a MgB_2/Fe reaction layer of about 10 μm. To prevent reaction between Cu and MgB_2 the Fe reaction barrier should be about 3 times as thick.

[83] Hušek, I. and Kováč, P. "Evaluation of core density during the tow-axial rolling of BSCCO/AG composite". *Superconductor Science and Technology* **13**, 385–390 (2000).

[84] Kingery, W. *Introduction to Ceramics.* Wiley, New York, (1976).

[85] Dancer, C., Bevan, A., Mikheenko, P., Abell, J., Todd, R., and Grovenor, C. "Does magnesium diboride sinter?". presented at ASC 2006, Seattle (Wa), USA, August (2006).

[86] Kováč, P., Hušek, I., Grovenor, C., and Salter, C. "Properties of as-deformed and post-annealed MgB_2/Fe(Fe-alloy) composite wires". *Superconductor Science and Technology* **16**, 292–296 (2003).

[87] Massalski, T. and Okamoto, H. *Binary alloy phase diagrams.* ASM International, (1986).

[88] Boschman, J. *On the resistive transition of composite superconductors.* PhD thesis, University of Twente, (1991).

[89] Schlachter, S., Goldacker, W., Reiner, J., Zimmer, S., Liu, B., and Obst, B. "Influence of the preparation process on microstructure, critical current density and Tc of MgB_2 powder-in-tube wires". *IEEE Transactions on Applied Superconductivity* **13**, 3203–3206 (2003).

[90] Lezza, P., Abacherli, V., Clayton, N., Senatore, C., Uglietti, D., Suo, H., and Flukiger, R. "Transport properties and exponential n-values of Fe/MgB_2 tapes with various MgB_2 particle sizes". *Physica C* **401**, 305–309 (2004).

[91] Jiang, C., Hatakeyama, H., and Kumakura, H. "Preparation of MgB_2/Fe tapes with improved Jc property using MgH_2 powder and a short pre-annealing and intermediate rolling process". *Superconductor Science and Technology* **18**, L17–L22 (2005).

[92] Collings, E., Lee, E., Sumption, M., Tomsic, M., Wang, X., Soltanian, S., and Dou, S. "Continuous- and batch-processed MgB_2/Fe strands-transport and magnetic properties". *Physica C* **386**, 555–559 (2003).

[93] Ferrando, V., Orgiani, P., Pogrebnyakov, A., Chen, J., Li, Q., Redwing, J., Xi, X., Giencke, J., Eom, C., Feng, Q., Betts, J., and Mielke, C. "High upper critical field and irreversibility field in MgB_2 coated-conductor fibers". *Applied Physics Letters* **87**, 252509 (2005).

[94] Dhallé, M and Toulemonde, P and Beneduce, C and Musolino, N and Decroux, M and Flükiger, R. "Transport and inductive critical current densities in superconducting MgB_2". *Physica C* **363**, 155–165 (2001).

[95] Schlachter, S., Frank, A., Ringsdorf, B., Orschulko, H., Obst, B., Liu, B., and Goldacker, W. "Suitability of sheath materials for MgB_2 powder-in-tube superconductors". *Physica C* **445-448**, 777–783 (2006).

[96] `http://www.engineeringvillage2.org`.

[97] Civale, L., Serquis, A., Hammon, D., Liao, X., Coulter, J., Zhu, Y., Holesinger, T., Peterson, D., and Mueller, F. "High critical currents in powder in tube MgB_2 wires: influence of microstructure and heat treatments". *IEEE Transactions on Applied Superconductivity* **13**, 3347–3350 (2003).

[98] Dou, S., Horvat, J., Soltanian, S., Wang, X., Qin, M., Zhou, S., Liu, H., and Munroe, P. "Transport critical current density in Fe-sheathed nano-SiC doped MgB_2 wires". *IEEE Transactions on Applied Superconductivity* **13**, 3199–3202 (2003).

[99] Eyidi, D., Eibl, O., Wenzel, T., Nickel, K., Schlachter, S., and Goldacker, W. "Superconducting properties, microstructure and chemical composition of MgB_2 sheathed materials". *Superconductor Science and Technology* **16**, 778–788 (2003).

[100] Fabbricatore, P., Greco, M., Musenich, R., Kovac, P., Husek, I., and Gomory, F. "Influence of the sintering process on critical currents, irreversibility lines and pinning energies in multifilamentary MgB_2 wires". *Superconductor Science and Technology* **16**, 364–370 (2003).

[101] Fang, H., Padmanabhan, S., Zhou, Y., Putman, P., and Salama, K. "High I_c in iron-clad MgB_2 tape". *IEEE Transactions on Applied Superconductivity* **13**, 3207–3209 (2003).

[102] Feng, Y., Yan, G., Zhao, Y., Wu, X., Pradhan, A., Zhang, X., Liu, C., Liu, X., and Zhou, L. "High critical current density in MgB_2 Fe wires". *Superconductor Science and Technology* **16**, 682–684 (2003).

[103] Feng, Y., Yan, G., Zhao, Y., Liu, C., Fu, B., Zhou, L., Cao, L., Ruan, K., Li, X., Shi, L., and Zhang, Y. "Superconducting properties of MgB_2 wires and tapes with different metal sheaths". *Physica C* **386**, 598–602 (2003).

[104] Fischer, C., Rodig, C., Haessler, W., Perner, O., Eckert, J., Nenkov, K., Fuchs, G., Wendrock, H., Holzapfel, B., and Schultz, L. "Preparation of MgB_2 tapes using a nanocrystalline partially reacted precursor". *Applied Physics Letters* **83**, 1803–1805 (2003).

[105] Fu, B., Feng, Y., Yan, G., Liu, C., Zhou, L., Cao, L., Ruan, K., and Li, X. "High transport critical current in MgB_2/Fe wire by in situ powder-in-tube process". *Physica C* **392-396**, 1035–1038 (2003).

[106] Fujii, H., Togano, K., and Kumakura, H. "Enhancement of critical current density of in situ processed MgB_2 tapes by WB addition". *Superconductor Science and Technology* **16**, 432–436 (2003).

[107] Fujii, H., Togano, K., and Kumakura, H. "Fabrication of MgB_2 tapes sheathed with carbon steels by ex situ and in situ methods". *IEEE Transactions on Applied Superconductivity* **13**, 3217–3220 (2003).

[108] Goldacker, W., Schlachter, S., Reiner, J., Zimmer, S., Nyilas, A., and Kiesel, H. "Mechanical properties of reinforced MgB_2 wires". *IEEE Transactions on Applied Superconductivity* **13**, 3261–3264 (2002).

[109] Haessler, W., Rodig, C., Fischer, C., Holzapfel, B., Perner, O., Eckert, J., Nenkov, K., and Fuchs, G. "Low temperature preparation of MgB_2 tapes using mechanically alloyed powder". *Superconductor Science and Technology* **16**, 281–284 (2003).

[110] Ko, J.-W., Yoo, J., Kim, Y.-K., Kim, H.-D., Oh, K.-H., Choe, S., Chung, H., Chung, S. J., Kumakura, H., Matsumoto, A., and Togano, K. "Influence of Cu addition on microstructure and transport properties in MgB_2 tapes". *IEEE Transactions on Applied Superconductivity* **13**, 3214–3216 (2003).

[111] Kumakura, H., Matsumoto, A., Fujii, H., Kitaguchi, H., Ooi, S., Togano, K., and Hatakeyama, H. "Fabrication and properties of powder-in-tube processed MgB_2 tapes and wires". *Journal of Low Temperature Physics* **131**, 1085–1093 (2003).

[112] Ma, Y., Kumakura, H., Matsumoto, A., Hatakeyama, H., and Togano, K. "Improvement of critical current density in Fe-sheathed MgB_2 tapes by $ZrSi_2$, ZrB_2 and WSi_2 doping". *Superconductor Science and Technology* **16**, 852–856 (2003).

[113] Malagoli, A., Tumino, A., Braccini, V., Ferdeghini, C., Siri, A., Martini, L., Vignola, C., Previtali, V., Volpini, G., and Grasso, G. "Magnetic field dependence of the critical current in MgB_2 and Bi-2223 superconducting tapes fabricated by the powder-in-tube method". *IEEE Transactions on Applied Superconductivity* **13**, 3328–3331 (2003).

[114] Matsumoto, A., Kumakura, H., Kitaguchi, H., and Hatakeyama, H. "Effect of SiO_2 and SiC doping on the powder-in-tube processed MgB_2 tapes". *Superconductor Science and Technology* **16**, 926–930 (2003).

[115] Matsumoto, A., Hatakeyama, H., Kitaguchi, H., Togano, K., and Kumakura, H. "The superconducting properties of MgB_2 (stainless steel) tapes fabricated by the PIT process". *IEEE Transactions on Applied Superconductivity* **13**, 3225–3228 (2003).

[116] Ruan, K., Li, H., Yu, Y., Wang, C., Cao, L., Liu, C., Du, S., Yan, G., Feng, Y., Wu, X., Wang, J., Liu, X., Zhang, P., Wu, X., and Zhou, L. "Transport critical current density of Fe sheath MgB_2 tapes sintered at different temperatures". *Physica C* **386**, 578–580 (2003).

[117] Serquis, A., Civale, L., Hammon, D., Liao, X., Coulter, J., Zhu, Y., Jaime, M., Peterson, D., Mueller, F., Nesterenko, V., and Gu, Y. "Hot isostatic pressing of powder in tube MgB_2 wires". *Applied Physics Letters* **82**, 2847–2849 (2003).

[118] Song, K., Park, C., Lee, N., Jang, H., Ha, H., Ha, D., Oh, S., Sohn, M., Ko, R., Kwon, Y., and Joo, J. "Fabrication and properties of MgB_2 stainless-steel tapes by PIT process". *IEEE Transactions on Applied Superconductivity* **13**, 3221–3224 (2003).

[119] Suo, H., Lezza, P., Uglietti, D., Beneduce, C., Abächerli, V., and Flükiger, R. "Transport critical current densities and n factors in mono- and multifilamentary MgB_2/Fe tapes and wires using fine powders". *IEEE Transactions on Applied Superconductivity* **13**, 3265–3268 (2003).

[120] Tachikawa, K., Yamada, Y., Enomoto, M., Aodai, M., and Kumakura, H. "Effects of metal powder addition on the structure and critical current of Ni-sheathed PIT MgB_2 tapes". *IEEE Transactions on Applied Superconductivity* **13**, 3269–3272 (2003).

[121] Yamamoto, K., Osamura, K., Balamurugan, S., Nakamura, T., Hoshino, T., and Muta, I. "Mechanical and superconducting properties of PIT-processed MgB_2 wire after heat treatment". *Superconductor Science and Technology* **16**, 1052–1058 (2003).

[122] Bhatia, M., Sumption, M., Tomsic, M., and Collings, E. "Influence of heat-treatment schedules on the transport current densities of long and short segments of superconducting MgB_2 wire". *Physica C* **407**, 153–159 (2004).

[123] Feng, Y., Yan, G., Zhao, Y., Liu, C., Liu, X., Zhang, P., Zhou, L., Sulpice, A., Mossang, E., and Hebral, B. "Preparation and enhancement of critical current density in MgB_2 wires and tapes". *Journal of Physics: Condensed Matter* **16**, 1803–1811 (2004).

[124] Fischer, C., Habler, W., Rodig, C., Perner, O., Behr, G., Schubert, M., Nenkov, K., Eckert, J., Holzapfel, B., and Schultz, L. "Critical current densities of superconducting MgB_2 tapes prepared on the base of mechanically alloyed precursors". *Physica C* **406**, 121–130 (2004).

[125] Fu, M., Chen, J., Jiao, Z., Kumakura, H., Togano, K., Ding, L., Zhang, Y., Chen, Z., Han, H., and Chen, J. "Mechanical properties and bending strain effect on Cu-Ni sheathed MgB_2 superconducting tape". *Physica C* **406**, 53–57 (2004).

[126] Goldacker, W., Schlachter, S., Obst, B., Liu, B., Reiner, J., and Zimmer, S. "Properties of reinforced MgB_2 wires with thin filaments". Institute of Physics Conference Series, Eucas 2003 (2003).

[127] Goldacker, W., Schlachter, S., Obst, B., Liu, B., Reiner, J., and Zimmer, S. "Development and performance of thin steel reinforced MgB_2 wires and low-temperature in situ processing for further improvements". *Superconductor Science and Technology* **17**, S363–S368 (2004).

[128] Goldacker, W., Schlachter, S., Liu, B., Obst, B., and Klimenko, E. "Considerations on critical currents and stability of MgB_2 wires made by different preparation routes". *Physica C* **401**, 80–86 (2004).

[129] Goldacker, W., Schlachter, S.I., Obst, B., and Eisterer, M. "In situ MgB_2 round wires with improved properties". *Superconductor Science Technology* **17**, S490–S495 (2004).

[130] Hascicek, Y., Aslanoglu, Z., Arda, L., Akin, Y., Sumption, M., and Tomsic, M. "Fabrication and testing of W&R MgB_2 coils using CTFF Cu/MgB_2wires and the sol-gel insulation process". *Advances in Cryogenic Engineering: Transactions of the ICMC* **711**, 541–545 (2004).

[131] Kikuchi, A., Iijima, Y., Yoshida, Y., Banno, N., Takeushi, T., and Inoue, K. "Microstructure and superconductivity of MgB_2 synthesized by using Mg-based compound powders". *Physica C* **412-414P2**, 1174–1178 (2004).

[132] Kitaguchi, H., Matsumoto, A., Hatakeyama, H., and Kumakura, H. "V-I characteristics of MgB_2 PIT composite tapes: n-values under strain, in high fields, or at high temperatures". *Physica C* **401**, 246–250 (2004).

[133] Kumakura, H., Kitaguchi, H., Matsumoto, A., and Hatakeyama, H. "Upper critical fields of powder-in-tube-processed MgB_2/Fe tape conductors". *Applied Physics Letters* **84**, 3669–3671 (2004).

[134] Ma, Y., Kumakura, H., Matsumoto, A., Takeya, H., and K., T. "Superconducting properties of powder-in-tube MgB_2 tapes without and with WSi_2 addition". *Physica C* **408-410**, 138139 (2004).

[135] Matsumoto, A., Kumakura, H., Kitaguchi, H., and Hatakeyama, H. "Effect of impurity additions on the microstructures and superconducting properties of in situ-processed MgB_2 tapes". *Superconductor Science and Technology* **17**, S319–S323 (2004).

[136] Tachikawa, K., Yamada, Y., Katagiri, K., Kumakura, H., Iwamoto, A., and Watanabe, K. "Effects of metal powder addition in Ni-sheathed pit MgB_2 tapes". *Advances in Cryogenic Engineering: Transactions of the ICMC* **711**, 561–568 (2004).

[137] Tanaka, K., Okada, M., Hirakawa, M., Yamada, H., Kumakura, H., and Kitaguchi, H. "Fabrication and transport properties of MgB_2 (SUS316/Cu) multifilament wires". *IEEE Transactions on Applied Superconductivity* **14**, 1039–1041 (2004).

[138] Yamada, H., Hirakawa, M., Kumakura, H., Matsumoto, A., and Kitaguchi, H. "Critical current densities of powder-in-tube MgB_2 tapes fabricated with nanometer-size Mg powder". *Applied Physics Letters* **84**, 1728–1730 (2004).

[139] Arda, L., Ozdemir, M., Akin, Y., Aktas, S., Tomsic, M., and Hascicek, Y. "Field dependence of the critical current density of MgB_2 conductors between 4.2 K and 30 K up to 20 T". *IEEE Transactions on Applied Superconductivity* **15**, 3281–3283 (2005).

[140] Braccini, V., Nardelli, D., Malagoli, A., Tumino, A., Fanciulli, C., Bernini, C., Siri, A., and Grasso, G. "MgB_2 tapes with non-magnetic sheath: effect of the sintering temperature on the superconducting properties". *IEEE Transactions on Applied Superconductivity* **15**, 3211–3214 (2005).

[141] Chen, S., Tan, K., Glowacki, B., Yeoh, W., Soltanian, S., Horvat, J., and Dou, S. "Effect of heating rates on superconducting properties of pure MgB_2, carbon nanotube- and nano-SiC-doped in situ MgB_2/Fe wires". *Applied Physics Letters* **87**, 182504–1–3 (2005).

[142] Dhallé, M., Van Weeren, H., Wessel, W., Den Ouden, A., Ten Kate, H., Hušek, I., Kováč, P., Schlachter, S., and Goldacker, W. "Scaling the reversible strain response of MgB_2 conductors". *Superconductor Science and Technology* **18**, S253S260 (2005).

[143] Eisterer, M. "Influence of disorder on H_{c2}-anisotropy and flux pinning in MgB_2". *Physica Status Solidi C* **2**, 1606–1614 (2005).

[144] Eisterer, M., Krutzler, C., and Weber, H. "Influence of the upper critical-field anisotropy on the transport properties of polycrystalline MgB_2". *Journal of Applied Physics* **98**, 33906–1–5 (2005).

[145] Fang, H., Gijavanekar, P., Zhou, Y., Putman, P., and Salama, K. "Development of Fe-sheathed MgB_2 wires and tapes for electric power applications". *IEEE Transactions on Applied Superconductivity* **15**, 3200–3203 (2005).

[146] Fang, H., Gijavanekar, P., Zhou, Y., Liang, G., Putman, P., and Salama, K. "High critical current of Cu-sheathed MgB_2 wire at 20 K". *IEEE Transactions on Applied Superconductivity* **15**, 3215–3218 (2005).

[147] Holubek, T., Kováč, P., and Melišek, T. "Current transfer length in MgB_2/Fe mono-core wire and approximation of the interface layer resistivity". *Superconductor Science and Technology* **18**, 1218–1221 (2005).

[148] Jiang, C., Nakane, T., and Kumakura, H. "Enhanced J_c-B performance in MgB_2 Fe tapes with nanometre Si_3N_4 addition". *Superconductor Science and Technology* **18**, 902–906 (2005).

[149] Jiang, C., Hatakeyama, H., and Kumakura, H. "Effect of nanometer MgO addition on the in situ PIT processed MgB_2/Fe tapes". *Physica C* **423**, 45–50 (2005).

[150] Kikuchi, A., Iijima, Y., Banno, N., Takeuchi, T., and Inoue, K. "Microstructure and J_c-B performance of powder-in-tube MgB_2 wire made by using Mg_2Cu powders with low melting point". *IEEE Transactions on Applied Superconductivity* **15**, 3207–3210 (2005).

[151] Kitaguchi, H. and Kumakura, H. "Superconducting and mechanical performance and the strain effects of a multifilamentary MgB_2/Ni tape". *Superconductor Science and Technology* **18**, S284–S289 (2005).

[152] Kondo, T., Badica, P., Nakamori, Y., Orimo, S., Togano, K., Nishijima, G., and Watanabe, K. "MgB_2 Fe superconducting tapes made using mechanically milled powders in Ar and H_2 atmospheres". *Physica C* **426-431**, 1231–1237 (2005).

[153] Kováč, P., Hušek, I., Melišek, T., Dhalle, M., Muller, M., and Den Ouden, A. "The effect of shape and deformation in ex situ MgB_2 W/Fe composite wires". *Superconductor Science and Technology* **18**, 615–622 (2005).

[154] Kováč, P., Hušek, I., Melišek, T., and Strbik, V. "Basic properties of rectangular MgB_2/FeNiCo and MgB_2/Fe wires made in situ". *Superconductor Science and Technology* **18**, 856–860 (2005).

[155] Kumakura, H., Kitaguchi, H., Matsumoto, A., and Hatakeyama, H. "Improved superconducting properties of in-situ PIT-processed MgB_2 tapes". *IEEE Transactions on Applied Superconductivity* **15**, 3184–3187 (2005).

[156] Lezza, P., Gladyshevskii, R., Senatore, C., Cusanelli, G., Suo, H., Flükiger, and R. "Anisotropy of J_c in Ex Situ MgB_2/Fe Monofilamentary Tapes". *IEEE Transactions on Applied Superconductivity* **17**, 3196–3199 (2005).

[157] Pachla, W., Kovac, P., Husek, I., Melisek, T., Muler, M., Strbik, V., Mazur, A., and Presz, A. "The effect of hydrostatic extrusion on the $J_c(B)$ characteristic of ex situ MgB_2 wires". *Superconductor Science and Technology* **18**, 552–556 (2005).

[158] Perner, O., Haessler, W., Fischer, C., Fuchs, G., Holzapfel, B., Schultz, L., and Eckert, J. "Enhanced critical current density in nanocrystalline mechanically alloyed MgB_2 bulk and Fe sheathed tapes". *IEEE Transactions on Applied Superconductivity* **15**, 3192–3195 (2005).

[159] Soltanian, S., Wang, X., Horvat, J., Dou, S., Sumption, M., Bhatia, M., Collings, E., Munroe, P., and Tomsic, M. "High transport critical current density and large H_{c2} and H_{irr} in nanoscale SiC doped MgB_2 wires sintered at low temperature". *Superconductor Science and Technology* **18**, 658–666 (2005).

[160] Sumption, M., Bhatia, M., Buta, F., Bohnenstiehl, S., Tomsic, M., Rindfleisch, M., Yue, J., Phillips, J., Kawabata, S., and Collings, E. "Solenoidal coils made from monofilamentary and multifilamentary MgB_2 strands". *Superconductor Science and Technology* **18**, 961–965 (2005).

[161] Tanaka, K., Kitaguchi, H., Kumakura, H., Yamada, H., Hirakawa, M., and Okada, M. "Fabrication and transport properties of an MgB_2 solenoid coil". *Superconductor Science and Technology* **18**, 678–681 (2005).

[162] Tanaka, K., Kitaguchi, H., Kumakura, H., Hirakawa, M., Yamada, H., and Okada, M. "Fabrication and transport properties of MgB_2 mono-core wire and solenoid coil". *IEEE Transactions on Applied Superconductivity* **15**, 3180–3183 (2005).

[163] Xu, H., Feng, Y., Xu, Z., Li, C., Yan, G., Mossang, E., and Sulpice, A. "Effect of sintering temperature on properties of MgB_2 wire sheathed by low carbon steel tube". *Physica C* **419**, 94–100 (2005).

[164] Yamada, H., Hirakawa, M., Kumakura, H., Matsumoto, A., and Kitaguchi, H. "Superconducting properties of powder-in-tube MgB_2 tapes prepared with fine powders". *IEEE Transactions on Applied Superconductivity* **15**, 3337–3340 (2005).

[165] Haessler, W., Birajdar, B., Gruner, W., Herrmann, M., Perner, O., Rodig, C., Schubert, M., Holzapfel, B., Eibl, O., and Schultz, L. "MgB_2 bulk and tapes prepared by mechanical alloying: Influence of the boron precursor powder". *Superconductor Science and Technology* **19**, 512–520 (2006).

[166] Hata, S., Yoshidome, T., Sosiati, H., Tomokiyo, Y., Kuwano, N., Matsumoto, A., Kitaguchi, H., and Kumakura, H. "Microstructures of MgB_2/Fe tapes fabricated by an in situ powder-in-tube method using MgH_2 as a precursor powder". *Superconductor Science and Technology* **19**, 161–168 (2006).

[167] Hishinuma, Y., Kikuchi, A., Iijima, Y., Yoshida, Y., Takeuchi, T., and Nishimura, A. "Fabrication of MgB_2 superconducting wires as low activation superconducting materials for an advanced fusion reactor application". *Fusion Engineering and Design* **81**, 2467–2471 (2006).

[168] Jiang, C., Nakane, T., and Kumakura, H. "Pinning enhancement in nano-SiC and Si_3N_4 doped MgB_2 tapes: A comparative study". *Physica C* **436**, 118–122 (2006).

[169] Kim, J., Yeoh, W., Xu, X., Dou, S., Munroe, P., Rindfleisch, M., and Tomsic, M. "Superconductivity of MgB_2 with embedded multiwall carbon nanotube". *Physica C* **449**, 133–138 (2006).

[170] Kim, J., Yeoh, W., Qin, M., Xu, X., Dou, S., Munroe, P., Kumakura, H., Nakane, T., and Jiang, C. "Enhancement of in-field $J_c$in MgB_2 Fe wire using single- and multiwalled carbon nanotubes". *Applied Physics Letters* **89**, 122510 (2006).

[171] Kováč, P., Hušek, I., Melišek, T., Martinez, E., and Dhalle, M. "Properties of doped ex and in situ MgB_2 multi-filament superconductors". *Superconductor Science and Technology* **19**, 1076–1082 (2006).

[172] Kováč, P., Hušek, I., Melišek, T., Haessler, W., and Herrmann, M. "Improvement of current density by texture and I_c anisotropy in thin filament MgB_2/Fe tapes". *Superconductor Science and Technology* **19**, 998–1002 (2006).

[173] Kováč, P., Hušek, I., Melišek, T., Kulich, M., and Strbik, V. "MgB_2 composite wires with Fe, Nb and Ta sheaths". *Superconductor Science and Technology* **19**, 600–605 (2006).

[174] Kuroda, T., Nakane, T., Uematsu, H., and Kumakura, K. "Doping effects of nanoscale Fe particles on the superconducting properties of powder-in-tube processed MgB_2 tapes". *Superconductor Science and Technology* **19**, 1152–1157 (2006).

[175] Lezza, P., Senatore, C., and Flukiger, R. "Improved critical current densities in B_4C doped MgB_2 based wires". *Superconductor Science and Technology* **19**, 1030–1033 (2006).

[176] Ma, Y., Xu, A., Li, X., Zhang, X., Awaji, S., and Watanabe, K. "Enhanced critical current density of MgB_2 superconductor synthesized in high magnetic fields". *Japanese Journal of Applied Physics* **45**, L493–L496 (2006).

[177] Ma, Y., Zhang, X., Nishijima, G., Watanabe, K., Awaji, S., and Bai, X. "Significantly enhanced critical current densities in MgB_2 tapes made by a scaleable nanocarbon addition route". *Applied Physics Letters* **88**, 072502 (2006).

[178] Nakane, T., Kitaguchi, H., Fujii, H., and Kumakura, H. "Improvement of ex-situ MgB_2 powder in tube processed tapes using MgH_2 powder". *Physica C: Superconductivity and its Applications* **445-448**, 784–787 (2006).

[179] Nakane, T., Kitaguchi, H., and Kumakura, H. "Ex situ fabrication of MgB_2 Al tapes with high critical current density". *Superconductor Science and Technology* **19**, 528–533 (2006).

[180] Pachla, W., Morawski, A., Kovac, P., Husek, I., Mazur, A., Lada, T., Diduszko, R., Melisek, T., Strbik, V., and Kulczyk, M. "Properties of hydrostatically extruded in situ MgB_2 wires doped with SiC". *Superconductor Science and Technology* **19**, 1–8 (2006).

[181] Schlachter, S. I., Goldacker, W., Frank, A., Ringsdorf, B., and Orschulko, H. "Properties of MgB_2 superconductors with regard to space applications". *Cryogenics* **46**, 201–207 (2006).

[182] Shcherbakova, O., Dou, S., Soltanian, S., Wexler, D., Bhatia, M., Sumption, M., and Collings, E. "The effect of doping level and sintering temperature on $J_c(H)$ performance in nano-SiC doped and pure MgB_2 wires". *Journal of Applied Physics* **99**, 08M510 (2006).

[183] Takahashi, M., Tanaka, K., Okada, M., Kitaguchi, H., and Kumakura, H. "Relaxation of trapped high magnetic field in 100 m-long class MgB_2 solenoid coil in persistent current mode operation". *IEEE Transactions on Applied Superconductivity* **16**, 1431–1434 (2006).

[184] Xu, H., Feng, Y., Yan, G., Li, C., and Xu, Z. "Investigation of MgB_2 Fe wires with different diameters". *Superconductor Science and Technology* **19**, 1169–1172 (2006).

[185] Xu, H., Feng, Y., Xu, Z., Yan, G., Li, C., Mossang, E., and Sulpice, A. "Effects of TiB_2 doping on the critical current density of MgB_2 wires". *Physica C* **443**, 5–8 (2006).

[186] Yamada, H., Hirakawa, M., Kumakura, H., and Kitaguchi, H. "Effect of aromatic hydrocarbon addition on in situ powder-in-tube processed MgB_2 tapes". *Superconductor Science and Technology* **19**, 175–177 (2006).

[187] Zhang, X., Ma, Y., Gao, Z., Yu, Z., Nishijima, G., and Watanabe, K. "Enhancement of J_c-B properties in $MoSi_2$-doped MgB_2 tapes". *Superconductor Science and Technology* **19**, 699–702 (2006).

[188] Zhang, X., Gao, Z., Wang, D., Yu, Z., Ma, Y., Awaji, S., and Watanabe, K. "Improved critical current densities in MgB_2 tapes with ZrB_2 doping". *Applied Physics Letters* **89**, 132510 (2006).

[189] Zhang, X., Ma, Y., Gao, Z., Yu, Z., Nishijima, G., and Watanabe, K. "The effect of different nanoscale material doping on the critical current properties of in situ processed MgB_2 tapes". *Superconductor Science and Technology* **19**, 479–483 (2006).

[190] Portney, L. G. and Watkins, M. P. *Foundations of Clinical Research: Applications to Practice*. Prentice Hall, (2000).

[191] Buzea, C. and Yamashita, T. "Review of the superconducting properties of MgB_2". *Superconductor Science and Technology* **14**, R115–R146 (2001).

[192] Cardwell, D. and Babu, N. "Processing and properties of single grain (RE)-Ba-Cu-O bulk superconductors". *Physica C* **445-448**, 1–7 (2006).

[193] Grivel, J., Eibl, O., Birajdar, B., Andersen, N., Abrahamsen, A., Pinholt, R., Grasso, G., Haessler, W., Herrmann, M., Perner, O., Rodig, C., Pachla, W Kovac, P., Husek, I., Mikheenko, P., Abell, S., and Homeyer, J. "Combined X-ray and electron microscopy study of MgB_2 powders, wires and tapes". *Journal of Physics Conference Series* **43**, 107–110 (2006).

[194] Gurevich, A. "Enhancement of the upper critical field by nonmagnetic impurities in dirty two-gap superconductors". *Physical Review B* **67**, 184515 (2003).

[195] Gurevich, A., Patbaik, S., Braccini, V., Kim, K., Milke, C., Song, X., Cooley, L., Bu, S., Kim, D., Choi, J., Belenky, L., Giencke, J., Lee, M., Tian, W., Pan, X., Siri, A., Hellstrom, E., Eom, C., and Larbalestier, D. "Very high upper critical fields in MgB_2 produced by selective tuning of impurity scattering". *Superconductor Science and Technology* **17**, 278–286 (2004).

[196] Koshelev, A. and Golubov, A. "Mixed state of a dirty two-band superconductor: application to MgB_2". *Physical Review Letters* **90**, 177002 (2003).

[197] Gonnelli, R., Daghero, D., Calzolari, A., Ummarino, G., Dellarocca, V., Stepanov, V., Kazakov, S., Zhigadlo, N., and Karpinski, J. "Evidence for single-gap superconductivity in $Mg(B_{1-x}C_x)_2$ single crystals with x=0.132 from point-contact spectroscopy". *Physical Review B* **71**, 060503 (2005).

[198] Yamamoto, A., Shimoyama, J., Ueda, S., Iwayama, I., Horii, S., and Kishio, K. "Effects of B_4C doping on critical current properties of MgB_2 superconductors". *Superconductor Science and Technology* **18**, 1323–1328 (2005).

[199] Van Weeren, H. Normal zone propagation in Nb_3Sn superconductors. Master's thesis, University of Twente, (2002).

[200] Van den Eijnden, N. Normal zone propagation in Nb_3Sn and MgB_2 conductors. Master's thesis, University of Twente, (2004).

[201] Dresner, L. *Stability of superconductors.* Plenum Press, (1995).

[202] Bae, D., Kang, H., Ahn, M., Sim, K., Kim, Y., Yoon, Y., and Ko, T. "Normal zone propagation characteristics of the HTS wires by heat energy applied". *Cryogenics* **46**, 373–377 (2006).

[203] Vysotski, V., Ilyin, Y., Rakhmanov, A., and Takeo, M. "Quench development analysis in HTSC coils by use of the universal scaling theory". *IEEE Transactions on Applied Superconductivity* **11**, 1824–1827 (2001).

[204] Arfken, G. *Mathematical Methods for Physicists.* Acadamic Press, Inc., (1985).

[205] Cherry, W. and Gittleman, J. "Thermal and electrondynamic aspects of the superconductive transition". *Solid State Electronics* **1**, 287 (1960).

[206] Morton, K. and Mayer, D. *Numerical solution of partial differential equations,*. Cambridge University Press, (1994).

[207] Dresner, L. "Propagation of normal zones in composite superconductors". *Cryogenics* **16**, 675–681 (1976).

[208] Den Ouden, A., Van Weeren, H., Wessel, W., Ten Kate, H., Kirby, G., Siegel, N., and Taylor, T. "Normal zone propagation in high-current density Nb_3Sn conductors for accelerator magnets". *IEEE Transactions on Applied Superconductivity* **14**, 279–282 (2004).

[209] Tritt, T., editor. *Thermal conductivity, theory, properties and applications.* Kluwer Academic, (2004).

[210] Miller, J., Lue, J., and Dresner, L. "Investigation of stability of composite superconductors in typical coil configurations". *IEEE Transactions on Magnetics* **13**, 24–27 (1977).

[211] Martínez, E., Lera, F., Martínez-López, M., Yang, Y., Schlachter, S., Lezza, P., and Kováč, P. "Quench development and propagation in metal/MgB_2 conductors". *Superconductor Science and Technology* **19**, 143–150 (2006).

[212] Scherer, M. and Turowski, P. "Investigation of the propagation velocity of a normal-conducting zone in technical superconductors". *Cryogenics* **18**, 515–520 (1978).

[213] Boxman, E., Dudarev, A., and Ten Kate, H. "The normal zone propagation in ATLAS B00 model coil". *IEEE Transactions on Applied Superconductivity* **12**, 1549–1552 (2002).

[214] Bauer, P. *Stability of superconducting strands for accelerator magnets.* PhD thesis, Technische Universität Wien, (1998).

[215] Gambardella, U., Saggese, A., Sessa, P., Guarino, A., Pace, S., Masullo, G., Matrone, A., Petrillo, E., and Quarantiello, R. "Stability measurements in multifilamentary MgB_2 tapes". presented at ASC 2006, Seattle (Wa), USA (2006).

[216] Troxel, J. "Glidcop dispersion strengthened copper: potential applications in fusion power generators". *IEEE Thirteenth Symposium on Fusion Engineering* **2**, 761–765 (1989).

[217] Stenvall, A., Korpela, A., Mikkonen, R., and Grasso, G. "Stability considerations of multifilamentary MgB_2 tape". *Superconductor Science and Technology* **19**, 184–189 (2006).

[218] Kitaguchi, H., Kumakura, H., and Togano, K. "Strain effect in MgB_2/stainless steel superconducting tape". *Physica C* **363**, 198–201 (2001).

[219] Kováč, P., Dhallé, M., Melišek, T., Van Eck, H., Wessel, W., Ten Haken, B., and Hušek, I. "Dependence of the critical current in ex situ multi- and mono-filamentary MgB_2/Fe wires on axial tension and compression". *Superconductor Science and Technology* **16**, 600607 (2003).

[220] Anderson, J., Cai, X., Feldmann, M., Polyanskii, A., Jiang, J., Parrell, J., Marken, K., Hong, S., and Larbalestier, D. "The influence of intermediate roll characteristics on the residual crack density and critical current density in multifilamentary (Bi, $Pb)_2Sr_2Ca_2Cu_3O_x$ tapes". *Superconductor Science and Technology* **12**, 617–623 (1999).

[221] Passerini, R., Dhallé, M., Witz, G., Seeber, B., and Flükiger, R. "Engineering the precompression of Bi,Pb(2223): the influence of the geometry of the metallic matrix on the mechanical properties of tapes". *IEEE Transactions on Applied Superconductivity* **11**, 3018–3021 (2001).

[222] Passerini, R., Dhallé, M., Giannini, E., Witz, G., Seeber, B., and Flükiger, R. "The influence of thermal precompression on the mechanical behaviour of Ag-sheathed (Bi,Pb)2223 tapes with different matrices". *Physica C* **371**, 173–184 (2002).

[223] Van der Laan, D. *Flux pinning and connectivity in polycrystalline high-temperature superconductors.* PhD thesis, University of Twente, (2004).

[224] Jewell, M., Lee, P., and Larbalestier, D. "The influence of Nb_3Sn strand geometry on filament breakage under bend strain as revealed by metallography". *Superconductor Science and Technology* **16**, 1005–1011 (2003).

[225] Ten Haken, B., Beuink, A., and Ten Kate, H. "Small and Repetitive Axial Strain Reducing the Critical Current in BSCCO/Ag Superconductors". *IEEE Transactions on Applied Superconductivity* **7**, 2034–2037 (1997).

[226] Cheggour, N., Ekin, J., Clickner, C., Verebelyi, D., Thieme, C., Feenstra, R., and Goyal, A. "Reversible axial-strain effect and extended strain limits in Y-Ba-Cu-O coatings on deformation-textured substrates". *Applied Physics Letters* **83**, 4223–4225 (2003).

[227] Cheggour, N., Ekin, J., and Thieme, C. "Magnetic-Field Dependence of the Reversible Axial-Strain Effect in Y-Ba-Cu-O Coated Conductors". *IEEE Transactions on Applied Superconductivity* **15**, 3577–3580 (2005).

[228] Van der Laan, D. and Ekin, J. "Large intrinsic effect of axial strain on the critical current of high-temperature superconductors for electric power applications". *Applied Physics Letters* **90**, 052506 (2007).

[229] Godeke, A., Van Weeren, H., Dhallé, M., Ten Kate, H., Jewell, M., Lee, P., and Larbalestier, D. "Correlations Between Strain Induced Crack Formation, Premature Dissipation in Voltage-Current Transitions and Non-elastic Scaling Behavior of Nb_3Sn Wires". presented at ASC 2004, Jacksonville (Fl), USA, August (2004).

[230] Cheggour, N. and Hampshire, D. "A probe for investigating the effects of temperature, strain, and magnetic field on transport critical currents in superconducting wires and tapes". *Review of Scientific Instruments* **71**, 4521–4530 (2000).

[231] Ten Haken, B., Godeke, A., and Ten Kate, H. "The influence of compressive and tensile axial strain on the critical properties of Nb_3Sn Conductors". *IEEE Transactions on Applied Superconductivity* **5**, 1909–1912 (1995).

[232] Kitaguchi, H., Itoh, K., Kumakura, H., Takeuchi, T., Togano, K., and Wada, H. "Strain effect in Bi-based oxide/Ag superconducting tapes". *IEEE Transactions on Applied Superconductivity* **11**, 3058–3061 (2001).

[233] Dhallé, M., Den Ouden, A., Ten Kate, H., Holubek, T., Hušek, I., and Kováč, P. "Filament to matrix current transfer in composite superconductors: going beyond the first-order approximation". presented at ASC 2006, Seattle (Wa), USA, August (2006).

[234] Cardwell, D. and Ginley, D. *Handbook of superconducting materials.* Institute of Physics Publishing, (2003).

[235] Angst, M., Puzniak, R., Wisniewski, A., Jun, J., Kazakov, S. M., Karpinski, J., Roos, J., and Keller, H. "Temperature and Field Dependence of the Anisotropy of MgB_2". *Physical Review Letters* **88**, 167004 (2002).

[236] Eisterer, M., Zehetmayer, M., and Weber, H. "Current percolation and anisotropy in polycrystalline MgB_2". *Physical Review Letters* **90**, 247002 (2003).

[237] Goldacker, W. and Schlachter, S. "Influence of mechanical reinforcement of MgB_2 wires on the superconducting properties". *Physica C* **378-381**, 889–893 (2002).

[238] Jorgensen, J., Hinks, D., and Short, S. "Lattice properties of MgB_2 versus temperature and pressure". *Physical Review B* **63**, 224522 (2001).

[239] Vogt, T., Schneider, G., Hriljac, J., Yang, G., and Abell, J. "Compressibility and electronic structure of MgB_2 up to 8 GPa". *Physical Review B* **63**, 220505 (2001).

[240] Nyilas, A., Osamura, K., and Sugano, M. "Mechanical and physical properties of Bi-2223 and Nb_3Sn superconducting materials between 300 K and 7 K". *Superconductor Science and Technology* **16**, 1036–1042 (2003).

[241] `http://www.goodfellow.com`.

[242] Kaye, G. and Laby, T. *Tables of physical and chemical constants, and some mathematical functions*. Longmans: London, (1966).

[243] `http://www.specialmetals.com/`.

[244] Kováč, P., Melišek, T., Dhallé, M., Den Ouden, A., and Hušek, I. "Critical currents of MgB_2 wires prepared in situ and ex situ subjected to axial stress". *Superconductor Science and Technology* **18**, 1374–1379 (2005).

[245] Lorenz, B., Meng, R., and Chu, C. "High-pressure study on MgB_2". *Physical Review B* **64**, 012507 (2001).

[246] Tang, J., Qin, L.-C., Gu, H.-W., Matsushita, A., Takano, Y., Togano, K., Kito, H., and Ihara, H. "Structural and electronic properties of superconductor MgB_2 under high pressure". *Journal of Physics: Condensed Matter* **14**, 10623–10626 (2002).

[247] Kitaguchi, H., Matsumoto, A., Hatakeyama, H., and Kumakura, H. "Critical current of magnesium diboride/stainless steel composite tapes under tensile or compressive strains". *Superconductor Science and Technology* **16**, 976–979 (2003).

[248] Kotegawa, H., Ishida, K., Kitaoka, Y., Muranaka, T., Nakagawa, N., Takagiwa, H., and Akamitsu, J. "Evidence for strong-coupling s-wave superconductivity in MgB_2: ^{11}B-NMR study of MgB_2 and the related materials". *Physica C* **378**, 25–32 (2002).

[249] Kitaguchi, H. and Kumakura, H. "Superconducting and mechanical performance and the strain effects of a multifilamentary MgB_2/Ni tape". *Superconductor Science and Technology* **18**, S284–S289 (2005).

[250] Bai, H., Luo, J., D, J., and Sun, J. "Particle size and interfacial effect on the specific heat of nanocrystalline Fe". *Journal of Applied Physics* **79**, 361–364 (1996).

[251] Junod, A., Wang, Y., Bouguet, F., Sheikin, I., Toulemonde, P., Eskildsen, M., Eisterer, M., Weber, H., Lee, S., and Tajima, S. "Specific heat of ceramic and single crystal MgB_2". *Physica C* **388-389**, 107–108 (2003).

[252] Fisher, R., Guangtao, L., Lashley, J., Bouquet, F., Philips, N., Hinks, D., Jorgensen, J., and Crabtree, G. "Specific heat of $Mg^{11}B_2$". *Physica C* **385**, 180–191 (2003).

[253] Bauer, E., Paul, C., Berger, S., Majumdar, S., Michor, H., Giovaninni, M., Saccone, A., and A, B. "Thermal conductivity of superconducting MgB_2". *Journal of Physics: Condensed Matter* **13**, L487–L493 (2001).

[254] Jung, C., Park, M., Kang, W., Kim, M., Lee, S., and Lee, S. "Temperature- and magnetic field-dependent resistivity of MgB_2 sintered at high-temperature and high-pressure condition". *Physica C* **353**, 162–166 (2001).

[255] Bejan, A. *Heat Transfer*. John Wiley & Sons, Inc., (1993).

[256] Benford, D., Powers, T., and Mosely, S. "Thermal conductivity of Kapton tape". *Cryogenics* **39**, 93–95 (1999).

Summary

With the discovery of its superconducting properties in 2001, MgB_2 is the latest superconductor for use in large scale applications such as superconducting magnets.

Compared to other metallic superconductors like Nb-Ti and Nb_3Sn, it has the advantage of a higher T_c (40 K), which enables magnets to operate at higher temperatures ($\sim$ 20 K) and cuts down cooling costs. Compared to high-T_c conductors such as $YBa_2Cu_3O_x$ and $Bi_2Sr_2Ca_2Cu_3O_x$ on the other hand, it is a relatively simple compound and therefore easier to synthesise. Together with the abundance of magnesium and boron, this causes its presently estimated cost-to-performance ratio to be a factor of ~ 100 lower than that of high-T_c conductors.

MgB_2 conductors are fabricated with the Power-In-Tube technology, a technique that is already applied for Nb_3Sn and Bi-based high-T_c superconductors. In this study the ex-situ route is chosen, in which pre-reacted MgB_2 powder is sealed in a metal tube that is subsequently drawn into wires or rolled into tapes. The resulting conductors consist of a composite metal matrix embedding MgB_2 filaments.

Such a composite conductor can break already in an early stage of wire drawing. A first possible cause is the particle size of the MgB_2 powder. In the as-purchased powder, the largest particles ($\sim$ 100 μm) cause stress concentrations in the matrix during deformation. An effective technique to reduce the particle size is shear milling, in which the as-purchased powder is suspended in a fluid and milled with a relatively large number of small milling balls ($d \sim 3$ mm). Due to shear stresses, the maximum particle size reduces to $\sim$ 2 μm after 48 h of milling. However, care has to be taken with the choice of suspension fluid. Ethanol and isopropanol leave carbon in-between the MgB_2 grains, compromising the superconducting properties of the MgB_2 filament.

A second possible cause of premature wire breakage during drawing is the choice of matrix materials, which is not only dictated by ease of deformation but also by a number of functional requirements. The matrix should be a highly conducting material such as Cu or Al to provide stabilisation against thermal disturbances. Unfortunately, MgB_2 tends to react strongly with such materials so that a practical wire typically has a bimetal matrix consisting of a chemically compatible inner layer and a highly conducting outer layer. These type of materials often have a different hardness, which may lead to breakage of the hardest of

them due to different flow characteristics of the individual metals. Model calculations and experiments show that careful selection of the volume fractions of the matrix metals can prevent premature breakage.

One important parameter dictating the critical current density of the conductor is the maximum attainable filament density, since it determines the degree of grain-to-grain connectivity. For the ex-situ route, drawing alone leads to insufficient powder density due to the poor flow characteristics of the hard MgB_2 particles. With tape rolling significantly higher filament densities can be achieved, resulting in a factor of 5-10 higher critical current density.

Addition of Pb to the MgB_2 filaments can facilitate powder flow by acting as a lubricant during deformation. This is demonstrated by the higher maximum reduction that can be achieved during drawing. Pb also enhances the thermal stability of the conductors at high currents and low magnetic fields.

To illustrate trends and prospects in the development of MgB_2 conductors a statistical study of critical current versus magnetic field data published over the years 2003-2006 was conducted. The main progress in the development of MgB_2 conductors is found in the field retention of the critical current. Between 2003 and 2006 the usable field range has, on average, increased by 25 %. This progress is mainly a consequence of the trend towards in-situ conductors, in which unreacted Mg and B are put into the matrix as separate phases. In this type of conductor low-level doping can better be controlled and increases the field retention of the critical current. It was found that carbon-based dopants tend to enhance the field retention of the critical current more than non carbon-based dopants. This could suggest that carbon based dopants improve the second critical field as well as magnetic flux line pinning, while non-carbon based dopants only enhance pinning.

One of the requirements on MgB_2 conductors used in magnets is imposed by the need to protect the device against thermal instabilities. Already small heat releases of the order of μJ can cause the conductors' temperature to rise locally above its critical temperature, creating a normal-conducting zone. The heat released in this zone can lead to a burnout of the conductor, unless the normal conducting zone is detected in time, protection circuits can be triggered and the current switched off.

The probability that a normal zone occurs is inversely proportional to the minimum quench energy. Measurements show the minimum quench energy of MgB_2 conductors to be typically a factor $\sim$ 1000 higher than in low-T_c conductors. Thus, the probability that a thermal disturbance induces a normal zone is significantly lower than in low-T_c conductors.

The ease of protection against burnout depends on the speed with which the normal zone propagates. High-T_c conductors typically display quasi-static heating and detection is difficult. In low-T_c conductors protection is easier due to the relatively fast propagation of the normal zone, with several m/s. In MgB_2 conductors the normal zone propagates a factor of $\sim$ 100 slower than in low-T_c conductors.

Thus, protection is considerably easier than with high-T_c conductors but requires more care than in low-T_c conductors.

In magnets large Lorentz forces act on the superconducting windings, which influence the superconducting properties. Application of MgB_2 conductors in magnets requires that they withstand these electro-mechanically induced strains.

The strain dependence of the critical current show two regimes. For compressive strains and at low tensile strain levels, MgB_2 conductors show a linear and reversible strain dependence of the critical current, while at higher tensile strain levels the wire is damaged and the critical current degrades steeply and irreversibly.

The boundary between the two regimes is, to first order, dictated by the thermal pre-strain that the matrix exerts on the filaments. This implies that the maximum strain that an MgB_2 conductor can tolerate can be increased by choosing a matrix material that has a relatively large thermal expansion coefficient.

In the linear regime, the strain dependence of the critical current has an electronic origin. Important for magnet design is that in this reversible regime the strain dependence of the critical current at any given temperature and magnetic field can be predicted by knowing only three parameters: the strain sensitivity of the zero-temperature, zero-field extrapolation of the critical current; that of the critical temperature; and that of the zero-temperature extrapolation of the irreversibility field.

The general conclusion of this thesis is that at present MgB_2 already constitutes a practical superconductor for magnet applications requiring peak fields of 7-10 T at 4.2 K or 3-5 T at 20 K. It is likely that these fields will increase further. From a technical point of view, thermal stability and electro-mechanical issues can be addressed by careful conductor design, just like with any other technical superconductor.

Samenvatting (Summary in Dutch)

Met de ontdekking van supergeleidende eigenschappen in MgB_2 in 2001, is het de nieuwste supergeleider voor gebruik in grootschalige toepassingen zoals magneten.

Vergeleken met andere metallische supergeleiders zoals Nb-Ti en Nb_3Sn heeft MgB_2 het voordeel van een hogere T_c (40 K). Hierdoor kunnen magneten gebruikt worden bij een hogere temperatuur ($\sim$ 20 K), met lagere kosten voor koeling. Aan de andere kant, in vergelijking met keramische hoge-T_c geleiders zoals $YBa_2Cu_3O_x$ en $Bi_2Sr_2Ca_2Cu_3O_x$ is MgB_2 een relatief eenvoudige verbinding en dus makkelijker te synthetiseren. Samen met de ruime beschikbaarheid van magnesium en boor betekent dit dat de "prijs-kwaliteit" verhouding een factor ~ 100 lager liggen dan bij hoge-T_c geleiders.

MgB_2 geleiders worden gemaakt met de zogenaamde Poeder-In-Buis technologie. Deze techniek wordt al geruime tijd gebruikt voor Nb_3Sn en hoge-T_c geleiders op basis van bismuth. In dit onderzoek is de ex-situ route gekozen waarbij een metalen buis met voorgereageerd MgB_2 poeder wordt gevuld en vervolgens wordt getrokken tot draden of gewalst tot tapes. De resulterende geleider bestaat dan uit een composietmatrix met daarin MgB_2 filamenten.

Een dergelijk samengestelde geleider kan tijdens het draadtrekken al in een vroeg stadium breken. Een mogelijke oorzaak is de deeltjesgrootte van het MgB_2 poeder. In het aangekochte poeder kunnen tijdens het draadvormen de grootste deeltjes ($\sim$ 100 μm) spanningsconcentraties veroorzaken in de matrix. Een effectieve techniek om de deeltjesgrootte te reduceren is malen door middel van afschuifspanningen. Hierbij wordt het poeder in suspensie gebracht en vervolgens gemaald, waarbij een groot aantal kleine maalballetjes ($d \sim 3$ mm) afschuifspanningen veroorzaken in de deeltjes. Na 48 uur malen is de maximum deeltjesgrootte gereduceerd tot ~ 2 μm. Voorzichtigheid is geboden bij de keuze van het suspensie vloeistof. Bijvoorbeeld ethanol en isopropanol laten koolstof achter tussen de MgB_2 deeltjes waarbij de supergeleidende eigenschappen verslechteren.

Een andere mogelijke oorzaak van vroegtijdige breuk tijdens het draadtrekken is de keuze van het matrix materiaal. Deze keuze wordt niet alleen bepaald door het gewenste trekgedrag, maar ook door een aantal functionele vereisten. Een van

de vereisten is dat de matrix een lage thermische en elektrische weerstand heeft, zodat de geleider thermische stabiel is. Voorbeelden van zulke metalen zijn Cu en Al. MgB_2 reageert echter sterk met deze materialen, zodat praktische geleiders typisch een bi-metalen matrix hebben met een chemisch compatibel binnenste laag en een goed geleidende buitenste laag. Vaak hebben deze metalen echter ook verschillende hardheden die kunnen leiden tot breuk vanwege te sterk afwijkende vloeikarakteristieken. Modelberekeningen en experimenten tonen aan dat een zorgvuldige keuze van de volumefracties van de matrix metalen vroegtijdige breuk kan voorkomen.

Een belangrijke parameter die de kritieke stroomdichtheid in de geleider bepaalt is de maximaal haalbare dichtheid van het filament. Dit bepaalt in welke mate individuele deeltjes elektrisch contact hebben. Slechts trekken van ex-situ draad leidt to onvoldoende poederdichtheid vanwege het gebrekkige vloeigedrag van de harde MgB_2 poederdeeltjes. Het rollen tot een tape daarentegen leidt tot aanmerkelijk hogere filamentdichtheden, wat resulteert in kritieke stroomdichtheden die een factor 5-10 hoger zijn.

Toevoeging van Pb aan het MgB_2 poeder als smeermiddel tijdens de deformatie leidt tot gunstiger vloeigedrag. Dit resulteert in een hogere maximale reductie tijdens het trekken. Een ander voordeel van het toegevoegde Pb is een verhoogde thermische stabiliteit van de geleiders bij hogere stromen en lager magnetische velden.

Om tendensen en vooruitzichten in de ontwikkeling van MgB_2 geleiders to bestuderen werd een statistische studie uitgevoerd omtrent de veldafhankelijkheid van de kritieke stroom in geleiders waarover gepubliceerd werd tussen 2003 en 2006. In die jaren is het veldafhankelijkheid van de kritieke stroom gemiddeld verbeterd met 25 %. Deze vooruitgang is toe te schrijven aan de trend richting in-situ geleiders waarbij ongereageerd Mg en B als aparte materialen in de matrix worden gebracht. In dit type geleider kan het toevoegen van doteringen beter gecontroleerd worden en als gevolg daarvan verbetert de veldafhankelijkheid van de kritieke stroom. Doteringen die gebaseerd zijn op koolstof verbeteren de veldafhankelijkheid van de kritieke stroom meer dan doteringen die op andere materialen zijn gebaseerd. Dit kan erop duiden dat dotering gebaseerd op koolstof zowel de tweede kritieke veld als de pinning kracht van de magnetische fluxlijnen verbetert, terwijl andere doteringen alleen de pinning kracht verhogen.

Een van de vereisten voor MgB_2 geleiders in magneten wordt bepaald door het feit dat het instrument beveiligd moet kunnen worden tegen thermische instabiliteit. Kleine warmte ontwikkelingen van de grootte-orde μJ kunnen de temperatuur van de geleider lokaal doen stijgen boven de kritieke temperatuur. Hierbij wordt een normaal geleidende zone gecreëerd. De warmteontwikkeling in deze zone kan leiden tot doorbranden van de geleider, tenzij de normale zone op tijd wordt gedetecteerd, beveiligingscircuits worden geactiveerd en de stroom wordt uitgeschakeld.

De kans dat een normaal geleidende zone ontstaat is omgekeerd evenredig met

de "minimum quench energy". Metingen laten zien dat de "minimum quench energy" van MgB_2 geleiders typisch een factor $\sim$ 1000 hoger is dan typische waarden voor lage-T_c geleiders. Dit betekent dat de kans dat een thermische verstoring een normale zone veroorzaakt significant kleiner is.

Hoe goed de geleider beveiligd kan worden tegen doorbranden wordt bepaald door de snelheid waarmee de normale zone zich uitbreidt. In hoge-T_c geleiders is beveiliging relatief moeilijk omdat ze lokaal en quasi-statisch kunnen opwarmen na een thermische verstoring. In lage-T_c geleiders daarentegen is beveiliging relatief makkelijk door de snelle propagatie van de normale zone met enige meters per seconde. In MgB_2 geleiders propageert de normale zone met een factor $\sim$ 100 langzamer dan in lage-T_c geleiders. Dit betekent dat beveiliging aanzienlijk makkelijker is dan in hoge-T_c geleiders, maar meer zorgvuldigheid vereist dan in lage-T_c geleiders.

In magneten ondervinden de supergeleidende windingen hoge mechanische belasting vanwege de Lorentz krachten en de supergeleidende eigenschappen worden hierdoor beïnvloed. Het toepassen van MgB_2 geleiders in magneten vereist dat ze bestand zijn tegen deze elektro-mechanisch geïnduceerde rek.

De rekafhankelijkheid van de kritieke stroom heeft twee regimes. Voor druk (compressie) en lage rektoestanden heeft de kritieke stroom een lineaire en reversibel rekafhankelijkheid. Bij grotere rekwaarden beschadigt de draad en neemt de kritieke stroom abrupt en irreversibel af.

De grens tussen de twee gebieden wordt, in eerste aanleg, bepaald door de thermische voorspanning die de matrix uitoefent op de filamenten. Dit houdt in dat de maximale rek die een MgB_2 geleider kan verdragen kan worden verhoogd door een matrix materiaal te gebruiken met een relatief hoge thermische uitzettingscoëfficiënt.

In het lineaire gebied heeft de rekafhankelijkheid van de kritieke stroom een elektronische oorsprong. Belangrijk voor het ontwerpen van magneten is dat in dit reversibele gebied de rekafhankelijkheid van de kritieke stroom voor elke gegeven temperatuur en elk veld voorspeld kan worden met slechts drie parameters: de rekgevoeligheid van de naar 0 K en 0 T geëxtrapoleerde kritieke stroom; van de kritieke temperatuur; en van het naar 0 K geëxtrapoleerde "irreversibiliteits veld".

De algemene conclusie van dit proefschrift is dat de huidige MgB_2 geleiders al een praktische materiaal vormen voor toepassing in magneten waarbij een maximaal veld wordt vereist van 7-10 T bij 4.2 K of 3-5 T bij 20 K. Bovendien is het erg waarschijnlijk dat deze veldwaarden verder zullen stijgen. Vanuit technisch oogpunt zullen MgB_2 geleiders, net als alle andere praktische supergeleiders, zorgvuldig ontworpen moeten worden om te voldoen aan eisen omtrent thermische stabiliteit en electro-mechanische kwesties.

Dankwoord

"Ben je goed genoeg om te promoveren?" Een typische vraag van Herman ten Kate, ergens gedurende mijn afstuderen. Een flinke hoeveelheid MgB_2 geleiders, allerhande metingen en een flink proefschrift later ben ik toegekomen aan schrijven van het dankwoord. Het moge duidelijk zijn wat mijn antwoord op Hermans vraag was.

Terugkijkend, realiseer ik me dat het een erg multidisciplinair promotieonderzoek is geworden: van de preparatie van MgB_2 geleiders tot onderzoek naar de applicatie in magneten. Een dergelijk breed onderzoek is iets wat ik erg leuk vind om te doen. Dat betekent automatisch dat er ook veel mensen zijn die meegewerkt hebben aan het project en die ik hier wil bedanken.

Allereerst wil ik Herman bedanken, niet alleen voor bovenstaande vraag, maar ook voor de vrijheid die ik heb gekregen om een breed stuk onderzoek te doen.

Daarnaast wil ik Marc bedanken. Natuurlijk moet ik hem bedanken voor zijn inspirerende gedrevenheid, de geweldige begeleiding tijdens mijn promotie en het geduld waarmee hij de ruwe tekst van mijn proefschrift heeft nagekeken. Maar ik wil hem zeker ook bedanken voor de gezellige avonden bij Molly's, discussiërend over politiek of muziek en onder het genot van de nodige Murphy's.

Samen met Sander heb ik vele buisjes met MgB_2 poeder gevuld en vervolgens dagen achter elkaar draadjes getrokken. Dat laatste ging meestal gepaard met de fantastische muziek van Sky Radio.... Onze roadtrip naar Bratislava was erg gezellig en het bier is er ook nog goedkoop: "Huh, het bier is hier goedkoper dan water!". Daarnaast toonde Sander zich een geweldige technische steun en toeverlaat met een flink portie "drive". Niet voor niets is Sander één van mijn paranimfen. Sander, bedankt!

Bij SMI hebben wij menig draad getrokken. Jan en Koos, bedankt voor het gebruik van jullie infrastructuur en de wijze raad die jullie hebben gegeven gedurende het project.

I find myself lucky that I could perform experiments at other laboratories during the project. I would like to thank Dr. Pavol Kováč and Imrich Hušek for their hospitality during our visit at IEE in Bratislava, the help with the TAR experiments and the great discussions. During the evenings Tomáš Holúbek was always willing to show us around and point out the good pubs; thanks! I also spend some time at the University of Geneva for the rolling experiments. For this I would like to thank Prof. Flükiger for his hospitality and for the use of the

deformation machines and VSM. During my stay Paola Lezza helped me out a lot with the drawing and rolling machines. Paola, thanks a lot and good luck at Bruker!

Voor degene die de inhoud van dit proefschrift hebben gelezen is het duidelijk geworden dat praktische supergeleiders maken met MgB_2 poeder nogal wat voeten in de aarde heeft gehad. Louis van Winnubst en Shen Ran van de IMS groep hebben geholpen bij het prepareren van het MgB_2 poeder. Ook Frits Bakker van ECN heeft geweldig geholpen met de ICP metingen. Daarnaast heeft Marc Smithers de nodige HRSEM en EDX plaatjes geschoten. Bedankt daarvoor.

Na 6 jaar wereldwijd onderzoek naar praktische MgB_2 supergeleiders waren we ook wel eens nieuwsgierig naar het toekomstperspectief en trends van dit materiaal. Dit vergde een grondige statistische analyse waarvoor ik speciaal Esther wil bedanken, die mij in no-time het één en ander bijgebracht over statistiek.

Met Andries en Yuri heb ik vele nuttige discussies gevoerd over normal zone development. Als afstudeerder heeft Nick van den Eijnden een grondige basis gelegd voor het NZP werk met de eerste metingen op MgB_2 geleiders en heeft hij de numerieke code flink onder handen genomen. Heren, bedankt!

Graag wil ik ook Radboud bedanken. Hij heeft zeer grondig de tekst doorgenomen en zodoende (schoonheids) foutjes tot een minimum weten te beperken.

Met Yuri, Arend en Hennie heb ik het kantoor gedeeld. Zij maakten de periode dat ik aan het schrijven was enigszins draaglijk. Natuurlijk wil ik ook de rest van "T2" bedanken voor de gezellige tijd die ik de afgelopen vier jaar heb gehad. Daarnaast wil ik ook Ans & Inke bedanken voor het regelwerk, de "ATF" voor de leuke praatjes en borrels en mag ik ook zeker Harry niet vergeten voor de aanvoer van de vele liters helium.

During my life as a PhD student I shared frustrations and successes –small and big– with Koray, who is my other paranimph. It is always good to discuss these things with a co-PhD student and friend. Thanks, Koray!

Hoewel het er soms wel op lijkt, gaat het leven van een AIO niet alleen over promoveren. Ik wil mijn vrienden bedanken voor de leuke tijd die ik met ze heb en die mijn promovendusleven een stuk aangenamer hebben gemaakt. Daarnaast wil ik speciaal mijn ouders, Chris en Trudy, bedanken voor hun interesse en steun. Als laatste wil ik mijn lieve Irene bedanken voor haar steun, gezelligheid en liefde!

Harald.